

**TRANSPORT STUDIES OF SPIN POLARIZED
CARRIERS IN SEMICONDUCTORS**

By
SHAILESH KUMAR KHAMARI
PHYS03201104004

Raja Ramanna Centre For Advanced Technology, Indore

*A thesis submitted to the
Board of Studies in Physical Sciences
In partial fulfillment of requirements
for the Degree of*
DOCTOR OF PHILOSOPHY
of
HOMI BHABHA NATIONAL INSTITUTE

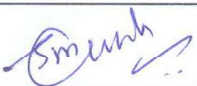
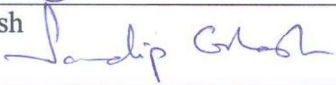


October 2016

Homi Bhabha National Institute¹

Recommendations of the Viva Voce Committee

As members of the Viva Voce Committee, we certify that we have read the dissertation prepared by Shailesh Kumar Khamari entitled “Transport Properties of spin polarized carriers in semiconductor” and recommend that it may be accepted as fulfilling the thesis requirement for the award of Degree of Doctor of Philosophy.

Chairman – Prof. P.A. Naik		Date: 27/11/2017
Guide / Convener – Prof. T. K. Sharma		Date: 27/11/17
Examiner – Prof. V. Venkataraman	V. Venkataraman	Date: 27/11/17
Member 1- Prof. H. S. Rawat		Date: 27/11/17
Member 2- Prof. K. S. Bindra		Date: 27/11/17
Member 3- Prof. S. K. Dixit		Date: 27/11/17
Member 4- Prof. Aparna Chakrabarti	Aparna Chakrabarti	Date: 27.11.17
Member 5- Prof. S. M. Gupta		Date:
External Member - Prof. Sandip Ghosh		Date: 27/11/17

Final approval and acceptance of this thesis is contingent upon the candidate's submission of the final copies of the thesis to HBNI.

I/We hereby certify that I/we have read this thesis prepared under my/our direction and recommend that it may be accepted as fulfilling the thesis requirement.

Date: 27/11/2017

Place: RRCAAT



Prof. T. K. Sharma

¹ This page is to be included only for final submission after successful completion of viva voce.

STATEMENT BY AUTHOR

+

This dissertation has been submitted in partial fulfillment of requirements for an advanced degree at Homi Bhabha National Institute (HBNI) and is deposited in the Library to be made available to borrowers under rules of the HBNI.

Brief quotations from this dissertation are allowable without special permission, provided that accurate acknowledgement of source is made. Requests for permission for extended quotation from or reproduction of this manuscript in whole or in part may be granted by the Competent Authority of HBNI when in his or her judgment the proposed use of the material is in the interests of scholarship. In all other instances, however, permission must be obtained from the author.



Shailesh Kumar Khamari

DECLARATION

I, hereby declare that the investigation presented in the thesis has been carried out by me. The work is original and has not been submitted earlier as a whole or in part for a degree / diploma at this or any other Institution / University.

Shailesh Khamari

Shailesh Kumar Khamari

List of Publications arising from the thesis

Journal

Published

1. “Numerical simulation of inverse spin Hall spectra in Pt/GaAs hybrid structure”, Shailesh K Khamari, V K Dixit and S M Oak, J. Phys. D: Appl. Phys., **2011**, 44, 265104
2. “Temperature dependence of the photo-induced inverse spin Hall effect in Au/InP hybrid structures”, Shailesh K. Khamari, S. Porwal, V. K. Dixit and T. K. Sharma, Appl. Phys. Lett. **2014**, 104, 042102
3. “A spin-optoelectronic detector for the simultaneous measurement of the degree of circular polarization and intensity of a laser beam”, Shailesh K. Khamari, S. Porwal, S. M. Oak and T. K. Sharma, Appl. Phys. Lett. **2015**, 107, 072108

Communicated

1. “Measurement of Spin Hall conductivity of n-GaAs epitaxial layer through inverse spin Hall Effect and optical orientation experiments” Shailesh K. Khamari, S. Porwal and T. K. Sharma
2. “Estimation of electron spin polarization from circular polarized Photoluminescence in strained quantum wells” Shailesh K. Khamari, S. Porwal and T. K. Sharma

Conferences

1. “A comparison of inverse spin hall spectra in Pt/III-V hybrid structures”, Shailesh K. Khamari and V. K. Dixit, American Inst. Of Physics Conf. Proc. **2012**, 1447, 1057
2. “Photo-Induced Inverse Spin Hall Effect in Au/InP hybrid structure, Shailesh K. Khamari”, S. Porwal, T. K. Sharma, S. M. Oak, Proceedings of International Workshop on Physics of Semiconductor Devices, Springer, **2014**, pp 855-857
3. “Spin-Optoelectronic device for light polarization and intensity detection” Shailesh K. Khamari, S. Porwal and T. K. Sharma, Proceedings of International Workshop on Physics of Semiconductor Devices, Bangalore-**2015**

Shailesh Khamari

Shailesh Kumar Khamari

Acknowledgement

I owe special debt of gratitude to many people who contributed to the completion of this work.

First and foremost, I would like to acknowledge and owe my deep and sincere gratitude to my supervisor Prof. T. K. Sharma, whose constant encouragement, valuable suggestions/ discussions and unhindered motivation have made my research life more smooth and enjoyable. His keen interest towards the scientific problems and prompt response to find out a feasible solution made me work without much of worries. Also, I am thankful to him for his patience while going through the initial phase of the report page by page. He will be happy to see the completion of this work in time. It is a pleasure to work with him.

My acknowledgements deservedly find a name as Dr. V. K. Dixit, for giving shape to my scientific intuition and research aptitude in the initial phases of my career and being there as a friend, philosopher and guide all through. I was enormously benefited from his willingness to share the best of scientific experiences and knowledge without any hesitation.

The person, who has helped me a lot in conducting the experiments needs to be mentioned specially. He is Mr. Sanjay Porwal, whose practical approach to the experiment and patience while optimizing the set up pushed me to measure those very small signals, which I would have not dared, otherwise.

Establishing the experimental set ups, would not have been possible, without the help of Mr. Alexander Khakha, who helped me in Lab automation and data acquisition. Thanks are due to Ravindra Jangir for useful discussions during the initial phase and to Dr. S.D. Singh for discussions and help in understanding *k.p*

methods. In my daily work I have been blessed with friendly and cheerful support of Mr. U. K. Ghosh. I simply cannot wish for a better or friendlier atmosphere.

I am also thankful to staff of Cryo-engineering and Cryo-module Development Division and Mechanical workshop, for providing support during the establishment of experimental set up.

As the head of division, initially Dr. S.M. Oak and later Dr. K. S. Bindra have made available their support in a number of ways. Without their support, this thesis would not have been completed. It is an honor for me to thank these stalwarts. I am grateful to the members of my Ph.D. advisory committee, for their critical comments and valuable suggestions.

I will like to acknowledge the company of Mr. Abhishek Chatterjee, who has worked with me in the lab, and I have learned a lot, while “teaching” him the art of electronic transport experiments. I would also like thank all the staff members of Semiconductor Physics and Devices Laboratory for providing their help by, wherever and whenever needed.

The much needed boost to my scientific carrier was provided by Prof. Surya Narayan Nayak, Sambalpur University. I am in shortage of words that can convey my gratitude towards him. Thank you Sir to provide me the support, that I needed the most during M.Sc and post M.Sc.

My wife “Payal” needs to be acknowledged specially for her patience and strength to tolerate my negligence during the writing period. She has sacrificed “her” weekends to check for various corrections in the thesis. Finally, I acknowledge my caring family and loving parents for my being and becoming. It was one of the dreams of my parents to see me completing my Ph.D. It is them, this work is dedicated.

Contents

	Page No
Synopsis	i
List of Figures	xi
List of Tables	xxiii
List of Symbols and Abbreviations	xxiv
Chapter 1 Introduction	1
1.1 Introduction to Semiconductor spintronics	1
1.2 Fundamental concepts	2
1.2.1 Spin orbit interaction	2
1.2.2 Optical orientation	5
1.2.2.1 Traditional approach	6
1.2.2.2 General approach	10
1.2.3 Spin relaxation	14
1.2.3.1 Elliot-Yafet mechanism	14
1.2.3.2 Dyakonov- Perel mechanism	15
1.2.3.3 Bir- Aronov- Pikus mechanism	17
1.2.3.4 Hyperfine interaction	18
1.2.4 Spin Hall Effect and Inverse Spin Hall Effect	18
1.2.4.1 Mechanism of Spin Hall Effect	22
1.3 Historical Overview of spin injection/detection experiments	24

1.3.1	Methods of Spin injection	24
1.3.2	Methods of Spin detection	25
1.3.3	Spin Hall Effect Measurements	27
1.4	Motivation behind this thesis	31
Chapter 2 Numerical Simulations for Inverse Spin Hall Effect		34
2.1	Necessity of numerical simulations	34
2.2	Methods adopted for numerical simulations	36
2.2.1	Sample geometry	36
2.2.2	Light propagation through a multilayer structure	37
2.2.3	Optical spin injection in semiconductors	40
2.2.4	Energy relaxation of photo-excited carriers	44
2.2.5	Spin relaxation of electrons	49
2.2.6	Tunneling and thermionic emission of photo-excited carriers	54
2.2.7	Role of high Z metals in the generation of ISHE signal	55
2.3	Numerical simulations of ISHE for Metal/Semiconductor Hybrid structures	56
2.3.1	Energy dependence of ISHE signal	56
2.3.2	Role of metal layer thickness in the magnitude of ISHE signal	58
2.3.3	Effect of the angle of incidence on the magnitude of ISHE	59
2.3.4	Barrier Height dependence of ISHE signal	60
2.3.5	Choice of III-V semiconductors	62
2.3.6	Choice of Metals	64

2.4	Theoretical predictionsfor Metal/Semiconductor Hybrid structures	65
Chapter 3 Sample fabrication and Experimental set up		67
3.1	Introduction	67
3.2	Sample fabrication	68
3.2.1	Metal-Organic Vapor Phase Epitaxy (MOVPE)	68
3.2.2	Device Fabrication	70
3.2.2.1	Chemical Cleaning	70
3.2.2.2	Photolithography	71
3.2.2.3	Metallization	73
3.2.3	Electrical characterization	75
3.3	Calibration of experimental set up	77
3.3.1	Calibration of orientation angle	78
3.3.2	Calibration of frequency	81
3.3.3	Calibration of retardation magnitude	82
3.3.4	Calibration with respect to beam position	84
3.4	Background signals and their minimization	86
3.4.1	Static birefringence	87
3.4.2	Modulated interference	88
3.4.3	Birefringence induced by experimental set up	89
3.5	Inverse Spin Hall Effect measurement set up	91
3.5.1	Optical alignment	91
3.5.2	Response of the measurement circuit	93

3.6	Polarization resolved photoluminescence set up	95
3.6.1	Comparison between two alternate experimental set ups	97
3.6.2	Principle of polarization analysis	98
Chapter 4	Observation of ISHE in Au/InP hybrid structure	101
4.1	Introduction	101
4.2	Sample preparation	102
4.3	ISHE Measurement	106
4.4	Temperature dependence of ISHE	109
4.4.1	Temperature dependent measurement	109
4.4.2	Estimation of Spin current density	110
4.4.3	Correlation with spin relaxation time	114
4.5	Outcome of the chapter	119
Chapter 5	ISHE measurements in bulk semiconductor	121
5.1	Introduction	121
5.2	Preliminary characterization of the high quality GaAs sample	125
5.3	Optical alignment	128
5.4	ISHE current extraction	129
5.5	Temperature dependence of ISHE signal	132
5.5.1	Local heating of the sample	133
5.5.2	Reflectivity	135
5.5.3	Spin injection	135
5.5.4	Impedance	137

5.6	Numerical estimation of Spin Diffusion current density	138
5.7	Measurement of Spin relaxation time	145
5.7.1	Analysis of polarization dependent PL	147
5.7.2	Estimation of spin relaxation time	150
5.8	Estimation of spin Hall conductivity	154
5.9	Outcome of the chapter	158
Chapter 6	ISHE measurements in quantum wells	160
6.1	Introduction	160
6.2	Quantification of the Electron spin polarization	163
6.2.1	k.p modeling to estimate the electron spin polarization	163
6.2.2	Effect of biaxial strain	166
6.2.3	Effect of quantum confinement	168
6.2.4	Combined effect of strain and quantum confinement	170
6.2.5	Effect of the split off band	171
6.3	Measurement of electron polarization in QW	173
6.4	Experimental estimation of electron spin polarization uniquely	177
6.4.1	Estimation Methods	177
6.4.2	Experimental verification	180
6.5	Estimation of spin injection efficiency from barrier to quantum well	186
6.6	ISHE measurement in GaAs/AlGaAs quantum well	191
6.7	Outcome of the chapter	195

Chapter 7 Fabrication of a spin optoelectronic device	196
7.1 Introduction	196
7.2 Methods for the detection of the degree of circular polarization of light	197
7.3 Factors contributing in the output of a conventional spin-phonic detector	199
7.4 Proposal of a three terminal device as one possible solution	201
7.5 Fabrication of two different detectors on a single chip	201
7.6 Simultaneous and independent measurement of I_{ISHE} and I_{PV}	204
7.7 Results and discussion	205
7.8 Investigation of cross talk between the two detectors made on a single chip	207
7.9 Outcome of the Chapter	210
Chapter 8 Summary and Future perspectives	212
9. Bibliography	217
10. Appendices	233
A. Spin-Orbit interaction	233
B. Stokes vector and Muller calculus	236
C. Electron scattering mechanism in III-V semiconductors	239

Synopsis

The field of Spin-optoelectronics aims to combine the intrinsic properties of the charge carriers and photons; namely the charge and spin of electrons with the angular momentum of photons [1]. Here, the quantum mechanical concept of spin brings some amazing new functionalities in the mainstream of charge based optoelectronics [2]. Investigators have long envisioned to bring semiconductor spin into the main stream opto-electronics for creating a new bunch of opportunities in semiconductors where novel devices were expected to emerge based on the utilization of electron spin as a new degree of freedom [3, 4]. Though, semiconductors offer many functional advantages over other materials, like very long relaxation time, high mobility of carriers, ultra-pure epitaxial layers, fabrication of heterostructures that often harness the quantum size effects in an effective manner, and also their matured fabrication technology, still the realization of spin-optoelectronic devices is in its infancy because the coupling of electrons with photons via their spin remains a major challenge. It is well understood that the critical technological issues such as injection, transport, control, and detection of spin have to be resolved before it can be integrated with the mainstream semiconductor technology [5]. Though several methods are proposed for enhancing the efficiency of spin injection into non-magnetic semiconductors, yet the detection of spin polarization is proven to be extremely onerous [6, 7]. Only a few reports are available on the detection of spin polarization in semiconductor materials. Optical techniques are often used for the detection of spin accumulation in semiconductors [8]. However, from the device point of view,

detection of spin-polarized transport in semiconductors through an electrical method is essential [9]. For this reason, many schemes to explore the spin degree of freedom in semiconductors have been pursued in recent years [10]. Various researchers use ferromagnetic metals to detect the spin polarized carriers [11]. This limits the experiments and applications of the functional devices below the curie temperature of the metal. Therefore, innovative ways for detecting the spin polarization without using magnetism and the magnetic materials have been earnestly sought [12]. Fundamental understanding of the spin injection and its transport in a given material system is essential for the realization of novel spin-optoelectronic devices. Spin Hall Effect (SHE) and its inverse mechanism known as Inverse Spin Hall Effect (ISHE) are considered to be the alternative mechanism, through which electron spin transport can be controlled and detected electrically without the usage of external magnetic field or magnetic materials [13, 14]. In this regard, various experimental efforts have been put to observe SHE/ISHE in nonmagnetic semiconductor materials [15]. Photo-induced Inverse Spin Hall Effect, which converts the photo generated spin current density to a transverse current density is thought to be a bridge between traditional optoelectronics and spin optoelectronics. Furthermore, semiconductor quantum structures like quantum wells or quantum dots are expected to increase the performance of spin optoelectronic devices [16].

This doctoral research, which was carried out at the Semiconductor Physics and Devices Laboratory of RRCAT Indore, contributes to the transport study of spin polarized carriers in various III-V semiconductor bulk and quantum well structures. Here, spin polarized carriers are injected into semiconductor

materials by the optical orientation technique. In order to verify the spin polarization of carriers, an electronic method based on ISHE is used. In order to facilitate the process of spin separation, a metal/semiconductor hybrid structure is judiciously chosen. A clear ISHE signal is recorded over a broad temperature range where the process of spin relaxation of photo-induced hot electrons is explained by invoking various scattering mechanisms. In the next step, ISHE signal is observed in bulk semiconductors without the involvement of a metallic layer, and also in the quantum wells. The relaxation time of spin polarized carriers is measured by analyzing the polarization properties of photoluminescence (PL) signal which originates from the radiative recombination of spin polarized carriers in semiconductors. By coupling the ISHE measurements with polarization dependent PL, the magnitude of spin Hall conductivity is estimated for bulk GaAs. In case of quantum well structures, spin transfer efficiency from barrier to quantum well layer is estimated by analysing the polarization properties of PL signal. Finally, a proof of concept demonstration of a spin-optoelectronic device, which can detect light intensity and polarization simultaneously in an integrated optoelectronic platform is also shown. The thesis is organized as follows:

In **Chapter 1**, an introduction of Spin-Optoelectronics technology is provided by highlighting its advantages over the conventional optoelectronics. Historical overview of different technologies like spin injection/detection in nonmagnetic semiconductors and the concept of SHE and ISHE experiments are briefly described. Various fundamental physical concepts that are used during the course of this thesis work, like spin orbit coupling, optical orientation, spin

relaxation are also discussed. Finally, a critical summary of the available literature is also given before moving to the motivation of the proposed research work carried out during the course of this thesis.

Chapter 2 forms the foundation of the present thesis. In general, the signal level in ISHE experiments are extremely low that may sometime lie in pico Ampere range. Moreover, the available literature on this subject is very limited. This makes the realization of such experiments extremely challenging. One needs to have a prior knowledge of necessary experimental conditions including their influence on the magnitude of ISHE signal. In this chapter, relevance of various parameters like light wavelength, angle of incidence, optimal combination of metal/semiconductor hybrid structure is discussed through systematic numerical calculations based on the fundamental physical concepts. It is realized that a thin film of high Z material having a large spin Hall conductivity is ideal for an efficient detection of spin polarization. Systematic numerical calculations based on the analysis of both energy and spin relaxation phenomena for optically induced hot electrons, tunneling and thermionic transport effects at the metal/semiconductor interface and circular dichroism for the light transmitted through the metal layer are carried out. It is understood that a semiconductor with small spin orbit splitting is an ideal candidate for the injection of spin polarized carriers under certain conditions. One therefore needs to fabricate a metal/semiconductor hybrid structure where spin injection and separation are carried out in semiconductor and metallic sections of the device respectively. By analyzing different III-V semiconductors like GaAs, InP, InAs and InSb, and also the metals like Au, Pt,

and Ti, it is observed that Au/InP hybrid structure offers the best possible combination for measuring the ISHE signal. The methodology of numerical calculations is briefly discussed in this chapter including the relevant fundamental physical mechanisms. Results of the numerical calculations are shown in this chapter which are also compared with the experimental data available in literature.

Chapter 3 is devoted to the sample preparation method, experimental set up and the techniques that are extensively used in this work. The chapter starts with a brief introduction of the metal-Organic Vapor Phase Epitaxy (MOVPE) technique, which is used to grow the epitaxial samples that are used in this work. MOVPE growth conditions of all the relevant samples are summarized here. The device fabrication techniques like thermal and electron beam evaporation, photolithography are also briefly summarized. Characterization techniques like resistivity and capacitance measurements are also elaborated in this chapter. Further, the concept behind the technique of polarization modulation is discussed in brief. The chapter also include a brief discussion on various experimental artefacts that are inherently present in such kind of experiments along with the possible methods for their minimization. The chapter ends with the explanation of the techniques that are used to calibrate the experimental set up for the measurement of spin relaxation time and inverse spin hall current.

Chapter 4 describes the measurement of Photo-induced Inverse Spin Hall Effect in Au/InP Hybrid structure under the optimized experimental conditions

that are predicted in chapter 3. The laser wavelength and angle of incidence were chosen as predicted by the numerical simulations. For this work, MOVPE grown moderately doped ($n \sim 3.6 \times 10^{17} \text{ cm}^{-3}$) InP epitaxial layers of high crystalline quality are carefully chosen. Au/InP hybrid device is then fabricated and the measurements of ISHE are performed under various conditions for testing the theoretical predictions. It is seen that the dependence of measured signal on the degree of circular polarization and also on the angle of incidence strongly agrees with the theoretical predictions which confirms that the ISHE phenomenon is successfully observed in our device. Further, this chapter elaborates a model for the spin relaxation of optically generated hot electrons in semiconductors. The model is validated by performing the ISHE measurements over a broad temperature range of 10 to 300 K.

Chapter 5 describes the measurement of ISHE in bulk semiconductors. The observation of ISHE phenomenon in bulk semiconductors is extremely challenging since the magnitude of ISHE signal could be three orders low when compared with a metal/semiconductor hybrid device. Though the signal level in metal/semiconductor hybrid structure is higher, a suitable combination is always necessary because of the practical reasons. In this context, an all-semiconductor device offers flexibility in terms of the ability of potential variation by external bias, device structure and the doping profile. With this in mind, ISHE experiments are performed on MOVPE grown GaAs thin film of high crystalline quality. A clear signature of ISHE phenomenon is seen over a broad temperature range and the results are described in this chapter. Furthermore, the results from the optical

orientation experiments where spin relaxation time of electrons in GaAs is estimated by analyzing the degree of circular polarization of PL signal are also presented in this chapter. It is observed that the electron spin relaxation time in n type GaAs ($n \sim 3.2 \times 10^{18} \text{ cm}^{-3}$) critically depends on temperature and decreases from 2.47 ns at 10 K to 0.55 ns at 200 K. By using this spin relaxation time, the spin diffusion equation is then solved to find out the spin current density. By correlating the calculated spin current density with the values, the magnitude of spin Hall conductivity is estimated. It is found to vary from $4.17 \text{ } \Omega^{-1}\text{cm}^{-1}$ at 10 K to $12.3 \text{ } \Omega^{-1}\text{cm}^{-1}$ at 200 K. It is also realized that the inclusion of the phonon and dynamic impurity scattering in numerical calculations is necessary for estimating the values of spin Hall conductivity over a given temperature range.

Chapter 6 describes the results from the optical orientation technique for the measurement of electron polarization and spin Hall conductivity in quantum well structures. Quantum structures are of great interest for observing ISHE related phenomenon since the physical properties of such structures are considerably modified by the quantum confinement effects. Due to the quantum confinement induced changes in the band structure, the relation between PL polarization and electron spin density is expected to be significantly modified. For this work, various quantum wells having either compressive or tensile strain are carefully chosen. It is highly intriguing to note that the degree of circular polarization of emitted PL signal corresponding to the recombination of electrons with light and heavy holes is found to be very different in case of tensile strained GaAsP/AlGaAs quantum well. Further, the spin transfer efficiency from the

barrier to quantum well material is also estimated, which strongly depends on the sample temperature. Finally, the results on ISHE measurement for GaAs/AlGaAs quantum well structure are also presented.

In **Chapter 7**, various possibilities for the fabrication of some novel devices based on the fundamental concepts described in previous chapters are discussed. The first device which can be thought of is a spin-optoelectronic detector which can record the polarization state of a laser beam. Note that the spin polarized carriers are injected into a semiconductor layer for creating a spin imbalance that ultimately lead to the generation of ISHE signal. It is already shown in chapter 4 that the magnitude of ISHE signal varies linearly with the degree of circular polarization of incident laser beam. It therefore prompted us to fabricate a spin optoelectronic detector which can convert the polarization information of a laser beam into electrical signal. For this purpose, we choose an Au/InP hybrid structure for the development of ISHE based detector due to the aforementioned reasons. It is successfully demonstrated that the magnitude of ISHE signal indeed varies linearly with the degree of circular polarization of laser beam, however, the signal also depends on the laser intensity. It therefore limits the capabilities of the fabricated device towards an unambiguous detection of the polarization state of a laser beam. A novel design is thereafter proposed, where a three terminal device is made by incorporating two independent detectors on the same chip that are used to measure the degree of circular polarization and intensity of a laser beam simultaneously and independently. The principle of operation of device is based on the two independent fundamental phenomena occurring in Au/InP hybrid

structures, namely, Inverse Spin Hall Effect (ISHE) and the Photo-Voltaic (PV) Effect. The magnitude of ISHE and PV signals is simultaneously measured across the two pairs of contacts that are made on the top of device. A proof of concept device is made, which successfully helps in the realization of proposed concepts. The all-electronic compact device is fast, operates at room temperature, and opens up the possibility of many applications in an integrated optoelectronic platform. Details of the fabrication and results from the indigenously developed device are summarized in this chapter.

Finally in **Chapter 8**, we conclude by summarizing the main results of the thesis with a brief discussions about the scope of future works in the emerging area.

References:

1. Michael Oestreich, Jens Hübner, Daniel Hägele, Markus Bender, Nils Gerhardt, Martin Hofmann, Wolfgang W. Rühle, Heinz Kalt, Thorsten Hartmann, Peter Klar, Wolfram Heimbrodt, Wolfgang Stolz; *Spintronics: Spin Electronics and Optoelectronics in Semiconductors*; Springer Berlin Heidelberg, Berlin (2001)
2. D.D. Awschalom and M. E. Flatte, *Nature Physics*, **3**, 153 (2007)
3. S. Hövel, N. C. Gerhardt, M. R. Hofmann, F.Y. Lo, D. Reuter, A. D. Wieck, E. Schuster, H. Wende and W. Keune, *Physica status solidi (C)*, **6**, 436 (2009)
4. N. P. Ong, *Nature*, **455**, 741 (2008)

5. S. A. Wolf, D.D. Awschalom, R. A. Buhrman, J. M. Daughton, S. von Molna, M. L. Roukes, A. Y. Chtchelkanova, D. M. Treger, *Science*, **294**, 1488 (2001)
6. G Schmidt, *J. Phys. D: Appl. Phys.*, **38**, R107 (2005)
7. Tomoyasu Taniyama, Eiji Wada, Mitsuru Itoh and Masahito Yamaguchi; *Nature Asia Materials*, **3**, 65 (2011)
8. R. Fiederling, M. Keim, G. Reuscher, W. Ossau, G. Schmidt, A. Waag & L. W. Molenkamp, *Nature*, **402**, 787 (1999)
9. Xiaohua Lou, Christoph Adelmann, Scott A. Crooker, Eric S. Garlid, Jianjie Zhang, K. S. Madhukar Reddy, Soren D. Flexner, Chris J. Palmstrøm and Paul A. Crowell, *Nature Physics*, **3**, 197 (2007)
10. Y. Kato, R. C. Myers, A. C. Gossard & D. D. Awschalom, *Nature*, **427**, 50 (2004)
11. A. Bhattacharya, Md Zunaid Baten and Pallab Bhattacharya, *Appl. Phys. Lett.*, **108**, 042406 (2016)
12. David Awschalom and Nitin Samarth, *Physics* **2**, 50 (2009)
13. Jairo Sinova, Sergio O. Valenzuela, J. Wunderlich, C. H. Back, and T. Jungwirth; *Rev. Mod. Phys.* **87**, 1213 (2015)
14. J. Wunderlich, A. C. Irvine, Jairo Sinova, B. G. Park, L. P. Zârbo, X. L. Xu, B. Kaestner, V. Novák and T. Jungwirth, *Nature Physics* **5**, 675 (2009)
15. Y. K. Kato, R. C. Myers, A. C. Gossard, D. D. Awschalom, *Science*, **306**, 1910 (2004)
16. J. D. Koralek, C. P. Weber, J. Orenstein, B. A. Bereaving, Shou-Cheng Zhang S. Mack & D. D. Awschalom, *Nature*, **458**, 610 (2009)

List of Figures

Chapter 1

- 1.1 Schematic band diagram known as the $E-k$ diagram of conventional zinc-blend semiconductors 4
- 1.2 E-k diagram showing (a) k-dependent Dresselhaus spin splitting and (b) Zeeman splitting 5
- 1.3 Schematic diagram of the dipole allowed transitions for left and right circularly polarized light. The Relative transition probabilities are indicated by the circled numbers 8
- 1.4 Schematic diagram showing the constant energy contour in k -space. 10
- 1.5 Schematic of the (a) Hall Effect and (b) Spin Hall Effect showing the charge and spin accumulations respectively. The corresponding Fermi level positions are also shown in the figure. Here B , F , v and σ are the magnetic field, force on electron, electron velocity and electron spin magnetic moment respectively 19
- 1.6 Picture illustrating Spin Hall Effect and Inverse Spin Hall Effect 22

Chapter 2

- 2.1 Schematic of the sample geometry considered (a) Shows the mechanism along with the angle of incidence (b), (c) and (d) show the 3-dimensional view, top view and side view of the metal semiconductor hybrid structure respectively. 37

2.2	Change in degree of circular polarization (ρ_{II}) and intensity (I_1) of circularly polarized light after passing through Air/Au/GaAs multilayer system. The thickness of Au layer is assumed to be 20 nm.	39
2.3	(a) Band structure of GaAs calculated using 8 band $k.p$ method. The corresponding parabolic approximations are also shown as dotted lines. (b) Energy of electrons excited from different bands as a function of excitation light energy.	41
2.4	Projections of different angular momentum states on various bands calculated using the same 8 band $k.p$ method	42
2.5	Relative oscillator strength of various transitions occurring from different valence band states and the respective electron spin polarizations as a function of excitation photon energy	42
2.6	$N(E_e)$ for two different excitation energies (a)1.6 and (b) 2 eV, showing the contributions from different transitions	44
2.7	Electron scattering time due to polar optical phonon as a function of electron energy	46
2.8	The Energy distribution of spin polarized electron in the conduction band, excited by photon energy of 1.62eV (a) and 1.74 eV (b). Black, green lines correspond to the distribution created by polarized light $N(E_e)$ and distribution after energy relaxation $N_E(E_e)$ respectively	49

2.9	The Energy distribution of spin polarized electron in the conduction band, excited by photon energy of 1.62eV. Black, green and blue lines correspond to the distribution created by polarized light $N(E_e)$, and distribution after energy relaxation $N_E(E_e)$ and distribution after both energy and spin relaxation $N_{S,E}(E_e)$ respectively	52
2.10	Energy distribution of spin polarized electron in the conduction band, excited by photon energy of (a)1.6 eV and (b) 2eV. Black, green and blue lines correspond to the distribution created by polarized light $N(E_e)$, distribution after energy relaxation $N_E(E_e)$ and distribution after energy and spin relaxation $N_{S,E}(E_e)$ respectively	53
2.11	Net spin polarization at the time of generation (P) and after transport to the interface ($P_{S,E}$) as a function of excitation photon energy	53
2.12	E_{ISHE} and $P_{S,E}$ as a function of incident photon energy	57
2.13	E_{ISHE} as a function of metal layer thickness for various values of spin diffusion length (L_S)	58
2.14	Dependence of E_{ISHE} on angle of incidence at various excitation energy	59
2.15	(a) E_{ISHE} spectra for different barrier height, 0.4 eV (green curve), 0.3 eV (red curve), 0.2 eV (black curve) and 0 eV (blue curve), (b) Variations of the energy of two peaks (A and B) as function of barrier height	61
2.16	Comparison of E_{ISHE} spectra for 20 nm Au coated GaAs, InP, InAs and InSb	62

Chapter 3

3.1	Photograph of MOVPE machine used in this work	69
3.2	Photograph of the mask aligner and spin coating system	71
3.3	Photograph of the thermal and e-beam evaporation system that are used in this work	73
3.4	Schematic of the Hall bar structure used to measure ISHE. (a) After photolithography and chemical etching and (b) after metallization of contact pads	73
3.5	(a) Real Photograph and (b) schematic of the experimental set up for electronic transport measurements. Here (1) represents the cryo-cooler (2) Magnet pole pieces (3) Gauss meter (4) Sample heater (5) Temperature sensor and (6) sample holder	75
3.6	Schematic of the experimental set up for the calibration of PEM module	77
3.7	Calibration with respect to the orientation angle	79
3.8	Oscilloscope trace of the experiment shown in figure 3.6	81
3.9	Schematic experimental setup for calibrating the retardation magnitude	82
3.10	Results of retardation calibration	82
3.11	The calibration parameter a_3 (explained in text) at different position of PEM	84
3.12	Correction factor because of variation in retardation value along the length and breadth of PEM	85

3.13	Background signal before (filled) and after (open) PEM isolation for n+GaAs sample (square), Commercial Si detector (circle) and PMT (triangle)	87
3.14	Measured static birefringence of different optical elements at different probe wavelengths	89
3.15	(a) Schematic and (b) photograph of experimental set up for ISHE measurements	91
3.16	$M_1(f)$ and $M_2(f)$ as a function of signal frequency. $M_1(f)$ is also fitted with appropriate relation to find out the cut off frequency.	93
3.17	Relation between measured current and applied current. Linear relation confirms the suitability of the measurement	94
3.18	Alternate experimental set ups for polarization resolved PL measurement. In (a) PEM is used in the excitation arm, where as in (b) PEM is used in the collection arm	95
3.19	Photograph of the experimental set up to measure the polarization resolved photoluminescence	97
Chapter 4		
4.1	Schematic of the Au/InP hybrid structure, used to measure ISHE	102
4.2	(a) Resistivity of Au film (20 nm) deposited on SI InP plotted as a function of temperature. Inset shows the Van-der Pauw geometry. (b) Temperature dependent barrier height at the Au/InP interface plotted as a function of temperature. Inset shows the schematic of the layer structure	103

4.3	Resistance of the device used to measure ISHE at temperatures in the range of 45 to 300 K. Inset shows the experimental configuration	104
4.4	Schematic diagrams illustrating (a) mechanism and measurement geometry of the photo-induced inverse spin Hall effect and (b) schematic of experimental setup of the ISHE measurements. J_s , σ_s , CPL, and PEM stand for the spin current density, electron spin angular momentum, circularly polarized laser, and photo elastic modulator, respectively	105
4.5	Magnitude of I_{ISHE} plotted as a function of degree of circular polarization	107
4.6	Dependence of I_{SIHE} on the angle of incidence (filled square). Numerically calculated values are also plotted in the same graph (solid line)	108
4.7	(a) I_{ISHE} as a function of degree of circular polarization for 100, 200 and 300 K. (b) Peak value of I_{ISHE} as a function of temperature	109
4.8	(a) Temperature dependence of σ_{SH} and γ for Au, (b) Estimated value of J_s^0 as a function of temperature	112
4.9	(a) Measured values of the J_s^0 injected spin current density (curve i) plotted as function of sample temperature and the corresponding fitted curves, by considering ionized impurity scattering only (curve ii) and by considering polar optical phonon	

(POP), inter valley (IV), piezo-electric potential (PZ), and deformation potential (DP) scattering mechanisms (curve iii). (b) The calculated τ_p (curve Total) and the contributions corresponding to various scattering mechanisms, plotted as functions of sample temperature 116

Chapter 5

5.1	(a, b, c) Different scheme to detect ISHE in bulk semiconductors, E, B and J denotes the Electric field, Magnetic field and current density respectively	123
5.2	Measured (a) carrier concentration (b) Hall mobility, and (c) conductivity as a function of temperature	125
5.3	PL spectra at different positions of the sample, when the beam position is scanned (a) horizontally and (b) vertically. Note that the PL spectra are vertically shifted for the clarity in viewing	125
5.4	Schematic diagram of the fabricated sample	126
5.5	Current-Voltage measurement across two pair of contacts	127
5.6	(a) Photocurrent as a function of light beam position along the Hall bar channel, and (b) The minimum of photocurrent as a function of incidence angle	128
5.7	The measured current (I_m) $\sim \delta_0$ for linearly polarization parallel to the PEM axis and along 45 degree to the PEM axis (at 10 K)	130
5.8	I_{ISHE} as a function of incidence angle	131
5.9	The magnitude of I_{ISHE} plotted as a function of sample temperature	132

5.10	50K PL spectra recorded at 300 μ W and 20 mW laser power	133
5.11	Reflectivity of GaAs at $\theta \sim 45^\circ$ as a function of temperature	134
5.12	Numerically calculated values of spin injection probability as a function of photon energy	135
5.13	Sample impedance, measured across the contacts 1 and 3 of figure 5.4, plotted as a function of temperature	136
5.14	The calculated $\Phi(z)$ and $\Delta n(z)$ for typical values of α , s_1 and τ . Band bending at the surface of GaAs and at the interface of n ⁺ GaAs/ SI GaAs are also shown	142
5.15	(a) I_{++} and I_{+-} for GaAs at 10 K. (b) (I_{++}) and (I_{+-}) are plotted as a function of relative angle between quarter wave plate and linear polarizer	147
5.16	PL intensity and degree of circular polarization (ρ_l) plotted as function of energy recorded at several temperatures varying from 10 to 200 K	148
5.17	Variation of ρ_l with incident power for (a) n ⁺ GaAs and (b) p ⁺ GaAs at 10K.	149
5.18	Estimated Spin relaxation time (τ_S) versus sample temperature. Corresponding fitting is also shown as solid line	150
5.19	Variation of σ_{SH} with sample temperature. Circles (●) show the measured values while Square (■) represents the numerically calculated value. On the other hand, triangle (▲) represents the extrapolated value of σ_{SH} following Matsuzaka et al.	154

Chapter 6

- 6.1 Schematic showing ISHE measurement in quantum well sample 162
- 6.2 Surface of constant energy for (a) bulk, unstrained semiconductor and (b) quantum well 166
- 6.3 Components of $m_j=3/2$ angular momentum on hh and lh states as a function of ΔE_{lh} for different values of k 167
- 6.4 The projection of $|3/2, 3/2\rangle$ angular momentum state on (a) hh and (b) lh levels of quantum well of width L_w (corresponding to $k_z = \pi/L_w$) is plotted against in plane momentum ($k_{||}$) 169
- 6.5 The projection of $|3/2, 3/2\rangle$ angular momentum state on (a) hh and (b) lh levels of GaAs quantum well of width L_w (corresponding to $k_z = \pi/L_w$) and biaxial strain ($\epsilon=0.2\%$). The cases of tensile and compressive strain are compared with the unstrained case, which is shown as dotted line 171
- 6.6 A comparison of 4 band and 6 band calculation to show the effect of split off band on ζ_{hh} . (a) and (b) show the differences for GaAs for $k = 0.02 \text{ \AA}^{-1}$ and 0.04 \AA^{-1} respectively. (c) and (d) show the differences for InP for $k = 0.02 \text{ \AA}^{-1}$ and 0.04 \AA^{-1} respectively. (e) and (f) show the differences in $E-k$ diagram in GaAs and InP. 172
- 6.7 Experimental set up to measure degree of circular polarization of PL. Here LP, QWP, C, M, L, S and PEM denote the linear polarizer, quarter wave plate, Chopper, mirror, Lens, Sample and Photo-elastic modulator respectively 174
- 6.8 I_{+I} and I_{-I} for GaAs/AlGaAs quantum well (b) I_{+I} plotted against the relative angle between quarter wave plate a linear 174

	polarizer	
6.9	I_{++} and I_{+-} for InGaAs/GaAs quantum well (b) I_{+-} plotted against the relative angle between quarter wave plate and linear polarizer	175
6.10	I_{++} and I_{+-} for GaAsP/AlGaAs quantum well (b) I_{+-} plotted against the relative angle between quarter wave plate and linear polarizer	175
6.11	ξ_{hh} and ξ_{lh} along with their ratio as a function of $ \langle f_{h,\pm 3/2} \rangle ^2$	180
6.12	I_{++} and I_{+-} for GaAs/AlGaAs quantum well	181
6.13	PL spectra at different temperatures showing the deconvoluted peaks	183
6.14	Integrated intensity of individual peaks are plotted against (a) sample temperature and (b) Incident intensity. (c) PL peak of thick ($L_w=14$ nm) GaAsP quantum well	184
6.15	Measured I_{+-} spectra are plotted for three different temperatures (a) 10 K, (b) 75 K and (c) 150 K. They are also fitted by taking ξ_{lh}/ξ_{hh} as a fitting parameter, shown in blue curve. The estimated spectra assuming $\xi_{lh}/\xi_{hh}=-1$ is also shown as red curve.	185
6.16	Estimated value of ξ_{lh}/ξ_{hh} as a function of temperature. The individual values of ξ_{lh} and ξ_{hh} estimated by comparing it with figure 6.11, are also shown. (b) Estimated value of ρ_e as a function of temperature	186

6.17	Temperature dependence of PL peak corresponding to (a) Quantum well and (b) barrier of a GaAs/AlGaAs quantum well	189
6.18	Degree of circular polarization of light (ρ_l) and (b) spin polarization of electron (ρ_e) in barrier and quantum well	190
6.19	Spin transfer efficiency is compared for two different quantum wells	190
6.20	Schematic of the fabricated Hall bar structure and measured current voltage behavior at 300 K	192
6.21	Measured I_{ISHE} as a function of applied voltage at three different temperatures	194
6.22	Estimated spin Hall angle in GaAs/AlGaAs quantum well as a function of sample temperature	194

Chapter 7

7.1	The magnitude of I_{ISHE} plotted as a function of (a) degree of circular polarization, and (b) Intensity of a laser beam	201
7.2	(a) Two terminal device to measure only ISHE, (b) Three terminal device for the measurement of I_{ISHE} and I_{PV} simultaneously.	203
7.3	(a) I - V graph of contacts (1,2) and (2,3) respectively. (b) Measured I_{PV} and numerically estimated I_{ISHE} in Au/InP structure. For I_{ISHE} calculation, the barrier height is taken to be 0.72 eV. The spectra are normalized to their peak values.	203
7.4	Schematic of experimental set up to measure I_{ISHE} and I_{PV} simultaneously.	205

7.5	(a) I_{ISHE} as a function of Δ , (b) I_{ISHE} as a function of the degree of circular polarization (ρ_l) at three laser powers only for the first quarter of sine wave. On top of figure 7.5 (a), polarization ellipses corresponding to various retardations are shown.	206
7.6	ISHE plotted as a function of ρ_l in the presence and absence of mechanical chopper	207
7.7	Simultaneous measurement of the intensity and polarization state of light, (a) A comparison of I_{ISHE} measured at 50 kHz across the contacts '1'&'2' and '2'&'3'. and (b) A comparison of I_{PV} measured at 172 Hz chopping frequency across the contacts '1'&'2' and '2'&'3' as a function of incident laser power	209

List of Tables

1.1	The wave functions of bands with their coordinate and spin part	6
1.2	Dipole operators for electromagnetic wave of different polarization	7
1.3	Relative dipole matrix elements for various allowed transitions	8
1.4	Results to illustrate the estimated value of σ_{SH} from the literature	30
2.1	Material parameters taken in numerical simulations of ISHE	47
3.1	MOVPE growth details of the structures used	69
3.2	Fitting parameter to calibrate the PEM	84
5.1	Fitted parameters to obtain I_{ISHE}	131
6.1	Details of the quantum well sample and the estimated parameters	174

Chapter 1

Introduction

1.1 Introduction to Semiconductor spintronics

Spintronics is a field that simultaneously utilizes two independent degrees of freedom; namely charge and spin to manipulate the operation of electronic devices [1]. Starting from the pioneering work of Mott, who gave the concept of spin dependent transport in ferromagnetic metals, enormous attention has been given to metallic structures such as spin valves and Magneto-resistive Random Access Memory (MRAM) [2-4]. Giant Magneto-resistance (GMR) Effect is a key invention [5, 6], which won the Nobel Prize of Physics for the year 2007. The hard disk drives of almost every computer that are in use today are based on GMR effect [7]. Lately, various spintronics phenomena were observed in semiconductors also [8, 9]. It provides a unique opportunity of coupling the Optics with Spintronics leading to the field of spin-optoelectronics [10]. Even though, this is rather a recent field, many of the contemporary research rely closely on experiments and concepts in diverse areas of physics like crystal growth, magnetism, semiconductor physics, optics, and nanotechnology [11, 12]. It is realized that the technical issues such as

injection, transport, control, and detection of electron spin have to be resolved before it can be integrated with the existing semiconductor technology [13]. However, contrary to the case of metallic spintronics, where involvement of external magnetic fields and magnetic materials is essential, in semiconductor spintronics, one aspires to operate the devices without relying on ferromagnetic materials. Here, spin information is exploited by the use of spin-orbit interaction arising from that in the constituent atoms and from the polarity of their bonding [14, 15]. In centrosymmetric semiconductors like Ge and Si the latter contribution is absent. However in non-centrosymmetric semiconductors, both the contributions are present. Since most of the direct band gap materials, used in optoelectronic devices are non-centrosymmetric in nature, spin-orbit interaction plays a key role in semiconductor spin-optoelectronics.

1.2 Fundamental concepts

1.2.1 Spin orbit interaction

In atomic physics, spin-orbit interaction enters into the picture because of the interaction of electronic spin magnetic moment with the magnetic field originated from the Lorentz transformation of the electric field of atomic core. Alternatively, it can be seen as the interaction between electric field of atomic core and electronic dipole moment, originated from the Lorentz transformation of the electronic spin magnetic moment. Using the Thomas precession, which takes care of the non-inertial frame, the spin orbit splitting energy is given by [16]

$$E_{so} = -\frac{\lambda_c^2}{4\hbar} [\mathbf{p} \times \nabla V_a] \cdot \boldsymbol{\sigma} \quad (1.1)$$

Where, λ_c is the Compton wavelength, p is the momentum, V_a is the Coulomb potential of the atomic core, and σ is the vector of Pauli spin matrices. In a solid, it is still expressed as the same equation, but the potential is now replaced by the effective crystal potential and the coupling constant λ increased by six orders of magnitude [17]. It modifies the band structure in a considerable manner and governs almost all spin related phenomena in semiconductors as described below.

- (i) Energy bands in solids are expressed as the Eigen states of total angular momentum (J). By combining the spin angular momentum (s), with the orbital angular momentum (l), where $l=0$ and 1 for the conduction and valence band respectively for zinc-blende semiconductors, $J = l \pm s$ becomes $\pm 1/2$ for conduction band, $\pm 3/2$ and $\pm 1/2$ for the valence band states respectively.
- (ii) Spin orbit coupling splits the states with $J=3/2$ and $J=1/2$ by an energy Δ_{so} and forms the split off (so) states. Therefore, the valence band state is two-fold degenerate at the Γ point called heavy hole (hh) with $m_j = \pm 3/2$ and light hole (lh) with $m_j = \pm 1/2$. Following the convention generally adopted in semiconductor physics, the figure 1.1 explains the band diagram of a typical direct band gap semiconductor near $k=0$, along with their respective $|J, m_j\rangle$ notations [18].

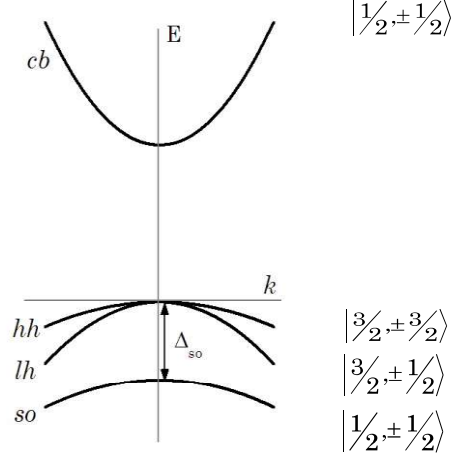


Figure 1.1 Schematic band diagram known as the E - k diagram of conventional zinc-blend semiconductors [18]

- (iii) The electron and hole states feel a k -dependent effective magnetic field, which further splits these levels according to their spin states. For example, the conduction band dispersion is given by [19]

$$E_c(k) = \frac{\hbar^2 k^2}{2m_e^*} + \gamma_D \{ (k_y^2 - k_z^2) k_x \sigma_x + c.p. \} \quad (1.2)$$

where m_e^* is the effective mass of electrons in conduction band, + c.p. denotes a sum over cyclic permutations of the indices x , y , z . γ_D is known as the Dresselhaus coefficient and is decided by the spin orbit coupling in semiconductors [17]. It is shown schematically in figure 1.2, where it is compared with the spin splitting induced by the external magnetic field, through Zeeman interaction. Though the energy splitting is relatively small when compared with other phenomena that are common in semiconductor

optoelectronics, it has profound effect on the spin relaxation of electrons. Similar expressions are available for the valence bands [19].

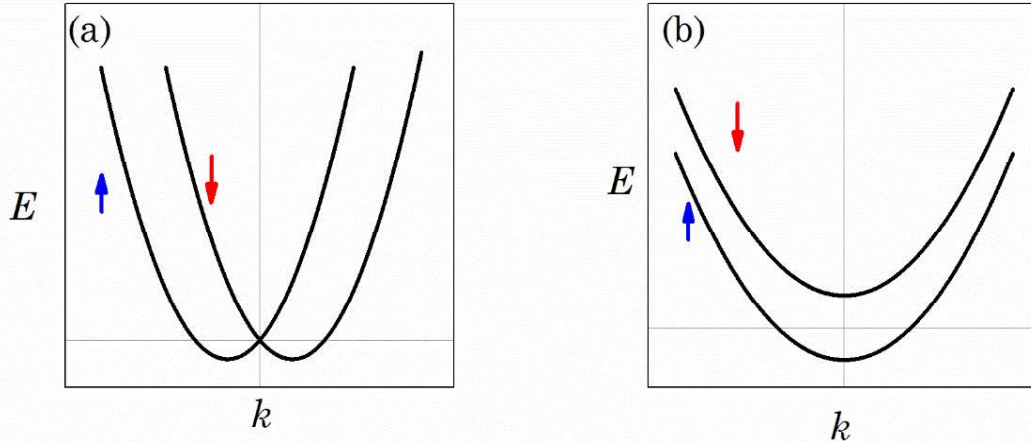


Figure 1.2 E-k diagram showing (a) k-dependent Dresselhaus spin splitting and (b) Zeeman splitting [17]

- (iv) It is known that the scattering cross section of electrons under the influence of the coulomb potential of impurities becomes spin dependent due to spin orbit coupling. It affects the extent of various phenomena like anomalous Hall Effect in ferromagnets and extrinsic spin Hall Effect in non-magnetic semiconductors [17].

1.2.2 Optical orientation

The method of Optical orientation refers to injection of spin polarized electrons into semiconductors by the absorption of circularly polarized light. It is based on the following fundamental physical concepts.

1.2.2.1 Traditional approach

As already discussed, at Γ point ($k=0$), conduction band and valence band of zincblende semiconductors are designated by their angular momentum and their projection on the quantization axis, as shown in figure 1.1. Their wave function can be expanded as respective spatial (X, Y, Z) and spin part (\uparrow and \downarrow) and are shown in table 1.1.

Table 1.1 The wave functions of bands with their coordinate and spin part

Conduction band: $ cb\rangle$	$ \frac{1}{2}, \frac{1}{2}\rangle \equiv iS \uparrow\rangle$ $ \frac{1}{2}, -\frac{1}{2}\rangle \equiv iS \downarrow\rangle$
Heavy hole: $ hh\rangle$	$ \frac{3}{2}, \frac{3}{2}\rangle \equiv \frac{-1}{\sqrt{2}} (X+iY)\uparrow\rangle$ $ \frac{3}{2}, -\frac{3}{2}\rangle \equiv \frac{1}{\sqrt{2}} (X-iY)\downarrow\rangle$
Light hole: $ lh\rangle$	$ \frac{3}{2}, \frac{1}{2}\rangle \equiv \frac{-1}{\sqrt{6}} (X+iY)\downarrow\rangle + \sqrt{\frac{2}{3}} Z\uparrow\rangle$ $ \frac{3}{2}, -\frac{1}{2}\rangle \equiv \frac{1}{\sqrt{6}} (X-iY)\uparrow\rangle + \sqrt{\frac{2}{3}} Z\downarrow\rangle$
Split off: $ so\rangle$	$ \frac{1}{2}, \frac{1}{2}\rangle \equiv \frac{1}{\sqrt{3}} (X+iY)\downarrow\rangle + \sqrt{\frac{1}{3}} Z\uparrow\rangle$ $ \frac{1}{2}, -\frac{1}{2}\rangle \equiv \frac{1}{\sqrt{3}} (X-iY)\uparrow\rangle - \sqrt{\frac{1}{3}} Z\downarrow\rangle$

Here X, Y and Z stand for the Cartesian coordinates whereas \uparrow & \downarrow denote the relevant spin parts of the Bloch amplitude. The transition probabilities between any of the two states (a & b) due to the light absorption is given by the dipole matrix element, $P_{ab} = \langle a|P|b\rangle$ where P is the dipole matrix operator. Since the conduction band is spherically symmetric, the only non-zero matrix elements are

$$\langle S|P_x|X\rangle = \langle S|P_y|Y\rangle = \langle S|P_z|Z\rangle = \frac{-i\hbar}{m_0} P_0 \quad (1.3)$$

And all the other components vanish. For example,

$$\langle S|P_y|X\rangle = \langle S|P_z|Y\rangle = \langle S|P_x|Z\rangle = 0 \quad (1.4)$$

The quantity P_0 is almost constant for III-V semiconductors and particularly in optical orientation experiments, the relative magnitude of matrix elements between bands is more important than their absolute values. Hence, the non-zero element can be taken as one. Again, the spin parts are ortho-normal functions [20]. From these conditions, the transition matrix elements for different combinations of a & b can be calculated for a known dipole matrix operator, which depends on the polarization of electromagnetic wave. For a light beam propagating along positive z direction, the dipole matrix operators are as given below [20]

Table 1.2 Dipole operators for electromagnetic wave of different polarization

Polarization	P
Linear Polarization along x	P_x
Linear Polarization along y	P_y
Left circular Polarization	$1/\sqrt{2} (P_x + i P_y)$
Right circular Polarization	$1/\sqrt{2} (P_x - i P_y)$

Table 1.1 and 1.2 along with equation (1.3) and (1.4) give the following values of dipole matrix elements for left circularly polarized light.

Table 1.3 Relative dipole matrix elements for various allowed transitions

Band (a)	$ J, m_J\rangle$	Band (b \uparrow):	Band (b \downarrow):
$ hh\rangle$	$ \frac{3}{2}, \frac{3}{2}\rangle$	$ \frac{1}{2}, \frac{1}{2}\rangle$	$ \frac{1}{2}, -\frac{1}{2}\rangle$
	$ \frac{3}{2}, -\frac{3}{2}\rangle$	$1/\sqrt{2}$	0
$ lh\rangle$	$ \frac{3}{2}, \frac{1}{2}\rangle$	0	0
	$ \frac{3}{2}, -\frac{1}{2}\rangle$	0	$1/\sqrt{6}$
$ so\rangle$	$ \frac{1}{2}, \frac{1}{2}\rangle$	0	0
	$ \frac{1}{2}, -\frac{1}{2}\rangle$	0	$2/\sqrt{6}$

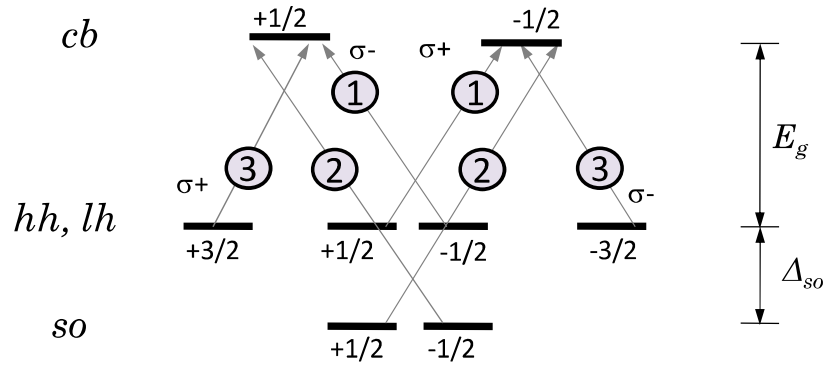


Figure 1.3 Schematic diagram of the dipole allowed transitions for left and right circularly polarized light. The Relative transition probabilities are indicated by the circled numbers [18]

It can be seen that the hh and lh states are coupled with different spin polarization in the conduction band. These transitions are traditionally shown in a

schematic diagram for both the left and right circularly polarized light, as shown in figure 1.3.

Keeping in mind that the strength of a transition is proportional to the square of respective matrix element, the probability of transitions from $|\frac{3}{2}, \pm \frac{3}{2}\rangle$, $|\frac{3}{2}, \pm \frac{1}{2}\rangle$ and $|\frac{1}{2}, \pm \frac{1}{2}\rangle$ states varies in the ratio 3:1:2 respectively. Therefore, the degree of spin polarization of electron (ρ_e), when excited by left circularly polarized light with energy (E_{ph}) satisfying the relation, $E_g < E_{ph} < E_g + \Delta_{so}$, is

$$\rho_e = \frac{3(+1)+1(-1)}{3+1} = 0.5 \quad (1.5)$$

On the other hand, when E_{ph} exceeds $E_g + \Delta_{so}$, ρ_e is be given by

$$\rho_e = \frac{3(+1)+1(-1)+2(-1)}{3+1+2} = 0 \quad (1.6)$$

Therefore, in case of the condition $E_g < E_{ph} < E_g + \Delta_{so}$, typically half population of the photo-generated electrons are expected to be spin polarized in case of unstrained bulk materials. However, if the degeneracy between heavy and light holes is lifted, because of strain or quantum confinement, then one can expect even a larger fraction of electron population to be spin polarized upto a limiting case of 100% provided the condition of $E_g(hh) < E_{ph} < E_g(lh)$ is satisfied [21]. Though this traditional picture gives correct explanation for the near band edge transitions, it is too naïve for explaining the general transitions. Note that the bands are the Eigen states of angular momentum operator only near the Γ ($k=0$) point, that too along

the quantization directions only. Therefore, a more appropriate approach is needed for a general transition.

1.2.2.2 General approach

Even for near band edge transitions, electrons will have all the possible k -vector maintaining the degeneracy. In bulk cubic semiconductors, this constant energy contour is the surface of sphere. This is schematically shown in figure 1.4, where $k_{||}$ stands for k_x and k_y directions. This notation is quiet helpful while dealing with the quantum structures.

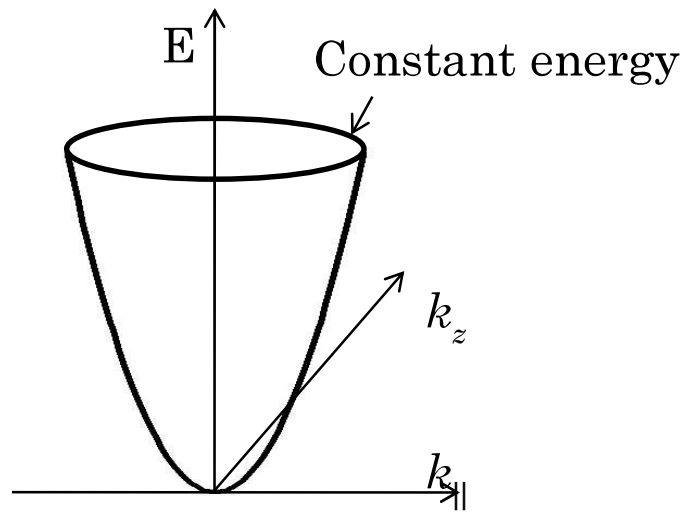


Figure 1.4 Schematic diagram showing the constant energy contour in k -space

Therefore, average over all the directions has to be taken into account for calculating the average spin orientation. Along any arbitrary direction (θ, ϕ) , the wave function of each states (hh , lh and so) can be written as per the relation given by Towe et al. [22].

$$\begin{pmatrix} X' \\ Y' \\ Z' \end{pmatrix} = \begin{pmatrix} \cos\theta \cos\phi & \cos\theta \sin\phi & -\sin\theta \\ -\sin\phi & \cos\phi & 0 \\ \sin\theta \cos\phi & \sin\theta \sin\phi & \cos\theta \end{pmatrix} \begin{pmatrix} X \\ Y \\ Z \end{pmatrix}$$

$$\begin{pmatrix} \uparrow' \\ \downarrow' \end{pmatrix} = \begin{pmatrix} e^{-i\phi/2} \cos\frac{\theta}{2} & e^{i\phi/2} \sin\frac{\theta}{2} \\ e^{-i\phi/2} \sin\frac{\theta}{2} & e^{i\phi/2} \cos\frac{\theta}{2} \end{pmatrix} \quad (1.7)$$

Each of the bands in Table 1.1 can now be expressed suitably using these rotation matrices. When average is taken above all the directions, it is observed that, both hh and lh states consists of equal fraction of $|\frac{3}{2}, \pm \frac{3}{2}\rangle$ and $|\frac{3}{2}, \pm \frac{1}{2}\rangle$. i.e.

$$|hh\rangle = \frac{1}{\sqrt{2}} |\frac{3}{2}, \pm \frac{3}{2}\rangle + \frac{1}{\sqrt{2}} |\frac{3}{2}, \pm \frac{1}{2}\rangle$$

$$|lh\rangle = \frac{1}{\sqrt{2}} |\frac{3}{2}, \pm \frac{3}{2}\rangle + \frac{1}{\sqrt{2}} |\frac{3}{2}, \pm \frac{1}{2}\rangle \quad (1.8)$$

This leads to the fact that, ρ_e corresponding to hh states alone is 0.5 as can be seen from the relation

$$\rho_e = \frac{3 \times \frac{1}{2} (+1) + 1 \times \frac{1}{2} (-1)}{3 \times \frac{1}{2} + 1 \times \frac{1}{2}} = 0.5 \quad (1.9)$$

Similarly, ρ_e corresponding to lh states alone is also 0.5. Therefore, for the case of $E_g < E_{ph} < E_g + \Delta_{so}$, ρ_e becomes 0.5 irrespective of the density of states of hh and lh states. This is in sharp contrast to the previous approach, where hh and lh states produces electrons with opposite degree of spin polarization; +1 and -1 respectively.

On the other hand, split-off band states are still pure Eigen states of $|\frac{1}{2}, \pm \frac{1}{2}\rangle$ and therefore, it produces electrons with degree of spin polarization of -1.

Further when $E_{ph} \gg E_g$, the band mixing because of $k.p$ interaction has to be taken in to account. This is done by expressing the respective bands with the help of Luttinger-Kohn Hamiltonian [23]. It has been shown that, for $E_{ph} \sim E_g + \Delta_{so}$, the lh state acquires much of the characters of $|\frac{1}{2}, \pm \frac{1}{2}\rangle$, and hence ρ_e decreases [24]. It should be noted that, for the case of $E_{ph} > E_g + \Delta_{so}$, ρ_e decreases because of the two reasons; one is because of the onset of transitions related to split-off band states and the other is because of the increase of $|\frac{1}{2}, \pm \frac{1}{2}\rangle$ character of lh states. However, at this energy, the joint density of states corresponding to split-off band is too less to explain the observations made. Therefore, the majority of decrease in ρ_e is because of the lh and not by the so states [24]. Notwithstanding the underline physical details, the main results are identical to equations 1.5 and 1.6. This is the reason that the former approach is followed more traditionally. However, during the course of this thesis work, the general approach is followed whenever found necessary.

Furthermore, Luttinger-Kohn Hamiltonian is used to calculate the electron spin polarization in cases, where the degeneracy between hh and lh states is lifted either by quantum confinement or strain. By numerical integration, it has been shown that ρ_e approaches nearly one, when hh and lh states are completely decoupled.

For the detection of spin polarization of electrons, the same selection rule, explained in section 1.3 is used. The only difference is that the degree of circular polarization of luminescence (ρ_L) is measured to extract the information about ρ_e [20]. From the same analysis, it is clear that in case of bulk unstrained semiconductors, when ρ_L is measured along the direction of spin polarization, the following relation holds

$$\rho_e = 2 \rho_L \quad (1.10)$$

This means, a spin polarized electron system with $\rho_e = 1$, gives rise to luminescence, whose degree of circular polarization is 0.5. This directly follows from the Bloch wave function of hh and lh states. This method has been traditionally used to measure the spin injection efficiency into the LEDs [25, 26]. However, because of practical constraints, it may not be always possible to measure ρ_L along the direction of spin polarization. In that case, the relation becomes [27]

$$\rho_e = \frac{2\rho_L}{\cos(\theta_0)} \quad (1.11)$$

Where, θ_0 is the angle between the spin polarization vector and the detection direction. Since the recombination of carriers almost always happen at $k=0$, the split-off band states have negligible effect on the detection mechanism and ρ_e becomes equal to ρ_L , whenever the hh and lh states are decoupled due to strain or quantum confinement. However, these two states have different angular dependences given by [28]

$$\rho_e = \frac{(1 + \cos^2 \theta_0)}{2 \cos(\theta_0)} \rho_L, \quad \text{for } hh \text{ state}$$

$$\rho_e = \frac{-(5 - 3 \cos^2 \theta_0)}{2 \cos(\theta_0)} \rho_L, \quad \text{for } lh \text{ state} \tag{1.12}$$

These equations are of potential use while correlating the electron polarization to the light circular polarization in a quantum well.

1.2.3 Spin relaxation

In this subsection, various spin relaxation mechanisms in semiconductors are introduced. Generally, any fluctuation or inhomogeneity of spin interaction can lead to spin relaxation. However, there are a few mechanisms which are more relevant in III-V semiconductors which are discussed in this section [29-32] and are summarized here,

1.2.3.1 Elliot-Yafet mechanism

This mechanism was first proposed by Elliott [33] and Yafet [34] while studying the spin relaxation in silicon and alkali metals. It originates from the fact that, in the presence of spin-orbit coupling, the exact Bloch states are not spin eigen states but a superposition of different spin components. Since the coupling is weak, they are still labeled as “up” and “down” spin states, with respect to some quantization axis. However it implies that whenever the spatial part of wave function undergoes a transition because of momentum scattering, a finite probability exist to flip the spin from “up” to “down”, leading to spin relaxation [29]. Under this mechanism, spin-

orbit coupling leads to the spin-flip electron-impurity scattering. The spin relaxes during the scattering, which is why the spin relaxation rate is directly proportional to momentum relaxation rate. Typically in III-V semiconductors an electron has to undergo 10^5 scattering events before a spin flip occurs [32]. The spin relaxation time because of Elliott-Yafet (EY) mechanism is given by [29, 30]

$$\frac{1}{\tau_s^{EY}} = A \frac{\langle E_e \rangle^2}{E_g^2} \eta^2 \left(\frac{1-\eta/2}{1-\eta/3} \right)^2 \frac{1}{\tau_p} \quad (1.13)$$

Here E_e is the energy of electrons in the conduction band, $\eta = \Delta_{so}/(E_g + \Delta_{so})$ and τ_p is the momentum relaxation time. A is a dimensionless constant which is governed by the dominant scattering mechanism. This mechanism is present in semiconductors with and without a center of inversion symmetry, although it is most prominent in the centro-symmetric ones. It is especially important in narrow-band-gap and high impurity semiconductors. In GaAs material, EY mechanism is predominant at very low temperatures especially below 5 K [30].

1.2.3.2 D'yakonov- Perel' mechanism

D'yakonov and Perel' proposed an efficient mechanism of spin relaxation through spin-orbit coupling in systems which lack inversion symmetry, like Zinc-blende semiconductors, was by [35]. In this case, the degeneracy between electrons with the same k but different spin states is lifted for $k \neq 0$. This energy difference acts as an effective k dependent magnetic field and results in spin precession with angular frequency $\Omega(k)$ during the time between collisions. In the presence of momentum scattering, the magnitude and direction of k changes in an uncontrolled way. Thus

the precession axis and frequency change randomly between adjacent scattering events which lead to spin relaxation. It is known as the D'yakonov and Perel' (DP) spin relaxation mechanism.

There are two regimes for DP spin relaxation [30]. (i) Strong scattering regime where $\langle\Omega\rangle\tau_p \ll 1$. Here $\langle\Omega\rangle$ is the ensemble average precession frequency. The spin relaxation time in this regime is estimated as $1/\tau_s = \langle\Omega^2\rangle\tau_p$ according to the random walk theory. This is also known as motional narrowing i.e. stronger momentum scattering leads to longer spin relaxation time. (ii) Weak scattering regime where $\langle\Omega\rangle\tau_p \geq 1$. In this regime, the momentum scattering no longer slows the spin relaxation. In contrast, via the spin-orbit coupling, momentum scattering provides an additional channel for spin relaxation, making τ_s directly proportional to τ_p . In most of the cases, III-V semiconductors fall in the strong scattering regime. The associated relaxation time is given by [30]

$$\frac{1}{\tau_s^{DP}} = \frac{8}{105} (2\gamma_D)^2 \frac{\langle E_e \rangle^3}{\gamma_3} \tau_p \quad (1.14)$$

Here, γ_D is the Dresselhaus coefficient which deals with the inversion asymmetric nature of bulk III-V semiconductors, γ_3 is a constant that depends on the scattering mechanism. It is a dominant mechanism in most of the type III-V semiconductors. Furthermore, its impact is higher at large energy as is obvious from equation (1.14) due to the cube of energy of electrons.

1.2.3.3 Bir- Aronov- Pikus mechanism

Usually exchange interaction between electrons does not lead to spin relaxation as it preserves the total spin. However, in a p-type semiconductor, when holes are present in abundance, electron-hole exchange interaction swaps the spin of electrons while holes keeps their total spin conserved. This is called Bir-Aronov-Pikus (BAP) mechanism after the name of their founders [36]. However, the holes themselves lose their spins very fast because of valence band mixing through EY mechanism. Therefore, holes act as a reservoir for spin: spin-polarized electrons dump their spin into this reservoir, in which the spins will get lost very fast [31]. The spin-flip scattering probability depends on the state of the holes like whether they are degenerate or non-degenerate, bound with acceptors or free, fast or thermalized etc. For a non-degenerate hole system, assuming the scattering is predominantly because of heavy holes, due to their larger density of states, the spin relaxation time is given by [30]

$$\frac{1}{\tau_s^{BAP}} = \frac{2}{\tau_0} n_h a_B^3 \frac{\langle v \rangle}{v_B} \quad (1.15)$$

Where a_B is the exciton Bohr radius, n_h is the hole density, $\langle v \rangle$ is the average electron velocity, $v_B = 1/(\mu a_B)$ with μ being the reduced mass of the interacting electron-hole pair. τ_0 is related to the exchange splitting of exciton ground state (Δ_{exc}) as $1/\tau_0 = (3\pi/64) (\Delta_{exc})^2 / (E_B \hbar)$, E_B is the exciton binding energy.

1.2.3.4 Hyperfine interaction

Exchange of electron spin with nuclear spin through hyperfine interaction can lead to spin relaxation. When the nucleus of the constituent atoms contains a finite spin, it interacts with the electronic spin and is a potential source of spin relaxation [31]. For moving electrons, this interaction is negligible, as electrons move fast across the nuclei with random spins by averaging their actions. However, it is more important for the case of electrons that are confined at impurity levels or in quantum dots. On an average for donor-bound electrons in GaAs, the hyperfine field is equivalent to an effective magnetic field of 5.4mT [37]. It can lead to spin relaxation in semiconductor quantum structures where high density electrons are confined to ultralow dimensions.

1.2.4 Spin Hall Effect and Inverse Spin Hall Effect

As mentioned in the earlier part of this chapter that a major quest in semiconductor spintronics is related to the ability of control and detection of electronic spin without involvement of external magnetic field and magnetic materials. The prediction of Spin Hall Effect (SHE) is a major step forward in this direction. It refers to the generation of transverse spin current by a charge current in a material with relativistic spin-orbit coupling [17]. The generated spin current has the direction of spin polarization vector perpendicular to both spin and charge current directions. Conceptually, it is similar to the Anomalous Hall Effect observed in ferromagnets, where a transverse voltage is generated because of asymmetric scattering of electrons with different spin orientation. Spin Hall Effect (SHE), which

was initially predicted in 1971 by D'yakonov and Perel' describes the generation of a spin current perpendicular to a spin-unpolarized charge current in the presence of spin-orbit coupling [38, 39]. In their proposal, they suggested a spin-dependent Mott scattering of unpolarized electrons at the impurity site, which leads to a spatial separation of charge carriers with opposite spins. However, the term "Spin Hall Effect" was first introduced by Hirsch [40], where he explained the general phenomenon in any semiconductors or ferromagnetic material above curie temperatures and thus brought it to the attention of the spintronics community.

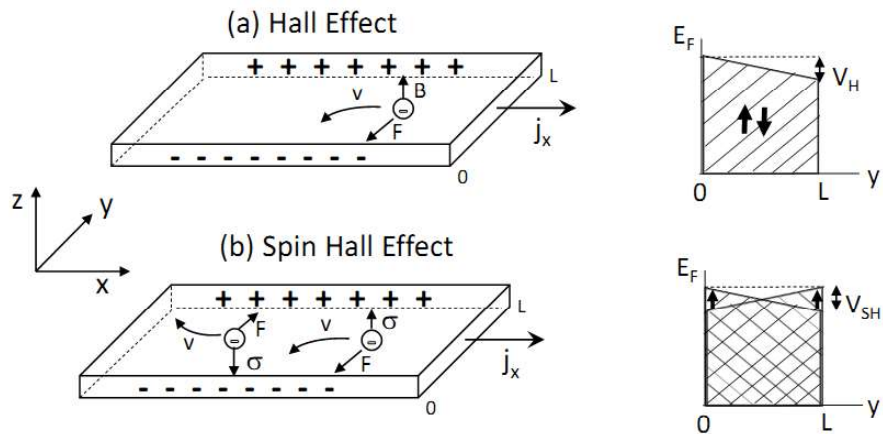


Figure 1.5 Schematic of the (a) Hall Effect and (b) Spin Hall Effect showing the charge and spin accumulations respectively. The corresponding Fermi level positions are also shown in the figure. Here B , F , v and σ are the magnetic field, force on electron, electron velocity and electron spin magnetic moment respectively [40].

It is better understood, if an analogy is drawn with the Hall Effect, where charges accumulate at the sample boundaries due to the action of the Lorentz force in magnetic field, giving rise to a transverse electric field. Similarly

in the absence of magnetic field, spin orbit coupling ensures spatial separation of electrons with opposite spin. It is schematically shown in figure 1.5.

In case of Hall Effect, spin-up and spin-down electrons share the Fermi level but the Fermi level is different at the two edges of the sample because of electron accumulations. The difference between the Fermi levels at the two edges of the sample provides Hall voltage V_H . On the other hand, in case of spin Hall Effect, electrons with different spin orientations accumulate at the two edges of the sample. Therefore, the difference in the Fermi levels for each spin at both edges of the sample is V_{SH} , but it is of opposite sign for spin up and down electrons. This is seen as transverse spin imbalance. However, since the number of electrons with up and down spins is same, no charge imbalance results.

The Onsager relation predicts that a spin current will lead to transverse charge imbalance in presence of spin orbit coupling [21]. This is known as Inverse spin Hall Effect (ISHE). This phenomena is called extrinsic spin Hall effect as the presence of impurities is necessary for this spin dependent scattering [41]. In contrast, the possibility of a strong intrinsic spin Hall Effect entirely due to spin-orbit interaction is also predicted by Sinova et al. [42] and Murakami et al. [43], based on linear response microscopic theories of strong spin-orbit coupled system, which occurs even in the absence of any scattering process. Numerous experimental and theoretical studies in recent times have led to a number of spin Hall devices in various materials [44-46]

Phenomenologically, these phenomena can be explained in following simple ways [21]. In the absence of spin-orbit coupling, the charge and spin current are written in terms of drift-diffusion equations as follows,

$$\begin{aligned}
q^{(0)} &= -\mu n E - D \nabla n \\
q_{ij}^{(0)} &= -\mu E_i P_j - D \frac{\partial P_j}{\partial x_i}
\end{aligned} \tag{1.16}$$

Here, q_{ij} is the spin current along i direction because of the electrons that are spin polarized along j direction. μ , D and P are the mobility, diffusion coefficient and spin polarization density respectively. In this formula, other forms of current like a temperature gradient are not included. On the other hand, in presence of spin orbit coupling, these two terms get coupled and the equations are rewritten as follow

$$\begin{aligned}
q_i &= q_i^{(0)} + \gamma \varepsilon_{ijk} q_{jk}^{(0)} \\
q_{ij} &= q_{ij}^{(0)} - \gamma \varepsilon_{ijk} q_k^{(0)}
\end{aligned} \tag{1.17}$$

Here ε_{ijk} is the unit anti symmetric tensor and γ is a dimension less parameter called the spin Hall angle. Equation (1.17) explains both the spin Hall Effect and inverse spin Hall Effect in terms of coupled equations. It must be noted here that the combined drift-diffusion type equations are only valid in weakly spin orbit coupled systems. In case of strongly spin-orbit coupled systems, where intrinsic spin Hall Effect prevails, such type of equations are difficult to be written [47]. Irrespective of their microscopic origin, the two effects are pictorially explained as follows,

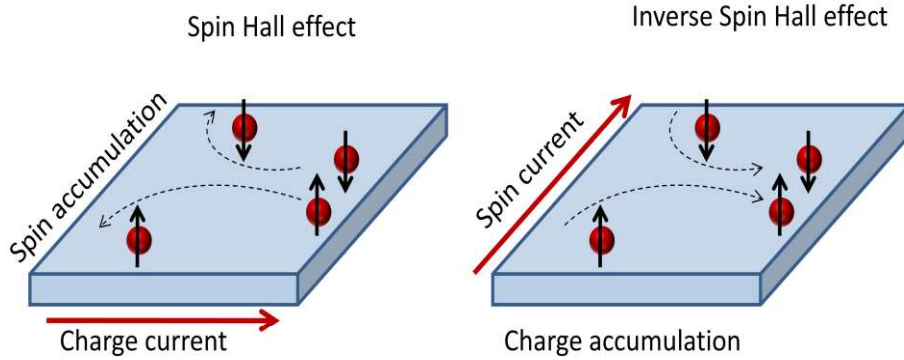


Figure 1.5 Picture illustrating Spin Hall Effect and Inverse Spin Hall Effect

1.2.4.1 Mechanisms of Spin Hall Effect

There are two distinct physical origin of SHE, one is the extrinsic mechanism, where the scattering by impurity is the primary criteria and the other is the intrinsic mechanism, where the band structure of the materials plays a critical role [47, 17]. Extrinsic mechanism is controlled by spin-orbit interaction with impurities, which is further classified as (i) Skew scattering and (ii) Side-Jump scattering mechanism.

Skew scattering arises from the asymmetry of electron-impurity scattering in presence of spin-orbit interaction. As explained by Vignale et al. [17] spin-orbit interaction with spherically symmetric impurities conserves separately the orbital and the spin angular momentum, L_z and S_z . Thus the scattering cross section depends not only on the scattering angle, but also on the relative sign of L_z and S_z . This creates an asymmetry between the numbers of electrons of a particular S_z that are scattered in opposite directions. This gives rise to the spatial separation of electrons with spin polarization along different directions. Obviously, the sign of the

effect depends on the sign of the potential. However, as pointed out by Sinova et al.[47], this simple model of considering the spin-orbit coupling in the disorder potential alone is valid only when spin-orbit coupling in the bands is not strong enough to split the degenerate spin sub bands. Otherwise, the spin-orbit coupling of different bands and their effects on disorder potential have to be considered for detailed calculation of skew scattering mechanism.

The side-jump is a subtle effect originating from the anomalous form of the velocity operator in spin-orbit coupled systems. For a weak spin orbit coupled system, like GaAs, the velocity operator gets a new term and is given by [17]

$$v = \frac{\hbar k}{m^*} + \frac{2\lambda_c^2}{\hbar} \nabla V_{imp}(r) \times \sigma \quad (1.18)$$

Thus, a transverse velocity depending on the orientation of spin polarization is added to the normal linear velocity, giving rise to the side jump contribution to the SHE.

The intrinsic mechanism is associated with the spin-dependent band structure of the material, e.g. with the Dresselhaus term in bulk zinc-blende semiconductors, and with the Rashba term in a quantum well [17]. It depends on the fact that electron spin with momentum k precesses under the influence of the effective magnetic field $B(k)$ that is originated from the spin-orbit coupling. When a steady state electron distribution represented by a sphere in k -space is disturbed by the applied electric field, the electrons will have different k values and hence will get out of the alignment with the effective magnetic field $B(k)$. The spin realignment

process tilts the spin away from the original orientations, which is in opposite directions on the opposite sides of the Fermi sphere. Hence a spin current appears. The Detailed analysis of different mechanism governing the spin Hall Effect is highly involved and is given various specialized text in this field [47-48].

1.3 Historical Overview

1.3.1 Methods of Spin injection

Most of the semiconductors are naturally nonmagnetic in nature. Therefore, to exploit the spin dependent properties in these semiconductors, the first task is to create non equilibrium population of spin polarized electrons. This is the concept of spin injection and is one of the foremost challenges that semiconductor spintronics community faces [50]. Creating a spin-polarized current in a semiconductor at room temperature is a herculean task. However, there exist several ways through which it can be realized as summarized in the subsequent text.

Various electrical methods like attaching a ferromagnetic metal with the semiconductor [50], use of dilute magnetic semiconductors [51] or Heusler alloys [52], and design of spin selective tunnel barriers [53] are some of the techniques that are frequently used for this purpose. Simultaneously, the optical method of spin injection using circularly polarized light of appropriate energy has been evolved as the cleanest method of spin injection, which does not depend significantly on the surface/interface conditions. Rather, it is governed by the choice of the energy

of circularly polarized light beam and the band structure of underlying semiconductor material [20].

Optical spin orientation was first demonstrated in 1968 by Lampel [54]. Subsequently, Parson, D'yakonov & Perel' and Meier & Zakharchenya did the major work in this field [20, 55, 56]. Initially, much of the works are concentrated in p-type GaAs, where there are no equilibrium electrons, and hence the detection gets easier. D'yakonov & Perel' showed in 1971 that even in n-type GaAs optical orientation is possible by replacing the equilibrium electrons with the photo-generated electrons [56]. Later this approach has been used to inject spin into many other III-V semiconductors and their quantum wells. This method has become highly standardized and has been used to characterize the spin transport across the ferromagnet/semiconductor interface [57].

1.3.2 Methods of Spin detection

Similar to the spin injection methods, there are both electrical and optical methods to detect the electronic spin. In the electrical methods, ideally the same type of ferromagnetic structures that are used for electrical spin injection are used for spin detection also. Because of the spin-dependent density of the contacts, the resistance is different for the carriers with spin orientation parallel or anti parallel to the magnetization direction of ferromagnet [58]. This is the GMR (Giant Magneto Resistance) effect as explained in the earlier part of this chapter, and is the easiest method of spin detection for electrically injected spin. This method has also been used to detect the optically induced spin polarization [59]. Tunnel diode based

arrangement using ferromagnetic contacts for detecting the spin in a non-local geometry is also proposed [60]. This non-local detection of electron spin was first demonstrated in a metallic lateral spin valve structure by Johnson and Silsbee [61]. This has been used for the detection of spin accumulation in GaAs by using a Fe/GaAs (001) hetero-structures in 2007 by Lou et al. [62]. However, validity of this approach has been questioned under certain conditions, mostly because of the presence of fringe magnetic fields produced by the ferromagnetic contacts [8, 63]. They produce local Hall Effect in the semiconductor materials, which hamper the measurement. Furthermore, electrical detection cannot offer a quantitative and model independent estimate of spin polarization, rather a numerical fitting of the electrical signals is required. Therefore, the most preferred method for estimating the spin injection is the optical method.

The principle behind optical method of spin detection is precisely opposite to the optical method of spin injection. Here, the degree of circular polarization of the luminescence is measured to extract the information about electron spin polarization [20]. It has been shown that 100 % spin polarized electron system with unpolarized holes gives rise to light with degree of circular polarization 0.5. The degree of circular polarization of the radiation therefore serves as a useful and direct measure of the carrier density spin state as well as its change under the influence of external factors and relaxation processes. In fact, historically this method has been the preferred choice to estimate the spin injection efficiency by electrical methods by using a LED structure [25, 52]. Ohno et al. [52] and

Fiederling et al. [25], independently demonstrated this approach in InGaAs and GaAs quantum well LED respectively. Since these early demonstrations, a large number of similar studies have been reported, where a variety of quantum well materials and spin injection methods are used [26, 64].

Beside, these two primary methods of spin detection, various methods like resonant pick-up coil method [65], Kerr rotation spectroscopy [66] have also been used to detect electron spin density and their transport under different configurations.

1.3.3 Spin Hall Effect Measurements

Along with their theoretical proposals, D'yakonov and Perel' also suggested several experimental techniques to detect the SHE [39]. Two of their proposals namely, the Kerr magneto-optical microscopy and circularly polarized electro-luminescence from the sample edges, have been used successfully for this purpose [66, 67]. Using a magneto-optical Kerr microscope, Kato et al. [66] scan the spin polarization across a current carrying channel and observed the first clear signal of SHE in semiconductors. From the measurement of Kerr ellipticity and Kerr angle, they observed accumulation of different spins at the two different edges of the sample because of extrinsic mechanism. On the other hand, Wunderlich et al. [67] pass current in a 2 dimensional hole gas and observed circularly polarized LEDs placed nearby and called it intrinsic mechanism. Sih et al. [68] showed that in any non-magnetic materials, SHE can be used to generate spin current. Using the same Kerr magneto-rotation microscopy, Matsuzaka et al. [69] measured the SHE in GaAs of

different carrier concentrations. However, since in a non-magnetic homogeneous semiconductor, spin accumulation is not accompanied by a charge accumulation, SHE does not necessarily leads to an electrical voltage, which makes it difficult to be probed. Pershin et al. [70] proposed a voltage probe of SHE by making the semiconductor inhomogeneous either in resistivity or in carrier concentration, in the direction of spin accumulation. Nonetheless, because of charge accumulations, ISHE is easier to probe [47]. It is expressed by the following relation

$$E_{ISHE} = \frac{\gamma}{\sigma_c} \left(\vec{J}_s \times \hat{\sigma} \right) \quad (1.19)$$

Here, E_{ISHE} is the electric field generated because of the spin current J_s . $\hat{\sigma}_s$ is the unit vector along the spin polarization direction, σ_c is the charge conductivity of the sample and γ is the spin Hall angle. Further, an important material parameter governing the ISHE, called the Spin Hall Conductivity spin Hall conductivity (σ_{SH}) is defined as $\sigma_{SH} = \gamma \sigma_c$. Several groups have observed ISHE in nonmagnetic semiconductors [71, 72]; by injecting spin current electrically or optically. However, σ_{SH} is at least two order less in semiconductor as compared to high Z-metals and therefore measuring ISHE in semiconductors is still a challenging task. For this reason, Ando et al. [73,74] proposed to coat a thin film of Pt over GaAs and to measure the ISHE in Pt/GaAs hybrid structures. In GaAs layer, absorption of circularly polarized light lead to the generation of spin-polarized carriers, which thereafter move towards the metallic layer. It induces a pure spin-current into the Pt layer through the interface. This pure spin-current is converted into a transverse

electrical voltage due to the ISHE in Pt layer. Systematic changes of the ISHE signal were observed upon changing the direction and ellipticity of the circularly polarized light, consistent with the expected phenomenology of the photo-induced ISHE. Unlike other methods of detecting spin polarized carriers, where spin-current is accompanied by a diffusive or drift charge current [75, 76] , the method proposed by Ando et al. [73,74] is because of pure spin current due to the open circuit conditions. In recent years, various theoretical and experimental efforts have been put to estimate σ_{SH} both in metals and semiconductors which are summarized in table 1.4.

Table 1.4 Results to illustrate the estimated value of σ_{SH} from the literature

Material	Structure	Type and doping (cm ⁻³)	σ_{SH} ($\hbar/e \Omega^{-1}m^{-1}$)	Estimation method (Temperature)	Ref.
GaAs	Thin film	n (1 x 10 ¹⁶)	0.5	Kerr microscopy(30 K)	[66]
GaAs	Thin film	n (3 x 10 ¹⁷)	100	Kerr microscopy(30 K)	[69]
GaAs	Thin film	n (2 x 10 ¹⁸)	1.1-2	SHE (up to 75 K)	[76]
GaAs	Bulk	n	100	Ab-initio	[77]
GaAs	Bulk	n (1 x 10 ¹⁶)	2.97	Theory	[78]
GaAs	Bulk	n	2	Theory	[79]
GaAs	Bulk	n (2 x 10 ¹⁸)	4.9 ±2.8	ISHE (300K)	[80]
InGaAs	Thin film	n (3 x 10 ¹⁶)	0.5	Kerr microscopy(30 K)	[66]
Pt	Bulk		3.8 x 10 ⁵	STT,SHE (295 K)	[81]
Au	Thin film		4.1 x 10 ⁶	NL (295 K)	[82]
Al	Thin film		2.7 x 10 ³	NL (4.2 K)	[83]
Cu	Thin film		5.1 x 10 ⁴	SP (295 K)	[84]
U	Thin film		1.4 x 10 ⁴	SP, ISHE	[85]
Mo	Bulk		2.3 x 10 ³	SP (295 K)	[86]
Pd	Bulk		2.9 x 10 ⁴	STT,SHE (295 K)	[87]
Ag	Bulk		1.0 x 10 ⁵	SP (295 K)	[84]
Nb	Thin film		8.7 x 10 ³	NL (10 K)	[88]

MR: Magneto resistance, STT: Spin Transfer Torque, NL: Non Local methods, SP: Spin pumping

1.4 Motivation and Objectives

Though ISHE as a phenomenon is well established, detection of ISHE in semiconductors is still challenging because of the small value of spin Hall conductivity. It is one of the critical limitations which have restricted the realization of novel semiconductor devices based on the concepts of ISHE. Several uncertainties still persist, for example the dominant mechanism governing ISHE in some situations is not yet well understood. Several issues related to spin injection, spin relaxation of hot electrons, spin transfer across the interface of heterostructures and the temperature dependence of ISHE phenomenon have been intriguing the semiconductor spintronic community for quiet sometime. One of the main objectives of this thesis is to study such key issues which are extremely critical to the domain of semiconductor spintronics. Moreover, the aim is to do all this without involving any ferromagnetic material, such that the electronic spin related fundamental phenomena can be studied and related devices can be made without the need of external magnetic field.

Furthermore, we shall look for the answers of a few important questions which have been puzzling the physics community for quite sometimes and are listed below,

1. Why it is so difficult to observe ISHE in bulk semiconductors? Is there something that one can do for the realization of ISHE phenomenon in bulk semiconductors? One of the major aims is to look for those bottlenecks i.e. the scattering mechanisms which cause the spin relaxation in bulk semiconductors?

Fundamental understanding of those factors may help in the realization of ISHE in bulk semiconductors.

2. To explore some novel concepts where one can use new designs by incorporating multi-layers of different nonmagnetic materials. Can one use a multilayer design where key operations like the injection, separation and detection of electronic spin are carried out in different parts of the device? If possible then it will surely leads to the realization of useful semiconductor devices based on the concepts of ISHE.
3. Operating temperature is critically important in all the spin based devices. Several scattering mechanisms are already known to cause the spin relaxation at elevated temperatures. One of the major aims is to understand such scattering mechanisms and also to find out the maximum temperature up to which an ISHE based semiconductor device might operate? Can one tailor a new device structure such that a practical ISHE based device operates at room temperature?
4. Spin Hall conductivity or the spin Hall angle are the key parameters related to the observation of ISHE in semiconductor materials. Can those be measured by using the concepts of ISHE in case of bulk and quantum well (QW) structures?
5. Radiative recombination of spin polarized carriers leads to the emission of a polarized photoluminescence (PL) signal. Is it therefore possible to correlate the electron spin polarization to the emitted photoluminescence signal?

6. In case of a QW structure, one injects the spin polarized carriers in the barrier layer which thereafter recombine inside the well layer. Is it possible to comment on the spin injection and spin transfer across the interface by monitoring the polarization state of the PL signal emitted from the QW?
7. Finally, the ultimate aim of this thesis is to develop a practical device by exploiting the concepts of ISHE. If developed then such a device can help in the realization of a spin based communication systems. Innovative designs are to be used for the realization of such devices which shall be highly secure and might be able to work even at room temperature!

Chapter 2

Numerical Simulations for Inverse Spin Hall Effect

2.1 Necessity of numerical simulations

It has been shown that the measurement of ISHE in semiconductors needs special effort as the magnitude of ISHE signal is generally very low. Various techniques have been devised to enhance the signal-to-noise ratio. Recently, an effective and simple method has been demonstrated for detecting the spin current in a multilayer structure, where a thin film of high Z metal, like Pt or Au is coated over the semiconductor forming a hybrid structure [72]. The proposed device structure takes the advantage from the fact that due to optical selection rules, circularly polarized light generates spin-polarized electrons in the conduction band of Zinc-blende semiconductors. These electrons are distributed symmetrically in k -space and a few of them reach the metal layer by crossing the Schottky barrier to produce a pure spin current (J_s). Due to large spin-orbit coupling of metallic layer, the spin current produces transverse electric field (E_{ISHE}) according to equation (1.19) and attribute to the ISHE.

Spin and energy state of electrons produced by the circularly polarized light in semiconductor material are in non-equilibrium and they relax down to the equilibrium state values within the respective relaxation times. The typical time (τ_v) taken by the photo-generated electrons to reach the metal layer from semiconductor materials is ~ 1 ps. If the spin relaxation time (τ_s) and energy relaxation time (τ_E) are comparable to this time scale, significant spin and energy relaxation will occur. For thermalized electrons τ_s and τ_E are of the order of 10 to 100 ps; therefore, almost no relaxation is expected [89]. However, photo-generated electrons can possess energy much higher than the conduction band edge where the values of τ_s and τ_E are in sub-ps range which is typical in case of hot electrons [90]. Furthermore, all the mechanism involved here like energy and spin relaxation and tunneling are highly energy dependent. Therefore careful planning of experiments is required to detect the weak ISHE signal. In order to find the most optimum experimental conditions related to the excitation energy, angle of incidence and suitable material combination, systematic numerical simulations are mandatory. Thus, a prior knowledge of these parameters can help in a timely and successful execution of the planned experiments.

In this chapter, systematic numerical calculations based on the analysis of both energy and spin relaxation phenomena for optically induced hot electrons, tunneling and thermionic transport effects at the metal/semiconductor interface and circular dichroism for the light transmitted through the metal layer are carried out. It is understood that a semiconductor with small spin orbit splitting is an ideal

candidate for the injection of spin polarized carriers under certain conditions. One therefore needs to fabricate a metal/semiconductor hybrid structure where spin injection and separation are carried out in semiconductor and metallic sections of the device respectively. By analyzing different III-V semiconductors like GaAs, InP, InAs and InSb, it is observed that InP based hybrid structure offers the best possible combination for measuring the ISHE signal. The methodology of numerical calculations is briefly discussed in this chapter including the relevant fundamental physical mechanisms. Results of the numerical calculations are shown in this chapter, which are also compared with the experimental data available in literature.

2.2 Methods adopted for numerical simulations

2.2.1 Sample geometry

Schematic arrangement of the assumed sample geometry along with the incidence light directions that are considered for the numerical simulation is shown in figure 2.1. A metallic layer of thickness d is assumed to be deposited on the top of semiconductor layer. Thickness of semiconductor layer is much larger than the penetration depth of light such that the incident light is completely absorbed. Two electrical contacts are connected at the two ends of the metallic layer. Circularly polarized light is incident on this hybrid structure under a condition that the plane of incidence always makes 90° angle with the direction where voltage was measured. However, the angle of incidence is taken as a free parameter in our calculations.

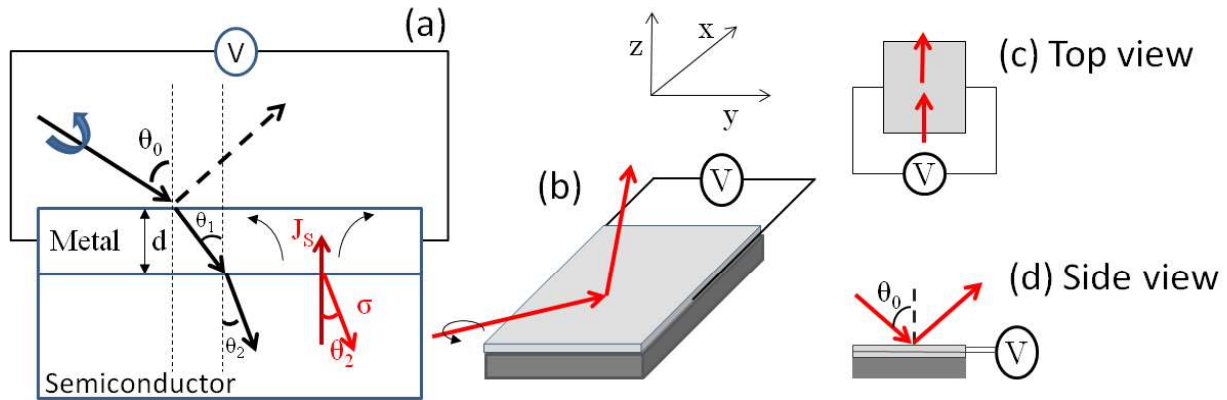


Figure 2.1 Schematic of the sample geometry considered (a) Shows the mechanism along with the angle of incidence (b), (c) and (d) show the 3-dimensional view, top view and side view of the metal semiconductor hybrid structure respectively.

2.2.2 Light Propagation through a multilayer structures

According to the geometry used here, light needs to pass through the top metallic layer before entering into the semiconductor for injecting spin polarized electrons. However, any general light beam can be decomposed into s and p polarized components, whose transmission coefficients are different and are highly dependent on the angle of incidence. Therefore, even though, circularly polarized light of particular intensity is incident on the metal layer, the degree of circular polarization (ρ_l) and the light flux injected into the semiconductor layer vary depending on the optical constants (n and k) of the layers, thickness of metal layer and angle of incidence. These quantities can be calculated by solving the matrix equation corresponding to light propagation in a multilayer system [73]. For solving

the matrix equation, the incident light has to be expressed in terms of component of s and p polarized light. The light intensity (I) is given by,

$$I = I_s + I_p = \frac{A^2}{1+A^2} I + \frac{1}{1+A^2} I \quad (2.1)$$

Here, A is the ellipticity of the incident light, and is given in terms of the ratio of major to minor axis of the ellipse. The degree of circular polarization (ρ_l) is given by,

$$\rho_l = \frac{2A}{1+A^2} \quad (2.2)$$

The transmission matrix is given by

$$\begin{pmatrix} B^{s(p)} \\ C^{s(p)} \end{pmatrix} = \begin{pmatrix} \cos \delta & (i \sin \delta) / \eta_1^{s(p)} \\ (i \sin \delta) \eta_1^{s(p)} & \cos \delta \end{pmatrix} \begin{pmatrix} 1 \\ \eta_2^{s(p)} \end{pmatrix} \quad (2.3)$$

Here $s(p)$ denotes the s and p polarized component, $\delta = 2\pi n_1 d \cos(\theta) / \lambda$ is the phase introduced because of transmission, λ is the wavelength of light, $\eta_r^p = n_r (\epsilon_0 / \mu_0)^{1/2} / \cos(\theta_r)$ and $\eta_r^s = n_r (\epsilon_0 / \mu_0)^{1/2} \cos(\theta_r)$. Where, $r = 0, 1, 2$ corresponds to air, metal and semiconductors respectively. θ_r is the incidence angle and is depicted in figure 2.1 (a). The transmission coefficient for s and p -polarized component are calculated by using the following relations [73,91].

$$\tau^s = \frac{2\eta_0^s}{\eta_0^s B^s + C^s} \quad \text{and} \quad \tau^p = \left(\frac{2\eta_0^p}{\eta_0^p B^p + C^p} \right) \frac{\cos \theta_0}{\cos \theta_2} \quad (2.4)$$

Similarly the transmittance is given by [73,91]

$$T^{s(p)} = \frac{4\eta_0^{s(p)} \operatorname{Re}(\eta_2^{s(p)})}{[\eta_0^{s(p)} B^{s(p)} + C^{s(p)}][\eta_0^{s(p)} B^{s(p)} + C^{s(p)}]^*} \quad (2.5)$$

Here, $\operatorname{Re}(\eta_2^{s(p)})$ is the real part of $\eta_2^{s(p)}$. This changes the ellipticity and Intensity of light injected into the semiconductors (ρ_{ll} and I_l respectively) and is given by

$$\rho_{ll} = \frac{2A_1}{1+A_1^2}, \quad A_1 = \frac{\operatorname{Re}(\tau^s)}{\operatorname{Re}(\tau^p)} A \quad (2.6)$$

$$I_l = I^s T^s + I^p T^p = \left(\frac{A^2}{1+A^2} T^s + \frac{1}{1+A^2} T^p \right) I \quad (2.7)$$

The number of spin polarized electrons generated inside the semiconductor is proportional to the product of ρ_{ll} and I_l . The optical constants are taken from reference [92]. For a typical case of Au-GaAs system $\rho_{ll} I_l$, and their product are plotted as a function of incident angle in figure 2.2.

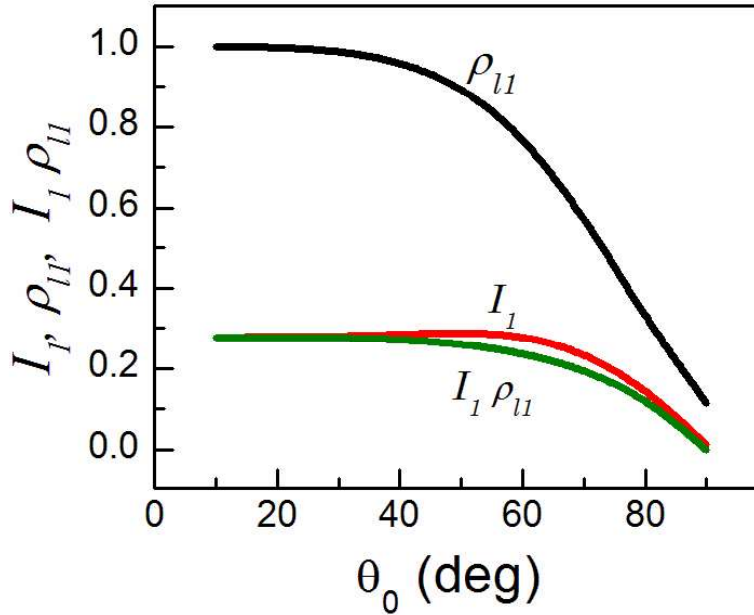


Figure 2.2 Change in degree of circular polarization (ρ_{ll}) and intensity (I_l) of circularly polarized light after passing through Air/Au/GaAs multilayer system. The thickness of Au layer is assumed to be 20 nm.

2.2.3 Optical spin injection in semiconductors

After propagating through the multilayer, the circularly polarized light generates spin polarized electrons in the semiconductor as explained in section 1.2.2. Since only those electrons, which have momenta towards the interface only decides the ISHE, average need not be taken over all the directions. Therefore band structure can be calculated for a particular k , which can be rotated for different angle of incidences [93,94]. To start with, it is assumed that the spin polarization direction coincides with the electron momenta. Under this condition, the band structure can be calculated by putting $k_z=k$, $k_x=k_y=0$. This is shown in figure 2.3 (a). It can either be obtained by assuming parabolic approximations or with the help of numerically calculated band structure. The band structure of GaAs calculated using 8 band $k.p$ method is shown in figure 2.3 (a). The corresponding bands for parabolic approximations are also shown in the same figure as dotted lines. The arrow shows the different possible transitions induced by photons of 2 eV energy. It is clear that electrons excited from different bands will have different energy in the conduction band, which can be calculated from the relation

$$E_{ph} = E_g + E_c(k) + E_v(k) \quad (2.8)$$

Here $E_v(k)$ represents all the valence bands. Under parabolic approximations, the relation will be

$$E_{\text{ph}} = E_g + \frac{\hbar^2 k^2}{2m_e^*} + \frac{\hbar^2 k^2}{2m_h^*} \quad \text{for heavy and light holes}$$

and

$$E_{\text{ph}} = E_g + \Delta_{\text{so}} + \frac{\hbar^2 k^2}{2m_e^*} + \frac{\hbar^2 k^2}{2m_h^*} \quad \text{for split off holes} \quad (2.9)$$

The energy of the electrons, thus calculated are plotted in figure 2.3 (b) as a function of excitation energy.

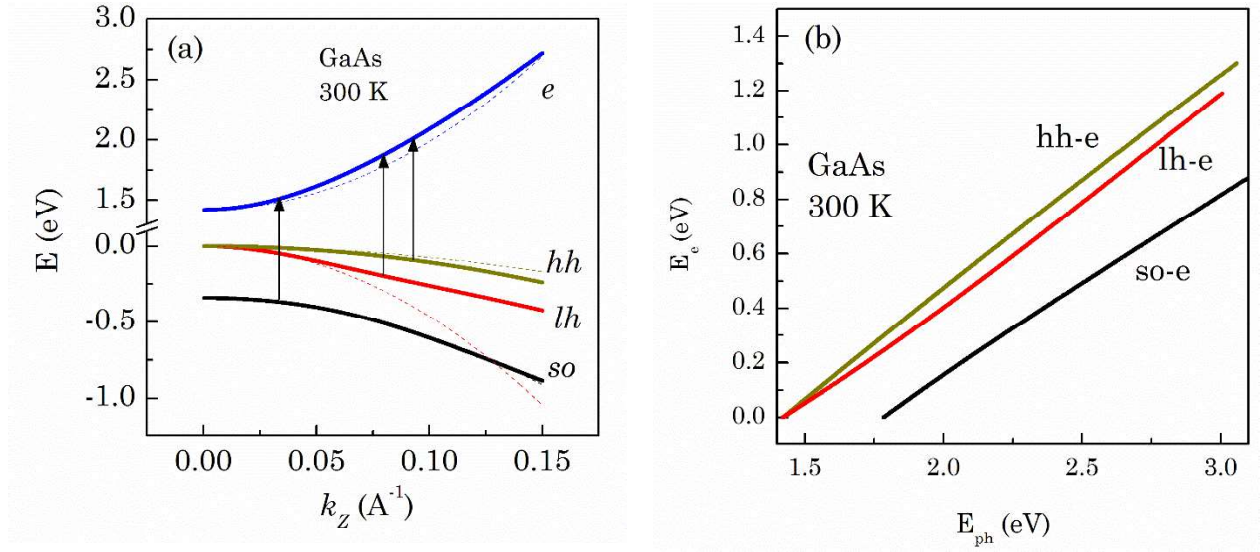


Figure 2.3 (a) Band structure of GaAs calculated using 8 band $k.p$ method. The corresponding parabolic approximations are also shown as dotted lines. (b) Energy of electrons excited from different bands as a function of excitation light energy.

Once the energy distribution of electron is estimated, their relative numbers (N) and degree of spin polarization (ρ_e) is needed to compute the ISHE voltage. These parameters are affected by band mixing at finite k . Therefore the projections of different angular momentum states on various bands are calculated using the same 8 band $k.p$ method and are shown in figure 2.4.

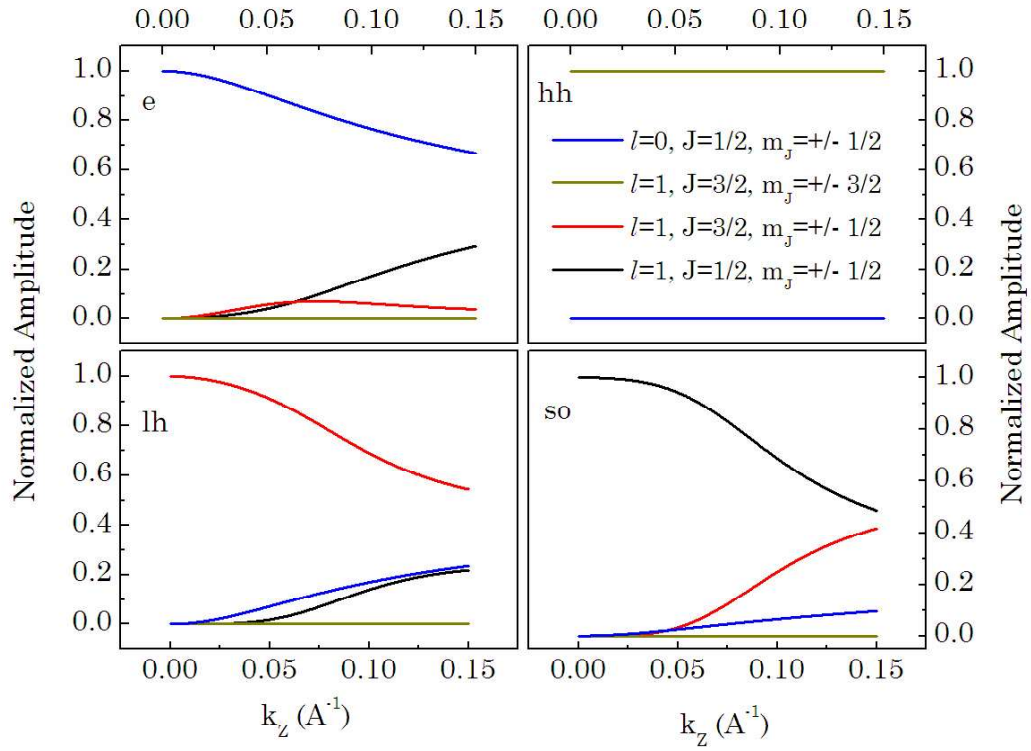


Figure 2.4 Projections of different angular momentum states on various bands calculated using the same 8 band $k.p$ method.

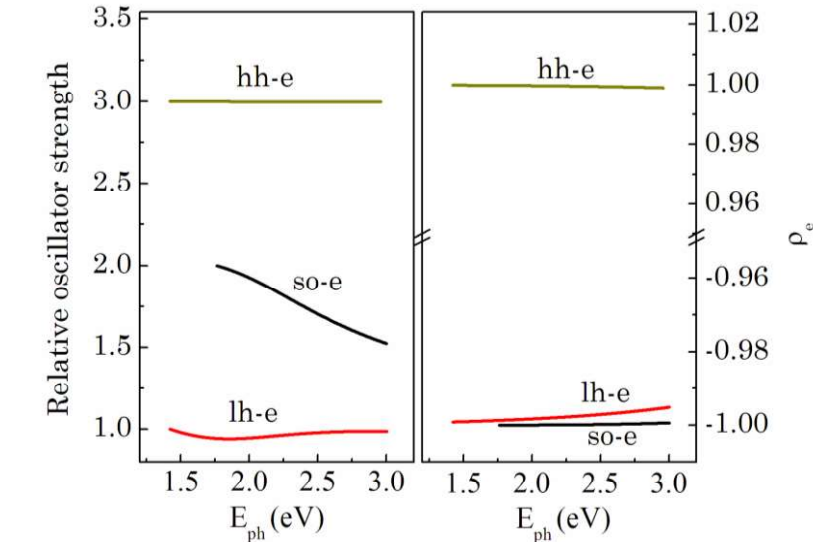


Figure 2.5 Relative oscillator strength of various transitions occurring from different valence band states and the respective electron spin polarizations as a function of excitation photon energy.

The oscillator strength deciding N and corresponding ρ_e for different angular momentum states are given in table 1.3. Now, for a given photon energy, the energy (or k) of a different transitions are known from figure 2.3. For a given k , the components of different angular momentum states are known from figure 2.4 and for a particular angular momentum state, the oscillator strength is known from table 1.3. Using this, the relative oscillator strength of transitions occurring from different valence band states and the respective electron spin polarizations are calculated and shown in figure 2.5. From figure 2.3 (b) and figure 2.5, the energy distribution of spin polarized electrons; $N(E_e)$, for particular photon energy is calculated. $N(E_e)$ is allowed to spread as Gaussian distribution with standard deviation of 25meV because the calculations are carried out at 300K. Figure 2.6 shows $N(E_e)$ for two different excitation energies (1.6 and 2 eV), where the contributions from different transitions were separately marked. Here positive and negative values of $N(E_e)$ correspond to number of electrons with spin $+\hbar/2$ and $-\hbar/2$ respectively. The corresponding distributions calculated from parabolic approximations are also shown in the same figure. It can be noted that, only $lh-e$ distribution at $E_{ph} = 2$ eV is significantly different for the two cases. Therefore, either of the two methods can be used, particularly at lower excitation energy. It can be seen here that the total integrated area vanishes for $E_{ph}=2$ eV, where as it is positive for $E_{ph}=1.6$ eV. This is consistent with the well known result that significant injection of spin polarized carriers are possible only when the energy of the light falls in between E_g and $E_g+\Delta_{so}$.

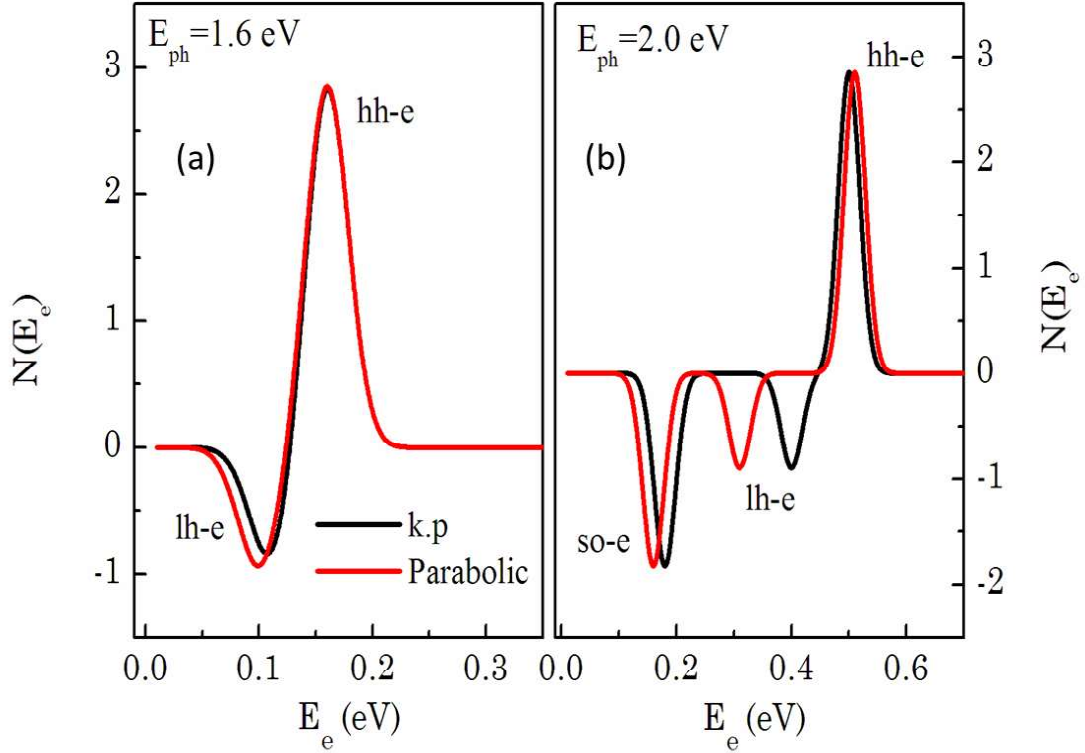


Figure 2.6 $N(E_e)$ for two different excitation energies (a) 1.6 and (b) 2 eV, showing the contributions from different transitions.

For a different angle of incidence, the same method can be applied by suitably replacing the k vector as $k_z = k \cos \theta_2$, $k_x = k \sin \theta_2$ and $k_y = 0$. The angle of incidence and coordinate system is as explained in figure 2.1. Similar method is applied to calculate $N(E_e)$ for different III-V materials.

2.2.4 Energy relaxation of photo-excited carriers

The photo-generated electrons need to propagate to the metal/semiconductor interface to contribute to E_{ISHE} . During their propagation, they relax partially and the amount of relaxation depends on the relaxation rate and the time of travel. Several scattering mechanism leads to energy relaxation in Zinc blende

semiconductors [95]. However, in III-V semiconductors, at room temperature, the dominant mechanism for energy relaxation is the polar optical phonon (POP) scattering [96]. For a moderately doped semiconductor, the contribution from carrier-carrier scattering can be safely neglected. Because of higher energies of the photo generated hot electrons, the contribution of ionized impurity scattering is also very minimal. The energy relaxation time is related to the scattering time (τ) as

$$\tau_E = \left(\frac{E_e}{E_p} \right) \tau \quad (2.10)$$

Here E_p is the optical phonon energy. For POP scattering, τ is related to E_e by the relation [97]

$$\frac{1}{\tau_{POP}} = \frac{q^2 \omega_p \left(\frac{k_o}{k_\infty} - 1 \right)}{2\pi k_o \epsilon_o \hbar \sqrt{2E_e/m^*}} \left[n(E_p) \sinh^{-1} \left(\frac{E_e}{E_p} \right)^{1/2} + [n(E_p) + 1] \sinh^{-1} \left(\frac{E_e}{E_p} - 1 \right)^{1/2} \right] \quad (2.11)$$

Here $n(E_p) = [\exp(-E_p/kT) - 1]^{-1}$ is the probability that a phonon with energy E_p is present. k_o and k_∞ are the static and high frequency dielectric constant respectively (Table 2.1). The scattering time (τ_{POP}) is a weak function of electron energy over the wide energy range considered here and stays relatively constant. This is plotted in figure 2.7.

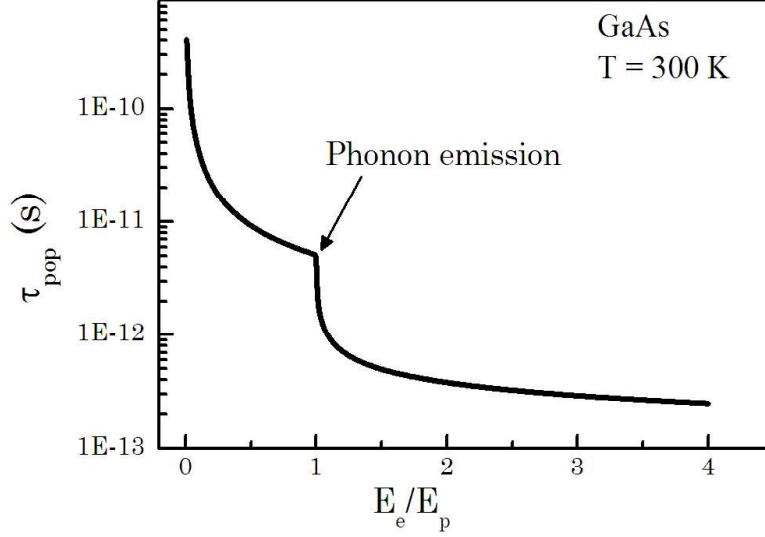


Figure 2.7 Electron scattering time due to polar optical phonon as a function of electron energy.

However, when the kinetic energy of the electron becomes larger than the separation energy of Γ - L and Γ - X valley, inter-valley scattering dominates the scattering rate. The Γ - L and Γ - X separation energy for various III-V semiconductors are given in Table 2.1. Hence, for excitation energy higher than 2 eV, these types of hot electrons are abundantly present. Therefore, for the realistic estimate of energy relaxation time, inter-valley scattering has to be taken into account. The following relation gives inter-valley scattering rate (τ_{iv}) [97]

$$\frac{1}{\tau_{iv}} = \frac{\pi D_{iv}^2 V}{2\rho\omega} [n(\omega)g(E_e + \omega - \Delta E_{iv}) + (n(\omega) + 1)g(E_e - \omega - \Delta E_{iv})] \quad (2.12)$$

Where, D_{iv} is the inter-valley deformation potential, V is the number of identical valley, ρ is the mass density, $g(E_e)$ is the density of state at E_e , and ΔE_{iv} is the inter-valley separation energy. Total scattering rate is given by $1/\tau = 1/\tau_{POP} + 1/\tau_{iv}$.

Table 2.1 Material parameters taken in numerical simulations [16, 101]

	Material	GaAs	InP	InAs	InSb
Parameter	Unit				
$E_g(\text{at } 300\text{K})$	eV	1.42	1.34	0.354	0.17
Δ_o	eV	0.34	0.11	0.41	0.8
E_p	meV	38	43	30	25
$\Delta E_{iv}(\Gamma\text{-L})$	eV	0.3	0.59	0.73	0.51
$\Delta E_{iv}(\Gamma\text{-X})$	eV	0.48	0.85	1.02	0.83
m_e^*	m_o	0.067	0.08	0.023	0.014
m_{hh}^*	m_o	0.51	0.6	0.41	0.43
m_{lh}^*	m_o	0.086	0.089	0.026	0.015
m_{so}^*	m_o	0.15	0.17	0.16	0.19
k_o	$8.85 \times 10^{-12} \text{F/m}$	12.85	12.5	15.15	16.8
k_∞	$8.85 \times 10^{-12} \text{F/m}$	10.88	9.61	12.3	15.7
Γ	eV A^{-3}	27.58	18.32	27.18	760.1

Using relations 2.10-2.12, the energy relaxation rate is calculated as a function of electron energy. The general trend is that, τ_E decreases with increase in electron energy. After knowing τ_E , an estimate of the time of travel is required to calculate the amount of relaxation. It depends on the distance from the interface where the electrons are generated. It is governed by the absorption coefficient and the velocity of photo-generated electrons which can be estimated from the kinetic energies. For a given energy of excitation, absorption coefficient is taken from the literature [6] and velocity is estimated as explained in section 2.2.3.

To implement the above model, the semiconductor substrate is divided into layers of 10 nm width. The light intensity at each layer is calculated by taking into consideration the wavelength dependent absorption coefficient. Thus, each layer contains three information; depth from the surface, number of spin polarized electrons and their energy distributions. The total energy distribution of electrons is obtained by adding the contribution from each layer. From the known distance from the depth, and relaxation times, the contribution of each layer to the energy relaxed distribution is estimated. This is done by propagating electrons layer by layer towards the surface and simultaneously calculating the energy relaxed distribution, $N_E(E_e)$.

Figure 2.8 gives the $N_E(E_e)$ for GaAs, excited by two different photon energies. Here, only electrons excited from hh are considered and a similar distribution for electrons excited from lh states is possible. Large distortion for the case of $E_{ph}=1.74$ eV is because of higher energy of electrons, which leads to shorter relaxation time. In either case, the distribution of electrons at the interface is considerably different than that were at the bulk. However, the area under the curve is same for both the distributions. It is because carrier recombination is not considered here.

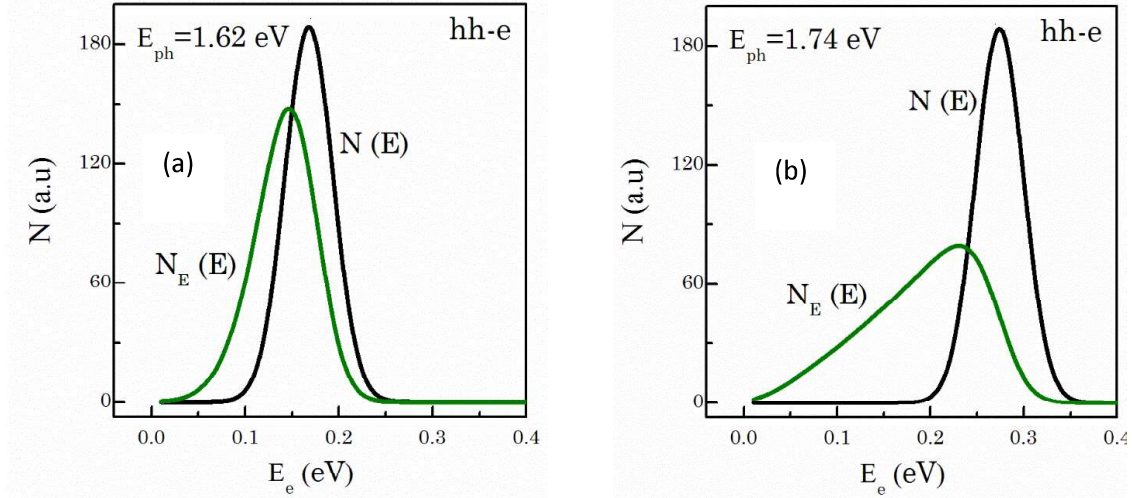


Figure 2.8 The Energy distribution of spin polarized electron in the conduction band, excited by photon energy of 1.62eV (a) and 1.74 eV (b). Black, green lines correspond to the distribution created by polarized light $N(E_e)$ and distribution after energy relaxation $N_E(E_e)$ respectively.

2.2.5 Spin relaxation of electrons

While traveling to the interface, the electronic spin also relaxes following the same manner in which the relaxation of kinetic energy occurs. However, the spin relaxation time is considerably different from the kinetic energy relaxation time. As explained in section 1.2.3, there are various mechanisms for spin relaxation. However, at 300K, the dominant mechanism is DP type and that is related with the k -dependent spin splitting of the conduction band of GaAs [30,98 -100]. This splitting is due to the experience of k -dependent effective magnetic field on the electrons present in the conduction band. This has two contributions, one is due to the bulk inversion asymmetry (BIA), which is related to non-cento-symmetric nature of GaAs while the other is related to structural inversion asymmetry (SIA), which is a result of the built in electric field at the Schottky barrier. The strength of electric field

depends on the carrier density and barrier height at the interface. For a known dopant density, the position dependent electric field can be estimated by solving Poisson's equation. Since the electron momentum varies randomly due to the predominant phonon scattering, spin precesses randomly between adjacent scattering events which lead to spin relaxation. The effective magnetic field due to BIA is given by the Dresselhaus term [30, 99,100].

$$\Omega_{BIA}(k) = 2\gamma_D \left[k_x(k_y^2 - k_z^2), k_y(k_z^2 - k_x^2), k_z(k_x^2 - k_y^2) \right] \quad (2.13)$$

Whereas, Rashba term due to SIA is given by

$$\Omega_{SIA}(k) = 2\beta \left[(k_y E_z - k_z E_y), (k_z E_x - k_x E_z), (k_x E_y - k_y E_x) \right] \quad (2.14)$$

Here γ_D and β are Dresselhaus and Rashba coefficients respectively. k_i and E_i ($i = x, y, z$) are the components of linear momentum and electric field along i -direction. Because of k^3 dependence of $\Omega_{BIA}(k)$, this term dominates over $\Omega_{SIA}(k)$, as the energy of electrons increases. Because of the vector nature of $\Omega_{BIA}(k)$ and $\Omega_{SIA}(k)$, one must take precaution to add their respective components and for this following procedure is adopted here. Direction perpendicular to the interface of hybrid structure is taken as z -axis; y -axis is the direction along which voltage was detected and x -axis is the line of intersection of plane of incidence and interface. These are suitably shown in figure 2.1. In this frame, the direction of electric field is taken along the z -axis. For any particular incidence angle, the frame is rotated such that, z -axis become the direction of spin alignment (θ_2 in figure 2.1a). Since this is a rotation in z - x plane, E_y remains zero in the rotated frame, whereas, E_x and E_z are given by $E_x = E \sin \theta_2$ and

$E_z = E \cos\theta_2$. Using E_x , E_y , E_z , and k_x , k_y , k_z , Ω_{SIA} is calculated from equation (2.14). Total effective magnetic field is given by $\Omega = \Omega_{\text{SIA}} + \Omega_{\text{BIA}}$. Since the spin is assumed to be aligned initially along the z axis in the rotated frame, spin relaxation time (τ_s) along the z -axis is only considered. It is given by the following relation [30]

$$\frac{1}{\tau_s} = \frac{1}{\gamma_3} \left[\langle \Omega^2 \rangle - \langle \Omega_z \rangle^2 \right] \tau_p \quad (2.15)$$

Here $\langle \rangle$ denotes the average over all the k states. For polar optical phonon scattering, $\gamma = 41/6$ [30]. For the case, where there is no electric field, only Ω_{BIA} term will be present and the analytical expression for equation 2.15 can be found in the literature [30,99]. However, in presence of electric field, numerical averaging has to be carried out. Here, τ_p is given by equation (2.11) and all the other symbols have their usual physical meanings. The values of material parameters involved in numerical simulations are taken from reference [101]. In short, spin relaxation time increases as $(E_e)^{-3}$ and is inversely proportional to the momentum relaxation time.

The same method, as explained in section 2.2.4 is used to calculate the energy and spin relaxed electron distribution, $N_{S,E}(E_e)$. The barrier height for Au/GaAs is known to be 0.6 eV, which decreases depending on the incident light intensity because of the photovoltaic effect [102]. In general, the typical optical intensity is in the range of a few mWcm^{-2} and for this range barrier height becomes 0.32 eV. Therefore, to estimate the Rashba contribution to the relaxation time, we have assumed the barrier height to be 0.32 eV and calculated the position-dependent electric field accordingly. From the known energy of light beam, the k vector associated with

the electrons excited from different bands are estimated and are used in equation 2.7 for estimating the value of τ_s . For this case, the electron distribution is given by figure 2.9 for hh - e transition.

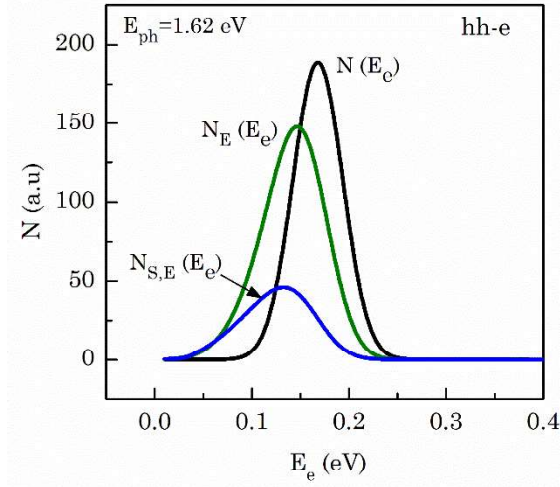


Figure 2.9 The Energy distribution of spin polarized electron in the conduction band, excited by photon energy of 1.62eV. Black, green and blue lines correspond to the distribution created by polarized light $N(E_e)$, and distribution after energy relaxation $N_E(E_e)$ and distribution after both energy and spin relaxation $N_{S,E}(E_e)$ respectively.

In this case, the area under the curve reduces because of spin relaxation. The importance of this calculation is clear from figure 2.10, where transitions from all the valence band states (hh , lh and so) are considered simultaneously. For 2 eV excitation energy, shown in figure 2.10 (b), peaks corresponding to hh - e and lh - e transitions are greatly reduced, however peak corresponding to so - e transition is still significant. It is due to the higher energy of electron involved with the hh - e and lh - e transitions, which causes faster spin relaxation.

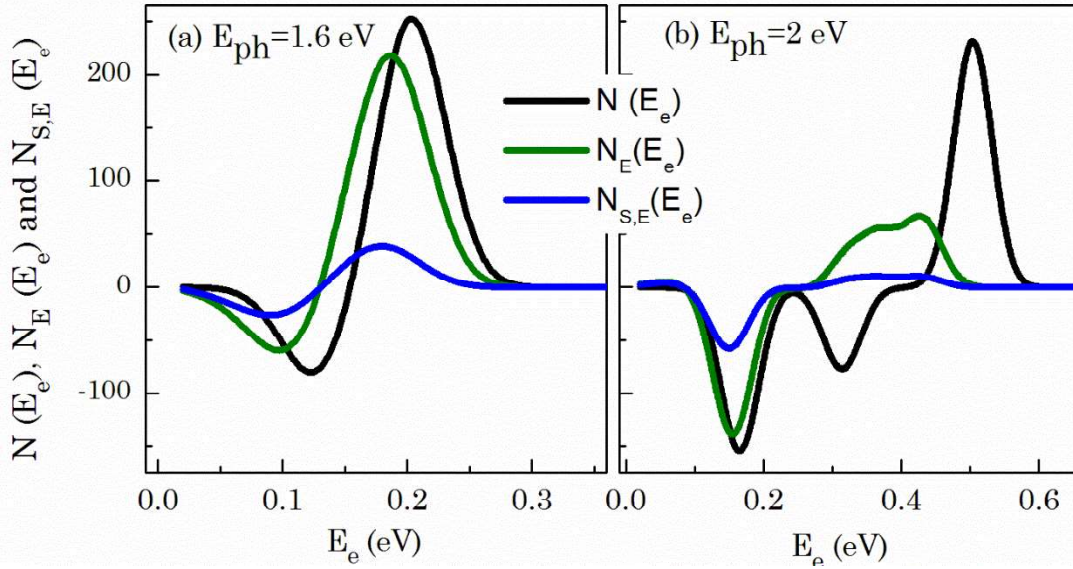


Figure 2.10. Energy distribution of spin polarized electron in the conduction band, excited by photon energy of (a)1.6 eV and (b) 2eV. Black, green and blue lines correspond to the distribution created by polarized light $N(E_e)$, distribution after energy relaxation $N_E(E_e)$ and distribution after energy and spin relaxation $N_{S,E}(E_e)$ respectively.

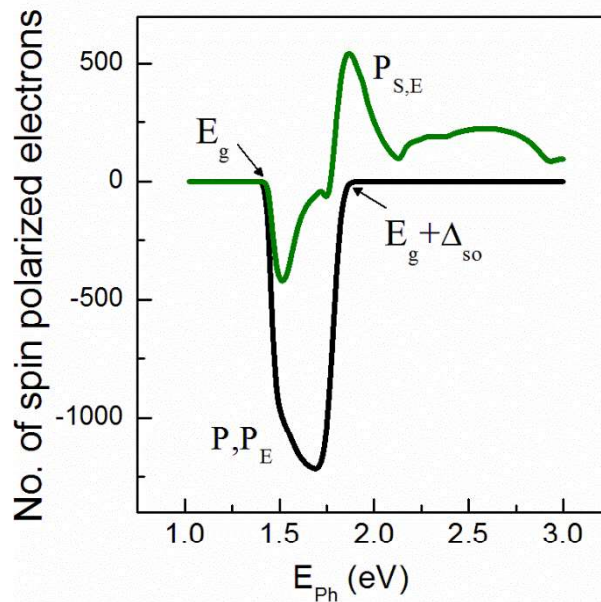


Figure 2.11 Total no of spin polarized electrons at the time of generation (P) and after transport to the interface ($P_{S,E}$) as a function of excitation photon energy.

Therefore, the distribution of electrons after they reach the interface is considerably different from that at the bulk. This means that though the total no of spin polarized electrons at the time of generation [$P = \sum N(E_e)$] is zero, it will be non-zero, after their transport to the metallic layer [$P_{S,E} = \sum N_{S,E}(E_e)$]. For the case of 1.6 eV excitation energy, *so-e* transition is absent and the peak related to *hh-e* & *lh-e* transitions are less affected, as shown in figure 2.10 (a). These general cases of P and $P_{S,E}$ are shown as a function of E_{ph} in figure 2.11.

2.2.6 Tunneling and Thermionic emission photo-excited carriers

The photo-generated electrons in semiconductor cross the barrier by either tunneling or thermionic emission. In the absence of magnetic impurities, the spin flip scattering in the depletion layer is neglected, which is a good approximation. The transport of polarized carrier across Fe/GaAs interface has been studied by several researchers [103]. They concluded that the spin current has mainly tunneling contribution and thermionic emission contribution is rather negligible. It is because of the spin dependent density of states in ferromagnetic Fe. The thermionic emission contribution to spin current is negligible because electrons lands at the potential minimum at the Fe/GaAs interface (formed because of image force lowering) and lose their spin information faster than in Fe. However, the high Z metals that are considered here are paramagnetic in nature and the density of states are not spin dependent. Thus, it is reasonable to believe that both the thermionic emission and tunneling mechanisms contribute to the spin current. The

probability of crossing the barrier is a function of E_e , and is given by Chang's model [104] and is given below,

$$T(E_e) = \exp\left(-R\sqrt{\Phi_b(\Phi_b - E_e)}\right) \exp\left\{\frac{R.E_e}{2} \ln\left(\frac{E_e}{2\Phi_b - E_e}\right)\right\} \quad (2.16)$$

where, $R = \frac{2}{q\hbar} \sqrt{\frac{m_e^* \mathcal{E}}{N_d}}$

N_d is dopant density and Φ_b is the barrier height. Therefore, the spin current depends on $N_{S,E}(E_e)$ and can be expressed with the following equation.

$$J_s^0 = \int_0^{\infty} N_{S,E}(E_e) T(E_e) dE_e \quad (2.17)$$

2.2.7 Role of high Z metals in the generation of ISHE signal

It is understood that, the spin current injected in to the metallic layer diffuse inside it and forms a transverse spin current, whose magnitude is given by equation 2.17.

The ISHE field is given by

$$\vec{E}_{ISHE} = \frac{\gamma}{\sigma_C} \left(\vec{J}_s \times \hat{\sigma} \right) \quad (2.18)$$

Here, average value of spin current density is taken, which is averaged over the entire thickness of the metal. The spin current density varies with the distance from the interface because of spin relaxation in the metal itself, which is given by [73]

$$J_s(z) = J_s^0 \left[\frac{\sinh\{(t-z)/L_S\}}{\sinh(t/L_S)} \right] \quad (2.19)$$

Here, t and L_S are the thickness of film and spin diffusion length respectively. From equation 2.19, $\langle J_S \rangle$ is calculated as

$$\langle J_S \rangle = \frac{1}{t} \int_0^t J_S(z) dz = \left(\frac{-L_S}{t} \right) \frac{[1 - \cosh(t/L_S)]}{\sinh[t/L_S]} J_S^0 \quad (2.20)$$

For the simulation purpose, both the spin relaxation time and spin Hall conductivity in the metals are taken to be independent of the electron energy.

2.3 Numerical simulations of ISHE for Metal/Semiconductor Hybrid structures

Based on the above mentioned mechanism, the magnitude of ISHE signal is numerically calculated for the Metal/Semiconductor hybrid structures and its dependence on several parameters is predicted. Unless otherwise mentioned, the case of Au (20 nm) coated GaAs substrate ($N_d \sim 10^{16} \text{ cm}^{-3}$) is considered.

2.3.1 Energy dependence of ISHE signal

As explained in section 2.2.3, an effective injection of spin polarized carriers is possible only when the energy of incident light falls between E_g and $E_g + \Delta_{so}$. However, energy dependent spin relaxation of electrons ensures that the spin polarized electrons are available at the interface for excitation energy much larger than $E_g + \Delta_{so}$. The ISHE field generated (E_{ISHE}) is estimated using the equations 2.17-2.19 and is plotted in figure 2.12. Comparison is also made with the net no of spin polarized electrons at the interface ($P_{S,E}$) for better illustration purpose. One can note that the E_{ISHE} spectra also shows broad negative and positive peaks

similar to $P_{S,E}$ spectra but the positions are shifted in the energy axis because lower energy carriers cannot cross the barrier. The magnitude of E_{ISHE} has two extrema, one at 2.1 eV and the other at 2.7 eV. The polarity of E_{ISHE} changes at 2.3 eV and a similar observation is reported by Kurebayashi et al. [103] on spin current in the Fe/GaAs hybrid structure. It happens due to the respective contributions arising from the three competing upward transitions i.e. heavy hole to conduction band, light hole to conduction band and split-off to conduction band respectively.

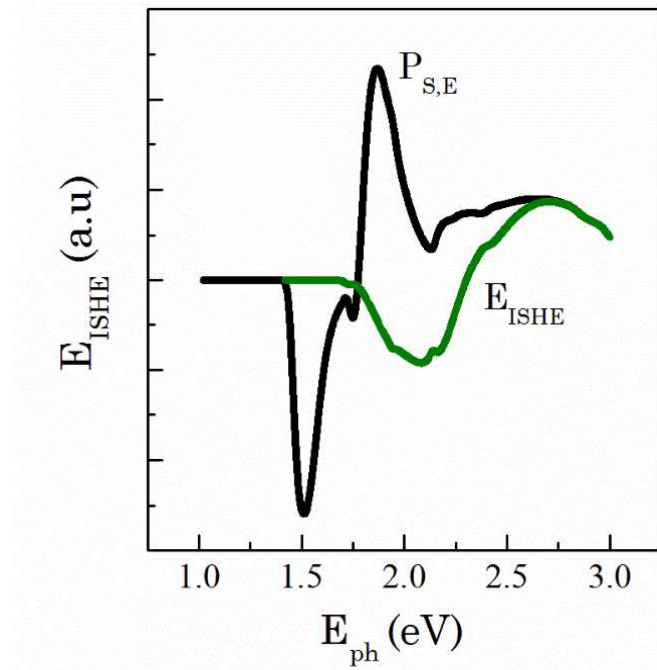


Figure 2.12 E_{ISHE} and $P_{S,E}$ as a function of incident photon energy.

This is to be noted that the optical excitation starts at a much lower energy (1.43 eV) and the selection rule predicts the injection of 50% spin polarized electrons in the range of 1.43- 1.76 eV which should vanish at high energy. However, in contrast to this, E_{ISHE} is observed at energy higher than 1.75 eV, i.e. nearly at the

onset of $sh-e$ transition and remains non-zero up to 3 eV. This may be surprising at first sight, but the energy-dependent phenomena (relaxation and tunneling) have made it possible. For $E_{ph} > 2.5$ eV, E_{ISHE} matches with $P_{S,E}$ because. At this energy, almost all the photo generated electrons will cross the Schottky barrier and contribute to E_{ISHE} .

2.3.2 Role of metal layer thickness in the magnitude of ISHE signal

E_{ISHE} depends on the metal layer thickness via two parallel mechanism. First is the decrease in light intensity and ρ_{II} , with increasing layer thickness. This reduces the number of spin polarized electrons and hence reduces J_s^0 . On the other hand, for thickness below the spin diffusion length (L_s), the terms before J_s^0 in equation 2.19 decrease. The two opposite mechanism provides an optimized thickness of metal layer leading the maximization of ISHE signal. Figure 2.13 shows the calculated values of E_{ISHE} as a function of thickness of metal layer for various values of L_s .

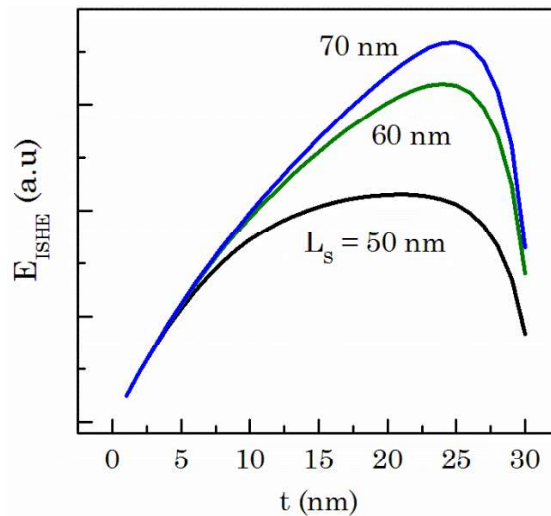


Figure 2.13 E_{ISHE} as a function of metal layer thickness for various values of spin diffusion length (L_s).

2.3.3 Effect of the angle of incidence on the magnitude of ISHE

Figure 2.13 shows the effect of angle of incidence on the E_{ISHE} spectra. Numerical calculations were done for angles varying from 0° to 90° with step of 10° . It was done by calculating the change in light polarization by transmission at a particular angle, as explained in section 2.2.2 and change in electron spin polarization as described in section 2.2.3. It is observed that there is no change in the overall shape of the spectra, only the change in magnitude is observed, i.e. the peak positions are independent of the incident photon energy. The magnitude of E_{ISHE} at four representative excitation energies are plotted with the angle of incidence. These curves peak at around 60° incidence angle and become zero for normal incidence ($\theta_0 \sim 0^\circ$) as well as for grazing incidence ($\theta_0 \sim 90^\circ$). It is in strong corroboration with the experimental results reported by several researchers [73].

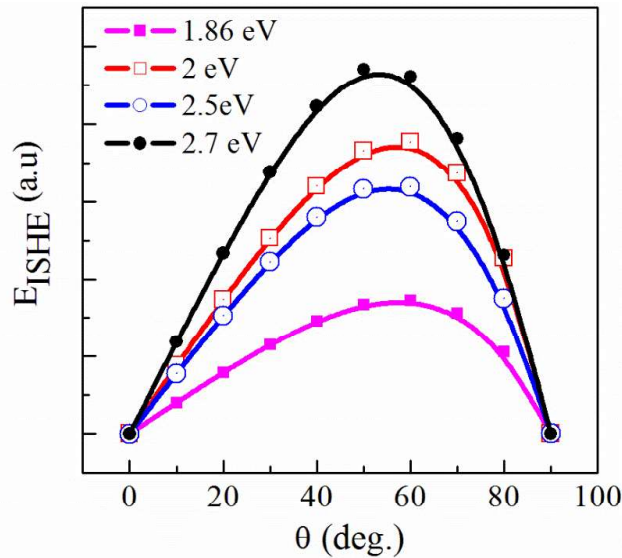


Figure 2.14 Dependence of E_{ISHE} on angle of incidence at various excitation energy.

Such a dependence originates from two important factors. First is because of the spin injection efficiency, which depends on ρ_{II} . It is maximum for normal incidence and gradually decreases at higher incidence angles. Second dependence comes from the angle between spin polarization vector of electron and spin current (θ_2 in figure 2.1 (a)). For near normal incidence ($\theta_2 \sim \theta_0 \sim 0$), $\sin \theta_2$ dependence of E_{ISHE} makes it negligible. Thus, in order to for achieving the maximum E_{ISHE} , an optimized angle of incidence is $\sim 60^\circ$.

2.3.4 Barrier height dependence of ISHE signal

Figure 2.15 (a) shows the E_{ISHE} spectra for different barrier heights varying from 0 to 0.5 eV. For clarity purposes, only three spectra corresponding to barrier heights of 0.4, 0.3, 0.2 and one more corresponding to hypothetical zero barrier heights are also plotted. Figure 2.15 (b) shows the variation of energy of two extrema labeled as A and B as a function of barrier height. It is noted that the E_{ISHE} spectra blue shift with the barrier height. The shift is due to the fact that at lower barrier height, lower energy electrons (excited by low energy photons) can also tunnel, which contribute significantly to the spin current because of their long relaxation time. An enhancement of the relaxation time helps in increasing the intensity of ISHE peaks. At lower barrier height, the magnitude of internal electric fields is also small and thus the Rashba contribution to the spin relaxation decreases which further increases the peak height. Another point to be noted is that at higher excitation energies, all curves are identical irrespective of the barrier height. It is because at these excitation energies, almost all the electrons reach the metallic layer (no

barrier exists) and therefore contribute to the spin current. For the high-energy electrons, contribution from the Dresselhaus term is much higher than that of the Rashba term, which makes the spectra independent of barrier height as shown in figure 21.5 (a). Normally, it is difficult to engineer the barrier height when fabricating Schottky diodes by using a given material. However, it can be manipulated by varying the intensity of incident light up to certain extent. Therefore, E_{ISHE} is expected to be a non-linear function of light intensity over a broad range. Although in general the typical optical intensity lies in the range of a few mWcm^{-2} . For this range, typical barrier height is 0.32 eV which stays approximately constant and under this condition E_{ISHE} will be proportional to the intensity of incident light.

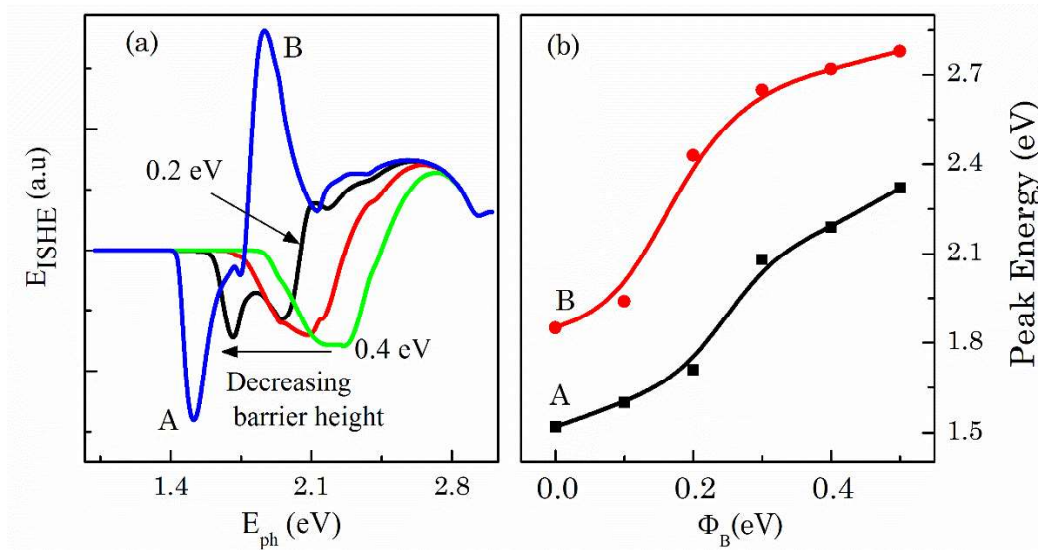


Figure 2.15(a) E_{ISHE} spectra for different barrier height, 0.4 eV (green curve), 0.3 eV (red curve), 0.2 eV (black curve) and 0 eV (blue curve), (b) Variations of the energy of two peaks (A and B) as function of barrier height.

2.3.5 Choice of III-V semiconductors

Numerical simulations, as described in the aforementioned work, are repeated for several III-V semiconductors like InP, InAs and InSb. The material parameters used in the calculations are listed in Table 2.1. Figure 2.16 shows the E_{ISHE} spectra for the various hybrid structures. A few important observations can be made from this graph. One such observation is related to the spectral range over which the spectra extends. Second is the relative magnitude while the third is the change in the polarity. The spectral range is decided by the band gap and band curvature of individual semiconductors and also the barrier height at the interface. The magnitude depends on the number of spin-polarized carriers that reach the metal layer before losing their spin information. It depends on the following factors. (i) Spin relaxation times in semiconductors (ii) Time taken by the carriers to reach the interface, and (iii) Barrier height at the interface.

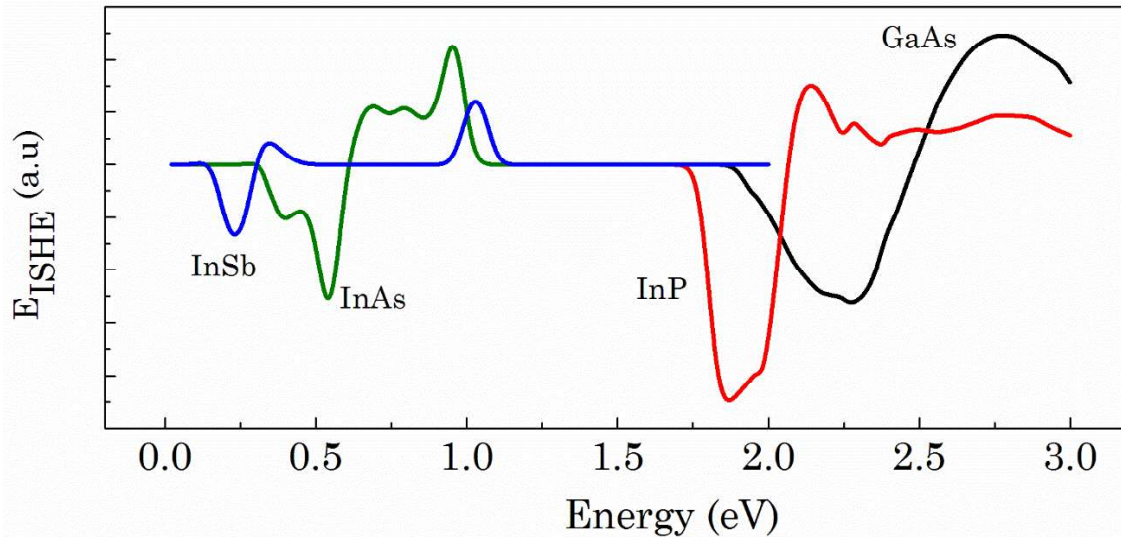


Figure 2.16 Comparison of E_{ISHE} spectra for 20 nm Au coated GaAs, InP, InAs and InSb.

It could be seen from figure 2.16 that the order of magnitude of E_{ISHE} is similar for all the materials. It may seem surprising at first sight because there is a large difference in the reported values of spin relaxation times for those semiconductors. At 0.5 eV kinetic energy, the relaxation times (which depends on spin orbit splitting via Dresselhaus coefficient) for GaAs, InP, InAs and InSb is calculated to be 0.8 ps, 1.3 ps, 0.1 ps and 0.08 ps respectively using equations 2.13-2.15. With this information, it appears that E_{ISHE} in InP and GaAs should be an order of magnitude higher than InAs and InSb. However, because of their very small effective mass (large mobility) electrons in InAs and InSb takes much smaller time to reach the interface, partially compensating the effect of smaller relaxation times. Again, the barrier height with Au is also smaller for lower band gap materials. This ensures that more electrons can tunnel through the barrier. The lower barrier electric field also minimizes Rashba contribution to the spin relaxation, as can be seen from equation 2.14. Further the two peaks of opposite polarity correspond to the onset of $hh-e$ and $so-e$ transitions. Therefore, the separation between them roughly corresponds to the split off gap in the material. From all these calculations, it turns out that the material InP has the largest peak value of E_{ISHE} which is mainly governed by the significantly small spin orbit coupling in this material.

2.3.6 Choice of metals

Though the calculations explained in this chapter are for Au coated semiconductors, similar calculations can be done for many of the metals. The choice of the metal for

such hybrid structure depends on several factors. The most important parameter to be looked at in this respect is the magnitude of spin Hall conductivity (σ_{SH}). In general, high Z metals are known to possess higher values of σ_{SH} . Table 1.4 describes the values of σ_{SH} for various metals that are taken from the literature. However, along with σ_{SH} , other aspects of the metals also need to be considered. These are as follow.

- i. It should be chemically stable, otherwise oxide formation at the ambient deteriorates the electrical properties.
- ii. It should not be ferromagnetic for avoiding a significant circular dichroism.
- iii. It should not be radioactive.
- iv. It should form stable Schottky contact with III-V semiconductors.
- v. It should be possible to deposit thin film with appropriate quality.

Considering all these factors, Au and Pt seems to be ideal choice for such applications. Though the results presented in this chapter are for thin film of Au, similar results are observed for Pt, because of similar optical properties, Schottky barriers height and spin Hall conductivity.

2.4 Theoretical predictions for the observation of ISHE in Metal/Semi-conductor hybrid structures

As discussed in the beginning of current chapter, final outcome of this chapter lies in predicting 1) an optimum layer combination/structure of metal/semiconductor hybrid structure and 2) appropriate experimental configuration/conditions for an unambiguous realization of ISHE. On the basis of numerical simulations, it is clearly understood that a metal/semiconductor hybrid structure is a good choice for an unambiguous realization of ISHE. It is also found that Au as a metallic layer is an excellent choice due to its high spin Hall conductivity. Similarly, InP is considered to be one of the most suitable semiconductor materials because of its small spin orbit coupling. Furthermore, an optimum thickness (~ 20 nm) of the metallic layer is found to be essential for maximizing the ISHE signal in Au/InP hybrid structure. Similarly, the angle of incidence of the impinging light is essential to be around 60° . It is also desired that the energy of the excitation source shall be carefully chosen for ensuring an efficient generation of spin polarized electrons in the conduction band. In case of InP semiconductor, the energy of the excitation source shall lie in the range of 1.75 to 2.1 eV. Importance of the theoretical predictions made in this chapter are successfully verified through meticulous experiments as described in the subsequent chapters of this thesis.

Chapter 3

Sample fabrication and Experimental set up

3.1 Introduction

This chapter describes the various sample fabrication techniques and experimental set up that are used in this work. All the samples used in this work are grown by MOVPE. Therefore, this chapter starts with an introduction of the MOVPE growth process. It is followed by the necessary growth details of all the samples which are studied during the course of this thesis. Thereafter, various device fabrication and characterization methods are explained. Since considerable effort and time has gone into establishing the experiment involving polarization modulation, special attention is given to the calibration of Photo Elastic Modulator (PEM) for its optimum performance. Muller matrix approach has been used, whose details are given in appendix-B. Detection of a low level signal which is free from all possible noise is a considerable challenge. Therefore a separate section is devoted to the identification and minimization of noises which are inherently present in the experimental setup. Subsequently, the experimental configurations that are used

for the measurement of ISHE and polarization resolved Photoluminescence in bulk and quantum well samples are discussed.

3.2 Sample fabrication

3.2.1 Metal-Organic Vapor Phase Epitaxy (MOVPE)

Metal-Organic Vapour Phase Epitaxy (MOVPE) is an epitaxial crystal growth technique used for growing high quality single crystalline thin films of a variety of semiconductor materials on different substrates. It has emerged as one of the most appropriate epitaxial crystal growth technique for producing high quality optoelectronic devices, thus making it suitable for industrial applications. In general, an epitaxial layer is formed from the precursor compounds that include metal organics in the vapour phase and may also include hydrides in form of gases. The precursors are transported into the reactor, made up of quartz, with the help of a carrier gas (generally hydrogen). The precursors arrive at the surface of a hot substrate kept on the high purity Graphite susceptor inside the quartz reactor. Heated surface of the susceptor provides a catalytic effect on the pyrolysis of precursors which are subsequently adsorbed on the surface of the substrate/growing layer. All the samples used in this work are grown by MOVPE using Aixtron (AIX-21) machine. Precursors are ultra-high purity Trimethyl Gallium (TMGa), TrimethylAluminium (TMAI), Arsine and Phosphine [105]. The photograph of the MOVPE machine is shown in figure 3.1 and the details of the samples along with their important growth parameters are given in table 3.1.

Table 3.1 MOVPE growth details of the structures used

Sample No	Material	T _G (°C)	V/III	Growth rate (Å/s)	Thickness (nm)	n (cm ⁻³)@ 77K	Substrate (orientation)
I. GaAs thin film							
S1(04012)	n-GaAs	770	86.4	4.8	2000	3.2 x 10 ¹⁸	SI-GaAs (001)
S2(04057)	p-GaAs	770	82.58	4.2	720	2.8 x 10 ¹⁹	SI-GaAs (001)
II. InP thin film							
S3(12027)	n-InP	650	278.	3	400	3.6 x 10 ¹⁷	n-InP (001)
III. GaAs/AlGaAs QW							
S4(04002)	Al _{0.38} Ga _{0.62} As	730	198.81	3.3	600		n-GaAs (001)
	GaAs	730	324.29	2.6	15.2		
	Al _{0.38} Ga _{0.62} As	730	198.81	3.3	600		
S5(04011)	Al _{0.38} Ga _{0.62} As	730	69.2	4.4	265		n-GaAs (001)
	GaAs	730	118.9	2.6	3.5		
	Al _{0.38} Ga _{0.62} As	730	69.2	4.4	265		
S6(04016)	Al _{0.38} Ga _{0.62} As	730	67.5	4.3	260		SI-GaAs (001)
	GaAs	730	118.9	2.8	4.5		
	Al _{0.38} Ga _{0.62} As	730	67.5	4.3	260		
IV. GaAsP/AlGaAs QW							
S7(04031)	Al _{0.38} Ga _{0.62} As	770	129.6	5.6	100		n-GaAs (001)
	GaAs _{0.87} P _{0.13}	770	357.7	3	8.7		
	Al _{0.38} Ga _{0.62} As	770	129.6	5.6	100		
V. InGaAs/GaAs QW							
S8(09023)	GaAs	510	110.2	1.25	100		n-GaAs (001)
	InGaAs	510	150.2	3	9.1		
	GaAs	510	110.2	2.5	30		



Figure 3.1 Photograph of MOVPE machine used in this work

3.2.2 Device Fabrication

3.2.2.1 Chemical Cleaning

It is extremely important to clean the semiconductor surface to remove all the contaminants before any kind of device fabrication steps. The substrate cleaning procedure involves two different aspects. The first is the removal of contaminants such as organic compounds and metal ions and the second is the removal of native oxides [106]. The presence of organic vapors even in the air in clean room, direct contact of greasy substance (including fingers) can cause the surface of semiconductor pick up those organic molecules and become contaminated. Generally, organic cleaning procedure is followed to remove spurious organic contaminants. One such method, which is used here is degreasing and consists of the following steps.

- Boiling in Tri-Chloro Ethane (TCE) for 10 minutes.
- Boiling in Acetone for 10 minutes.
- Soaking in Methanol for 10 minutes.
- Rinsing in de-ionized (DI) water to remove metallic ions.
- Drying of the substrate in pure Nitrogen.

Similarly, all the III-V semiconductors are readily oxidized by atmospheric Oxygen. Therefore generally, a thin layer of native oxide, of the order of 1-2 nm exists after long time exposure. Immersion in either acidic or basic dilute solution will dissolve these native oxides. For our purpose, 10 second dip in Dilute HCl (1:10 H₂O) is performed for oxide removal.

3.2.2.2 Photolithography

In this work, UV photolithography is performed, which uses UV light to transfer the pattern of photo mask to UV sensitive photoresist coated on the substrate. By absorbing the UV light, the exposed area of positive photoresist undergoes chemical changes, increasing its dissolution in developer solutions. Suitable developer is then used to develop the photoresist to get the desired pattern on the sample [107]. For the fabrication of Hall bar structures, following steps are adopted.

- Shipley S1813 positive photoresist (PPR) is spin coated over the sample containing conducting epitaxial layer over a semi insulating substrate. The thickness of PPR is suitably chosen depending on the thickness of the material that is to be etched. For thick layers (~4-5 μm), multiple coatings are required.

- PPR film is allowed to dry up in air and then soft baked at 95° C for 1 min.
- Using a suitable photo-mask, the PPR is exposed to UV light (365 nm) for 10.5 seconds and then developed using MFCD-26 developer for 1 minute. This makes the Hall bar structure over the sample, where the entire structure is covered with PPR.
- The uncovered part is then chemically etched by using $H_3PO_4/C_2H_5OH/H_2O_2$ solution of the ratio 3:6:1 kept at 35° C. The etch rate is measured to be around 40 nm/s. The etch time is decided by keeping in mind the complete removal of conducting layer from the regions outside the Hall bar.



Figure 3.2 Actual photograph of the mask aligner and spin coating system

3.2.2.3 Metallization

Metallization is an important step in the device fabrication process. In this work, two types of metallization process are used; thermal and e-beam evaporation [108,109]. In a thermal evaporation system, a resistive heater like metallic

filament or boat is used to melt the material and to raise its vapour pressure up to a useful range. On the other hand, in e-beam evaporation, electron beam of control energy is focused on the material by magnetic field, which subsequently evaporates the material. In both the cases, a high vacuum is required to make the vapour pressure larger than ambient pressure inside the vacuum chamber. It allows the metallic molecules to reach the sample/substrate without being scattered by other gas phase atoms/molecules which might be present in the vacuum chamber. It is generally observed that the quality of layer in terms of density and purity is better for the e-beam evaporation process when compared with thermal evaporation. Further, it is found that the e-beam system offer better repeatability and control over layer thickness compared to the thermal evaporation system. Therefore, during the course of this work, whenever very thin film (~few nm) of metal is required and quality of materials is of concern, e-beam evaporation is used. For general purpose contact formations, where 100s of nm of multilayer is needed, thermal evaporation is used. The photograph of thermal and e-beam evaporation system that are used in this work is shown in figure 3.3.



Figure 3.3 Photograph of the thermal and e-beam evaporation system that are used in this work

For the measurement of ISHE, Hall bar structure is fabricated using suitable mask shown in figure 3.4 (a). Thereafter, Au-Ge/Ni/Au multilayer is deposited over it using shadow mask technique, and is shown in figure 3.4 (b).

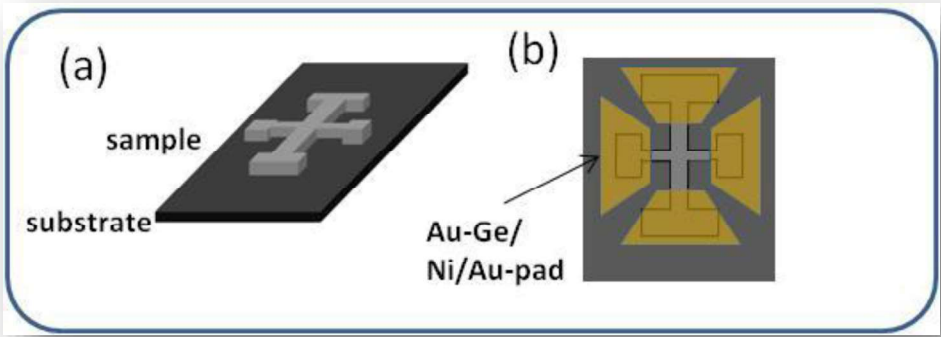


Figure 3.4 Schematic of the Hall bar structure used to measure ISHE. (a) After photolithography and chemical etching and (b) after metallization of contact pads

3.2.3 Electrical characterization

All the electrical measurements like the Current-Voltage (I-V) measurement and Hall measurements are performed with the help of Keithely 236 Source Measure Unit. An indigenously developed closed-cycle cryostat refrigerator (CCR) operating in the range from 40 to 330 K and a Cryocon make temperature controller (model: 32B) is used to control the sample temperature precisely. This arrangement was put in between two pole pieces of an electromagnet, which can provide dc electromagnet field up to 1.5 T. The sample holder has options to hold the sample either in parallel or perpendicular to the direction of magnetic field. For I-V measurements, the sample is mounted on gold coated thin sapphire plate from which back contact is made. For the front contact a thin gold rounded tip of 0.1 mm diameter is used. This rod can move up or down through a Teflon spacer by applying contact pressure in cantilever mode. For Hall measurements, the sample is mounted on thin bare sapphire plate, fixed with GE-Varnish, which efficiently transfers the heat to the cold head of CCR. Indium was used to solder the contacts to the sample. All the front and back contacts are taken out from the cryostat and connected to Triac connectors. These Triac connectors are then connected to the current voltage source meter, which can measure current in the range of ± 10 fA to ± 100 mA and voltage in the range of ± 100 μ V to ± 110 V. All the measurement systems are interfaced to a PC through IEEE GPIB cards. An actual photograph and a schematic diagram of the setup is shown below.

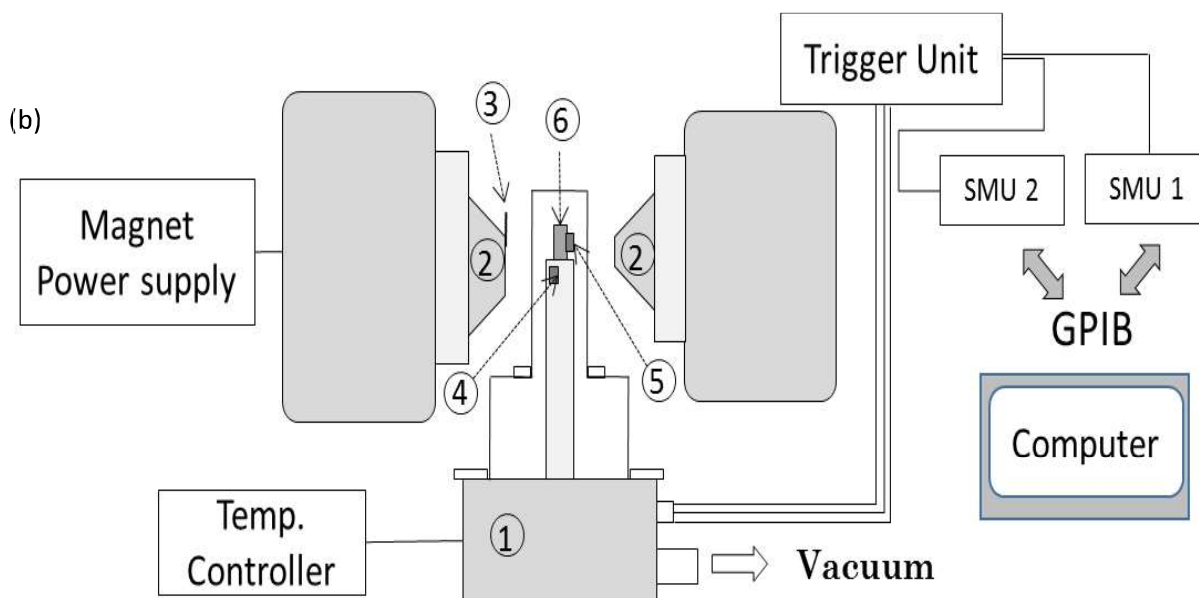
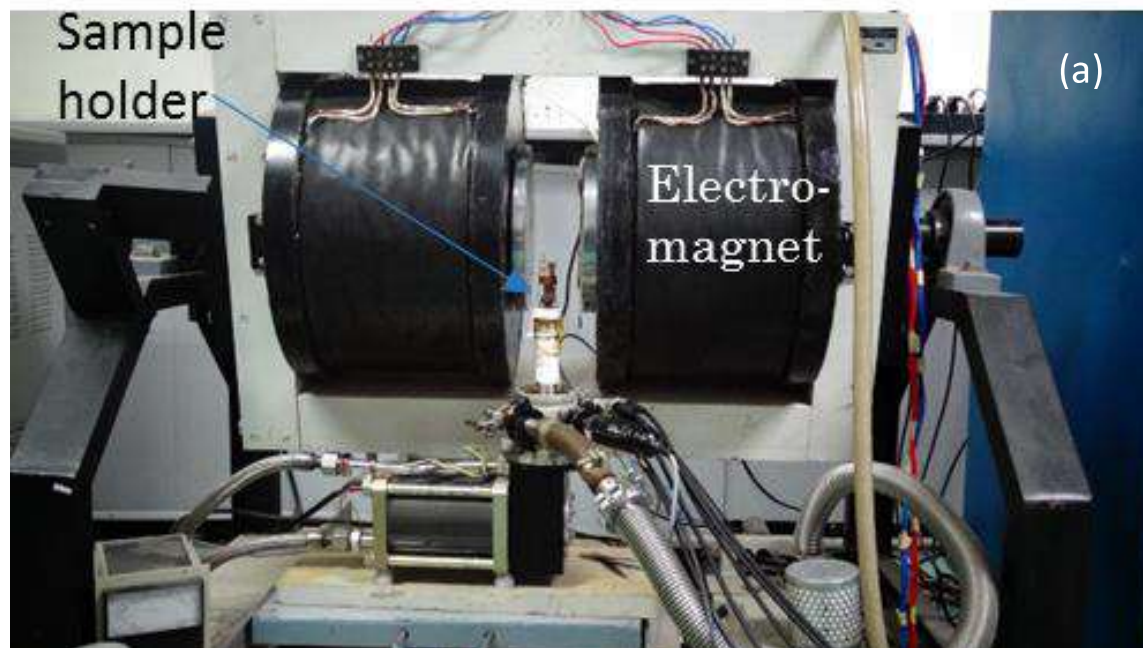


Figure 3.5 (a) Real Photograph and (b) schematic of the experimental set up for electronic transport measurements. Here (1) represents the cryo-cooler (2) Magnet pole pieces (3) Gauss meter (4) Sample heater (5) Temperature sensor and (6) sample holder

3.3 Calibration of photo-elastic modulator

The Photo-elastic modulator (PEM) is a device that uses the photo-elastic effect i.e. the stress induced birefringence for its operation [110, 111]. PEM produces sinusoidal phase retardation between the orthogonal components of light passing through it, which is given by

$$\delta(t) = \delta_s + \delta_0 \sin(\omega t) \quad (3.1)$$

Here δ_0 is the peak retardation, which can be controlled externally by suitable bias voltage and ω is the operating frequency, which is generally fixed for a particular device. δ_s is the residual static birefringence, which is very small and generally neglected. This highly precise and repetitive sinusoidal time variation of phase difference modulates the polarization state of a light beam accordingly. Because of its resonant operation, high sensitivity, wide spectral range, wide acceptance angle and high precision phase modulation, the PEM has been used in a variety of physical measurements, both in polarizer and analyzer geometry [112,113]. In an experimental set up, PEM generally succeeds or precedes a linear polarizer, which is rotated by an angle 45° with respect to the optic axis of PEM. Under this condition, the degree of circular polarization of light passing through it is given by [111]

$$\sin(\delta(t)) = \sin(\delta_0 \sin(\omega t)) = 2 \sum_{n=1}^{\infty} J_{2n-1}(\delta_0) \cos((2n-1)\omega t) \quad (3.2)$$

Generally, the properties of a real PEM device deviate from an ideal PEM, and there could be some variations in the operating characteristics of PEM module which are mainly vendor driven. Therefore, proper calibration of a PEM module is essential for a complicated experiment like ISHE. Usually, four different types of calibrations are needed. These are the calibration with respect to 1) orientation angle, 2) operating frequency, 3) retardation magnitude and 4) the laser beam spot on PEM element. Calibration procedure of PEM against these parameters is described below.

3.3.1 Calibration with respect to the angle of orientation

It is realized that the optic axis of PEM is not always parallel to the PEM edge. Such a mis-orientation might affect the experiments. Furthermore, it is always necessary to ensure that the vertical axis set by all the optical elements in a given experimental set up coincides. Therefore, it is essential to determine the exact optical axis in a given set up. For this, the optical elements are arranged as shown in figure 3.6.

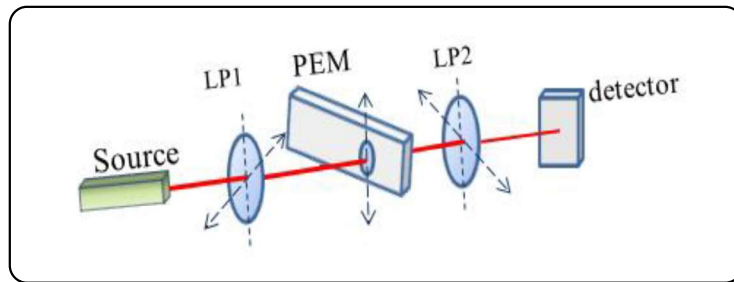


Figure 3.6 Schematic of the experimental set up for the calibration of PEM module

Here LP1 and LP2 are the two linear polarizers. Following steps are implemented for the PEM calibration,

- i. The LP1 and LP2 are set at approximately 45° and -45° degree to the PEM axis. Normal incidence at each of the optical elements is ensured and the second harmonic signal ($I_{2\omega}$) is recorded in the lock in.
- ii. The LP1 is turned until $I_{2\omega}$ is minimum (zero). It has to be done with an unpolarized source; otherwise the intensity will be affected by the orientation of LP1. In this case, LP1 is parallel to the PEM axis. The Muller calculus for this type of arrangement is

$$\begin{aligned}
 S_f &= M_{LP2}(45)M_{PEM}(0)M_{LP1}(0)S_i \\
 &= \frac{1}{4} \begin{pmatrix} 1 & 0 & 1 & 0 \\ 0 & 0 & 0 & 0 \\ 1 & 0 & 1 & 0 \\ 0 & 0 & 0 & 0 \end{pmatrix} \begin{pmatrix} 1 & 0 & 0 & 0 \\ 0 & 1 & 0 & 0 \\ 0 & 0 & \cos \delta & \sin \delta \\ 0 & 0 & -\sin \delta & \cos \delta \end{pmatrix} \begin{pmatrix} 1 & 1 & 0 & 0 \\ 1 & 1 & 0 & 0 \\ 0 & 0 & 0 & 0 \\ 0 & 0 & 0 & 0 \end{pmatrix} \begin{pmatrix} 1 \\ 0 \\ 0 \\ 0 \end{pmatrix} = \frac{1}{4} \begin{pmatrix} 1 \\ 0 \\ 1 \\ 0 \end{pmatrix}
 \end{aligned}$$

Here, M s are the corresponding Muller matrix of optical elements, the numerics in the brackets are the orientation angle of the respective optical elements in degree. S_i and S_f are the Stokes vector of incoming and outgoing light beam respectively. The photodiode reads only the first component of the Stokes vector ($S^{(0)}$), where only dc part is recorded. It can be noted that, any non-parallel component in M_{LP1} leads to 2ω component. The outcome of such an exercise is shown in figure 3. 7.

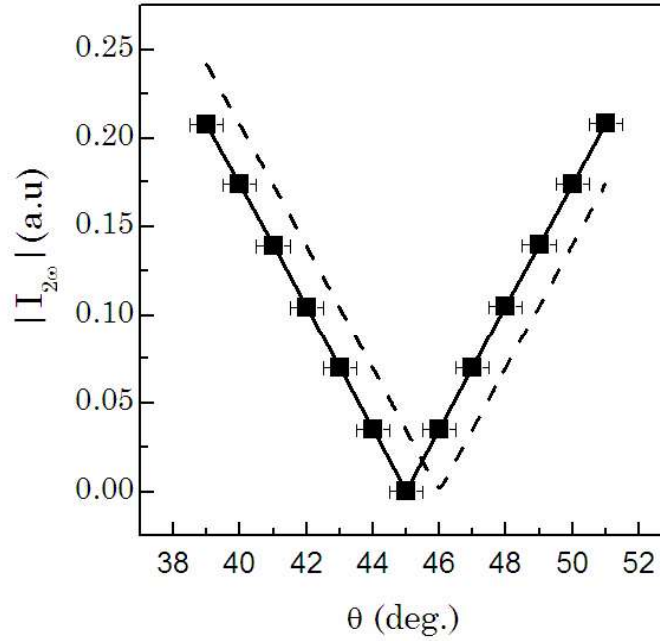


Figure 3.7 Calibration with respect to the orientation angle

- iii. It is found that $I_{2\omega}$ is minimum, when $\theta \sim 45^\circ$ as shown in figure 3.7. It means that the vertical axis set by LP1 and PEM are perfectly aligned within the error bars. Had there been some misalignment, the measured curve would have looked like the dotted line shown in figure 3.7. In that case, the LP1 would have to be rotated suitably to reach the minimum signal. Once that is done, LP1 is then rotated by exactly 45° from its current position.
- iv. Next the PEM is turn off and LP2 is rotated, until the dc signal is minimized, which ensures that the polarizers are crossed. LP1 and LP2 are now exactly 45° and -45° to the PEM respectively. Alignment is not disturbed throughout the experiment.

3.3.2 Calibration of operating frequency

To know the exact operating frequency, the aforementioned calibration experiment by keeping LP1 and LP2 at $+45^\circ$ and $+45^\circ$ orientation is repeated. In this case, the Muller matrices can be expanded as

$$S_f = M_{LP2}(45)M_{PEM}(0)M_{LP1}(-45)S_i = \frac{1}{4} \begin{pmatrix} 1 - \cos(\delta(t)) \\ 0 \\ -1 + \cos(\delta(t)) \\ 0 \end{pmatrix}$$

Therefore, the intensity recorded by the detector is given by

$$\begin{aligned} I &= \frac{1}{4} [1 + \cos(\delta_s + \delta_0 \sin \omega t)] = \frac{1}{4} [1 + (\cos \delta_s) \cos(\delta_0 \sin \omega t) - (\sin \delta_s) \sin(\delta_0 \sin \omega t)] \\ &= \frac{1}{4} [1 + \cos(\delta_s) J_0(\delta_0)] && I_{dc} \\ &\quad - \frac{1}{4} [2 \sin(\delta_s) J_1(\delta_0) \sin(\omega t)] && I_{1\omega} \\ &\quad + \frac{1}{4} [2 \cos(\delta_s) J_2(\delta_0) \sin(2\omega t)] && I_{2\omega} \end{aligned} \quad (3.3)$$

Here, J_n are the Bessel function of n'th order. Therefore, the $I_{2\omega}$ is expected to be very large compared to $I_{1\omega}$ because of small value of δ_s . Further care is taken to set δ_0 far away from 0 or 5.13 . This makes $J_2(\delta_0)$ reasonably large. Practice is followed to keep $\delta_0 = 0.25 \lambda$. This also keeps the 4th harmonic signal at low value, because of small value of $J_4(0.25)$. The waveform in the oscilloscope is read and the exact frequency is measured to be 99.7 kHz where a typical waveform is shown in the oscilloscope

trace given in figure 3.8. The operating frequency of the PEM is half of this frequency i.e. 49.85 kHz.

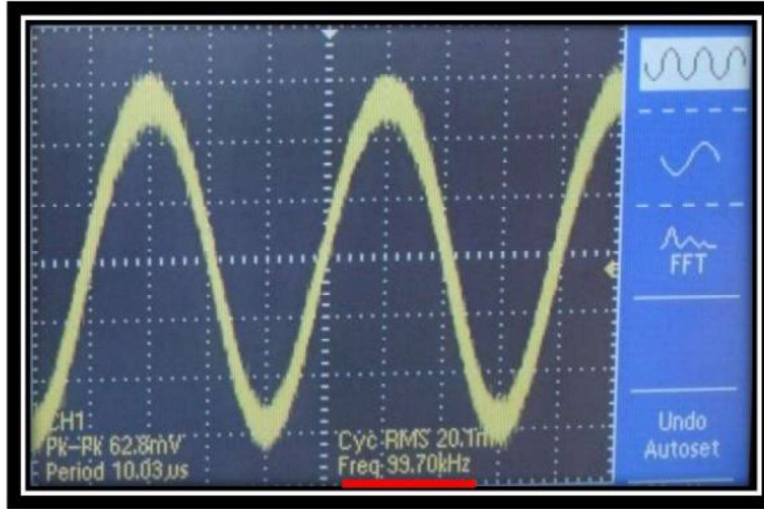


Figure 3.8 Oscilloscope trace of the experiment shown in figure 3.6

3.3.3 Calibration of retardation magnitude

Depending upon the experimental conditions, like the laser spot on the optical elements of PEM, beam diameter, and the incidence angle, the actual retardation magnitude (δ_0) may differ from the set value (δ_{set}). Therefore, it needs a systematic calibration against all these factors. There are many methods to calibrate the retardation magnitude. One of them is through the fitting of Bessel functions [114]. As explained in section 3.2.2, the $I_{1\omega}$ signal is measurable only when non-zero static birefringence δ_s is present. In our case no measurable value of $I_{1\omega}$ was obtained. Therefore, a quarter wave plate at a very small angle ($<5^\circ$) with respect to the linear polarizer is placed before the PEM. The modified set up is shown in figure 3.9. This ensured measurable value of both $I_{1\omega}$ and $I_{2\omega}$. Laser of wavelength 532 nm with

beam diameter of $\sim 100 \mu\text{m}$ is used and normal incidence at each of the optical elements is ensured. It also ensures that the laser beam passes through the centre of PEM element. The values of I_{dc} , $I_{1\omega}$ and $I_{2\omega}$, for different values of retardation (δ_{set}) are plotted in figure 3.10.

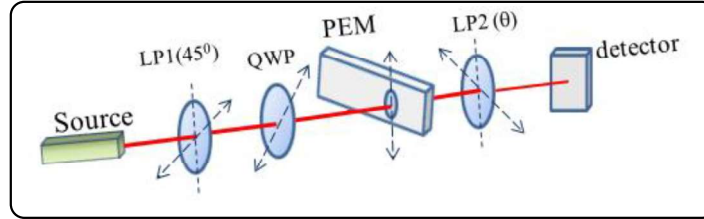


Figure 3.9 Schematic experimental set up for calibrating the retardation magnitude

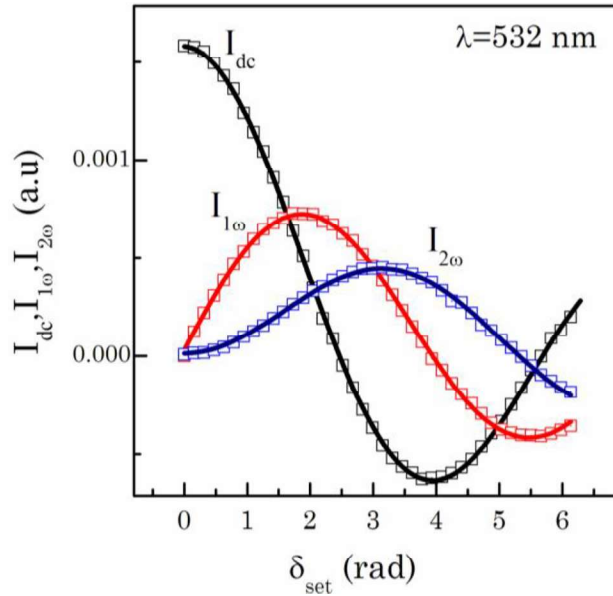


Figure 3.10 Results of retardation calibration

These terms are fitted with equation $y = a_1 + a_2 J_n(a_3 \delta_{set} + a_4)$, $n = 0, 1, 2$ respectively, to find out the presence of any offset. The parameters a_3 and a_4 relate the actual retardation to the set retardation through the relation of $\delta_0 = a_3 \delta_{set} + a_4$.

The dc term is rigid shifted for clear visibility. Table 3.2 shows the fitted parameters, where the offsets $a_3 \geq 98.8\%$, $a_4 \leq 2\%$ are obtained.

Table 3.2 Fitting parameter to calibrate the PEM

Harmonics	dc	1ω	2ω
Parameters			
a1	0.003	9E-6	6E-6
a2	0.0035	0.001	0.001
a3	0.989	0.988	0.985
a4	0.02	0.023	9.8E-4

3.3.4 Calibration with respect to laser beam spot on PEM element

It is realized that the calibration factors also depend on the position of laser beam spot on the optical element of PEM. According to the manufacturer, the modulation varies sinusoidally throughout the crystal as it moves away from the center [115]. This was tested, and proved to be correct. For this, the experiment is setup as shown in figure 3.6 and PEM is mounted on a manual X/Y translation stage. The beam is gradually scanned along the length and breadth of the optical elements. A black cardboard mask with a small orifice in the exact center is used to identify the center of PEM. By doing the analysis, as in section 3.3.3, the calibration parameters are obtained at each beam position. The parameter a_4 does not show any pattern, however a_3 shows well defined sinusoidal pattern, particularly along the length. However, along the breadth, even a_3 remains almost constant. The obtained parameters are plotted in figure 3.11 as a function of distance from the center. The

data points at each position correspond to the value determined from the fitting of different harmonics.

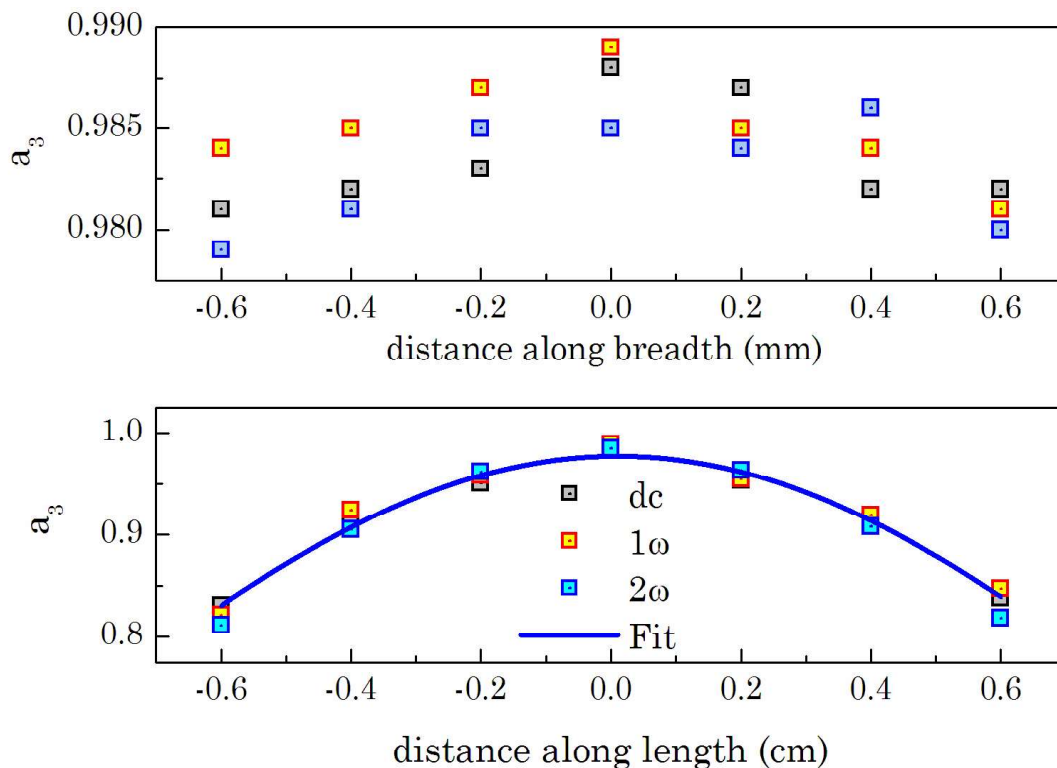


Figure 3.11 The calibration parameter a_3 (explained in text) at different position of PEM

Due to such variation, beam is always passed through the center of PEM. However, while dealing with light sources other than the laser, it is not always possible to focus the beam exactly at the center. Furthermore, the finite size of the beam also requires a correction factor. This takes into account the retardation, which is averaged over the beam diameter (w). Such a correction factor (C_δ) can be calculated as follows,

$$C_{\delta} = \frac{\int_{-\omega/2}^{\omega/2} I(x) a_3(x) dx}{\int_{-\omega/2}^{\omega/2} I(x) dx} \quad (3.4)$$

Where, I is the intensity at x , which depends on the beam profile. Since along the breadth, a_3 is almost constant, average can be taken along the length only. Figure 3.12 depicts C_{δ} for various beam diameters assuming uniform and Gaussian beam profile.

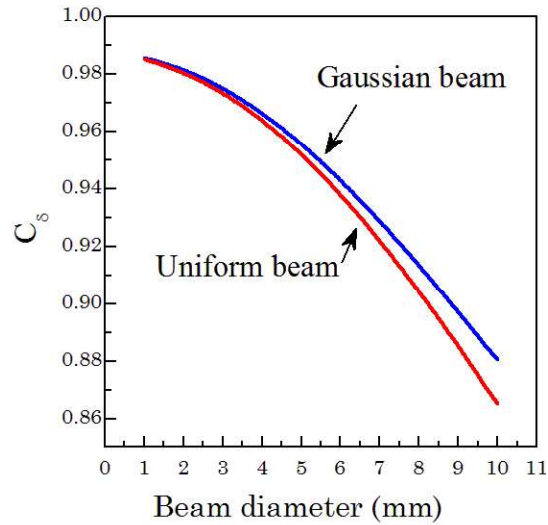


Figure 3.12 Correction factor because of variation in retardation value along the length and breadth of PEM

3.4 Background signals and their minimization

There are various background signals in a PEM based experimental set up, which can affect the experiment in a substantial way. Therefore, it is very important to identify them and minimize them as far as possible. Some of them are PEM electronic interference, modulated interference, residual birefringence and non-

normal incidence [116]. The first point is to record $I_{1\omega}$ and $I_{2\omega}$ in the experimental set up shown in figure 3.6. The presence of $I_{1\omega}$ indicates the presence of non-idealities in the set up.

3.4.1 PEM electronic interference

The very high electric field involved with the PEM generally couples with the measurement circuit and forms a background. In a typical experimental setup, the electric field radiated by PEM couples with the surface of optics table, which subsequently radiates at the same frequency and a current flows in the external circuit [116, 117]. To measure the PEM interference, the laser is switched off and the dark response of detector is measured by changing the retardation setting of the PEM. In general, the dark response (if any) increases linearly with retardation. It also depends on the quality of shielding around the detector. Therefore, it is different for different detectors. Hence it is important to measure this factor each time the measurement is performed. It was realized that their effect can be minimized by isolating the PEM completely from the table by placing it on wooden blocks and using insulated screws. The following figure shows the signal generated across a sample GaAs and across well shielded PMT (Make: Sciencetech, Model: PMT 01) & Si detector (Make: Hinds, Model: Det100) because of the PEM interference. It can be noted that this background signal reduces drastically after using proper insulation. After this measurement is done, the PEM and detector are not moved.

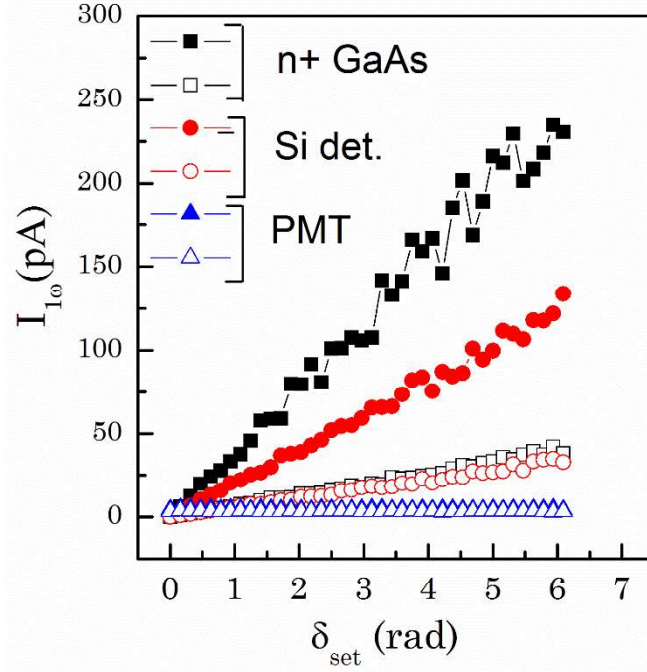


Figure 3.13 Background signal before (filled) and after (open) PEM isolation for n+GaAs sample (square), Commercial Si detector (circle) and PMT (triangle)

3.4.2 Modulated interference

The multiple reflection of laser light at the PEM surfaces causes the intensity to oscillate at the same frequency as the polarization. It is called modulated interference, which can affect the measurement in a significant way. To isolate the contribution of modulated interference, the laser light is passed through PEM, without any optical elements in between, and $I_{1\omega}$ and $I_{2\omega}$ signals as a function δ_0 are measured. If the modulated interference is present, they should follow $J_1(\delta_0)$ and $J_2(\delta_0)$ respectively. Sometimes, the presence of small misalignment or the frequency response of detectors causes the signal to deviate from this trend. However, it is important to measure these and all further signals have to be normalized to such an

intensity variation. It is measured that, for normal incidence at 532 nm, the intensity modulation (ΔI) because of modulated interference is given by

$$\frac{\Delta I}{I} \approx 2 \times 10^{-6} \quad (3.5)$$

Its effect is further minimized by slightly rotating the PEM about the vertical axis ($\sim 5^\circ$). On the other hand, by using the method explained in section 3.3.3, it is estimated that, the effect of such rotation on δ_0 is below 1%.

3.4.3 Residual birefringence

Residual stress in optical transparent materials often manifests itself as a polarization-dependent optical property, such as linear birefringence. Many factors contribute to birefringence in optical materials. For example, applied external pressure (from mounting hardware etc.); manufacturing processes (grinding, cutting, heating, bending etc.); handling and impact damage (chips, cracks, scratches). Since in PEM, there is induced birefringence, this residual birefringence is called static birefringence (δ_s). Presence of δ_s makes linearly polarized light to be elliptically polarized unintentionally. Hence, it should be minimized under all circumstances.

To measure δ_s , $I_{1\omega}$ and $I_{2\omega}$ readings are recorded as a function of δ_θ in a set up explained in figure 3.6 from which, the background measured in (3.4.1) and (3.4.2) are carefully subtracted. From equation (3.3) the ratio of $I_{1\omega}$ and $I_{2\omega}$ is given by

$$\frac{I_\omega}{I_{2\omega}} = \tan(\delta_S) \frac{J_1(\delta_0)}{J_2(\delta_0)}$$

$$\tan(\delta_S) = \left(\frac{I_\omega}{I_{2\omega}} \right) \frac{J_2(\delta_0)}{J_1(\delta_0)} \quad (3.6)$$

Ideally, it should be independent of δ_0 . Therefore δ_0 is selected, such that the values of J_1 and J_2 are non-zero. $\delta_0 = 0.4186$ is a very good choice, where $J_1(\delta_0) = J_2(\delta_0)$. The measured δ_S of the PEM are plotted in figure 3.14, which is measured to be very small and is not expected to affect the experiments in our case.

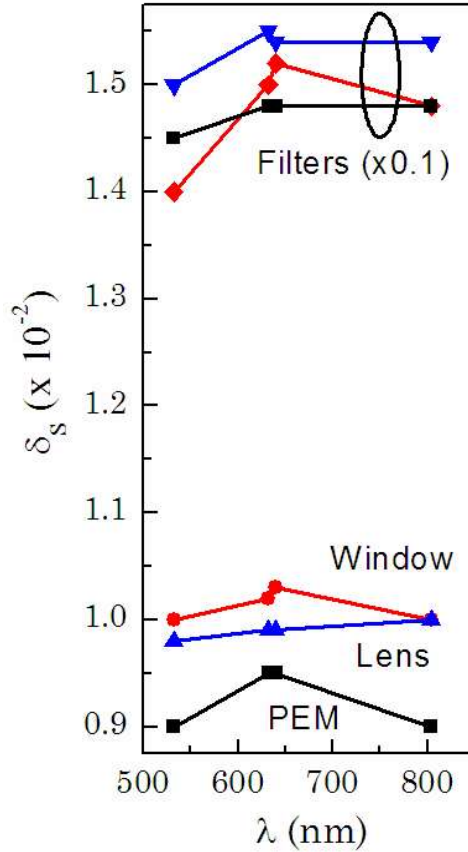


Figure 3.14 Measured static birefringence of different optical elements at different probe wavelengths

The other optical elements used in the complete set up like the window of cryostat, lenses, ND filter and laser filters are also tested for their residual birefringence and are plotted in figure 3.14. Because of higher δ_s , the laser filters are never used in the polarization optics line and are used either before the polarizer or after the analyzer.

3.5 ISHE measurement set up

3.5.1 Optical alignment

For the ISHE measurements, the samples are fabricated as discussed in section 3.2. Laser beam of suitable wavelength is modulated twice, once polarization modulated by using PEM and then intensity modulated by using a mechanical chopper. It is shown in figure 3.15 (a). Here ND, LP, PEM, C, S and L represents Neutral Density filter, linear polarizer, photo elastic modulator, chopper, sample and lens respectively. As explained in the previous section, ND filter is used before the linear polarizer to avoid static birefringence introduced by it. The sample is mounted on the cold finger of a closed cycle cryostat having an optical access. The entire optical elements are mounted on a special rotation stage to allow angle dependent measurements without disturbing their relative orientations. The signal across the sample is measured either in terms of voltage or current. In this set up, it is observed that current measurement is less susceptible to external noise than the voltage measurement. Therefore, ISHE current across the sample is measured.

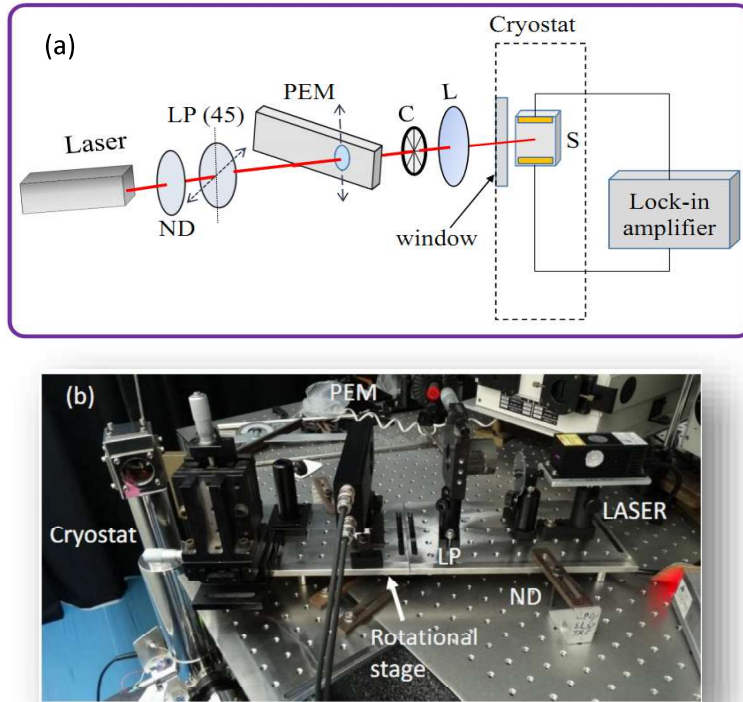


Figure 3.15 (a) Schematic and (b) photograph of experimental set up for ISHE measurements

In this work, Glan-Taylor polarizer with extinction coefficient 10^{-5} (Thorlabs, model: GT15), quarter wave plate working in the range of 700 nm to 1200 nm (Thorlabs, model: AQWP10M-980) and Photo-elastic modulator operating at 50 kHz with frequency stability better than 25 ppm (Hinds Instruments, model: I/FS50), have been used. Three different lasers have been used in this work. These are the Diode pumped solid state laser emitting at 532 nm (Oxius, model: 532L-150-Col-PP-LAS-01670), Diode laser emitting at 804 nm (Sanghai dreams, model: SDL-808-LM-200T) and another diode laser emitting at 640 nm (Sanghai dreams, model: SDL-650-LM-050L). The signals were detected using a Lock-in amplifier (NF corporation, Model: LI5640). The temperature of the lab has been controlled at 20°C.

The presence of mechanical chopper has a special purpose in this set up. It is used to align the laser beam exactly at the center of the sample. By using the convex lens, the position of the light beam is scanned along the length of the sample and current is measured across it. The minimum of such current indicates that the contacts are now at equipotential line, and the light beam is exactly at the center. It also minimizes the effect of modulated interference on the measurement. Whenever, modulated interference is suspected, the laser intensity is reduced by a factor given by equation 3.5 and signal across the sample, synchronized to the chopper frequency is measured. If this signal is larger than or comparable to the ISHE signal measured, then realignment is done to minimize the effect of modulated interference.

3.5.2 Response of the measurement circuit

The sample is mounted on the cold finger of the cryostat. Thin copper wire of thickness ~ 0.1 mm and length ~ 25 cm are used to connect the contacts 1 and 3 of the sample with the outer circuit. Outside the cryostat, the signal is carried by coaxial cables of impedance 1.2Ω and capacitance 2.3 pF, which are nearly independent of frequency in the measured range. Since all the measurements are done at 50 kHz, it is important to measure the frequency response of the measurement circuit at least up to that limit. It is recorded by using the internal function generator of the Lock-in amplifier, which generates a signal of magnitude 1 mV and frequency ranging from 200 Hz to 101 kHz. Figure 3.16 is the obtained response function, $M_I(f)$ of the measuring circuit to this signal obtained by dividing

the measured voltage by applied voltage. This can be suitably fitted with the frequency dependence $M_1(f)=M_0/\sqrt{1+(f/f_c)^2}$, with $f_c = 76.45$ kHz. At 50 kHz, the measured voltage is 15 % less than the applied voltage. Further, the second harmonic of the signal $M_2(f)$ is also measured to ensure the absence of leakage of the signal to higher harmonics and are also shown in figure 3.16. The negligible magnitude of $M_2(f)$ confirms the absence of artifacts in the measurement circuit.

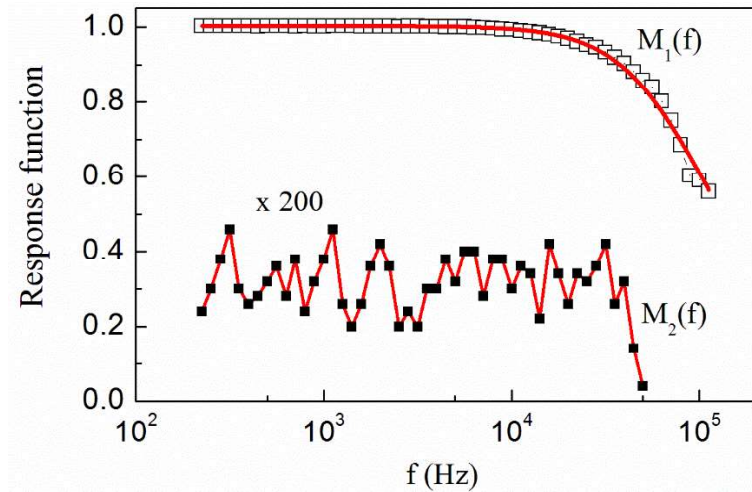


Figure 3.16 $M_1(f)$ and $M_2(f)$ as a function of signal frequency. $M_1(f)$ is also fitted with appropriate relation to find out the cut off frequency (see text).

Furthermore, the linearity of the measurement circuit for small signal detection is checked, by using the same internal function generator to apply voltage across a known resistor (8.5 M Ω at 50 kHz) and then measuring the current flow in the circuit. Figure 3.17 is the plot showing the linear relation between the measured current and applied current. The difference between them is the result of the response function $M_1(f)$.

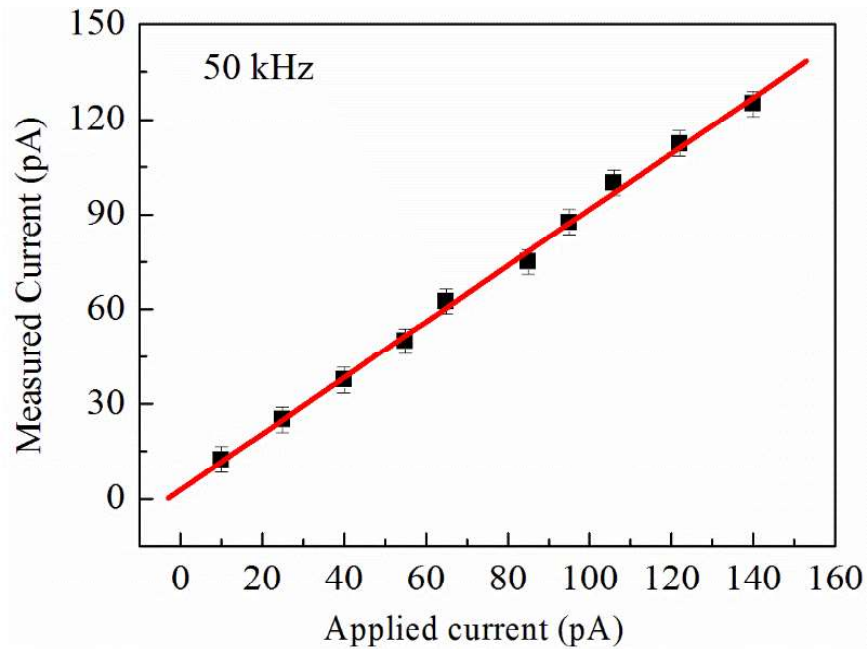


Figure 3.17 Relation between measured current and applied current. Linear relation confirms the suitability of the measurement.

3.6 Polarization resolved Photoluminescence set up

For the polarization resolved Photoluminescence measurements, an additional arm consisting of a quarter wave plate (QWP), an analyzer (LP2) and a laser filter (F) is added to figure 3.15. It is shown in figure 3.18 (a) and is used to analyze the degree of circular polarization of the photoluminescence excited by a circularly polarized light. The excitation arm is identical to figure 3.15 and both the experiments are conducted at same point on the sample in order to have one-to-one correlation.

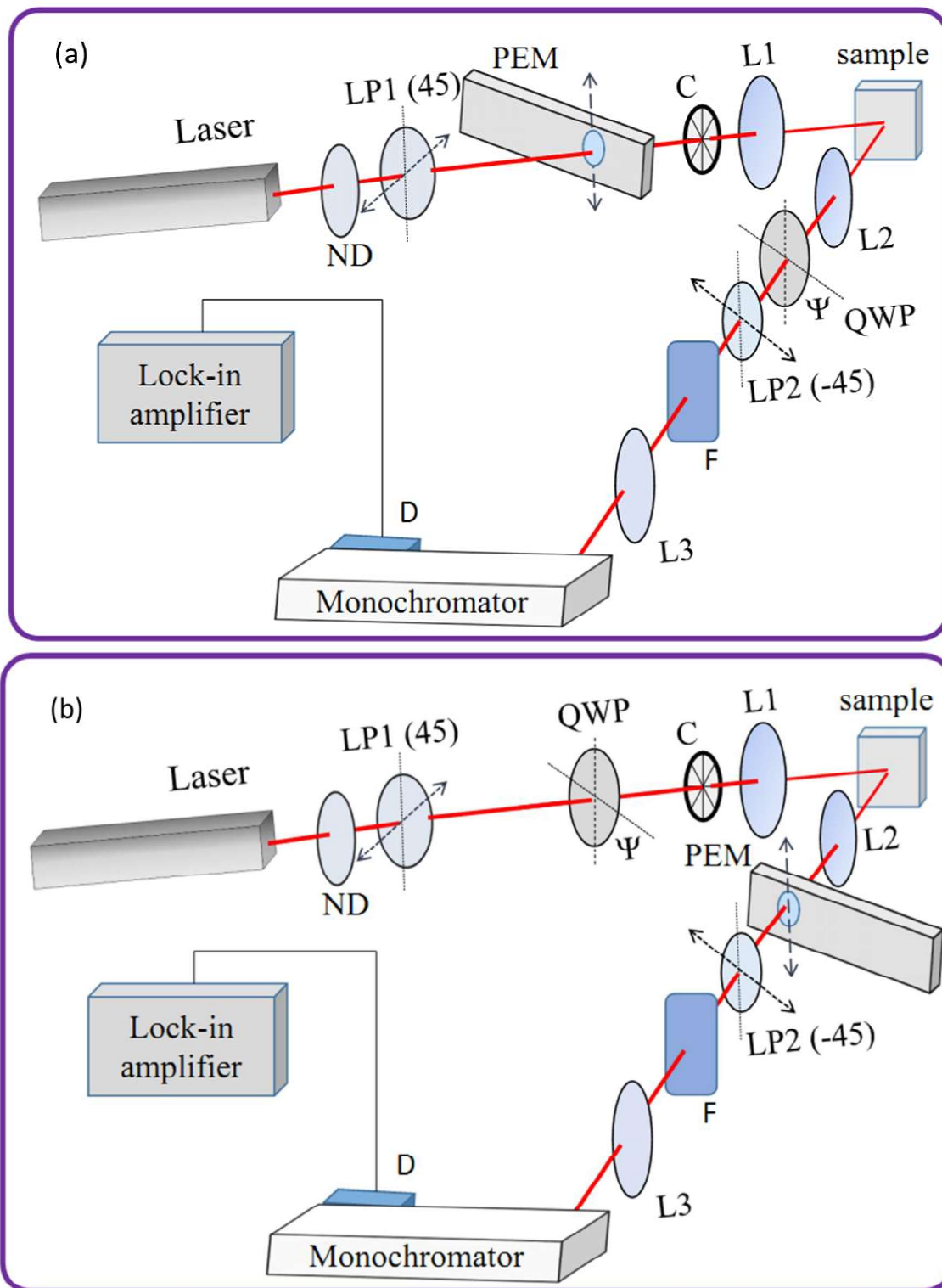


Figure 3.18 Alternate experimental set ups for polarization resolved PL measurement. In (a) PEM is used in the excitation arm, where as in (b) PEM is used in the collection arm

The experiments can also be conducted in an alternate set up as shown in figure 3.18 (b), where PEM is used in the collection arm instead of the excitation arm. Both the experiments have their respective advantages and disadvantages.

3.6.1 Comparison between two alternate experimental set ups

- i. In set up (a), laser can be conveniently passed through the center of PEM, however in set up (b), because of finite size of beam, a correction factor is needed as explained in section 3.3.4.
- ii. In set up (a), modulation at high frequency (here 50 kHz) minimizes the interaction between electron spin and lattice, allowing only the electronic phenomena to be studied, however in set up (b), small but finite hyperfine interaction has to be taken into account.
- iii. Set up (a) is susceptible to modulated interference, particularly when the degree of polarization is weak. This hinders the measurement of exact degree of polarization. This is not the case in set up (b), because the PL emitted is an incoherent beam and thus interference does not happen.
- iv. The retardation of quarter wave plate depends on the light wavelength, which can vary depending on the sample and the temperature. Therefore in set up (a) calibration at every wavelength is separately needed. However, in set up (b), the operating wavelength of PEM can be suitably chosen externally, reducing the need of separate calibration.

Ideally, both the arrangements should give similar results and any of the set ups can be chosen depending on the convenience, keeping the above conditions in mind. In most of the experiments which are done during the course of this thesis, set up (b) is used. A photograph of the actual setup is shown in figure 3.19.

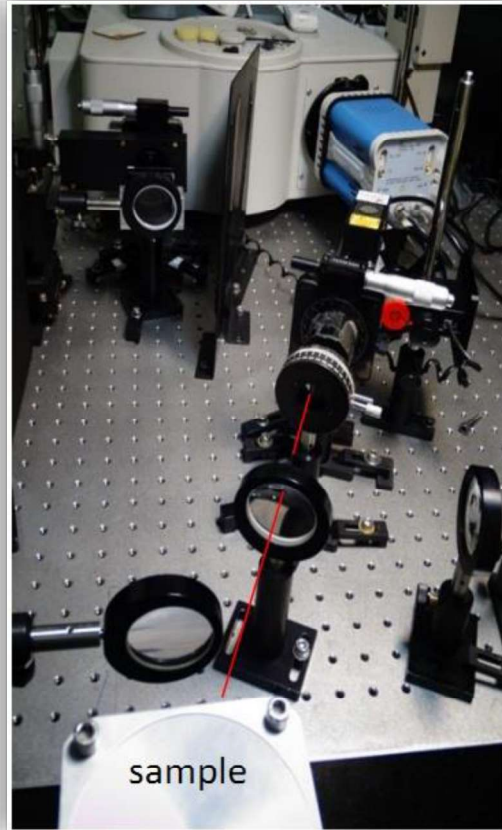


Figure 3.19 Photograph of the experimental set up to measure the polarization resolved photoluminescence

3.6.2 Principle of Polarization analysis

Since the samples that are considered here are non-birefringent, it does not introduce additional polarization in the incident light. The only effect sample will

have on it is to partially depolarize the light. Under this condition, the Stokes vector of the incident and emitted light are given by

$$S_1 = \begin{pmatrix} 1 \\ 0 \\ 0 \\ \sin(2\Psi) \end{pmatrix} \quad \text{and} \quad S_2 = \begin{pmatrix} 1 \\ 0 \\ 0 \\ \rho_l \sin(2\Psi) \end{pmatrix}$$

Where, ρ_l is the degree of circular polarization of the emitted light and Ψ is the orientation angle between the fast axis of QWP and LP1. The whole purpose of the experiment is to measure spectrally resolved ρ_l . When this light pass through analyzer assembly consisting of PEM and LP2, the stokes vector will be

$$S_3 = \begin{pmatrix} 1 + \rho_l \sin(2\Psi) \sin(\delta) \\ 0 \\ 1 - \rho_l \sin(2\Psi) \sin(\delta) \\ 0 \end{pmatrix}$$

Hence the detector reads $(1 + \rho_l \sin(2\Psi) \sin(\delta))$. From equation 3.2, the first harmonic component, as read by the Lock in amplifier is $[\rho_l \sin(2\Psi) J_1(\delta_0)]$. However, as this relation is derived from the normalized stokes vector, it has to be normalized with respect to the total intensity of the luminescence, which is measured by synchronizing the lock in amplifier to the frequency of mechanical chopper. Therefore, following steps are adopted to measure the polarization of photoluminescence

- i. The luminescence signal corresponding to the first harmonic of the chopper (I_c) and PEM (I_p) for a fixed Ψ and δ_0 are Measured. I_c gives the value of $I_+ + I_-$, where I_+ (I_-) is the intensity of emitted beam, which are co-

- (counter) polarized to the incident beam. Similarly, I_P gives the value of $I_+ + I_-$.
- ii. Ratio between them is taken which gives $[\rho_l \sin(2\Psi) J_1(\delta_0)]$.
 - iii. The same experiment is repeated for different Ψ and the result is fitted with $\sin(2\Psi)$ dependence. This step cancels out all the unwanted contributions from PEM background or modulated interference. Usually, a single δ_0 is sufficient, which is generally taken to be $\pi/2$.
 - iv. Usually, a calibration factor (C) is needed to take care of the misalignment of optics, if any and frequency response of the system. This is determined by passing circularly polarized light through the analyzing arm and taking the ratio of I_c and I_P . In the current experimental set up, it came out to be around 7.5 at 808 nm.
 - v. ρ_l is thus determined from the relation $\rho_l \sin(2\Psi) = C \frac{I_P}{I_c}$
 - vi. All the experiments are conducted with Hinds make Photo-elastic modulators (PEM-100) and Sciencetech photomultiplier tube (PMT-01, PMH-02).

Chapter 4

Observation of ISHE in Au/InP hybrid structure

4.1 Introduction

As explained earlier in chapter 2 that the magnitude of E_{ISHE} increases significantly by coating a thin film of high Z metals over III-V semiconductors because of the large value of spin Hall conductivity in those metals. Though GaAs has been explored for creating spin-polarized carriers, yet the other semiconductors can also be used. Recently a similar experiment was conducted in Pt/Ge hybrid structure. From the principle of operation of these structures, it is expected that a larger signal can be obtained if more photo-generated electrons reach the top metallic layer, without losing their spin information. Based on the numerical simulations, it is already predicted in chapter 2 that InP based hybrid structure offer highest possible values of E_{ISHE} , owing to its smallest spin orbit coupling among the conventional Arsenide/Phosphide semiconductors. A low value of spin orbit coupling in n-type InP leads to the longest spin relaxation time among various III-V semiconductors [118]. Moreover, the optical quality of InP epitaxial layers is

expected to be far better than Ge wafers. A low value of defect density is extremely helpful in minimizing the number of scattering centers which leads to long spin relaxation time. Similarly, as explained in chapter 2, Au metal offers the most suitable combination when grown on InP for observing the ISHE. In this chapter, the predictions made in chapter 2 are tested by performing ISHE measurements on Au/InP hybrid structures. Furthermore, a fundamental physical understanding of various scattering mechanisms which govern the magnitude of ISHE at various temperatures is also explored.

4.2 Sample Preparation

A semiconductor sample is picked, which consists of 500 nm thick lightly doped InP epilayer grown on (001) oriented semi-insulating (SI) InP substrate by MOVPE technique. The growth details of this sample are given in Table 3.1 in Chapter 3. The sample shows a room temperature electron concentration and mobility of $n=3.6 \times 10^{17} \text{ cm}^{-3}$ and $\mu = 2553 \text{ cm}^2 \text{ V}^{-1} \text{ s}^{-1}$, respectively. At 77 K, corresponding values are $n=5.2 \times 10^{16} \text{ cm}^{-3}$ and $\mu = 16400 \text{ cm}^2 \text{ V}^{-1} \text{ s}^{-1}$. A thin (20 nm) Au metallic layer is deposited by e-beam evaporation on square ($3 \times 3 \text{ mm}^2$) InP sample after suitable organic cleaning of the surface. The purity of Au source material used is 99.999 % and deposition was done at a rate of 1-2 Å/s. Finally, two 100-nm-thick Au-pads were evaporated by thermal evaporation at the two edges of Au thin layer which were used to measure the ISHE. The schematic of the sample geometry used here is presented in figure 4.1.

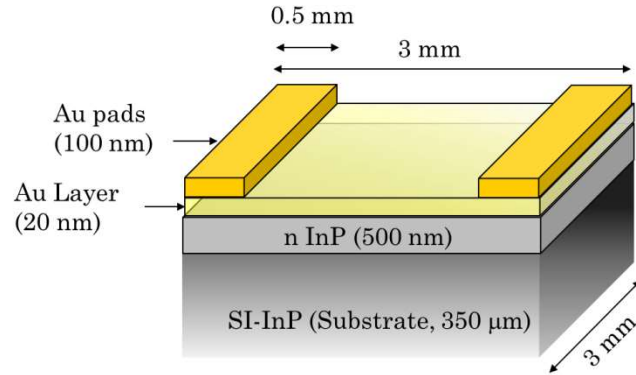


Figure 4.1 Schematic of the Au/InP hybrid structure, used to measure ISHE

The As deposited Au layer is characterized by its electrical resistivity and barrier height with InP. To measure the resistivity (ρ) of Au metallic layer, identical thin film of Au is deposited on SI InP during the same run as the device fabrication. ρ is measured by Van-der-Pauw geometry by passing a current of 1 mA in a temperature range of 45 to 300 K. The value of ρ varies from 347 $\mu\Omega$ cm at 300 K to 273.2 $\mu\Omega$ cm at 45 K as shown in figure 4.2 (a).

It can be compared with the standard value of bulk Au, which is 2.4 $\mu\Omega$ cm at 300 K [119]. Such a large value of resistivity is usually observed in evaporated thin films because of several effects including surface scattering and grain boundary scattering [120]. For film thickness below the electron mean free path (~ 37 nm at 300 K), the resistivity increase is further explained by taking the reduced Debye temperature into account [121].

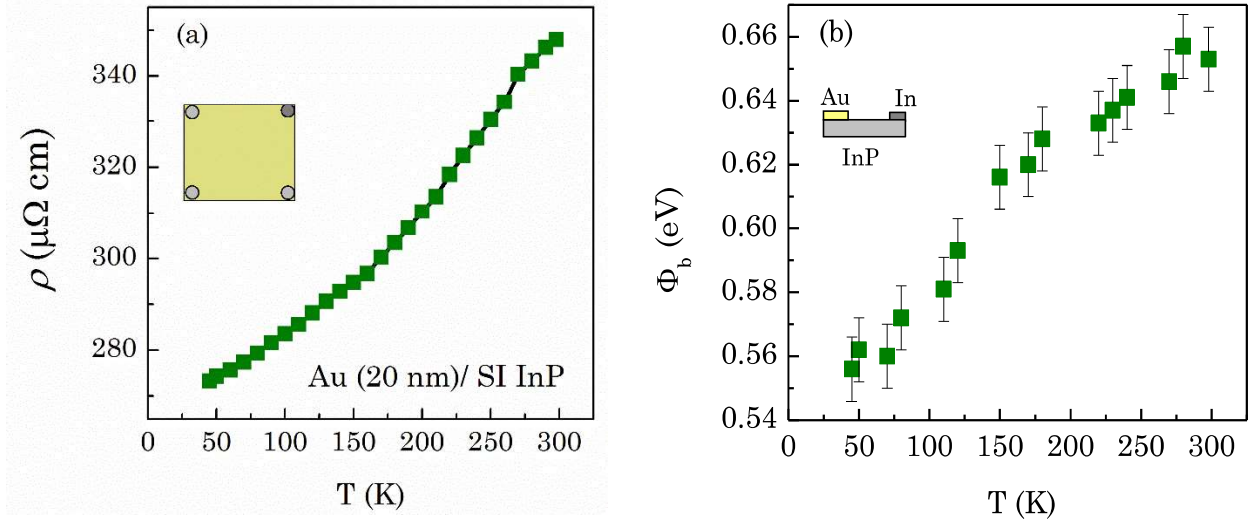


Figure 4.2 (a) Resistivity of Au film (20 nm) deposited on SI InP plotted as a function of temperature. Inset shows the Van-der Pauw geometry. (b) Temperature dependent barrier height at the Au/InP interface plotted as a function of temperature. Inset shows the schematic of the layer structure.

To characterize the Au/InP junction, identical film of Au is deposited as circular dots of diameter 0.8 mm. Prior to this, Indium contacts are annealed at 350°C to make the Ohmic contact. The approximate separation between the Ohmic and Schottky contact is kept 2 mm. Current-Voltage (I-V) measurements are done in a temperature range of 45 to 300 K to estimate the Schottky barrier height and ideality factor. In thermionic emission model, the forward Current-Voltage relation is given by $I = I_0 [\exp (eV/\eta kT)]$, where V is the applied forward bias, η is the ideality factor, e is the electronic charge and k is the Boltzmann constant [122]. I_0 is the saturation current given by $I_0 = AA^* T^2 \exp (-e\Phi_b/kT)$, where Φ_b is the Schottky barrier height, A is the area of the diode ($=5.02 \times 10^{-3} \text{ cm}^2$) and A^* is the effective Richardson constant ($=9.4 \text{ A cm}^{-2} \text{ K}^{-2}$). Thus, the barrier height is expressed as $\Phi_b =$

$(kT/e)\ln(AA^*T^2/I_0)$. The estimated barrier height varies from 0.55 to 0.65 eV over the temperature range of 45 to 300 K, and is shown in figure 4.2 (b). It has been shown that interface inhomogeneities lead to a large temperature dependence of Schottky barrier height [123]. Since in this case, the variation in Schottky barrier height is within 100 meV, this rules out any significant spatial inhomogeneity at the interface.

Further, the resistance (\mathfrak{R}) between two Au pads is measured as a function of temperature from I-V measurements. As shown in figure 4.3, I-V relation is observed to be linear in the whole temperature range where \mathfrak{R} varies from 79.2 Ω at 45 K to 99.5 Ω at 300 K. It follows the same trend as the resistivity of Au layer.

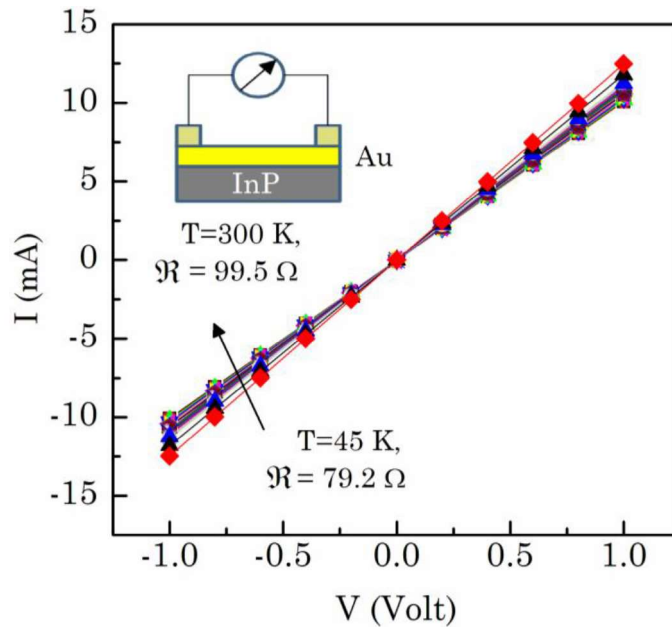


Figure 4.3 Resistance of the device used to measure ISHE at temperatures in the range of 45 to 300 K. Inset shows the experimental configuration.

4.3 ISHE measurements

As explained in chapter 2, circularly polarized light creates spin polarized electron hole pairs in their respective bands. Holes lose their spin information very quickly, whereas electrons can retain it for a longer time scale. These spin polarized electrons can produce a spin current in the Au layer which gives rise to ISHE signal. The schematic of the physical mechanism and experimental set up is shown in the following figure.

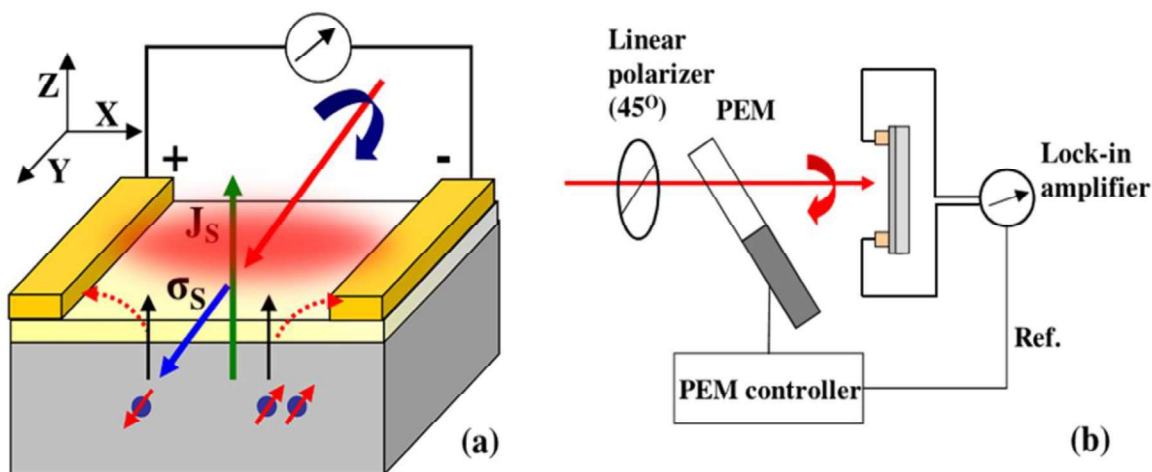


Figure 4.4 Schematic diagrams illustrating (a) mechanism and measurement geometry of the photo-induced inverse spin Hall effect and (b) schematic of experimental setup of the ISHE measurements. J_s , σ_s , CPL, and PEM stand for the spin current density, electron spin angular momentum, circularly polarized laser, and photo elastic modulator, respectively.

Using the standard procedure explained in section 3.3.1, the polarizer (LP) and PEM are oriented along $+45^\circ$ and 0° to the vertical. After passing the laser beam ($\lambda = 532 \text{ nm}$, $E_{ph} = 2.32 \text{ eV}$) through the linear polarizer, and the PEM, the beam is allowed to fall on the sample. The power of the laser beam (P_L) after passing through the PEM is kept at 10 mW. The PEM is rotated around its axis by

approximately 5 degree to avoid the residual contribution of modulated interference. Further, since the measurement is done across the Au layer only and the Schottky barrier is not the part of the measurement circuit, photovoltaic effect across the junction is not expected to contribute to the measurement. Throughout the measurement, the Y-Z plane is kept as the plane of incidence. Because of the planner geometry, the spin current will always be along Z direction. Therefore, E_{ISHE} will be along X-direction, as shown in the red dotted arrows in figure 4.4 (a). In this measurement setup, it is realized that the measurement of current instead of voltage improves the signal to noise ratio. Therefore, the ISHE signal is measured as the current flowing in the circuit (I_{ISHE}) at the modulating frequency of PEM (i.e. 50 kHz) by using standard lock-in amplifier technique.

It should be noted that a linearly polarized light with polarization plane inclined 45° to the PEM axis provides equal magnitude for the parallel and perpendicular component. Thus, when the phase shift ($\delta\theta$) is adjusted to be $\pi/2$, the PEM works as an oscillating quarter wave plate. The degree of circular polarization of the outgoing light (ρ_l) is given by $\rho_l = J_1(\delta\theta)$. Thus I_{ISHE} is measured by continuously varying ρ_l by controlling the phase shift externally. The time constant is kept at 300 ms and an averaging is taken over 100 consecutive readings. It should be noted that the Lock-in amplifier reads only the r.m.s. value, thus the peak value is estimated by multiplying the measured current with a factor of $\sqrt{2}$. Further as explained in section 3.5.2, to obtain I_{ISHE} , it is divided by the response function M_1 (50 kHz), which is equal to 0.85. Such a measurement showing the dependence

of I_{ISHE} with ρ_l at 300 K and 60° angle of incidence is shown in figure 4.5. Since the angular momentum carried by the light along the direction of light propagation is defined by ρ_l , a linear dependence of I_{ISHE} on ρ_l confirms the ISHE origin of transverse electric current.

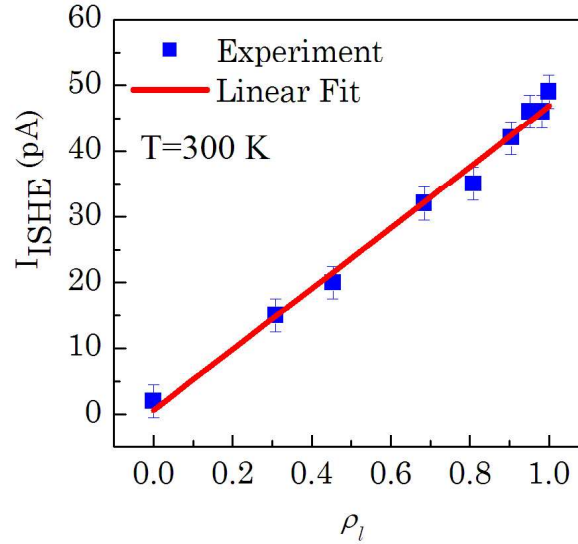


Figure 4.5 Magnitude of I_{ISHE} plotted as a function of degree of circular polarization.

To ascertain the ISHE origin of the signal, further experiments are conducted as described below,

- (i) As explained in section 2.3.3, the magnitude of I_{ISHE} peaks at an incidence angle ($\theta_0 \sim 60^\circ$) of circularly polarized light. Thus, I_{ISHE} is measured by varying the incidence angle and is shown in figure 4.6, which corroborates well with the theoretically predicted behavior.
- (ii) No measurable ISHE signal was recorded for Ti/InP sample, even though the junction properties are rather similar for both the metals. This is because Ti has considerably less spin Hall conductivity than Au. It also effectively rules out the presence of any photovoltaic contribution.

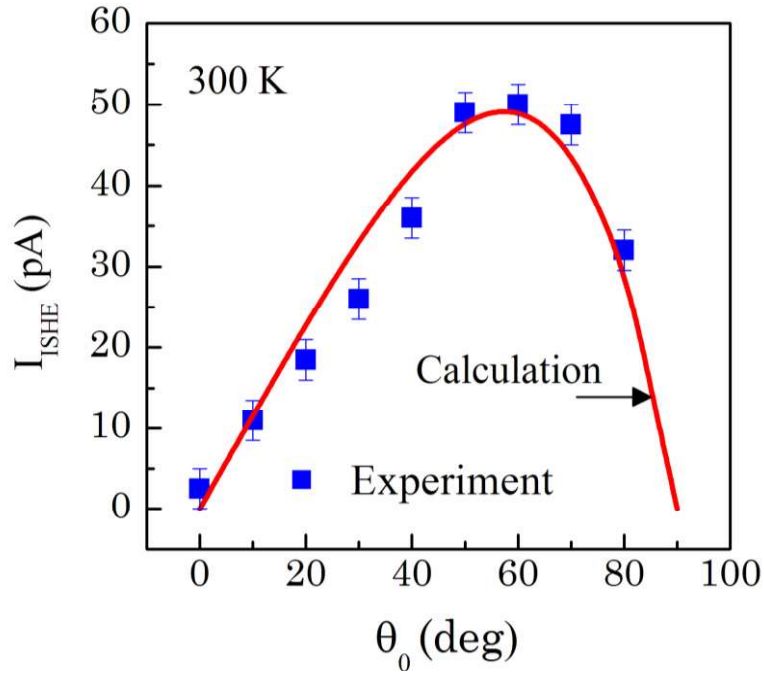


Figure 4.6 Dependence of I_{ISHE} on the angle of incidence (filled square). Numerically calculated values are also plotted in the same graph (solid line).

After confirming the ISHE origin of measured signal, few more experiments are conducted by studying the temperature dependence of I_{ISHE} in order to get more insight of the involved physical phenomena.

4.4 Temperature dependence of I_{ISHE}

4.4.1 Temperature dependent Measurements

Since all the physical phenomena that are involved here, like the electron transport, electron spin relaxation and tunneling at the interface are temperature dependent, I_{ISHE} is expected to have strong temperature dependence. Therefore temperature

dependence of I_{ISHE} is a source of information for exploring the underlying physical mechanism. Figure 4.7 (a) depicts the ρ_l dependence of I_{ISHE} at three dependent temperatures. A linear variation is observed at every temperature as obvious from figure 4.7 (a). Further, the peak values are plotted as a function of temperature in figure 4.7 (b). As expected, a strong dependence is observed with the magnitude of I_{ISHE} varying from 48 pA at 300 K to 452 pA at 45 K. Though the value of I_{ISHE} depends upon several factors, one can estimate the spin current density J_s^0 , injected into the Au layer, by the following analysis.

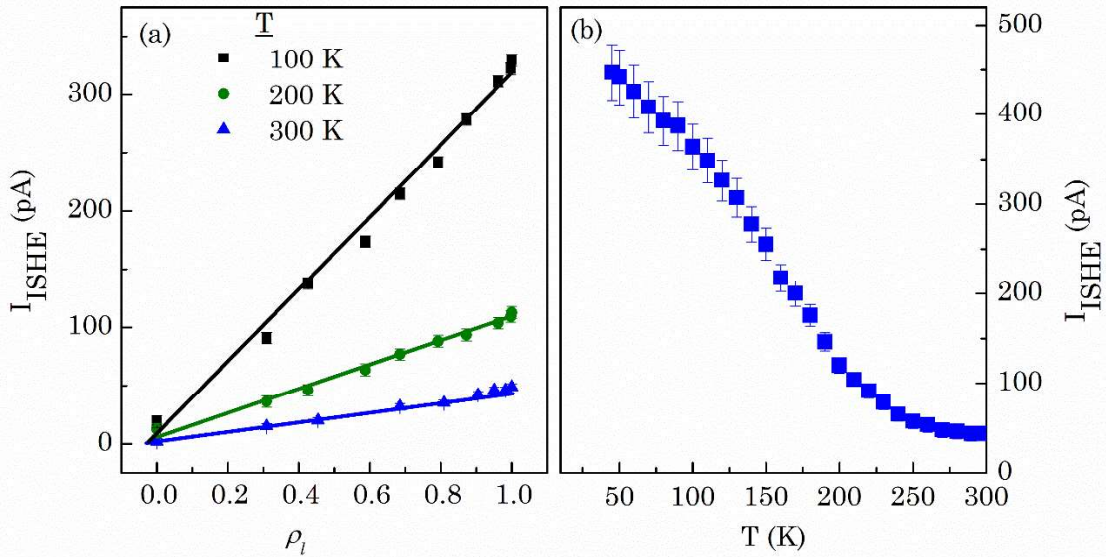


Figure 4.7 (a) I_{ISHE} as a function of degree of circular polarization for 100, 200 and 300 K. (b) Peak value of I_{ISHE} as a function of temperature

4.4.2 Estimation of Spin current density

As explained in section 2.2.7, the spin current density varies within the Au layer of thickness t , with the distance from the interface, which is given by equation (2.19)

as

$$J_s(z) = J_s^0 \left[\frac{\sinh\{(t-z)/L_s\}}{\sinh(t/L_s)} \right]$$

Here, L_s is spin diffusion length in Au and the direction perpendicular to the sample surface is taken as z direction.

The average spin current density is calculated as

$$\begin{aligned} \langle J_s \rangle &= \frac{1}{t} \int_0^t J_s(z) dz = \frac{J_s^0}{t \sinh[t/L_s]} \int_0^t \sinh\{(t-z)/L_s\} dz \\ &= \frac{J_s^0}{2t \sinh[t/L_s]} \int_0^t \left[e^{(t-z)/L_s} - e^{-(t-z)/L_s} \right] dz \\ &= \frac{J_s^0}{2t \sinh[t/L_s]} \left[-L_s e^{(t-z)/L_s} - L_s e^{-(t-z)/L_s} \right]_0^t \\ &= \frac{-L_s J_s^0 \left[2 - e^{t/L_s} - e^{-t/L_s} \right]}{2t \sinh[t/L_s]} \\ &= \frac{-2L_s J_s^0 \left[1 - \frac{e^{t/L_s} + e^{-t/L_s}}{2} \right]}{2t \sinh[t/L_s]} \\ \langle J_s \rangle &= \left(\frac{-L_s}{t} \right) \frac{[1 - \cosh(t/L_s)]}{\sinh[t/L_s]} J_s^0 \end{aligned} \quad (4.1)$$

From equation, (1.19)

$$E_{ISHE} = \frac{\gamma}{\sigma_C} \left(\vec{J}_s \times \hat{\sigma} \right)$$

Hence, the magnitude of the voltage developed across the two contacts will be

$$V_{ISHE} = \frac{d\gamma}{\sigma_C} \langle J_s \rangle \quad (4.2)$$

Where, d is the separation between two contacts ($= 2\text{mm}$), as shown in figure 4.1. Here, the transverse electric current (I_{ISHE}) is measured across two contact, which can be written as

$$I_{ISHE} = \frac{V_{ISHE}}{\mathfrak{R}} = \frac{\gamma d}{\mathfrak{R}\sigma_c} \langle J_S \rangle \quad (4.3)$$

\mathfrak{R} is the input impedance of the current measurement circuit, which is $10^6 \Omega$ for the present case.

$$\begin{aligned} I_{ISHE} &= \frac{\gamma d}{\mathfrak{R}\sigma_c} \left(\frac{-L_s}{t} \right) \frac{[1 - \cosh(t/L_s)]}{\sinh[t/L_s]} J_S^0 \\ &= \frac{\gamma d L_s}{\mathfrak{R}\sigma_c t} \left[\frac{\cosh(t/L_s) - 1}{\sinh(t/L_s)} \right] J_S^0 \end{aligned} \quad (4.4)$$

Since d and t are geometrically fixed, the observed temperature dependence of I_{ISHE} can be because of temperature dependence of γ , L_s and J_S^0 . For Au layer, L_s has been measured to be $63 \pm 15 \text{ nm}$, which is much larger than the thickness of Au-layer used in this experiment [124]. Therefore, any change in L_s because of temperature might not affect the magnitude of I_{ISHE} . The temperature dependence of γ can be estimated, if the temperature dependence of σ_{SH} and σ_c are known. As shown in figure 4.2 (a), temperature dependence of σ_c is already measured.

Researchers have reported the values of σ_{SH} or γ for Au at several temperatures both experimentally and theoretically [125-128]. For example, Mihajlovic et al. [126] reported a low value of γ at 4.5 and 295K for 60nm thick Au-nanowires. On the other hand, a relatively larger value of γ at room temperature for a FePt/Au nanowire system is reported by Seki et al. [127, 128]. They also found

that the value of γ vary with the thickness of Au Hall cross. In the absence of reliable experimental values of σ_{SH} for Au thin films over the entire temperature range, the values from the first principle calculations of Guo et al. [125] is taken as the limiting case. Nevertheless, our case where spin polarized electrons are injected into Au film across a Schottky barrier is different than the nanowire experiments where surface scattering plays an important role. Thereafter, the temperature dependence of γ is estimated by taking the ratio of numerically calculated values of σ_{SH} and the measured values of σ_c (inverse of ρ_c) in the range of 45 to 300 K and is shown in figure 4.8 (a).

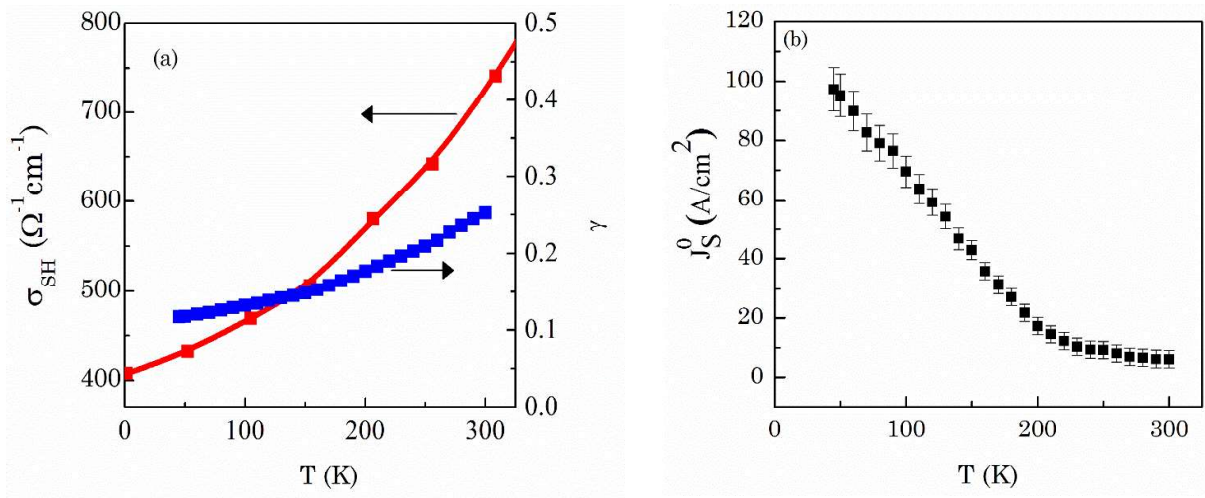


Figure 4.8 (a) Temperature dependence of σ_{SH} and γ for Au [125], (b) Estimated value of J_S^0 as a function of temperature

Once, the values of t , γ , d , σ_c and L_s are known, the spin current density (J_S^0) can be calculated from the measured values of I_{ISHE} by using equation (4.4). Using $t = 20\text{nm}$, $d=2\text{ mm}$, $L_s=63\text{ nm}$ and the measured value of σ_c at room temperature, equation 4.4 becomes,

$$J_s^0(A\text{ cm}^{-2}) = \frac{I_{ISHE}(A)}{\gamma(3.96 \times 10^{-11})} \quad (4.5)$$

The measured values of J_s^0 decrease from 97 A/cm² at 45 K to 4.3 A/cm² at 300 K as shown in figure 4.8 (b). The room temperature value of J_s^0 is similar to the value reported by Ando et al. [73] for Pt/GaAs hybrid structure and an order of magnitude larger than the value reported by Bottegoni et al. [80] for Pt/Ge hybrid structure. It is understood that the magnitude of J_s^0 depends on several parameters including the interfacial properties, wavelength of excitation and the nature of band structure. Hence, a quantitative estimate of J_s^0 is though desired but is a challenging process. Instead, the temperature dependence of J_s^0 can be analyzed with an aim of estimating the contribution of various scattering mechanisms over the temperature range of 45 to 300K.

4.4.3 Correlation with spin relaxation time

The estimated J_s^0 is proportional to the net polarization of electrons reaching the Au-layer, which can be estimated by taking a summation of contribution of all the electrons generated deep inside the sample [129]. i.e.

$$J_s^0 \propto \frac{\int_0^{\infty} N(x)e^{-\alpha x} dx}{\int_0^{\infty} e^{-\alpha x} dx} \quad (4.6)$$

Where $N(x)$ is the contribution of spin polarized electrons generated within x and $x+dx$, α is the absorption coefficient. If τ_s is the spin relaxation time, $N(x)$ is given by

$N(x) = N_0 e^{-x/\tau_s}$, where N_0 is the total electrons generated at x , τ is the time taken by

the electrons to reach the interface from x and is given by $\tau=x/v$, v being the saturation velocity of electrons in InP. Hence,

$$J_s^0 \propto \frac{N_0 \int_0^{\infty} \exp \left[-x \left(\alpha + \frac{1}{v\tau_s} \right) \right] dx}{\int_0^{\infty} \exp (-\alpha x) dx} = \frac{N_0 \alpha}{\alpha + \frac{1}{v\tau_s}}$$

Or,

$$J_s^0 \propto \left[1 + \frac{1}{\alpha v\tau_s} \right]^{-1} \quad (4.7)$$

Therefore, the estimated J_S^0 is intimately related to the spin relaxation time of the electrons and the variation of J_S^0 with temperature can be mainly attributed to the temperature dependence of τ_s . As is already explained in chapter 1, the most dominant process of spin relaxation in bulk III-V n type semiconductors is DP spin relaxation. The associated relaxation time is given by equation (1.14). DP mechanism has two different regimes with different dependence on the momentum relaxation time (τ_p). Regime I is the case, when the electron system is in equilibrium and is described by the Fermi Dirac statistics. In this case, the mean of velocity distribution is determined by τ_p , whereas the standard deviation of velocity distribution is determined solely by the temperature [30]. Under this condition τ_s becomes proportional to $(\tau_p)^{-1}$. On the other hand Regime II is the case, when the electron system is far from equilibrium. In this case, the mean of velocity distribution is determined by the optical excitation energy and the standard deviation of velocity distribution is determined by the momentum relaxation rate [1,

30]. Hence, the momentum relaxation opens another channel for spin relaxation because of the spin-orbit coupling and τ_s become proportional to τ_p .

There are many mechanism, like ionized impurity scattering (τ_{ii}), acoustic phonon deformation potential scattering (τ_{dp}), piezoelectric scattering (τ_{pe}), polar optical phonon scattering (τ_{pop}) and inter-valley scattering (τ_{iv}) that contribute to τ_p [97]. Further, since J_S^0 goes down with temperature, it can be said with confident that τ_s decreases with increasing temperature. Under regime I, this requires τ_p to increase with temperature. Out of all the scattering mechanism mentioned above, it is feasible only for ionized impurity scattering, where τ_p varies as $T^{3/2}$. While analyzing the transport of spin polarized carriers across the Schottky junctions, researchers have assumed this dependence [129]. Using the $T^{3/2}$ dependence of τ_s , the temperature dependence of J_S^0 is fitted using equation 4.7, where the agreement between theory (curve ii) and experiment (i) is found rather poor as shown in figure 4.9 (a). It clearly indicates that the temperature dependence of J_S^0 is not dominated by the ionized impurity scattering mechanism.

Under regime II, τ_p has to decrease with increase in temperature and is thus dominated by the combination of deformation potential scattering, piezoelectric scattering, polar optical phonon scattering and inter-valley scattering. For this case, τ_p is calculated by using Mathiessen's rule as $1/\tau_p = 1/\tau_{ii} + 1/\tau_{dp} + 1/\tau_{pe} + 1/\tau_{pop} + 1/\tau_{iv}$. The details of the scattering mechanisms are explained in Appendix C. Moreover, each term depends on temperature (T) and electron energy (E_e) in a

particular way. In most calculations, where electron system is in thermal equilibrium, E_e is replaced either by kT (for the non-degenerate case) or by E_F (for the degenerate case) [97]. On the other hand, for the non-equilibrium case, E_e and T have to be considered separately. The calculated value of τ_p , along with the contribution of different scattering mechanism is shown in figure 4.9 (b). These values of τ_p are then used to fit the temperature dependence of J_S^0 by using the relation $\tau_s = \kappa \tau_p$ and keeping κ as a fitting parameter.

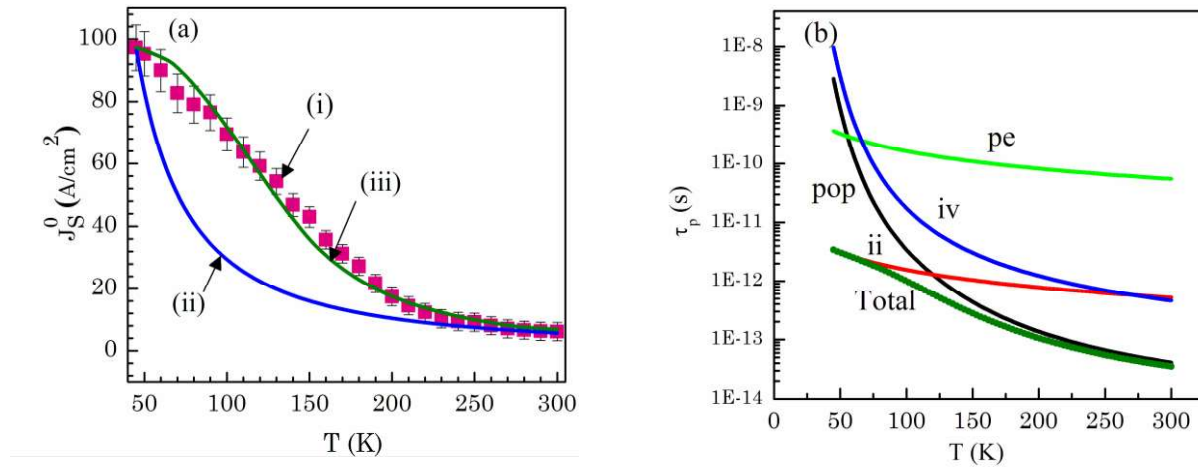


Figure 4.9 (a) Measured values of the J_S^0 injected spin current density (curve i) plotted as function of sample temperature and the corresponding fitted curves, by considering ionized impurity scattering only (curve ii) and by considering polar optical phonon (POP), inter valley (IV), piezo-electric potential (PZ), and deformation potential (DP) scattering mechanisms (curve iii). (b) The calculated τ_p (curve Total) and the contributions corresponding to various scattering mechanisms, plotted as functions of sample temperature.

Note that the energy of photo induced electrons will vary depending upon the case if these are excited from either the split-off or light/heavy hole valence band for a given photon energy. These values are calculated from the band structure of InP

using 8 band k.p method for $E_{ph}=2.33$ eV. The contribution from the split-off valence band is found to be negligible in this context since electrons excited from this band have smaller energy that reduces the probability of tunneling. On the other hand, electrons excited from heavy and light holes have nearly similar energy that is used as a parameter in the calculation. Varshni relation with suitable α and β parameters is used to calculate the temperature dependence of E_g [101]. It leads to a reasonable agreement between theory (curve c) and experiment as shown in figure 4.9 (a) for $\kappa = 3.84$.

Therefore, instead of using the assumption of equilibrium condition, it is appropriate to assume that the photo induced electrons are far from equilibrium over the time scale of ISHE. A minor difference between the two curves might arise due to several reasons, (i) electron-electron scattering is neglected in calculating the spin relaxation time. It is highly challenging since analytical solutions are not available. That is why, the single particle approximation is used. However, this contribution should be small because of the large energy of electrons that suppresses the coulomb scattering, (ii) temperature dependent spin Hall conductivity for Au is used, which is theoretically calculated for bulk Au metal. However, it is expected to be slightly different for a thin (20 nm) Au metallic film. Hence, absence of reliable experimental values of spin Hall conductivity of thin Au metallic film might be another reason.

4.5 Outcome of the chapter

Photo-induced ISHE is observed in the Au/InP hybrid structures at room temperature by measuring current (I_{ISHE}) across Au layer coated over MOVPE grown InP thin film. The ISHE origin of the measured signal is confirmed by observing following results.

- (i) Linear dependence of I_{ISHE} on the degree of circular polarization of incident light.
- (ii) Vanishing I_{ISHE} for normal incidence and fitting of angular dependence I_{ISHE} with theoretically predicted curve.
- (iii) Disappearance of I_{ISHE} , when Au is replaced with Ti

These observations are found to be in strong corroboration with the theoretical predictions made in chapter 2.

Further, in order to get more insight of the involved physical phenomena, I_{ISHE} is measured over a temperature range of 45 to 300 K. The measured I_{ISHE} is observed to be varying from 48 pA at 300 K to 452 pA at 45 K. By considering the spin Hall conductivity of Au layer, this measured I_{ISHE} is correlated with the spin carrier density injected from InP epilayer to Au metallic layer (J_S^0). The magnitude of J_S^0 increases from 4.3×10^4 to 9.7×10^5 A/m² when sample is cooled down from room temperature to 45K.

Numerical calculations based on the analysis of DP spin relaxation mechanism for optically induced hot electrons during their transport across the Au-InP interface are performed. It covers electron scattering due to ionized impurities, acoustic phonon deformation potential, piezoelectric potential, polar optical phonon and inter-valley scattering mechanisms. It is established that, the modeling of such kind of system must consider the photo induced electrons to be at non-equilibrium with the lattice. Further, it is also established that, in contrast to popular belief, ionized impurities scattering is not the predominant phenomena governing temperature dependent of I_{ISHE} . Rather, scattering by polar optical phonon dominates it over a wide temperature range.

Chapter 5

ISHE measurements in bulk semiconductors

5.1 Introduction

It is obvious from the theoretical predications made in chapter 2 and also from the experimental findings shown in chapter 4, that the coating of semiconductor material with a high Z metal of high spin-orbit coupling significantly improves the measured ISHE signal. In this context, the ISHE measurements in bulk semiconductors have two fold motivations.

- (i) In metal/semiconductor hybrid structures, spin injection and separation are carried out in semiconductor and metal layer respectively. One therefore needs to find a suitable combination of two distinct materials which in reality possess very different physical properties. The interface between these two materials also plays a critical role in hybrid structures [130]. In this context, an all-semiconductor device looks very attractive since it can provide the desired ability of potential variation and spin polarization by external bias, device structure and the doping profile [131].

(ii) The values of spin Hall angle (γ) and spin Hall conductivity (σ_{SH}) are not experimentally measured in case of most of the bulk semiconductors. Photo-induced ISHE measurement in bulk semiconductors is expected to be an appropriate method, which can be used to estimate the two parameters quite accurately. Though several reports exist but a systematic work where values of the two parameters for GaAs are discussed over a wide range of temperature is not yet available[66,69,76,79].

In the previous chapter ISHE measurement is considered in Au/InP hybrid structure. In that case, because of the presence of Schottky barrier, ISHE is observed even at light energy (E_{ph}) of 2.32 eV, which is much beyond the value of ($E_g+\Delta_{so}$) in InP. However, measurements in bulk required the light energy to be within E_g and $E_g+\Delta_{so}$. Since in case of InP, Δ_{so} is very small (0.108 eV), it is difficult to find a suitable laser source within this range. Furthermore, with change in temperature, this window ($E_g < E_{ph} < E_g + \Delta_{so}$) will shift. Therefore, the source has to be continuously tunable. Therefore, for the ease of measurement, GaAs is chosen, where Δ_{so} is relatively large (0.34 eV).

The operating principle behind photo-induced ISHE is already discussed in the previous chapters of this thesis. During the ISHE measurements, left (right) circularly polarized light can inject spin polarized electrons in semiconductors whose spin vector is oriented along the direction parallel (anti parallel) to the propagation direction. The magnitude of spin polarization of such electrons can be defined as $\rho_e = (n_+ - n_-)/(n_+ + n_-)$ where, n_+ and n_- represent the number of electrons

of spin vector parallel and anti-parallel to the axis of quantization respectively [20]. This spin density gradient near the surface induces spin diffusion current. Because of ISHE, this produces a transverse Electric field in the semiconductor, which is given by the following relation;

$$\vec{E}_{ISHE} = \frac{\gamma}{\sigma_c} \left(\vec{J}_s \times \hat{\sigma} \right) \quad (5.1)$$

Where all the symbols bear their usual physical meaning as explained in chapter 4. It is noted here that near band gap laser beam injects spin polarized electron hole pairs in the respective bands. However in bulk III-V semiconductors like GaAs, the photo-induced holes have very small spin relaxation times, typically in the femto-second range which is at least two orders smaller than that of the electrons[132]. Thus, the contribution of holes to the spin current is negligible.

In general, detection of ISHE signals in bulk III-V semiconductors is extremely challenging. A usual trick for observing the ISHE in bulk III-V semiconductors is to induce a spin polarization current component perpendicular to the motion of spin polarized electrons. A few researchers apply external magnetic field for orienting the electronic spin along a particular direction which is perpendicular to the electronic motion [74], while the others try external electric field for drifting the electrons along a direction which is perpendicular to the spin orientation [75]. Very recently, weak ISHE signal have been detected in heavily doped GaAs under oblique incidence conditions [80]. These three conditions are schematically described in figure 5.1. Application of electric field drags the electrons out of equilibrium far from the Γ point, sometime even to the L valley under

extreme conditions [133] and the measured values of parameters cannot be correlated with the equilibrium state. Furthermore, here the transverse voltage generated is not because of pure spin current, rather it is because of the current that is partially spin-polarized [133]. On the other hand, it is possible to measure the equilibrium value of γ through the near resonant optical excitation experiments that are performed under oblique incidence conditions. Since in n-type semiconductors, spin diffusion coefficient which is determined by the electron diffusion alone, is much larger than the charge diffusion coefficient, determined by the ambipolar diffusion [134], it provides an opportunity to probe predominantly spin current without the accompanying charge current.

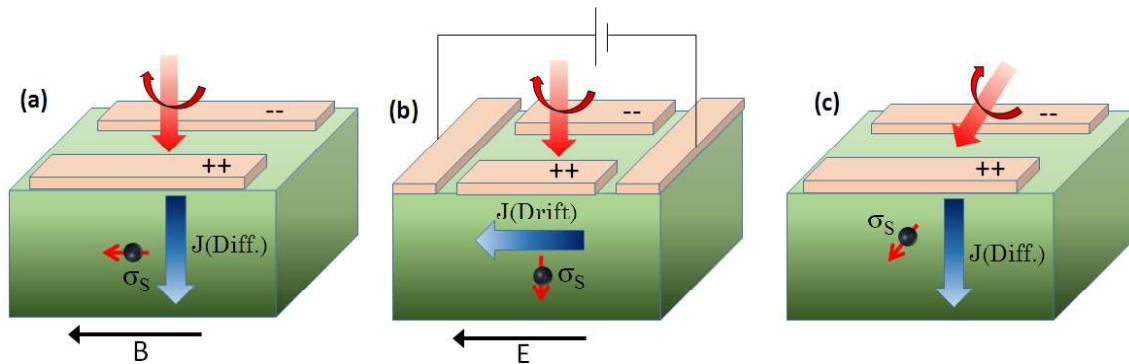


Figure 5.1 (a, b, c) Different scheme to detect ISHE in bulk semiconductors, E, B and J denotes the Electric field, Magnetic field and current density respectively.

In this chapter, ISHE measurements in MOVPE grown epitaxial GaAs thin film are reported. It is obvious that the crystalline quality of epitaxially grown GaAs material is expected to be far better than that of the heavily doped bulk GaAs material. Hence, ISHE measurement in these structures is expected to offer the material property with minimal influence of crystalline defects. The diffusion

equation is suitably modified by including thin film boundary conditions that provides appropriate values of the diffusion current density in the structure. Some other measurements for estimating the values of charge conductivity and spin relaxation time are also performed on the same sample for improving the reliability of spin Hall conductivity values. These measurements are performed in a broad temperature range, and the possible mechanisms governing the ISHE signal in bulk GaAs are discussed.

5.2 Preliminary characterization of the high quality GaAs sample

The sample consists of 2 μm thick *n*-type GaAs epitaxial layer grown on Semi insulating (SI) GaAs (001) substrate. The layer thickness is carefully chosen to be of the order of electron diffusion length in GaAs such that the transport of photo generated carriers can be described through conventional diffusion equation. More sample details are given in table 3.1. The carrier concentration and mobility is measured by Van-der-Pauw geometry using Indium point contacts, applying ± 100 μA current and ± 0.2 T magnetic field. The effects of other galvanometric phenomena are carefully eliminated by varying the polarity of current and magnetic field. Kiethley SMU 236 is used to apply/measure current/voltage. The results thus obtained are shown in figure 5.2. Almost constant carrier concentration is observed in the measured temperature range, which is a signature of degenerate carriers in GaAs and the same is reported by other researchers [135]. The mobility is also

almost temperature independent indicating the dominance of ionized impurity scattering in the transport process.

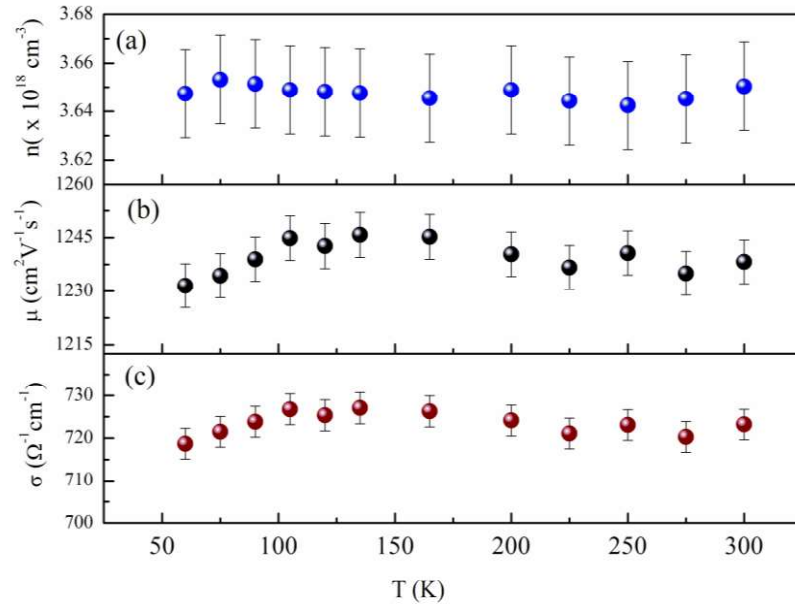


Figure 5.2 Measured (a) carrier concentration (b) Hall mobility, and (c) conductivity as a function of temperature

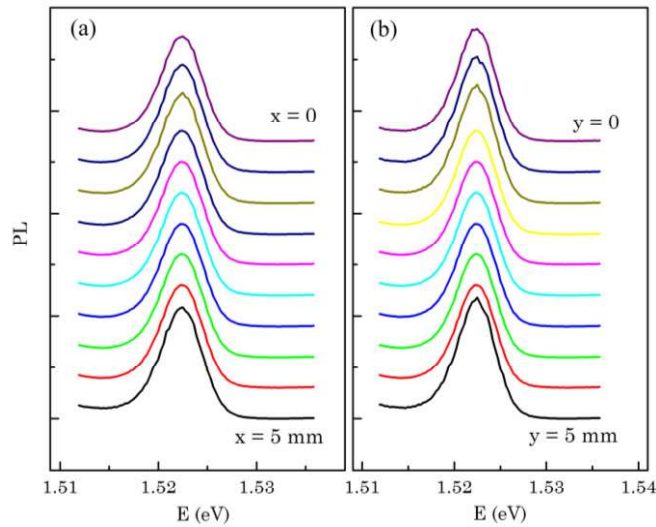


Figure 5.3 PL spectra at different positions of the sample, when the beam position is scanned (a) horizontally and (b) vertically. Note that the PL spectra are vertically shifted for the clarity in viewing.

The MOVPE grown samples are demonstrated to be spatially uniform. Nevertheless, the photoluminescence spectra is measured at 10K by loading the cryostat on a micrometer with 10 μm resolution and gradually scanning the micrometer along two perpendicular directions (x and y) at 0.5 mm step. Observation of identical PL spectra while moving in either direction across the whole sample confirms the uniformity of layer as shown in figure 5.3.

A piece of 5 x 5 mm² sample is cleaved from the whole structure and is cleaned thoroughly by following standard organic cleaning procedure. By using conventional UV photo-Lithography and chemical etching technique, Hall bar structure with channel width 250 μm and length 3 mm was fabricated as shown in figure 5.4 (a). Four 100-nm-thick electrodes (Au-Ge/Ni/Au), separated by 0.5 mm are realigned over them by thermal evaporation at a base pressure of 2-5 x 10⁻⁶ mbar as shown in figure 5.4 (b). Rapid thermal annealing at 450° C for 1 minute in 99.999% pure nitrogen ambient ensures low resistance Ohmic contact as confirmed by a linear current-voltage curve as shown in figure 5.5.

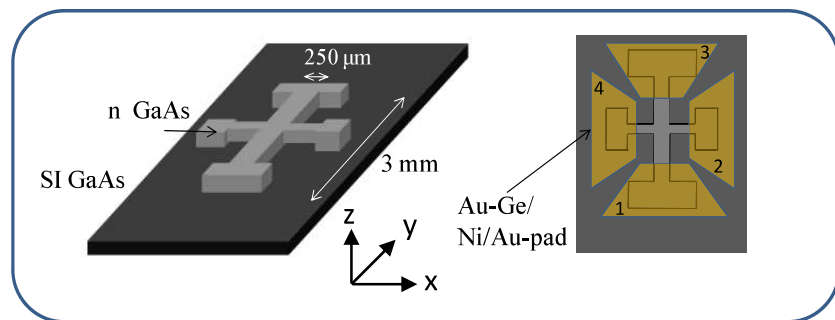


Figure 5.4 Schematic diagram of the fabricated sample

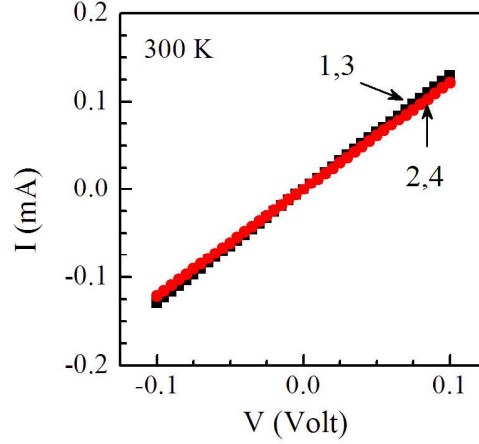


Figure 5.5 Current-Voltage measurement across two pair of contacts

5.3 Optical Alignment

The Polarizer (LP) and PEM are oriented along $+45^\circ$ and 0° to the vertical axis using the standard procedure explained in section 3.3.1. After passing the laser beam ($\lambda = 804 \text{ nm}$, $E_{ph} = 1.542 \text{ eV}$) through the linear polarizer, and the PEM, the beam is passed through lens (L) of focal length 7 cm, mounted on an (x, y, z) stage with resolution $10 \text{ }\mu\text{m}$, which focuses it to a circular spot size of diameter $200 \text{ }\mu\text{m}$, which makes the foot print area to be about $3.14 \times 10^{-4} \text{ cm}^2$. The power of the laser beam (P_L) after passing through the lens is kept at 20 mW. The photon flux (Φ) is estimated as

$$\Phi = \frac{P_L}{AE_{ph}(1.6 \times 10^{-19})} = 2.58 \times 10^{20} \text{ cm}^{-2} \text{ s}^{-1} \quad (5.2)$$

Apart from visual confirmation, photo current across the contacts (I_{PC}) are used to perfectly position the light beam at the centre of the sample. For this, the intensity of light is modulated using a mechanical chopper (C) operating at 180 Hz.

It is realized that, scanning along the stripes of device in figure 5.4 (a), the current across the two opposite pair of contacts become minimum, when the light beam is positioned exactly at the center. One such graph is shown in the following figure 5.6 (a). The variation of the minimum value of I_{PC} with angle of incidence predominantly follows the conventional $(1-R)$ relation, where R is the reflectivity of the GaAs surface.

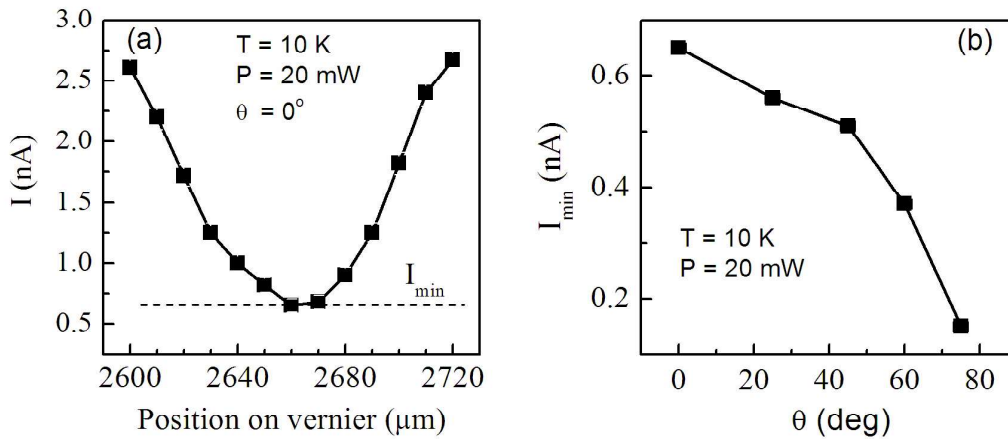


Figure 5.6 (a) Photocurrent as a function of light beam position along the Hall bar channel, and (b) The minimum of photocurrent as a function of incidence angle

5.4 ISHE current extraction

The modulated light beam creates oscillating spin polarized electrons with concentration gradient along the z-direction. The energy of diode laser ensures that the sample is excited under near-resonant conditions. High frequency (50 kHz) modulation of excitation laser source helps to minimize the hyperfine interaction of electronic and nuclear spin. Under steady state, the electronic spin redistributes depending on the spin diffusion length and recombination velocity. The diffusion of

electronic spin creates an electromotive force, which is transverse to the direction of spin polarization and concentration gradient. This polarization dependent current is measured across contact 1 and 3 by using Lock-in amplifier synchronized to the PEM operating frequency. The time constant is kept at 300 ms and averaging is taken over 221 consecutive readings.

The normalized stokes vector of light passing through the linear polarizer and PEM is

$$S = \begin{pmatrix} 1 \\ 0 \\ \cos \delta \\ \sin \delta \end{pmatrix} \quad (5.3)$$

$$\sin(\delta(t)) = \sin(\delta_0 \sin(\omega t)) = 2 \sum_{n=1}^{\infty} J_{2n-1}(\delta_0) \cos((2n-1)\omega t)$$

Since the ISHE current (I_{ISHE}), which is measured as the first harmonic of the signal, is a function of degree of circular polarization and intensity, it should depend on the retardation as $J_1(\delta_0)$. It is realized that, even when the direction of linearly polarized light (before the PEM) is made parallel to the PEM axis, a finite current exist in the circuit, which is proportional to the retardation magnitude, as shown in figure 5.7. This polarization independent component may arise from the PEM electronic interference, which is not completely nullified. Hence, the measured current (I_m) is fitted with the relation, $A_1[2J_1(\delta_0)] + A_2\delta_0 + A_3$, where A_1 , A_2 and A_3 are the components corresponding to I_{ISHE} , linear background and constant background respectively. Since the Lock-in amplifier reads only the r.m.s. value, the peak value is estimated by multiplying the extracted parameter A_1 with a factor of $\sqrt{2}$. To obtain

I_{ISHE} , it is further divided by the response function M_1 (50 kHz), which is equal to 0.85. The results of the above mentioned fitting are given in table 5.1.

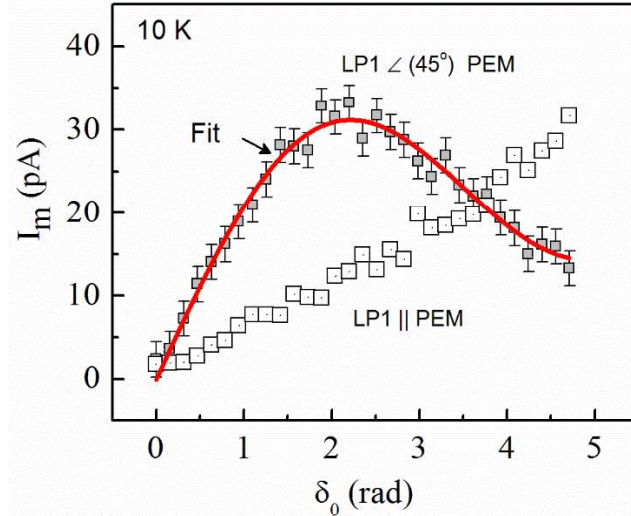


Figure 5.7 The measured current (I_m) \sim δ_0 for linearly polarization parallel to the PEM axis and along 45 degree to the PEM axis (at 10 K)

Table 5.1 Fitted parameters to obtain I_{ISHE}

Parameter	A_1	A_2	A_3	I_{ISHE}
Value	15.0 (± 0.6) pA	5.2 (± 0.18) pA/rad	0.8 (± 0.11) pA	24.95 (± 0.8) pA

The error bars shown in figure 5.7 represent the fluctuation in measured current at a given instant. However, the line shape analysis is carried out by considering the average data points. The same experiment is repeated for different angle of incidence and the extracted values of I_{ISHE} are plotted in figure 5.8. The disappearance of the signal for normal incidence and a peak at around 50 degree is a typical signature of ISHE as predicted from numerical simulations in Chapter 2.

A similar variation is already reported for metal/semiconductor hybrid structures as described in Chapter 4.

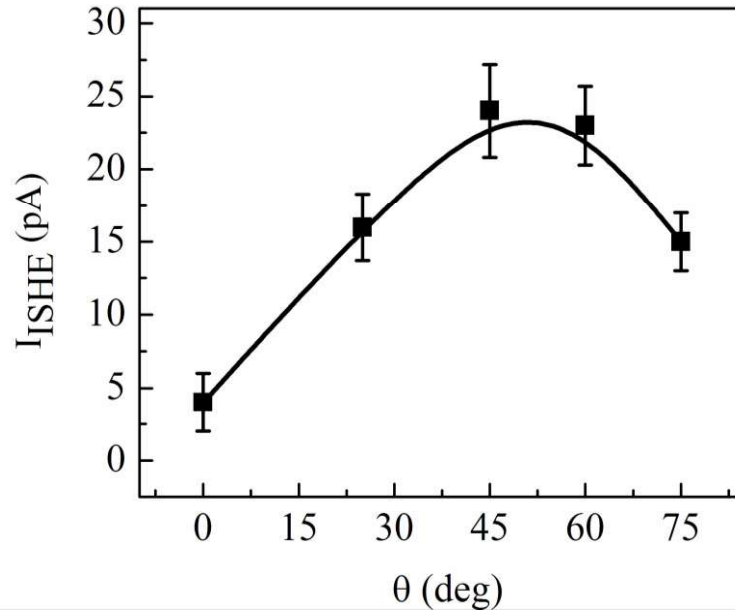


Figure 5.8 I_{ISHE} as a function of incidence angle

It should be noted that the spin independent phenomena like the Dember effect and photo-voltaic effect results in different angular dependence as compared to ISHE. Further confirmation of the ISHE origin of the signal comes from the fact that the polarization dependence disappears if the 804 nm diode laser is replaced by another laser having energy capable of exciting carriers from all the three valence bands. For example, when either 532 nm diode pumped solid state laser or 640 nm diode laser is used no measurable signal is recorded. Note that the performance of all the other optical elements like G.T polarizers and PEM remains quite satisfactory in this energy range.

5.5 Temperature dependence of ISHE signal

A clear signal of ISHE is observed in temperature range of 10 to 300 K as shown in figure 5.9. ISHE current signal increases from 11 pA at 300 K to 24.95 pA at 10 K. At the same time, the noise contribution reduces from 4 pA at 300 K to 2 pA at 10 K. Hence, lowering the sample temperature enhances the signal-to-noise ratio which is expected due to the obvious reasons. After carefully measuring the values of I_{ISHE} and σ_c , one requires only the spin current density for estimating the value of γ as can be appreciated from eqn. 5.1.

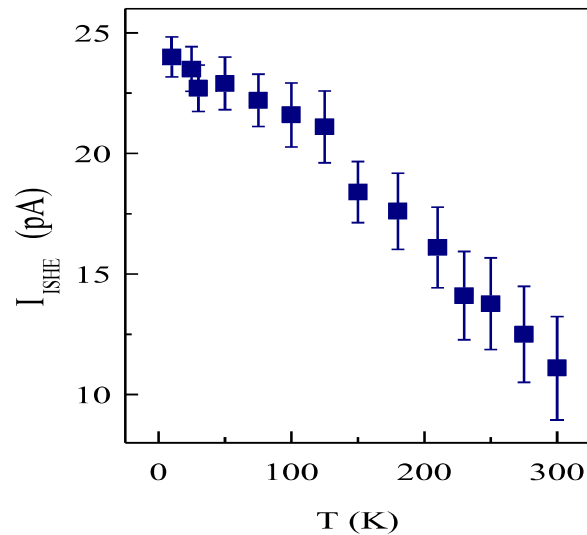


Figure 5.9 The magnitude of I_{ISHE} plotted as a function of sample temperature

Before assigning the measured temperature dependence of measured current to the intrinsic sample parameters, several extrinsic parameters need to be considered.

5.5.1 Local Heating of the sample

It is ensured that thermal equilibrium between the sample and cold finger of the cryostat is established by giving a sufficient wait time. The temperature is monitored by Si diode sensor mounted near the sample. The temperature fluctuation during the measurement is around 0.5 K. The sample is thermally well anchored with the cryostat to minimize the effect of local heating due to continuous irradiation by the laser beam. Furthermore, it is also monitored by observing the photoluminescence (PL) peak position. Generally, in n-type sample, local heating is one of the main reasons, which reduces the band gap of semiconductor and thus red shifts the PL peak. This effect is prominent at $T > 50$ K, where the red shift is typically 0.3 meV/K. Figure 5.10 shows 50 K PL spectra recorded at 300 μ W and 20 mW where the Peak intensity is normalized to observe the red shift due to sample heating. A nominal peak shift of about 1.1 meV is observed which corresponds to approximately 3 degree rise in the sample temperature.

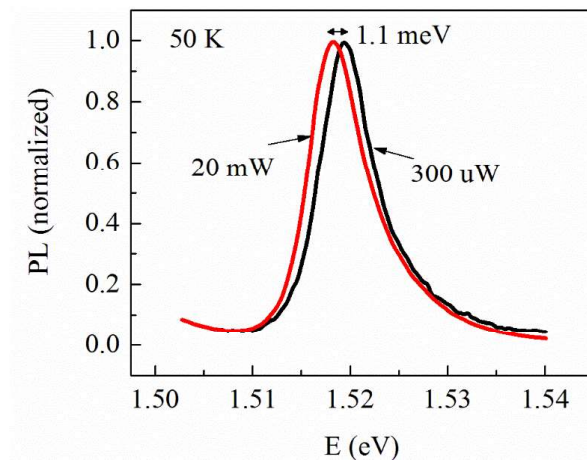


Figure 5.10 50K PL spectra recorded at 300 μ W and 20 mW laser power

In this work, whenever temperature is mentioned, it refers to the sample temperature which is measured by the Silicon diode sensor located on the backside of sample holder. However, the local temperature can be slightly higher (maximum 3 degrees) that primarily depends upon the laser power.

5.5.2 Reflectivity

The reflectivity of GaAs at 804 nm is measured for 45° incidence by monitoring the reflected light. Reflectivity of Fused silica window is properly taken into account. For 45° angle of incidence the reflectivity increases from 23 % to 26.5% as the temperature increases from 10 to 300 K. This minor increase is because of the reduction in band gap, which increases the difference between laser energy and band gap. This subsequently increases the value of dielectric constant.

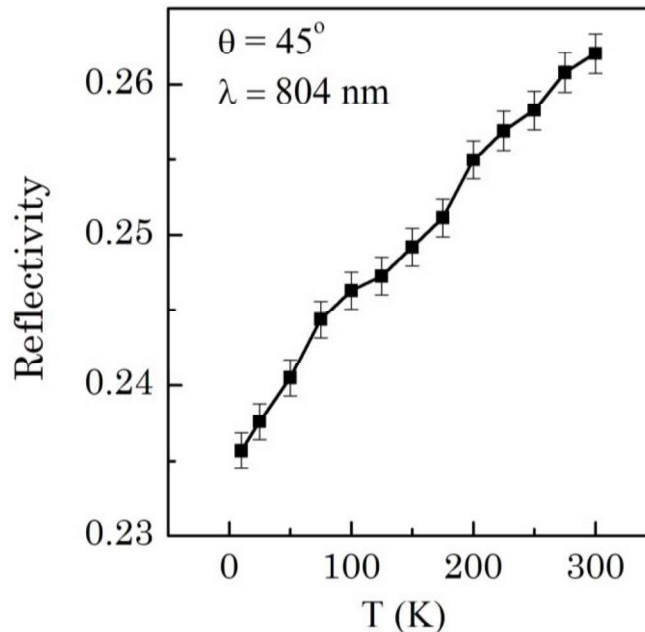


Figure 5.11 Reflectivity of GaAs at $\theta \sim 45^\circ$ as a function of temperature

5.5.3 Spin injection

As mentioned earlier that an increase in sample temperature results in the band gap shrinkage while the excitation laser energy is kept fixed at 1.542 eV. It is therefore important to look into the issue of degree of spin polarization of injected electrons (ρ_e) as a function of temperature. It is known that resonant excitation near band edge produces electron with $\rho_e = 0.5$. With increasing temperature, the band gap and inter-band matrix elements changes, which is given by Hubner et al. [136]. Using those values, the difference between E_{ph} and E_g is estimated to be 23 meV at 10 K which increases to 131 meV at 300 K. This changes the magnitude of wave vector (k) corresponding to a particular transition. At higher k , the light hole level picks up some fraction of the angular momentum state ($1/2, \pm 1/2$), which results in opposite spin polarization. This causes overall decrease in the electron spin polarization. A few researchers have claimed that the band gap shrinkage of semiconductor materials have an impact on the spin injection probability [137].

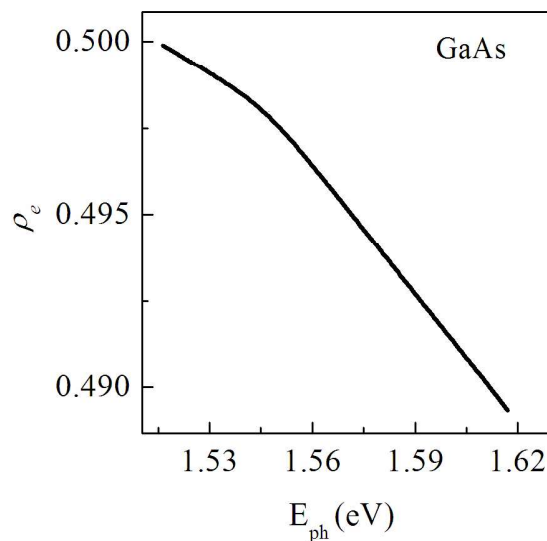


Figure 5.12 Numerically calculated values of spin injection probability as a function of photon energy [24]

Nastos et al. [24] have calculated that the spin injection probability for GaAs using 30 band k.p model, which can be zoomed in around band edge and is shown in figure 5.12. It can be seen that, the change in spin injection probability remains within 2% for an increase in excitation energy up to 100 meV above the band gap of GaAs. The band gap shrinks by only 100 meV over the temperature range of 10 to 300K and majority of this is shared by the electron kinetic energy because of its lower effective mass. Thus the kinetic energy of holes taking part in the transition is very small compared to the spin orbit splitting of GaAs ($\Delta_{SO}=0.34$ eV). Hence, the increase in temperature might not be able to alter the spin injection probability significantly.

5.5.4 Impedance

The impedance of the sample also varies a function of temperature, which is measured at 50 kHz and is plotted in figure 5.13. It decreases from 789 Ω at 10 K to 772 Ω at 300 K.

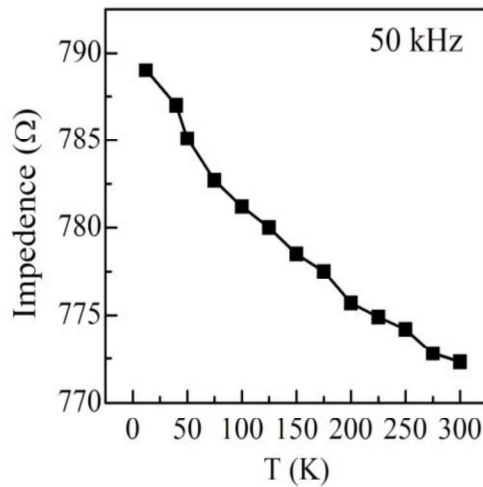


Figure 5.13 Sample impedance, measured across the contacts 1 and 3 of figure 5.4, plotted as a function of temperature

5.6 Numerical estimation of spin current density

Numerical calculation of the spin diffusion current density is carried out by solving the steady state one dimensional diffusion equation along the growth direction which is taken as the z -axis. A photon of flux Φ is assumed to incident on the sample surface at an angle of 45 degree with respect to the surface normal. The photo-generated electrons diffuse along z direction and form a steady state excess carrier density $\Delta n(z)$, which can be obtained by solving the one dimensional continuity equation given below, [138]

$$D \frac{d^2 \Delta n(z)}{dz^2} - \frac{\Delta n(z)}{\tau} + G(z) = 0 \quad (5.4)$$

Here, first term is the diffusion term, second term represents the recombination of excess carriers and the third term represents the generation of excess carriers which is defined by the Beer-Lambert relation given by $G(z) = \Phi(1-R)a \exp(-\alpha z)$. The symbols R , α , τ and D stand for the reflectivity, absorption coefficient, electron life time, and electron diffusion coefficient of GaAs epitaxial layer respectively.

This type of equation can be solved considering the approach of complimentary function and particular integral [139]. The complementary function in this case is

$$\left(D \nabla^2 - \frac{1}{\tau} \right) y(z) = 0, \quad \text{with } y = \Delta n(z)$$

Let the trial function be $y = e^{pz}$

$$\Rightarrow \frac{dy}{dz} = pe^{pz}, \quad \frac{d^2y}{dz^2} = p^2e^{pz}$$

$$\Rightarrow \left(D.p^2 - \frac{1}{\tau}\right)e^{pz} = 0 \quad \Rightarrow \left(D.p^2 - \frac{1}{\tau}\right) = 0$$

$$\Rightarrow p^2 = \frac{1}{D\tau} \quad \text{or,} \quad p = \frac{\pm 1}{\sqrt{D\tau}} = \frac{\pm 1}{L}$$

$$\Rightarrow \Delta n(z) = n_1 e^{z/L} + n_2 e^{-z/L}$$

Similarly, Particular Integral (P.I) for $G(z)$ is of the form e^{mz} and is given by

$$P.I. = \frac{e^{mz}}{f(m)}, \quad f = D\nabla^2 - \frac{1}{\tau}$$

$$P.I. = \frac{-I_0\alpha(1-r)e^{-\alpha z}}{D\alpha\nabla^2 - 1/\tau} = \frac{-I_0\alpha(1-r)e^{-\alpha z}}{D(\alpha^2 - 1/D\tau)}$$

$$= \frac{-I_0\alpha(1-r)}{D} \frac{e^{-\alpha z}}{\alpha^2 - 1/D\tau} = -I_0\alpha(1-r)\tau \frac{e^{-\alpha z}}{\alpha^2 L^2 - 1}$$

General solution is

$$\begin{aligned} \Delta n(z) &= C.F + P.I \\ &= n_1 e^{z/L} + n_2 e^{-z/L} - n_3 e^{-\alpha z} \end{aligned} \tag{5.5}$$

$$n_3 = \frac{I_0\alpha(1-r)\tau}{\alpha^2 L^2 - 1} \tag{5.6}$$

In case of bulk semiconductors, the boundary conditions are defined as follows [80]

$$J(0) = 0 \quad \text{and} \quad \Delta n(\infty) = 0, \quad \text{where}$$

$J(z_0) = qD \frac{d\Delta n(z_0)}{dz_0}$ is the diffusion current density at z_0

Here, the contribution of surface recombination velocity is neglected which might not be true in our case due to the limited thickness of the film which is of the order of penetration depth. Furthermore, the presence of surface states cannot be neglected. Therefore, the boundary conditions need to be modified. In the present case, the boundary conditions can be written as follows [140,141]

$$(i) \quad J(0) = \left(\frac{d\Delta n}{dz} \right)_{z=0} = s_1 \frac{\Delta n(0)}{D}$$

$$(ii) \quad J(d) = \left(\frac{d\Delta n}{dz} \right)_{z=d} = -s_2 \frac{\Delta n(d)}{D}$$

Where d is the thickness of epitaxial layer, s_1 is the surface recombination velocity of the front surface while s_2 represent the interface recombination velocity corresponding to n-GaAs/SI-GaAs interface. Note that a fraction of excess carriers will also be generated in SI-GaAs substrate. A majority of those carriers will be captured by the large density of trap states inside SI-GaAs [142]. For the purpose of present numerical simulations, s_2 is assumed to be inclusive of the trap states lying in SI-GaAs.

From equation (5.4),

$$\left(\frac{d\Delta n}{dz} \right) = \frac{n_1}{L} e^{x/L} - \frac{n_2}{L} e^{-x/L} + n_3 \alpha e^{-\alpha x}$$

From condition (i),

$$\begin{aligned}
\left(\frac{d\Delta n}{dz}\right)_{z=0} &= \frac{n_1}{L} - \frac{n_2}{L} + n_3\alpha = s_1 \frac{\Delta n(0)}{D} = \frac{s_1}{D}(n_1 + n_2 - n_3) \\
\Rightarrow n_1 \left(\frac{1}{L} - \frac{s_1}{D}\right) &= n_2 \left(\frac{1}{L} + \frac{s_1}{D}\right) - n_3 \left(\alpha + \frac{s_1}{D}\right) \\
\Rightarrow n_1 \left(\frac{D}{L} - s_1\right) &= n_2 \left(\frac{D}{L} + s_1\right) - n_3 (D\alpha + s_1) \\
\Rightarrow n_1 &= \frac{n_2 \left(\frac{D}{L} + s_1\right) - n_3 (D\alpha + s_1)}{\left(\frac{D}{L} - s_1\right)} \tag{5.7}
\end{aligned}$$

Similarly, from condition (ii),

$$\begin{aligned}
\frac{n_1}{L} e^{d/L} - \frac{n_2}{L} e^{-d/L} + n_3 \alpha e^{-\alpha d} &= \frac{-s_2}{D} (n_1 e^{d/L} + n_2 e^{-d/L} - n_3 e^{-\alpha d}) \\
\Rightarrow n_1 e^{d/L} \left(\frac{1}{L} + \frac{s_2}{D}\right) - n_2 e^{-d/L} \left(\frac{1}{L} - \frac{s_2}{D}\right) &= n_3 \alpha e^{-\alpha d} \left(\frac{s_2}{D} - \alpha\right)
\end{aligned}$$

Multiplying by D

$$n_1 e^{d/L} \left(\frac{D}{L} + s_2\right) - n_2 e^{-d/L} \left(\frac{D}{L} - s_2\right) = n_3 \alpha e^{-\alpha d} (s_2 - \alpha D) \tag{5.8}$$

Putting equation (5.7) in (5.8),

$$\begin{aligned}
&\frac{n_2 (s_1 + D/L)(s_2 + D/L) e^{d/L} - n_3 (s_1 + \alpha D)(s_2 + D/L) e^{d/L}}{(D/L - s_1)} + n_2 (s_2 - D/L) e^{-d/L} \\
&= n_3 (s_2 - \alpha D) e^{-\alpha d} \\
\Rightarrow n_2 (s_1 + D/L)(s_2 + D/L) e^{d/L} - n_3 (s_1 + \alpha D)(s_2 + D/L) e^{d/L} \\
&= n_3 (s_2 - \alpha D)(D/L - s_1) e^{-\alpha d} - n_2 (s_2 - D/L)(D/L - s_1) e^{-d/L}
\end{aligned}$$

$$\Rightarrow n_2 = n_3 \left[\frac{(s_2 - \alpha D)(D/L - s_1)e^{-\alpha d} + (s_1 + \alpha D)(s_2 + D/L)e^{d/L}}{(s_1 + D/L)(s_2 + D/L)e^{d/L} + (s_2 - D/L)(D/L - s_1)e^{-d/L}} \right] \quad (5.9)$$

Equation (5.6), (5.7) and (5.9) completely predicts the carrier distribution across the sample along with equation (5.5). Note that the excess carrier density is going to be significantly different from the case of bulk semiconductors. Using the excess carrier density profile, one can calculate the diffusion current density as,

$$J(z) = qD \frac{d\Delta n}{dz} \quad (5.10)$$

For heavily doped GaAs epitaxial layers, α is taken to be $2 \times 10^4 \text{ cm}^{-1}$ at the wavelength of excitation laser beam [143], while the reflectivity R for 45° angle of incidence is measured to be 26.5 % at room temperature. The surface recombination velocity of the front surface is taken as 10^6 cm^{-1} , following the values reported in literature for un-passivated GaAs [144]. The surface recombination velocity for n-GaAs/SI-GaAs interface is taken to be 10^8 cm s^{-1} which includes the contribution of trap states in SI-GaAs [142]. Using these values and a typical value of $\tau = 1 \text{ ns}$, the steady state carrier distribution $\Delta n(z)$ is estimated and plotted in figure 5.14.

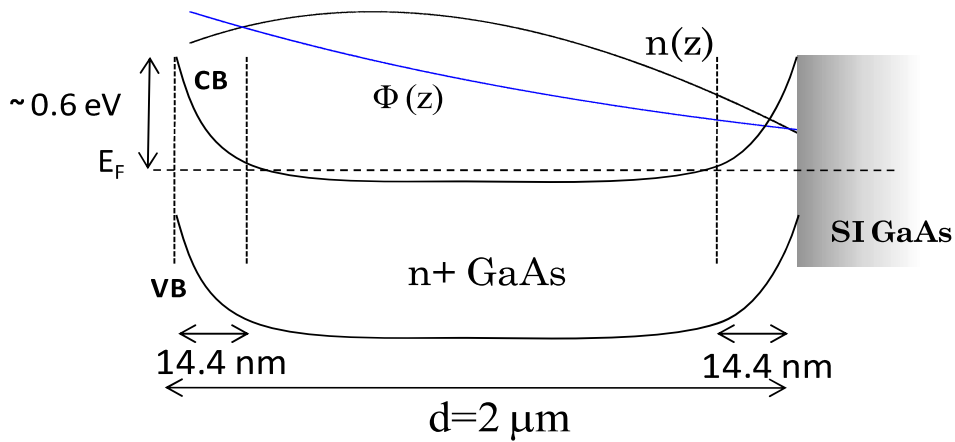


Figure 5.14. The calculated $\Phi(z)$ and $\Delta n(z)$ for typical values of α , s_1 and τ . Band bending at the surface of GaAs and at the interface of n⁺GaAs/ SI GaAs are also shown.

Identically, the spin density distribution and spin current density ($J_S(z)$) is determined by replacing τ , D and L by their spin counterpart; spin relaxation time (τ_S), spin diffusion coefficient (D_S) and spin diffusion length (L_S) respectively. Furthermore, only the spin component perpendicular to the direction of diffusion contributes to ISHE, therefore the effective spin density distribution lowered by a factor of $0.5\sin(\theta_1)$, where θ_1 is the angle of refraction. Here the factor 0.5 comes from the fact that the excess carriers generated are 50% spin polarized for near resonant excitation. Noting that $n_1\sin(\theta_1) = \sin(\theta)$, where n_1 is the refractive index of GaAs ($=3.3$) and θ is the angle of incidence ($=45^\circ$), the spin density distribution is estimated to be 0.1 times the excess carrier density distribution.

Therefore, the spin current density can be calculated provided the values of spin diffusion coefficient and spin diffusion length are known. Unfortunately, the reported values of electron diffusion coefficient in literature are usually estimated by considering the ambipolar diffusion of carriers which is not appropriate in the

present case as the spin diffusion coefficient in n-type semiconductors is defined mainly through the electron diffusion coefficient [134]. Under this condition, the diffusion coefficient is given by $eD_S/(\mu kT) = 2F_{1/2}(x)/F_{-1/2}(x)$, where, $x = (E_F - E_C)/kT$, $F_{1/2}$ and $F_{-1/2}$ represent the relevant Fermi integrals [145]. In this sample, the Fermi level is 51meV above the conduction band. $F_{1/2}$ and $F_{-1/2}$ are obtained by numerical integration and the diffusion coefficient is thereafter estimated by measuring the electron mobility from Hall experiments. The spin diffusion length is thereafter estimated by the relation $L_S = \sqrt{D_S \tau_{eff}}$, where τ_{eff} is the effective life time of spin polarized electrons in the conduction band. The value of τ_{eff} is governed by two parallel and independent mechanisms. One of them is related to the recombination of electrons with holes while another is associated with the spin relaxation of electrons. Since the number of spin polarized electrons is very small compared to the equilibrium carrier concentration of n+ GaAs, the holes will predominantly recombine with un-polarized electrons. Therefore, the net probability for the loss of spin polarization through recombination process is rather very small. It is therefore reasonable to assume that the loss of spin polarization is mainly governed by the spin relaxation process. Therefore, τ_{eff} can be measured by recording the spin relaxation time (τ_s). Once the values of D_S and τ_s are known, one can thereafter numerically calculate the spin current density (J_S) which further depends on the sample temperature through these two parameters. Nevertheless, the absolute value of J_S depends critically on parameter τ_s , which is measured by performing the optical orientation experiment as explained in the next section.

Here, few more issues need to be pointed out,

(1) Depending upon the surface conditions of the sample, there might be a change in the surface recombination velocity which will cause some variations in the spin current density. However, such a change turns out to be only $\sim 2\%$ for 10% variation in s_1 . Note that such a large variation in the values of s_1 is unexpected under present experimental conditions.

(2) In degenerate semiconductors, electron–electron scattering gives rise to a spin coulomb drag between the electrons moving with spin up and spin down. This effect is known for reducing the values of spin diffusion coefficient at high dopant concentrations. However, it remains below 1% at low temperatures. Similarly, spin-spin coupling effects that lead to Pauli blockade are also neglected in present study since those are more relevant in p-type semiconductors [146].

(3) The contribution of drift current is also ignored in our calculations. However, this is a safe approximation since the current flow is mainly governed by the diffusion of photo-generated electrons in case of heavily doped semiconductors. Note that the value of depletion width in our sample is only 14 nm which ensures that the most of the carriers are injected in flat band region of the sample.

(4) Only one dimensional continuity equation is solved implying that the in-plane contributions are ignored which is again a good approximation under the present experimental configuration.

5.7 Measurement of Spin relaxation time

Here, the steady-state optical orientation method is used, which have already been tried for heavily doped n-type semiconductors [20]. The fundamental mechanism of this technique is explained in section 1.2.2. Absorption of circularly polarized laser beam creates spin polarized electron-hole pairs in their respective bands. However, because of the valence band mixing effect in III-V semiconductors, holes lose their spin information over femto-second time scale. On the other hand, spin relaxation time of thermalized electrons is much longer. Note that the recombination rates of photo-generated carriers are generally independent of their spin. Although, spin dependent recombination of carriers was reported in GaAs by early researchers but the same was found to be governed by the presence of large number of vacancies and deep levels [147]. It is found that the present sample does not show any such mechanism which is expected due to the superior crystalline quality of MOVPE grown epitaxial layers. As mentioned earlier that the photo-generated holes predominantly recombine with the unpolarized electrons which gradually makes the electron system to be spin polarized where non-oriented electrons are replaced by the oriented ones with the photo-excitation process. The degree of spin polarization of these photo-excited electrons (ρ_e) can be accessed from the measurement of degree of circular polarization of the emitted PL (ρ_l) beam using equation 1.11. i.e. $\rho_l = (\rho_e \cos \theta_0)/2$, θ_0 is the angle between the spin polarization vector and the detection direction.

In this case, PL is collected at normal to the sample surface, therefore θ_0 also is the angle of incidence. In our measurements, θ_0 is kept at $\sim 45^\circ$ such that $\rho_e = 2\sqrt{2}\rho_j$. Although the value of ρ_e is 0.5 at the time of generation of electron-hole pairs but the measured value of ρ_e is expected to be much smaller due to the spin relaxation process. Therefore, the value of τ_S can be estimated from the measured value of ρ_e through the following relation [74],

$$\rho_e = \frac{0.5}{1 + \left(\frac{\tau_j}{\tau_s}\right)} \quad (5.11)$$

here $\tau_j = n/G$, G is number of electron hole pair generated per unit volume per unit time, τ_j is analogous to electron lifetime which is defined by the characteristic time during which the entire population of equilibrium electrons in n+ GaAs is replaced by photo-excited spin polarized electrons.

5.7.1 Analysis of Polarization dependent Photoluminescence

Following the description given in section 3.6, PL spectrum synchronized with either the mechanical chopper (I_+I_-) or PEM module (I_+I_-) are recorded at 10 K and are shown in figure 5.15 (a). In order to nullify the effect of any background signal that might be present in our experimental setup, both (I_+I_-) and (I_+I_-) are measured by rotating the quarter wave plate by angle Ψ with respect to the linear polarizer. Such a plot is shown in figure 5.15 (b) along with a fitted curve having $\sin(2\Psi)$ dependence. It implies that the PL spectrum remains the same but of opposite circular polarization when the quarter wave plate is rotated by 90° . A similar set of

PL measurements is independently performed on SI-GaAs substrate which confirms that no measurable contribution to ρ_l arises from the carriers injected in SI-GaAs substrate. Thereafter, ρ_l is determined from the relation $\rho_l \sin(2\Psi) = C(I_{++}I_{--})/(I_{+-}I_{-+})$, where C is the calibration factor and is taken to be 7.5 in our case.

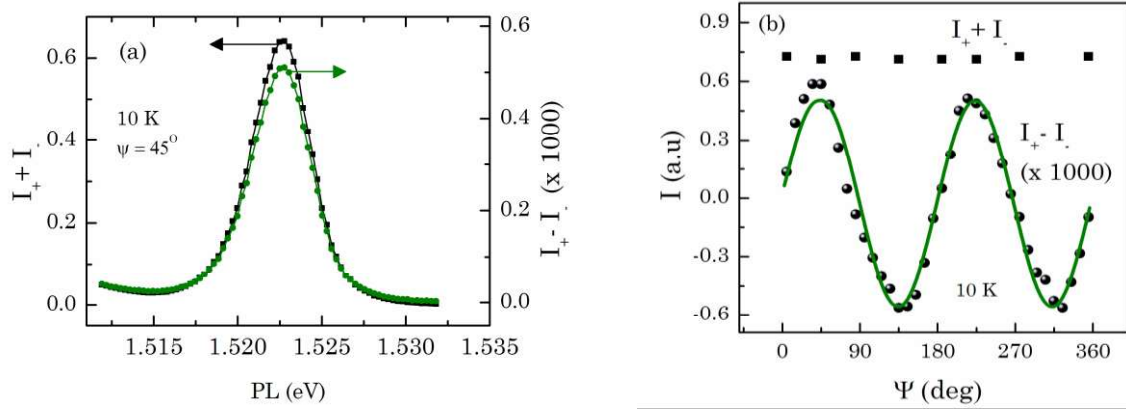


Figure 5.15 (a) $(I_{++}I_{--})$ and $(I_{+-}I_{-+})$ for GaAs at 10 K. (b) $(I_{++}I_{--})$ and $(I_{+-}I_{-+})$ are plotted as a function of relative angle between quarter wave plate and linear polarizer.

Figure 5.16 shows the measured PL spectra and ρ_l plotted as function of energy in the energy range of 10 to 200 K at 20 mW incident power. It is observed from figure 5.16 that the value of ρ_l increases at high energy tail of the PL spectra particularly at low temperatures. It may happen due to various reasons, for example, re-absorption of emitted photon [148], recombination of hot electrons [149], different band filling of spin up and down electrons [150] and weak signal-to-noise ratio towards the high energy tail of PL spectra.

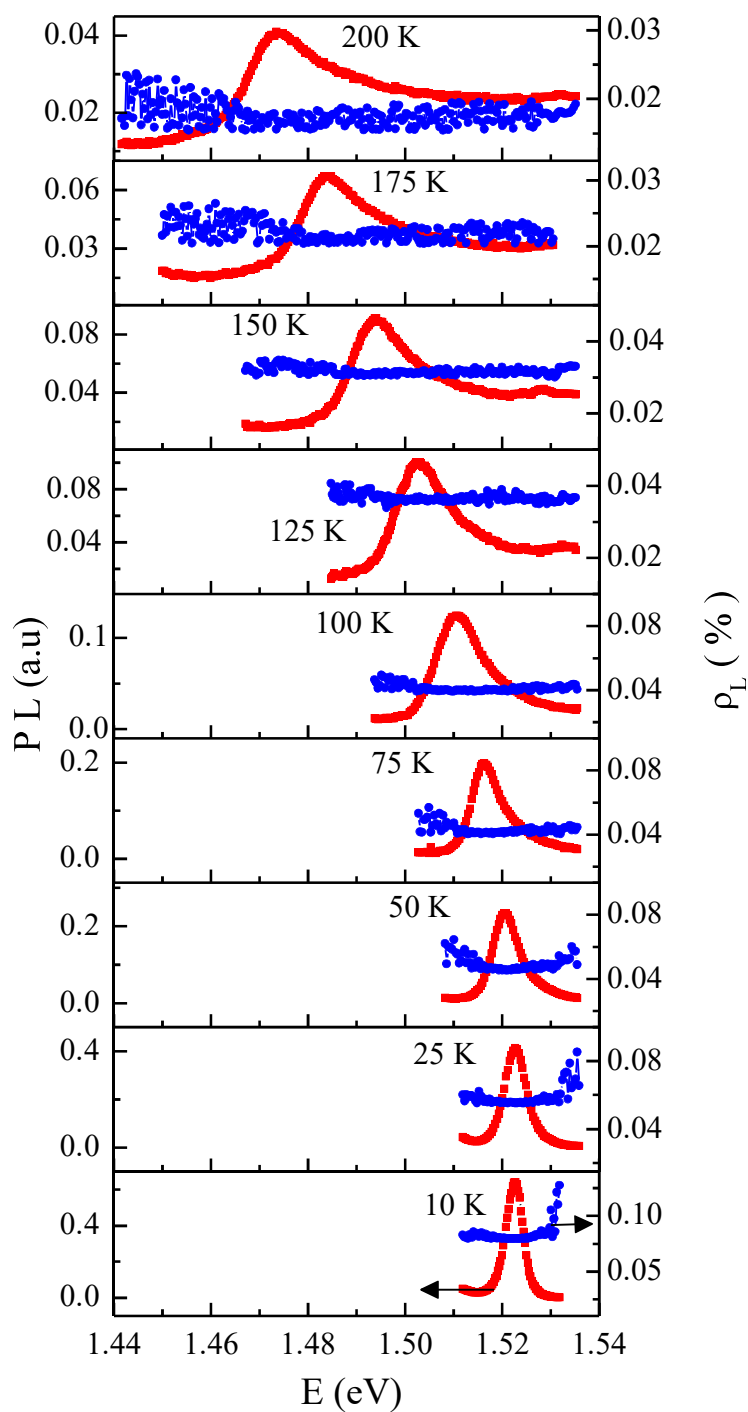


Figure 5.16 PL intensity and degree of circular polarization (ρ_L) plotted as function of energy recorded at several temperatures varying from 10 to 200 K

Note that the magnitude of ρ_l is very small which is expected due to the presence of large density of unpolarised electrons that are already present in the n^+ GaAs epitaxial layer. It is verified from the fact that the value of ρ_l increases with incident laser power as shown in figure 5.17 (a), which is in accordance with equation 5.12. On the other hand, the value of ρ_l remains almost constant for p^+ GaAs measured under identical conditions in figure 5.17 (b). In this case, the observed fall in ρ_l at higher power may be because of local heating in the sample.

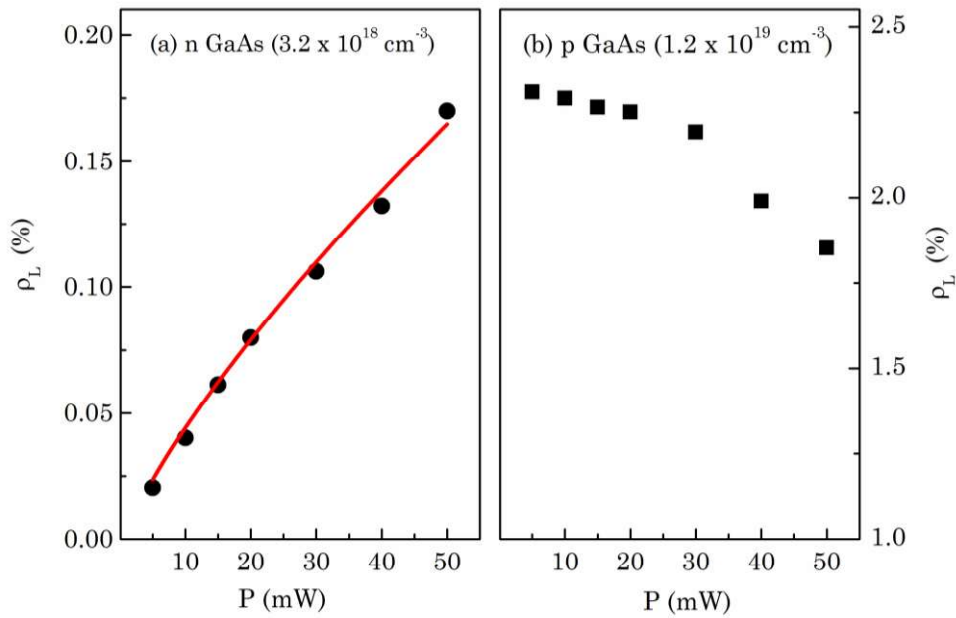


Figure 5.17 Variation of ρ_l with incident power for (a) n^+ GaAs and (b) p^+ GaAs at 10K.

5.7.2 Estimation of spin relaxation time

Keeping in mind the relation of $G=4(1-R)P_L\alpha/(\pi\omega^2E_{ph})$, and knowing the temperature dependent reflectivity from figure 5.12, the parameter G and the

corresponding value of τ_j is estimated. As the temperature increase from 10 to 200 K, τ_j is found to vary from 8.35×10^{-7} s to 8.66×10^{-7} s, because of minor variation in R with temperature. Finally, by incorporating the measured values of ρ_e and ρ_J in equation 5.12, τ_s is estimated to be 2.37 ns at 10 K, which decreases upto 0.5 ns at 200K and is shown in figure 5.18.

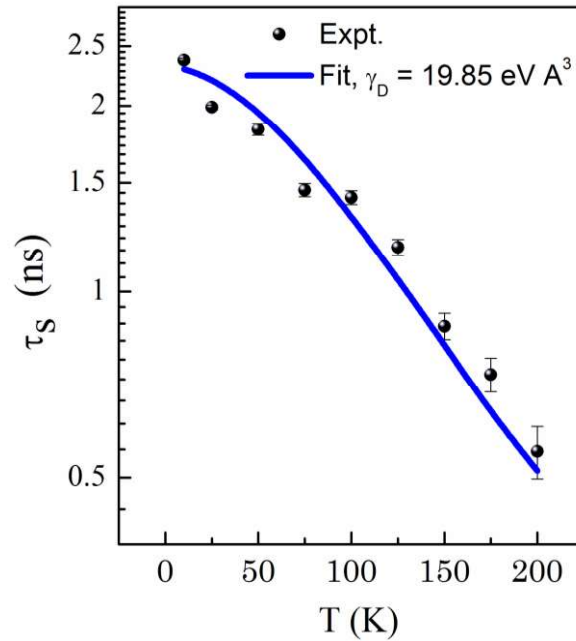


Figure 5.18 Estimated Spin relaxation time (τ_s) versus sample temperature. Corresponding fitting is also shown as solid line.

Next important task is to find out the fundamental mechanism which is responsible for the fall of τ_s with temperature as shown in figure 5.18. In the meantime, it is worthwhile to discuss a few important points that are related to the methodology adopted in this chapter. Here, it is assumed that the electron spin orientation is primarily governed by the band-to-band transitions and two photon

excitations are either subtle or absent. It is a valid approximation in our case since the power density of excitation source is moderate. Further, it is assumed that a significant re-absorption of emitted photon doesn't occur during our experiments. Once again it is a valid approximation in our case since the re-absorption of emitted photon is highly improbable because of Burstein moss shift caused by heavy doping of n+ GaAs epitaxial layer.

As explained in section 1.2.3, there exist several mechanisms which are associated with the spin relaxation of free electrons in III-V semiconductors. It is clear that the Dyakonov–Perel (DP) mechanism is the predominant route for spin relaxation in n-type GaAs epitaxial layers under the present experimental conditions. For bulk semiconductor in the absence of strain, τ_s is defined by the following relation,

$$\frac{1}{\tau_s^{DP}} = \frac{8}{105} (2\gamma_D)^2 \frac{\langle E_e \rangle^3}{\gamma_3} \tau_p \quad (5.12)$$

The value of τ_p can be estimated from the measured Hall mobility (μ) by using appropriate Hall factor (r_H). For ionized impurity scattering, the values of parameters are $r_H=415\pi/512$ and $\gamma_3= 6$, are used [29,30]. Several researchers have estimated the values of γ_D both theoretically [151,152], and experimentally [29,153], which lie in the range of 7.6 to 36 eV Å³. It is clearly evident from the abovementioned equation that the spin-relaxation time depends on the sample temperature via the temperature dependence of $\langle E_e \rangle$, and τ_p . However, since there is

no noticeable change in Hall mobility over the entire temperature range one can conclude that τ_p remains almost temperature invariant. Therefore, the temperature dependence of τ_s mainly arises through the term $\langle E_e^3 \rangle$. In case of degenerate semiconductors, the averaged value of $\langle E_e^3 \rangle$ can be approximated by E_f^3 , where E_f defines the Fermi level. However, note that this particular approximation is only valid only when $E_f/kT \geq 20$ [145, 154]. In view of this, a rather direct method is used to estimate the temperature dependence of $\langle E^3 \rangle$, which can be estimated as,

$$\langle E^3 \rangle = \frac{\int D(E,T)f(E,T)E^3 dE}{\int D(E,T)f(E,T)dE} \quad (5.13)$$

Where, $D(E,T)$ and $f(E,T)$ are the density of states and Fermi distribution respectively. Due to near resonant excitation and subsequent thermalization of optically injected electron-hole pairs, number of holes that participate in the recombination process are expected to lie at the top of the valence band. Note that the holes are the minority carriers in n-type GaAs. Due to this, the high energy tail of PL spectra is associated with the electron energy distribution in the conduction band. Hence, the PL spectrum is fitted with Fermi Dirac distribution in order to estimate the values of electron temperature (T_e) which matches with the lattice temperature. It ensures that there is no significant localized heating in the sample. Therefore, equation 5.13 can be used to estimate the required temperature dependence of $\langle E_e^3 \rangle$. Thereafter, the temperature dependence of τ_s is fitted with

equation 5.12 by using γ_D as a fitting parameter. The fitted value of γ_D comes (19.85 eVA³) closely matches with the values reported by other researchers [155, 156].

5.8 Estimation of the spin Hall conductivity

Once the value of τ_s is known, the spin current density profile $J_s(z)$ can be obtained through equation 5.10. $J_s(z)$ depends on temperature through τ_s and r . From the knowledge of $J_s(z)$ and the measured values of I_{ISHE} , temperature dependent γ is calculated by involving the equation (5.1). For this, $J_s(z)$ is numerically averaged over the sample cross section by discretizing it into N (= 200) layers of uniform thickness ($dz = 20$ nm). The averaged value of $J_s(z)$, *i.e.* $\langle J_s \rangle$ is further used in subsequent calculations. The footprint of light beam is circular in nature with diameter w of ~ 200 μm . Under this condition, the voltage developed across the two edges is given by

$$V_{ISHE} = \frac{\omega\gamma}{\sigma_c} \left(\langle \vec{J}_s \rangle \times \hat{\sigma} \right)$$

and corresponding current is given by the following relation,

$$I_{ISHE} = \frac{\omega\gamma}{\Re\sigma_c} \left(\langle \vec{J}_s \rangle \times \hat{\sigma} \right) \quad (5.14)$$

From the temperature dependence of σ_c , $J_s(z)$ and I_{ISHE} , γ is estimated. By multiplying it with the measured value of σ_c the value of σ_{SH} is obtained. Since the σ_c remains constant over the entire temperature range, only the values of σ_{SH} is plotted in figure 5.19 and it is understood that the variation of γ with temperature

is expected to be identical. The estimated values of σ_{SH} vary from $4.17 \Omega^{-1}\text{cm}^{-1}$ at 10 K to $12.3 \Omega^{-1}\text{cm}^{-1}$ at 200 K corresponding to the variation of γ from 0.006 to 0.017.

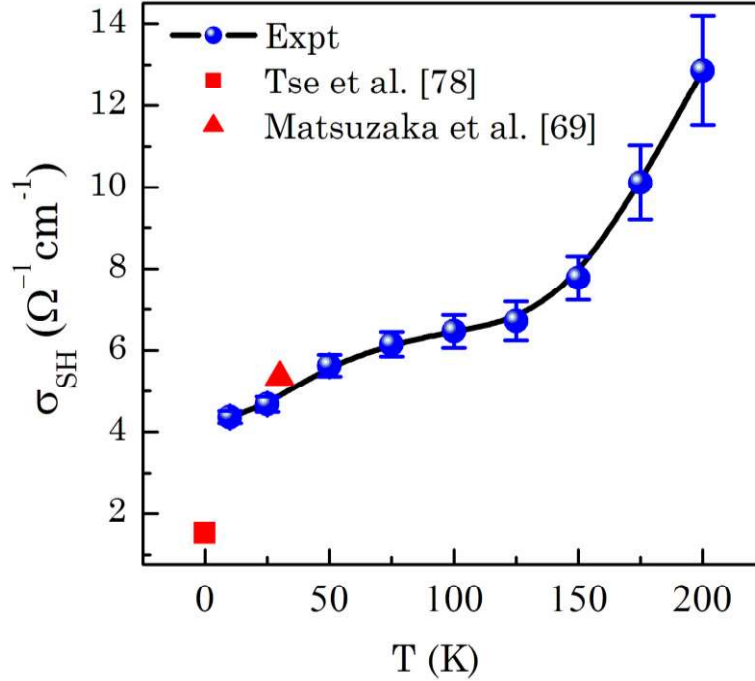


Figure 5.19 Variation of σ_{SH} with sample temperature. Circles (\bullet) show the measured values while Square (\blacksquare) represents the numerically calculated value [78]. One the other hand, triangle (\blacktriangle) represents the extrapolated value of σ_{SH} following Matsuzaka et al. [69]

At first instance, it is surprising since the measured value of I_{ISHE} decreases with temperature. However, it should be noted that the magnitude of I_{ISHE} also depends on τ_S , through the spin current density which decreases rapidly with temperature. Therefore, it is the combined temperature dependence of σ_{SH} and τ_S which causes I_{ISHE} to fall with the sample temperature. Here, it is understood that

σ_{SH} will have the unit of $\Omega^{-1}\text{cm}^{-1}$ ($\hbar/2e$), however, for brevity and to be consistent with existing literature, the factor ($\hbar/2e$) is generally omitted.

The temperature dependence of σ_{SH} (or γ) for heavily doped GaAs is not yet measured through any technique. However, Ehlert et al. [76] measured σ_{SH} for GaAs ($n = 2 \times 10^{16} \text{ cm}^{-3}$) in the temperature range of 5 to 75 K by fabricating a ferromagnetic Esaki diode structures. They reported very small values of σ_{SH} as compared to the values reported by us which is due to the difference in the dopant densities. Matsuzaka et al. [69] investigated the density dependence of σ_{SH} in GaAs at 30 K by using Kerr rotation microscopy. According to them, γ increases initially at low doping, and tends to saturate at the dopant density of $\sim 10^{18} \text{ cm}^{-3}$. The extrapolated value of σ_{SH} for $n \sim 3 \times 10^{18} \text{ cm}^{-3}$ is expected to be of the same order as shown in figure 5.19. It is really encouraging to learn that the results of two completely different measurement techniques match reasonably well. On the other hand, Bottegoni et al. [80] found γ to be at least one order less in bulk GaAs. There are some theoretical reports which describe the origin of ISHE and also the values of σ_{SH} have been quantitatively estimated by a few researchers [77-79,157-161]. Such studies reveal the dependence of σ_{SH} on various material parameters like carrier concentration, conductivity, strain, roughness, spin orbit coupling parameters etc. Since here homo-epitaxial GaAs sample is considered, no strain is expected. Furthermore, the transport of spin polarized electrons only along z a direction (normal to the sample surface) is considered, therefore, the sample

roughness issues can be easily neglected. Tse and Sarma [78] have proposed a theoretical model based on analytical solutions for both the side jump and skew scattering mechanisms in terms of Fermi energy and conductivity as given below,

$$\sigma_{SH}^{SJ} = \left(\frac{e^2 \lambda_0^2}{4\hbar} \right) n \quad \text{and}$$

$$\sigma_{SH}^{SS} = \left(\frac{-\pi m^* \lambda_0^2 \varepsilon_F}{3\hbar^2} \right) \sigma_c \quad (5.15)$$

Here λ_0 is the spin orbit coupling parameter given by [153],

$$\lambda_0 = \frac{P^2}{3} \left[\frac{1}{E_g} - \frac{1}{(E_g + \Delta_0)^2} \right]$$

P^2 is the square of inter band matrix element and Δ_0 is the split off gap. Considering $P^2 = 10.493 \text{ eV } \text{\AA}$, $E_g = 1.514 \text{ eV}$ and $\Delta_0 = 0.34 \text{ eV}$, $\lambda_0^2 = 5.09 \text{ \AA}^2$ can be estimated [16].

From equation 5.14, the total spin Hall conductivity turns out to be

$$\sigma_{SH} = \sigma_{SH}^{SS} + \sigma_{SH}^{SJ} = 1.52 \text{ } \Omega^{-1} \text{ cm}^{-1},$$

This corresponds to $\gamma = 0.002$ and the same is also shown in figure 5 at 0 K. Other contributions like the intrinsic term are considered to be negligibly small [157]. As pointed out by Tse and Sarma [78] that the estimated magnitude of spin Hall conductivity is subjected to some inaccuracy since the value of λ_0^2 is not accurately known for GaAs. Nevertheless, the temperature dependence of σ_{SH} particularly the rapid increase after 100 K can be talked about with confidence. Note that the calculations are done at 0K where the temperature dependence of mobility is

considered to predict the temperature dependence of σ_{SH} by including various material parameters like carrier concentration, and Fermi energy etc. [76, 162]. However, both of these parameters are almost constant in the present case, hence it cannot explain the observed temperature dependence of σ_{SH} . Note that only λ_0^2 is weakly dependent on temperature in equation (5.14), and varies from 5.09\AA^2 at 10K to 5.41\AA^2 at 200K [136]. Even hypothetically replacing ε_F with $\langle E_e \rangle$, the mean energy of electron system, cannot explain the magnitude and temperature dependence of measured σ_{SH} . Very recently, Tolle et al. [163] and Gorini et al. [158] have estimated the effect of lattice vibrations on the spin Hall conductivity of metallic films. They argue that simple extension of $T=0$ results to $T \neq 0$, will lead to erroneous result as the effect of electron-phonon interaction and interaction with dynamical impurities is not included. It seems highly reasonable here since the electron-phonon interaction in GaAs increases rapidly after 100K. It appears from the temperature dependence of σ_{SH} that several effects related to the lattice vibrations need to be taken into account for estimating the spin Hall conductivity in semiconductors at finite temperature. However, in the absence of analytical solution for similar interactions in compound semiconductors, the same cannot be included here.

5.9 Outcome of the chapter

In this chapter, photo-induced inverse spin Hall current (I_{ISHE}) is measured for MOVPE grown n type GaAs epitaxial layer by shining circularly polarized light at

an oblique incidence. By carefully minimizing all the spurious signals, reliable value of I_{ISHE} is measured in the temperature range of 10 to 200 K. A method is worked out to estimate the equilibrium value of spin Hall conductivity, which also requires the solution of diffusion equation by considering thin film boundary conditions and measurement of spin relaxation time to estimate the spin current density. By analyzing the degree of circular polarization of the PL, the spin relaxation time of the sample is estimated to be 2.37 ns at 10 K, which decreases monotonically to 0.55 ns at 200K. Putting this value in the diffusion equation, the spin current density is estimated. Comparing it with the measured I_{ISHE} , the spin Hall conductivity is estimated. This estimated spin Hall conductivity increases with temperature varying from $4.17 \Omega^{-1}\text{cm}^{-1}$ at 10 K to $12.3 \Omega^{-1}\text{cm}^{-1}$ at 200 K. The temperature dependence of spin Hall conductivity appears to be originated from the extrinsic mechanism. It is also noted that neither the absolute value nor the temperature dependence of spin Hall conductivity matches with the theoretical predictions. It is proposed that the contribution of phonons should be included while estimating the value of spin Hall conductivity whenever measurements are performed at a given temperature. The proposed method for the estimation of σ_{SH} can be applied for any semiconductor having a reasonable magnitude of spin orbit coupling. Further, the analysis presented here should be helpful in igniting thoughts for further research.

Chapter 6

ISHE measurements in quantum wells

6.1 Introduction

After performing the ISHE measurements in bulk semiconductors, the natural extension is to explore the quantum well based semiconductor hetero-structures. However, the concept of spin orbit coupling, spin relaxation and spin Hall Effect are significantly different in quantum well when compared with their bulk counterparts. The reduced symmetry in quantum wells also offer a possibility of competition between the two spin orbit field, namely Dresselhaus (Ω_{BIA}) and Rashba field (Ω_{SIA}) which are defined below (Appendix: A)

$$\Omega_{BIA}(k) = 2\gamma_D [k_x(k_y^2 - k_z^2), k_y(k_z^2 - k_x^2), k_z(k_x^2 - k_y^2)]$$

$$\Omega_{SIA}(k) = 2\beta [(k_y E_z - k_z E_y), (k_z E_x - k_x E_z), (k_x E_y - k_y E_x)]$$

The dependence of these two fields on crystallographic directions and the fact that $\Omega_{SIA}(k)$ depends on total electric field in the system, generates possibilities of manipulating the total spin orbit field either by engineering the quantum well

structure or by external electric field[1-3]. Because of the two spin orbit fields, the spin relaxation time depends critically on the exact structure of quantum wells including the quantum well width, strain and asymmetry, if any [4,5]. From the ISHE measurement point of view, there are a few fundamental differences between the bulk and quantum wells systems and those are described below,

- (i) During the PL measurements, a major fraction of the circularly polarized light is absorbed within the barrier layer leading to the generation of spin polarized electron-hole pairs. As mentioned earlier that the holes are expected to forget their spin polarization pretty soon and it is only the spin polarized electrons which are to be transported to the quantum well layer either by diffusion or drift. Due to the presence of defects at the barrier-well interface, spin relaxation occurs at the interface, which reduces the electron spin polarization in the quantum well [6].It has also been shown that the dissimilar spin orbit coupling at the two sides of the interface also affects the spin relaxation process.
- (ii) As explained in chapter 5, spin current can be generated along growth direction (z), because of the gradient of spin polarized carrier density. The flow of these spin polarized carriers produces I_{ISHE} depending upon the spin Hall conductivity of the bulk material. However, to characterize the quantum well, the spin polarized carriers need to flow in the plane of quantum well (x and y), as shown in figure 6.1. However, the gradient in these directions is generally much smaller than that in z direction. Hence the diffusion current density is small

resulting in very small value of I_{ISHE} . Therefore, bias is generally applied along the plane of quantum well to induce a spin current density (J_s) given by

$$J_s = J_c \rho_e \quad (6.1)$$

Here, J_c is the charge current density and ρ_e is the electron spin polarization in the quantum well. I_{ISHE} is then measured along the other in-plane direction transverse to the applied bias.

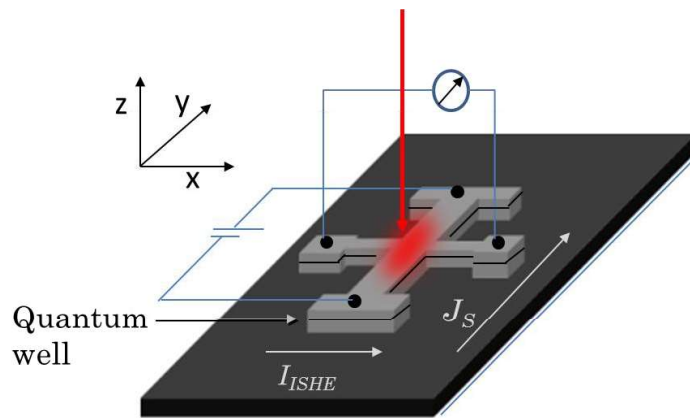


Figure 6.1 Schematic showing ISHE measurement in quantum well sample

(iii) As explained in chapter 1 and 5, in bulk semiconductors, ρ_e is conveniently estimated from the measured ρ_l by using the relation $\rho_e = (2 \rho_l)$. However, this correlation becomes tricky in quantum wells, particularly when strain is involved.

To address these issues, a simple model is developed based on band mixing with in the Luttinger-Kohn approach that helps to correlate the ρ_e and ρ_l in a strained quantum well. Thereafter, this method is used to estimate the spin loss

across the quantum well interface by measuring ρ_l both in the barrier and quantum well. After knowing the magnitude of ρ_e in the quantum well, equation 6.1 is used to estimate the spin Hall conductivity in the quantum well.

6.2 Quantification of electron spin polarization

As is clear from section 1.2.2, because of the degeneracy of hh and lh levels in bulk unstrained semiconductors at $k=0$, ρ_l and ρ_e are related by the relation $\rho_l = 0.5\rho_e$. However, if this degeneracy is lifted by either strain or quantum confinement, ρ_l can be significantly different from $0.5\rho_e$ and might approach a limiting case where $\rho_l = \rho_e$. Therefore, researchers have either used a bulk spin LED by neglecting the hh - lh splitting or thin quantum wells, where the hh - lh splitting is large enough to ignore the coupling between them [7-8]. Though practically important, the intermediate regime is seldom exclusively discussed. In this regime, the valence bands cease to be angular momentum Eigen states which alters the selection rules. For a general case, ρ_l can be written as $\xi\rho_e$, where ξ depends on the energy splitting between of hh and lh levels. The parameter ξ therefore governs the extent of band mixing in QW systems. Therefore, a model needs to be formulated for estimating the magnitude of ξ in an unambiguous manner.

6.2.1 k.p modeling to estimate the electron spin polarization

Generally, as explained in chapter 1, in experiments correlating ρ_l and ρ_e , different bands i.e. hh , lh and the conduction band are denoted by $|3/2, \pm 3/2\rangle$ and $|3/2,$

$\pm 1/2\rangle$, respectively, considering their zone center ($k=0$) nature. Under this condition, ξ is equal and opposite for $e-hh$ and $e-lh$, i.e. $\xi_{hh}=+1$ and $\xi_{lh}=-1$. However, for an arbitrary k , the states are not angular momentum Eigen states and are expressed as a linear combination of all the basis states, given by the Luttinger-Kohn (LK) Hamiltonian [9]. The dimension of such Hamiltonian is decided by the number of interacting bands considered. Since in an experiment like PL, only the states close to Γ point are probed, the states are generally expressed as 4 x 4 Hamiltonian [10]. This means the conduction band is a pure Eigen state of angular momentum operator and is written as $|1/2, \pm 1/2\rangle$, whereas hh and lh valence bands are expressed as admixtures of $|3/2, \pm 3/2\rangle$ and $|3/2, \pm 1/2\rangle$ states.

To be consistent with general experimental set up, the electron spin polarization direction can be considered as the z-axis, which coincides with the sample growth direction. Under this condition, the 4 x 4 Hamiltonian including the Bir-Pikus strain terms is given by [11]

$$H = H_{k,p} + H_{strain} = \begin{pmatrix} P + Q & -S & R & 0 \\ -S^+ & P - Q & 0 & R \\ R^+ & 0 & P - Q & S \\ 0 & R^+ & S^+ & P + Q \end{pmatrix} \quad (6.2)$$

$$\begin{aligned}
\text{Where } P &= \frac{\hbar^2}{2m_0} \gamma_1 k^2 - a_v (\varepsilon_{xx} + \varepsilon_{yy} + \varepsilon_{zz}) \\
Q &= \frac{\hbar^2}{2m_0} \gamma_2 (k_x^2 + k_y^2 - 2k_z^2) - \frac{b}{2} (\varepsilon_{xx} + \varepsilon_{yy} - 2\varepsilon_{zz}) \\
S &= \frac{\hbar^2}{2m_0} 2\sqrt{3} \gamma_3 (k_x - ik_y) k_z - d (\varepsilon_{xz} - i\varepsilon_{yz}) \\
R &= \frac{\hbar^2}{2m_0} \sqrt{3} [-\gamma_2 (k_x^2 - k_y^2) + 2ik_x k_y] + \frac{\sqrt{3}}{2} b (\varepsilon_{xx} - \varepsilon_{yy}) - id\varepsilon_{xy} \\
\varepsilon_{xx}, \varepsilon_{yy} \text{ and } \varepsilon_{zz} &\text{ are the respective strain elements}
\end{aligned}$$

Here a , b and d are the respective deformation potentials. γ_1 , γ_2 and γ_3 are the Luttinger parameters.

By numerically solving the Eigen value equation, the projections of different angular momentum states on the hh and lh valence band states are calculated. For example,

$$\begin{aligned}
\psi_h(k) &= \sum f_{h,m_J}(k) |J, m_J\rangle \\
\psi_l(k) &= \sum f_{l,m_J}(k) |J, m_J\rangle
\end{aligned} \tag{6.3}$$

Here, f_{h,m_J} and f_{l,m_J} are four \vec{k} dependent coupling coefficient, which decide the coupling between different states. However, to correlate with the experiment like PL, they have to be averaged over all the quasi degenerate states. In bulk isotropic semiconductors, it is a surface of a sphere in k space, as shown in figure 6.2 (a). Their contribution can be independently calculated by substituting $k_x = k \sin(\theta) \cos(\varphi)$, $k_y = k \sin(\theta) \sin(\varphi)$ and $k_z = k \cos(\theta)$ in equation (6.2) and repeating the calculations. Thereafter, the averaging is done as

$$\left| \langle f_{h,m_j}(k) \rangle \right|^2 = \frac{1}{4\pi} \int_0^{2\pi} \int_0^\pi |f_{h,m_j}(k)|^2 \sin\theta \, d\theta \, d\phi \quad (6.4)$$

Here, θ and ϕ are the polar and azimuthal angle respectively. For the case of a QW, the situation is a bit different where discrete circular regions, as defined in figure 6.2 (b), are defined as the surfaces of equal energy.

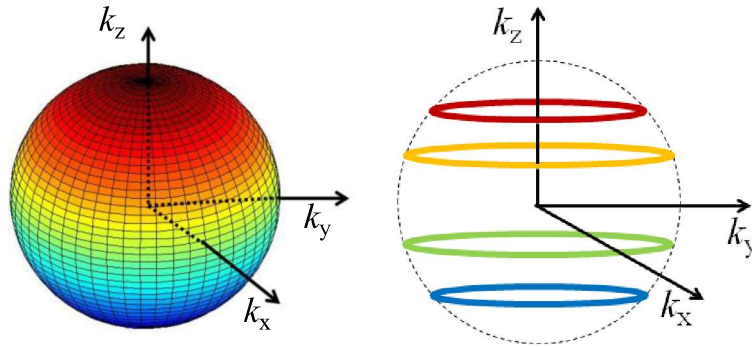


Figure 6.2 Surface of constant energy for (a) bulk, unstrained semiconductor and (b) quantum well

6.2.2 Effect of biaxial Strain

Introduction of strain reduces the symmetry of the crystal and hence alters the projections of angular momentum Eigen states on hh and lh . It is considered by Wang et al. [10] for the technologically important case of biaxial strain along [001], though strain along different directions can be easily taken into account. Under the influence of strain, the hh and lh levels split and thus, $\langle f_{h,m_j}(k) \rangle$ varies from the unstrained case. It is realized that the value of $\langle f_{h,m_j}(k) \rangle$ critically depends on the relative magnitude of Eigen energies of the respective bands and strain induced splitting between hh and lh (ΔE_{lh}) bands, and is thus k -dependent. By solving the

LK Hamiltonian for GaAs and taking average over the quasi degenerate states, $|\langle f_{h,m}(k) \rangle|^2$ and $|\langle f_{l,m}(k) \rangle|^2$ are calculated for known values of ΔE_{lh} and are shown in figure 6.3. The deviation from their unstrained values can be readily marked.

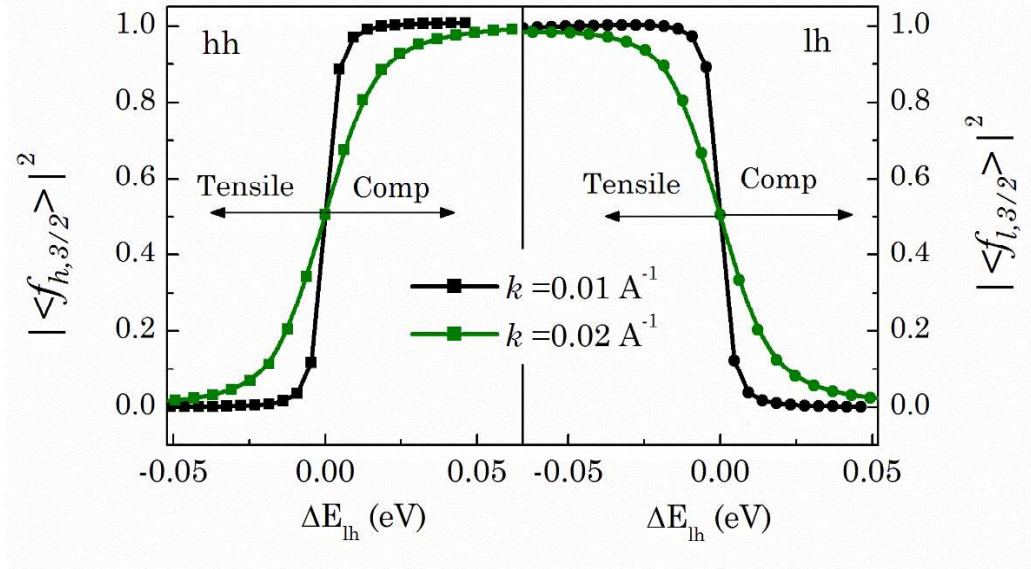


Figure 6.3 Components of the oscillator strength corresponding to $m_j=3/2$ for hh and lh bands as a function of ΔE_{lh} for two different values of k .

This clarifies that under compressive strain, the hh level contains predominantly $|3/2, \pm 3/2\rangle$ character and under tensile strain, it contains predominantly $|3/2, \pm 1/2\rangle$ character. Reverse is true for the lh band. However, the relative magnitude of the components of different angular momentum Eigen states for hh and lh bands depend on the magnitude of k . Though generally in case of PL, k is always considered to be negligible but there are a few mechanisms under which the value of k increase in non-trivial ways. For example, coulomb interaction between excitonic pair, hole trap at the defect states and thermal broadening [12,

13]. Under this condition, realizing that the ratio of transition probabilities to $|3/2, \pm 3/2\rangle$ and $|3/2, \pm 1/2\rangle$ is 3:1 and both transitions results in opposite light polarizations, ξ for hh and lh can be given by

$$\xi_{lh} = \frac{3|\langle f_{l,3/2} \rangle|^2 - |\langle f_{l,1/2} \rangle|^2}{3|\langle f_{l,3/2} \rangle|^2 + |\langle f_{l,1/2} \rangle|^2} = \frac{4|\langle f_{l,3/2} \rangle|^2 - 1}{2|\langle f_{l,3/2} \rangle|^2 - 1} \quad (6.5)$$

Thus, the values of $\bar{\xi}_{hh}$ and $\bar{\xi}_{lh}$ are also dependent on ΔE_{lh} and k and assigning constant values to these parameters lead to erroneous results.

6.2.3 Effect of quantum confinement

When there is quantum confinement, few points need special attention.

(i) The electrons and holes even in the lowest confined energy state have a finite out-of-plane momentum ($\pm k_z$), which is decided by the quantum well width (L_w), strain in the quantum well (ϵ) and exact potential profile.

(ii) Since k_z is now quantized, Eq. (6.4) cannot be averaged over all direction of θ , though the limits of φ are still applicable. This quantized value of θ are jointly decided by the in plane momentum $k_{||}$ ($=\sqrt{(k_x^2+k_y^2)}$) and k_z . They are shown in figure 6.2 (b) for the case of a QW.

It can be seen that the Luttinger-Kohn Hamiltonian, expressed in equation 6.2 is diagonal for $k_{||}=0$, in the absence of strain. This means the entire cross terms representing the coupling between bands vanish and the states can be expressed as

angular momentum Eigen states. In practice, k_{\parallel} is never zero, however, this condition is approached if $k_{\parallel} \ll k_z$, which is satisfied for narrow quantum well at low temperature. For a general quantum well, exact values of k_{\parallel} and k_z have to be taken into account.

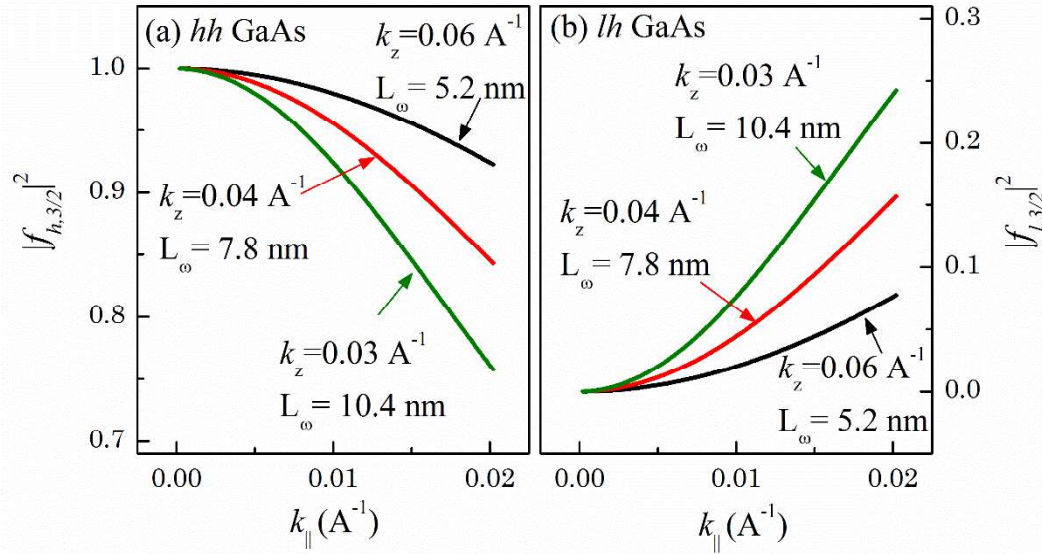


Figure 6.4 The projection of $|3/2, 3/2\rangle$ angular momentum state on (a) *hh* and (b) *lh* bands of quantum well of width L_w (corresponding to $k_z = \pi/L_w$) is plotted against in plane momentum (k_{\parallel})

Figure 6.4 depicts $|\langle f_{h,3/2}(k) \rangle|^2$ and $|\langle f_{l,3/2}(k) \rangle|^2$ for an unstrained GaAs quantum well as a function of k_{\parallel} for different values of k_z . The growth direction is assumed to be along (001). On a first approximation, ignoring the leakage of hole wave function to the barrier, k_z can be approximated as (π/L_w) . The corresponding values of L_w is also mentioned in the same graphs. As is expected, for $k_{\parallel} \rightarrow 0$, the *hh* and *lh* states become Eigen states of $|3/2, \pm 3/2\rangle$ and $|3/2, \pm 1/2\rangle$ respectively. The coupling increases with increase in k_{\parallel} . However, in this case, the components of *hh* and *lh* are not as significantly affected as in the case of bulk semiconductors. It is

because of the fact that the momenta of electrons and holes are largely decided by the quantum confinement, which decouples the hh and lh states up to significant extent. This is the primary reason why the particular effect is mostly overlooked. Taking the reduced mass of excitons in GaAs for example, even at 10K, the thermal contribution to $k_{||}$ alone is around 0.003 \AA^{-1} . Therefore, in realistic quantum wells, the hh and lh are not angular momentum Eigen states. This makes the estimation of ξ even more complicated.

6.2.4 Combined effect of strain and quantum confinement

The inclusion of strain in the quantum well either increases or decreases the splitting between hh and lh depending on whether it is compressive or tensile strain. Therefore, the value of $|\langle f_{h,3/2}(k) \rangle|^2$ and $|\langle f_{l,3/2}(k) \rangle|^2$ changes depending the strain in the quantum well. The cases of tensile and compressive strained quantum wells are shown separately in figure 6.5. It can be seen that, coupling between hh and lh is larger in tensile strained quantum well as compared to equivalent compressive strained case because of the proximity of hh and lh in case of the former.

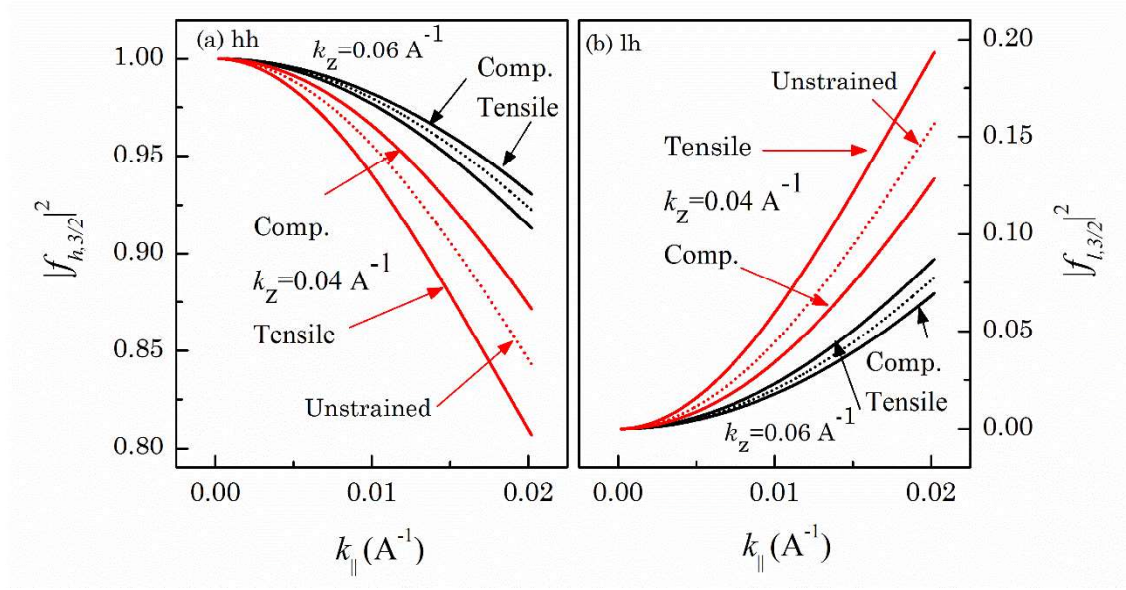


Figure 6.5 The projection of $|3/2, 3/2\rangle$ angular momentum state on (a) hh and (b) lh levels of GaAs quantum well of width L_w (corresponding to $k_z = \pi/L_w$) and biaxial strain ($\epsilon=0.2\%$). The cases of tensile and compressive strain are compared with the unstrained case, which is shown as dotted line.

6.2.5 Effect of the split off band

As explained in the previous section, 4 band Hamiltonian is usually considered for estimating the spin polarization where the effect of split off band is ignored. It can be justified from figure 6.6, where the inclusion of split off band is highlighted. For GaAs, almost no effect can be seen in ζ_{hh} even after considering a high k value of 0.06 \AA^{-1} . On the other hand in case of InP, where the split off gap is lower (0.108 eV), slight variation is obtained. It can also be seen from the plotted band diagram ($E-k$ diagram) of GaAs and InP. The deviation between the two approach starts at much larger k , which is generally not accessible in PL. Therefore, unless the split off

gap is very low, considering the 4 band approach is quite reasonable for analyzing the PL polarization.

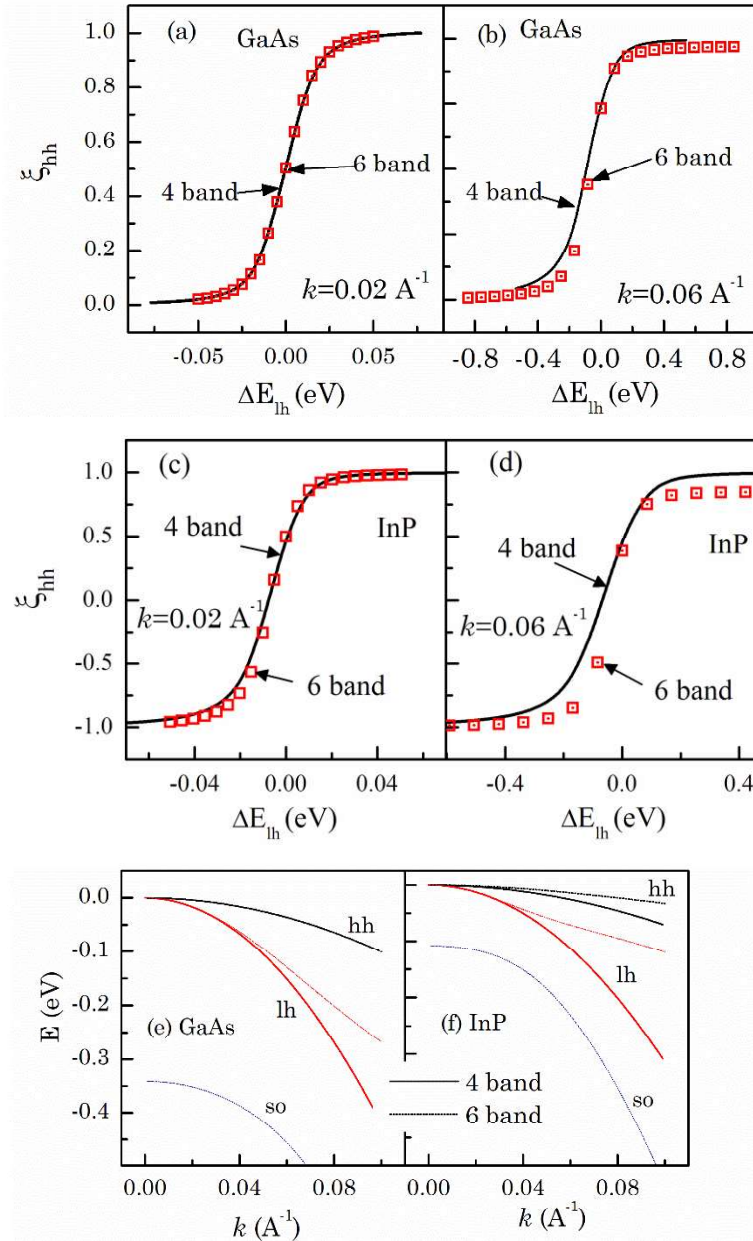


Figure 6.6 A comparison of 4 band and 6 band calculation to show the effect of split off band on ζ_{hh} . (a) and (b) show the differences for GaAs for $k = 0.02 \text{ \AA}^{-1}$ and 0.04 \AA^{-1} respectively. (c) and (d) show the differences for InP for $k = 0.02 \text{ \AA}^{-1}$ and 0.04 \AA^{-1} respectively. (e) and (f) show the difference in E - k diagram in GaAs and InP

These calculations can be associated with the realistic quantum wells, where the quantum well thickness decides the value of k_z . On the other hand, k_{\parallel} can be correlated to the temperature by considering only thermal broadening. Since the magnitude of $f_{h,3/2}$ depends both on k_z and k_{\parallel} , it is not always possible to uniquely estimate ρ_e from a single measurement. It is rather estimated through a systematic modelling where a correlation between ρ_l and ρ_e for a quantum well can be obtained.

6.3 Measurement of electron polarization in QW

As can be seen, the relation between ρ_l and ρ_e are different for strained and unstrained quantum wells. Accordingly, different quantum wells are chosen for the measurements. These are listed in table 6.1 along with the width of quantum well and the strain. More detail about the structure and growth are given in table 3.1. The experiment was conducted as explained in section 3.6. The only difference made is that the normal incidence is ensured and PL is collected in the back scattering geometry, as shown in figure 6.7. This is done to minimize the angular dependence of polarization of light emitted from hh and lh transitions. I_{++} and I_{+-} are independently measured by using a mechanical chopper and PEM respectively. As the optical excitation occur inside the barrier layer, suitable laser is chosen to excite spin polarized electron-hole pairs. These are also listed in table 6.1. The excitation power is fixed at 3.5 mW.

Table 6.1 Details of the quantum well sample and the estimated parameters

Sample No.	Quantum Well/ Barrier	L_w (Å)	ε (%)	ΔE_{lh} (meV)	E_{ph} (eV)	k_z (\AA^{-1})	ρ_l (%)	$f_{h,3/2}$	ξ	ρ_e (%)
S6	GaAs/ $\text{Al}_{0.37}\text{Ga}_{0.63}\text{As}$	45.2	0	14.2	2.32	0.041	2.1	0.994	0.995	2.11
S7	$\text{GaAs}_{0.89}\text{P}_{0.11}$ / $\text{Al}_{0.33}\text{Ga}_{0.67}\text{As}$	87.2	- 0.2	7.1	1.94	0.033	-0.7	0.981	-0.987	0.71
S8	$\text{In}_{0.07}\text{Ga}_{0.93}\text{As}$ / GaAs	91.0	+ 0.4	21.2	1.54	0.024	1.6	0.986	0.990	1.61

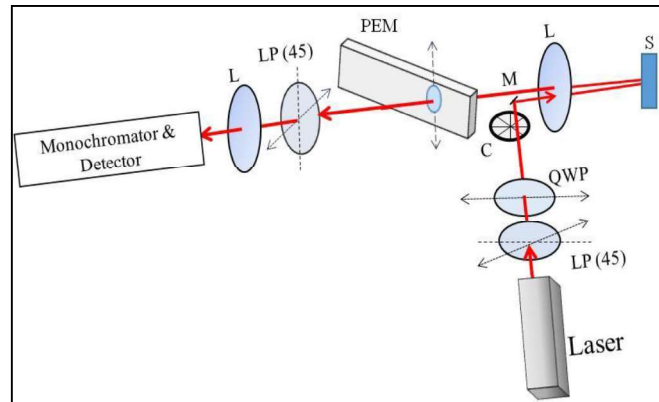


Figure 6.7 Experimental set up to measure degree of circular polarization of PL. Here LP, QWP, C, M, L, S and PEM denote the linear polarizer, quarter wave plate, Chopper, mirror, Lens, Sample and Photo-elastic modulator respectively

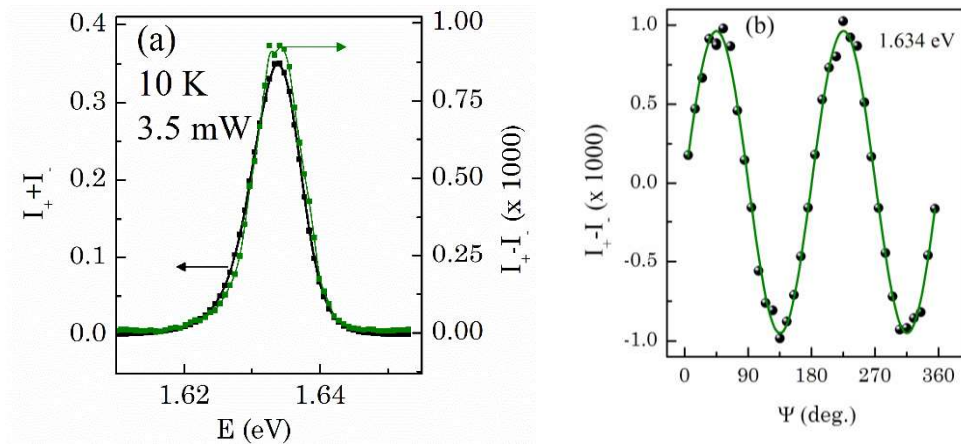


Figure 6.8 (a) $I_+ + I_-$ and $I_+ - I_-$ for GaAs/AlGaAs quantum well (b) $I_+ - I_-$ plotted against the relative angle between quarter wave plate and linear polarizer.

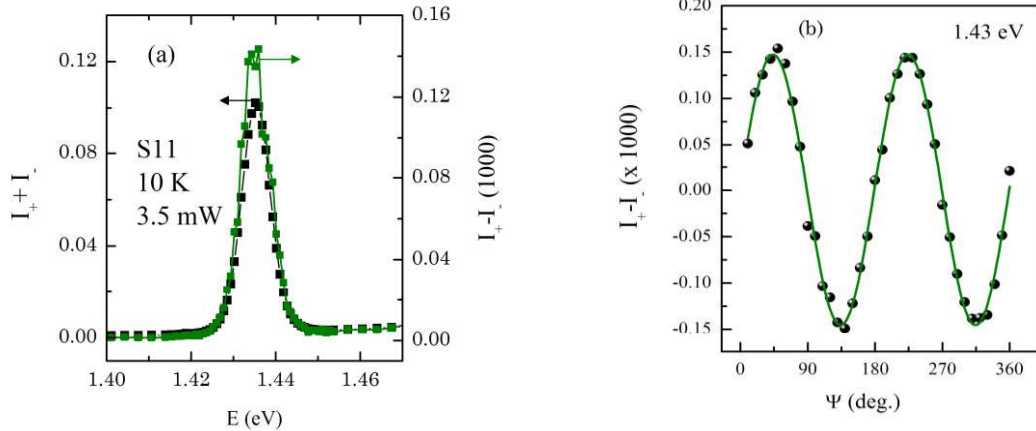


Figure 6.9 (a) I_{++} and I_{+-} for InGaAs/GaAs quantum well (b) I_{+-} plotted against the relative angle between quarter wave plate and linear polarizer

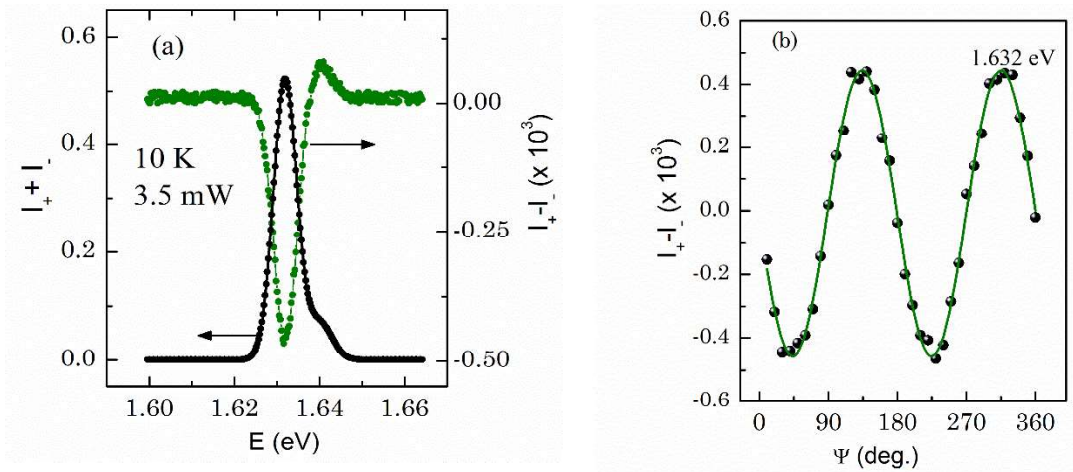


Figure 6.10 (a) I_{++} and I_{+-} for GaAsP/AlGaAs quantum well (b) I_{+-} plotted against the relative angle between quarter wave plate and linear polarizer

Figure 6.8 (a), figure 6.9 (a) and figure 6.10 (a) show the measured I_{++} and I_{+-} for the three quantum wells. For each of them, the magnitude of the I_{+-} at peak energy is plotted as a function of relative angle between quarter wave plate and linear polarizer in figure 6.8 (b), figure 6.9 (b) and figure 6.10 (b). The negative ρ_l in case of GaAsP/AlGaAs quantum well is because of the fact that, in this case,

the ground state is the lh state. A small peak at higher energy corresponding to hh level is also seen, which has positive ρ_l .

To estimate electron spin polarization the following procedure is adopted.

- (i) First, ρ_l is estimated from the measured $I_{+-}I$ as explained in section 3.6.
- (ii) To work out a relation between ρ_l and ρ_e , the values of k_z and $k_{||}$ are needed. For a given quantum well k_z is numerically calculated [14]. Initially $k_z = \pi/L_w$, L_w being the quantum well width, is assumed. From the known strain in the quantum well and assumed k_z , the effective mass of electrons in the quantum well is estimated by using the LK Hamiltonian. This is used to solve the one dimensional Schrodinger equation, under the envelope-function approximation, with a finite height potential. From the fitting of sinusoidal envelope function in the quantum well, the effective k_z is re-estimated. If the bands are highly non-parabolic in nature, this will require several iteration. Otherwise, single fitting gives fairly accurate value of k_z . These values are also mentioned in table 6.1. From the known temperature (T), average value of $k_{||}$ is estimated as $\sqrt{(2m^*kT)/\hbar}$.
- (iii) Using k_z and $k_{||}$, $|\langle f_{h,3/2} \rangle|^2$ is estimated as shown in figure 6.5 and corresponding ξ is estimated by using equation 6.5.
- (iv) ρ_e is estimated from ρ_l as, $\rho_e = \rho_l / \xi$.

The estimated values of ρ_e are mentioned in table 6.1. Though the incident power is kept same for all the three cases, ρ_e is observed to be much higher for GaAs/AlGaAs quantum well than the other two. This may be because of the

superior interface between the lattice matched GaAs and AlGaAs, which leads to efficient spin transfer from barrier to quantum well.

In these particular cases, because of large ΔE_{lh} as compared to the thermal energy ($T= 10\text{K}$), ξ is almost ± 1 and therefore, ρ_e is almost equal to ρ_l . However, this method of correlating the k.p calculations with the polarization analysis of PL can be used for a general quantum well, provided higher order hh and lh levels are far from their respective ground states. It should be noted that researchers have used theoretical calculations based on tight binding method [15], Variational method [16], atomistic method [17] or multi-band k.p methods [18] are performed for this purpose. However, the present method offers a simple model, which can explain the physical mechanism along with the quantitative estimation of ξ .

6.4 Experimental estimation of electron spin polarization uniquely

6.4.1 Estimation method

As already explained in the previous section, a correlation between the numerical simulations and experimental measurements are required to uniquely estimate the value of ρ_e in a quantum well. Particularly for the case like S7, where the separation between hh and lh levels are not significantly large compared to the thermal energy, no simple relation exist between ρ_l and ρ_e . Since ξ and ρ_e , both are unknown quantities, two independent measurements are needed to estimate the two parameters. Various experimental techniques are used for this purpose. Zhu et

al.[19] analyzed two different edges of electroluminescence peak to estimate the contribution from hh and lh to the light polarization in InGaAs quantum well. This method may be appropriate where the splitting between hh and lh is too large, so that coupling between the two bands is negligible. In principle, measurements at two different collection angles should be sufficient to estimate the two parameters independently. It is based on the idea that the light emitted from $e-hh$ and $e-lh$ transitions have different angular distribution of intensity and polarization [20]. However, measurements at higher angles suffer from the problem of Lambertian [20]. Also, the light emitted at non-normal angle undergoes a change in polarization, because of transmission at the interfaces of the multi-layers [20, 21].

Here we propose that the simultaneous measurement of the ρ_l for both the hh and lh related transitions ($e-hh$ and $e-lh$) along the quantization direction can be used to estimate ξ and ρ_e , which leads to unambiguous estimation of electron spin polarization in a strained quantum well. In a quantum well, the emitted intensity of right (left) circularly polarized light is given by the optical transition matrix between conduction band and hh and lh as

$$I_{\pm} \approx |\langle \Psi_c | p_{\pm} | \Psi_h \rangle|^2 |\langle \Phi_c | \Phi_h \rangle|^2 = \sum |\langle f_{h,m_j} \rangle|^2 |\langle \Psi_c | p_{\pm} | J, m_j \rangle|^2 |\langle \Phi_c | \Phi_h \rangle|^2 \quad (6.6)$$

Here p_{\pm} are the dipole operator for the right (left) circularly polarized light, given as $p_{\pm} = 1/\sqrt{2}(\mp p_x - ip_y)$ and $\Phi_c(\Phi_h)$ is the electron (hh) envelope functions respectively. $|\langle \Psi_c | p_{\pm} | J, m_j \rangle|^2$ is the dipole matrix element for a particular set of bands. When the ground states of the electron and hole in a quantum well are

considered, the overlap integral of envelope function become almost one and the transition matrix element is given by the corresponding dipole matrix element. Under this condition, $\bar{\xi}_{hh}$ and $\bar{\xi}_{lh}$ are given by equation 6.5, using two unknown variables, that are given by $|\langle f_{h,\pm 3/2} \rangle|^2$ and $|\langle f_{l,\pm 3/2} \rangle|^2$. However, since the angular momentum Eigen states constitute a complete set, one more relation is applicable i.e. $|\langle f_{h,\pm 3/2} \rangle|^2 = 1 - |\langle f_{h,\pm 1/2} \rangle|^2$. Therefore, both $\bar{\xi}_{hh}$ and $\bar{\xi}_{lh}$ can be expressed as a function of single variable $|\langle f_{h,\pm 3/2} \rangle|^2$, as in equation 6.7

$$\begin{aligned}\bar{\xi}_{hh} &= \frac{3|\langle f_{h,3/2} \rangle|^2 - |\langle f_{h,1/2} \rangle|^2}{3|\langle f_{h,3/2} \rangle|^2 + |\langle f_{h,1/2} \rangle|^2} = \frac{4|\langle f_{h,3/2} \rangle|^2 - 1}{2|\langle f_{h,3/2} \rangle|^2 + 1} \\ \bar{\xi}_{lh} &= \frac{3|\langle f_{l,3/2} \rangle|^2 - |\langle f_{l,1/2} \rangle|^2}{3|\langle f_{l,3/2} \rangle|^2 + |\langle f_{l,1/2} \rangle|^2} = \frac{3 - 4|\langle f_{h,3/2} \rangle|^2}{3 - 2|\langle f_{h,3/2} \rangle|^2}\end{aligned}\quad (6.7)$$

It is understood that, $\bar{\xi}_{hh}$ and $\bar{\xi}_{lh}$ are not the directly measurable quantities, rather, $\rho_l (= \bar{\xi}\rho_e)$ is experimentally measured. However, since ρ_e is same for both the transitions, the ratio of ρ_l for $e-lh$ and $e-hh$ transitions is equivalent to the ratio between $\bar{\xi}_{lh}$ and $\bar{\xi}_{hh}$.

It is clear from figure 6.4 and figure 6.5 that, $f_{h,\pm 3/2}$ varies from 0.5 for bulk system to 1 for ultrathin quantum wells. For this range, $\bar{\xi}_{hh}$ and $\bar{\xi}_{lh}$ are plotted along with their ratio in figure 6.11. It should be noted that, though the parameter $|\langle f_{h,\pm 3/2} \rangle|^2$ depends on the material system under consideration, figure 6.11 is a result of general equation 6.7 and therefore is independent of the material system.

It can be seen that, for a special case of negligible band mixing i.e. for $|\langle f_{h,\pm 3/2} \rangle|^2 \rightarrow 1$, $\xi_{hh} = 1 = -\xi_{lh}$. It is also noted that, ξ_{hh}/ξ_{lh} varies from -1 to +1 as $|\langle f_{h,\pm 3/2} \rangle|^2$ varies from 1 to 0.5 making it a sensitive probe to measure the band mixing. Therefore, to estimate ρ_e unambiguously, ρ_l is measured for both $e-hh$ and $e-lh$ transitions separately and their ratio is taken, which is equivalent to ξ_{lh}/ξ_{hh} . Then using figure 6.11, corresponding ξ_{hh} and ξ_{lh} are estimated individually. From the known values of ρ_l and ξ for either of the transitions, a unique value of ρ_e is estimated. For example, if the ratio of ρ_l for $e-hh$ and $e-lh$ transitions turns out to be -0.5 in a measurement, as shown by a dotted line in figure 6.11, then the corresponding values of ξ_{lh} and ξ_{hh} are -0.45 and 0.9 respectively (shown by the respective horizontal solid lines).

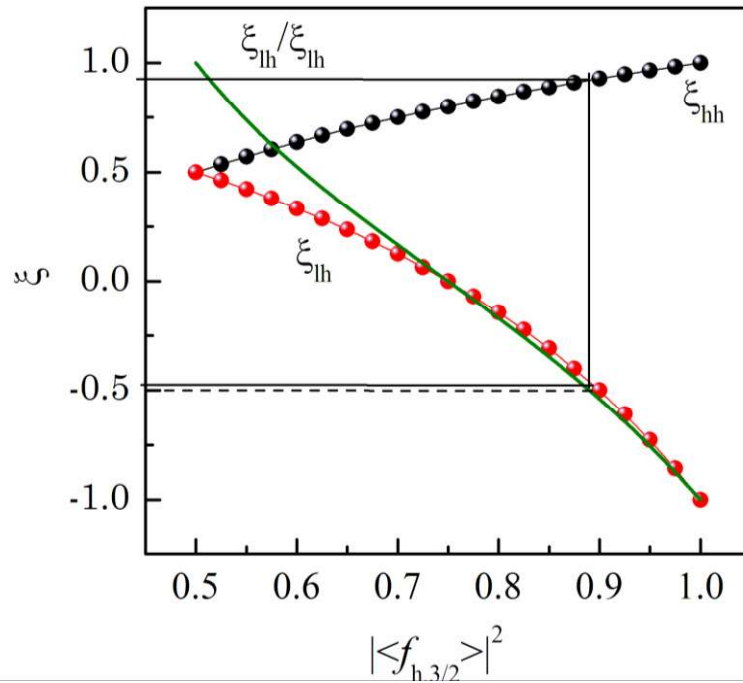


Figure 6.11 ξ_{hh} and ξ_{lh} along with their ratio as a function of $|\langle f_{h,\pm 3/2} \rangle|^2$

6.4.2 Experimental verifications

The above mentioned method requires that separate well defined peaks for $e-hh$ and $e-lh$ transitions are observed in the PL spectrum. Therefore, this method is most suited for the case when the ΔE_{lh} is not too high to depopulate the higher energy level, yet not too close to ensure that the two peaks are merged. For GaAs/AlGaAs quantum wells, ΔE_{lh} can be tuned by varying the quantum well width. However, it is difficult to observe separate lh peak, which is situated at high energy and has lower oscillator strength. For thick GaAs quantum well ($d \sim 15$ nm), opposite ρ_l at the two edges of the peak are observed. However, since the peaks are merged into one, contributions from individual bands are not well defined. This is shown in figure 6.12. Similar result is also observed by Zhu et al.[22]in InGaAs quantum well.

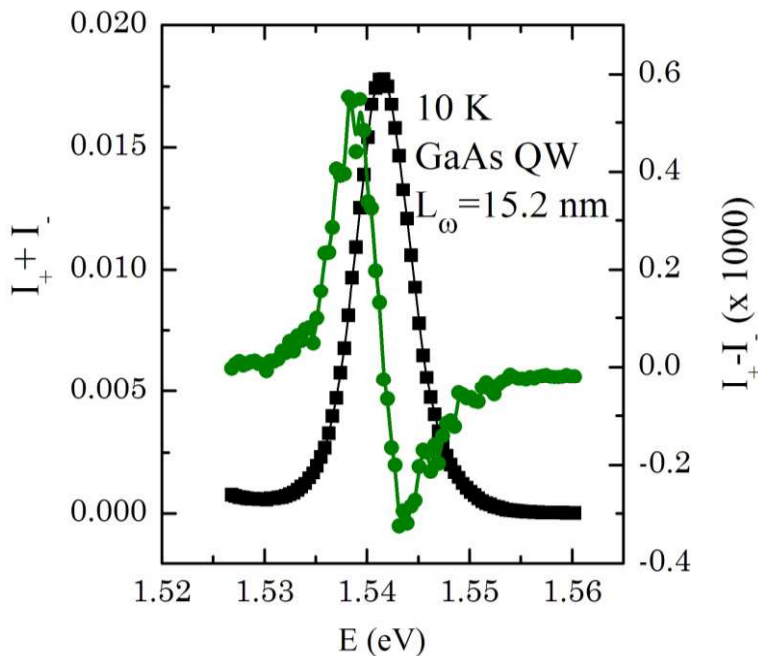


Figure 6.12 I_+ (black squares) and I_- (green circles) for GaAs/AlGaAs quantum well ($L_w=15.2$ nm)

In this regard, the tensile strained quantum well presents a unique case, because the light hole with lower oscillator strength can be the ground state and therefore, two peaks of comparable intensities can be observed. For this purpose, we specifically studied the case of tensile strained GaAs_{0.89}P_{0.11}-Al_{0.35}Ga_{0.65}As quantum well of quantum well width $L_w = 8.7$ nm.

Figure 6.13 shows the Photoluminescence spectra (I_{++} I.) at temperature between 10 K and 150 K, where two well resolved peaks are observed. From the fitting of the I_{++} I. curve, the intensity of both the peaks (I_{lh} and I_{hh}) are separately obtained. The lower and higher energy peaks are attributed to e - lh and e - hh transitions respectively. Sometimes spurious contributions due to the presence of magnetic impurities, circular dichroism in non-magnetic semiconductors, phonon replicas, recombination mediated by various impurity levels and confinement geometry considerably affect the correlation between ρ_l and ρ_e [23,24]. Jonker et al. [25] have analyzed the different components of the electroluminescence in GaAs/AlGaAs LED to get rid of this problem [25]. Therefore, it is necessary to ensure the nature of the peaks observed in the PL spectra.

We have adopted several methods to confirm the assignment of the two peaks, which are explained as follows. By solving simple one dimensional Schrodinger equation, the energy levels are estimated, from which it is seen that the light hole is the lowest valence band in this cases, which is separated from the heavy hole by approximately 7 meV.

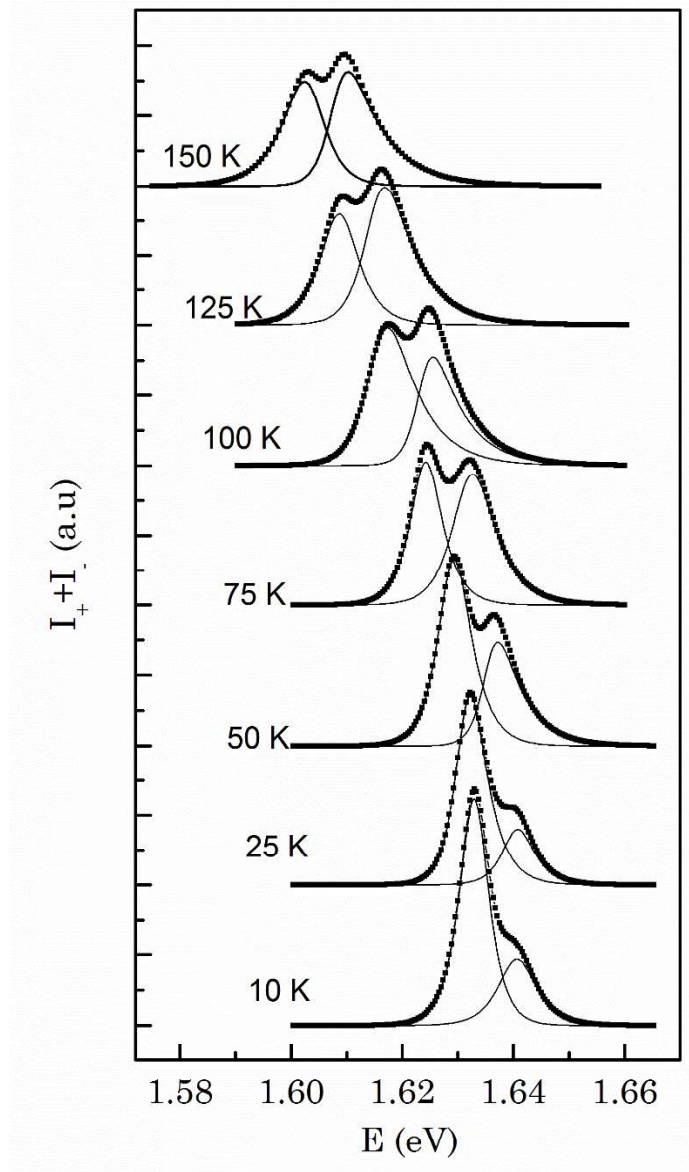


Figure 6.13 PL spectra at different temperatures showing the deconvoluted peaks.

Further, the relative increase in the intensity of higher energy peak with falling temperature, as shown in figure 6.14 (a), is a signature of light hole ground state system [26]. The excitonic nature of the peaks is confirmed by fitting the of incident power (P) dependence of integrated PL intensities (I_{hh} and I_{lh}) with the equation I_{hh} (I_{lh}) $\propto P^{\nu}$, as shown in figure 6.14 (b). For $e-lh$ and $e-hh$ peaks, the

exponent ν turn out to be 1.01 and 1.12 respectively. Furthermore, the disappearance of the higher energy peak at larger quantum well thickness rules out any possibilities of spurious contributions in the PL peaks. This is shown in figure 6.14 (c).

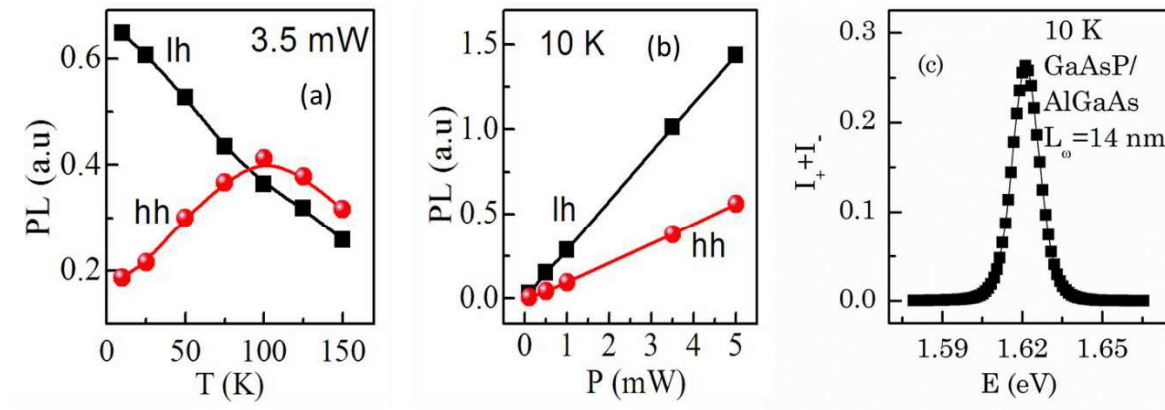


Figure 6.14 Integrated intensity of individual peaks are plotted against (a) sample temperature and (b) Incident intensity. (c) PL peak of thick ($L_w=14$ nm) GaAsP quantum well

To analyze the polarization properties of each peaks, following method is adopted.

- (i) For the case when both $e-hh$ and $e-lh$ transitions are present with in the PL peak, following relation is implied,

$$\begin{aligned}
 I_+ - I_- &= \rho_e \left(\xi_{hh} I_{hh} + \xi_{lh} I_{lh} \right) \\
 \Rightarrow I_+ - I_- &= \xi_{hh} \rho_e \left(I_{hh} + \frac{\xi_{lh}}{\xi_{hh}} I_{lh} \right)
 \end{aligned} \tag{6.8}$$

- (ii) $(I_+ - I_-)$ and individual values of I_{lh} and I_{hh} are experimentally measured. $(I_+ - I_-)$ is further multiplied by the calibration constant, which is nearly 7.5 in our experimental set up, as explained in section 3.6.

- (iii) (I_+-I_-) spectra are numerically fitted to equation 6.8 to obtain two parameters ξ_{lh}/ξ_{hh} and $\xi_{hh}\rho_e$. Note that, individual values of ξ_{hh} , ξ_{lh} and ρ_e cannot be extracted from this fitting.
- (iv) The value of ξ_{lh}/ξ_{hh} is used in figure 6.11 to extract individual values of ξ_{hh} and ξ_{lh} . This also gives unique value of ρ_e because the parameter $\xi_{hh}\rho$ is already known from (iii).

The measured value of I_+-I_- and corresponding fitting for three different temperatures are shown in figure 6.15. In the same plot, the case of $\xi_{lh}/\xi_{hh} = -1$ is also shown. It can be seen that, though at 10K, the measured I_+-I_- fits well with equation 6.8 for $\xi_{lh}/\xi_{hh} = -1$. However, with increasing temperature, the difference between the two increases and the magnitude of fitted parameter ξ_{lh}/ξ_{hh} decreases gradually. It is shown in figure 6.16 (a). This corresponds to decrease in the value of $|\langle f_{h,3/2} \rangle|^2$, as is expected from figure 6.11.

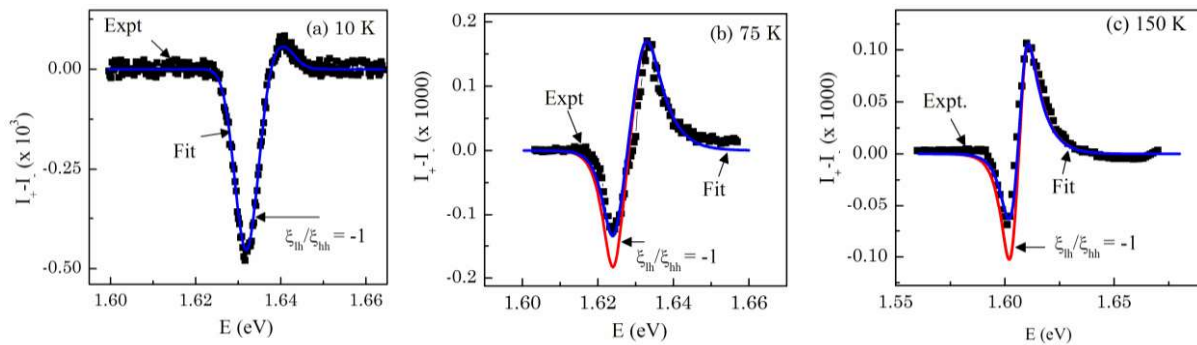


Figure 6.15 Measured I_+-I_- spectra are plotted for three different temperatures (a) 10 K, (b) 75 K and (c) 150 K. They are also fitted by taking ξ_{lh}/ξ_{hh} as a fitting parameter, shown in blue curve. The estimated spectra assuming $\xi_{lh}/\xi_{hh} = -1$ is also shown as red curve.

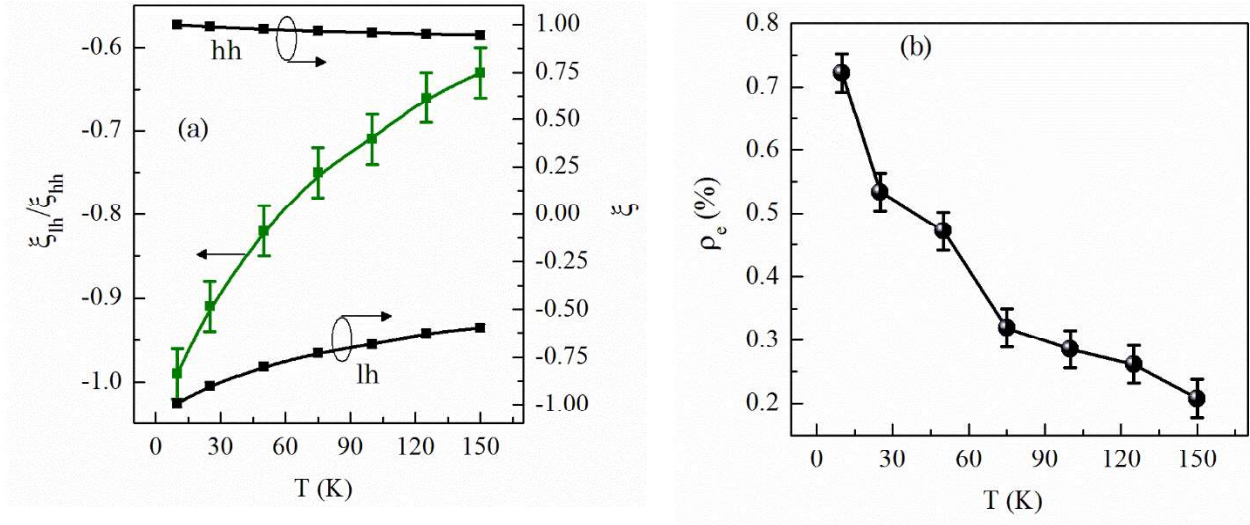


Figure 6.16 (a) Estimated value of ζ_{lh}/ζ_{hh} as a function of temperature. The individual values of ζ_{lh} and ζ_{hh} estimated by comparing it with figure 6.11 are also shown. (b) Estimated values of ρ_e as a function of temperature. The errors in the plotted values of ζ_{lh} and ζ_{hh} are within the dot size.

By correlating the estimated values of ζ_{lh}/ζ_{hh} with figure 6.11, individual values of $\bar{\zeta}_{lh}$ and $\bar{\zeta}_{hh}$ are determined and are also plotted in the same figure. It is observed that the ratio of $\bar{\zeta}_{lh}$ and $\bar{\zeta}_{hh}$ monotonically increases with rise in temperature.

Since the fitting also provides the parameter $\bar{\zeta}_{hh}\rho_e$, and the values of $\bar{\zeta}_{hh}$ are obtained from figure 6.16 (a), ρ_e can be unambiguously estimated and is plotted in figure 6.16 (b). A small value of ρ_e is probably because of the background of unpolarized electrons that already exist in the QW and also due to the spin relaxation of electrons while they cross the interface between the barrier and quantum well. However, irrespective of the spin relaxation and transport process, the present method can be used to measure the electron spin polarization in a

quantum well when the coupling between hh and lh bands is expected to be strong and PL feature corresponding to both the bands are observed experimentally.

6.5 Estimation of Spin injection efficiency from barrier to quantum well

One of the crucial issues in the development of spin optoelectronic devices based on quantum structures is the transmission of spin information through the heterogeneous systems. The loss of spin information across the interface between ferromagnetic metal spin injector and non-magnetic semiconductor has been studied for many years, where one can achieve a maximum of 1-2 % spin transfer [184]. On the other hand, substantially larger injection efficiency is observed in case of all-semiconductor systems because of better conductivity matching and better interfaces [185]. It has been identified that the structural defects such as stacking faults at the semiconductor-semiconductor interface are a major source of spin scattering at low temperatures ($T < 10$ K) [186]. In this analysis, the spin transfer across the injector-semiconductor interfaces are estimated by analysing the degree of circular polarization of light emitted from a LED situated near the interface. Most of the times, the spin transfer across the interface of LED is assumed to be ideal and no spin relaxation is considered. It is because, most of the experiments are conducted at liquid Helium temperature, where the spin relaxation times in the conventional semiconductors are much larger than the transport time of injected electrons from injector-semiconductor interfaces to LED. Puttisong et al. [187] have recently studied the spin injection at room temperature by considering the spin

relaxation during the transport of spin polarized electrons and also during their energy relaxation with in the LED. They have used spin dependent recombination ratio measurement for this purpose. Keeping this in mind, it is planned to estimate the spin loss during transport from barrier to quantum well in a GaAs/AlGaAs quantum well. For this, the degree of circular polarization of the light emitted from both the barrier material and quantum well are separately analyzed. The spin transfer efficiency is given by the ratio between them and can be written as

$$\eta = \frac{\rho_e^{GaAs}}{\rho_e^{AlGaAs}} = \frac{\xi_{AlGaAs} \rho_l^{GaAs}}{\xi_{GaAs} \rho_l^{AlGaAs}} \quad (6.9)$$

As is shown in the previous section, the correlation factor ξ are different for bulk material and quantum wells. In bulk unstrained materials, it is almost always 0.5 ($\xi_{AlGaAs}=0.5$), whereas, in quantum wells, it depends on several factors including the geometry of quantum wells and the sample temperature.

It is important to note that, for this kind of analysis, PL should be observable both from barrier and quantum well. Figure 6.17, shows the PL spectra corresponding to the barrier and quantum well of GaAs/AlGaAs quantum well with 43 Å quantum well thickness. The detail of the growth condition and structures are mentioned in table 3.1. The quantum well PL is observed upto room temperature, the barrier PL is observed only upto 100K. Hence analysis is carried out upto 100 K only. The higher temperature peaks of the barriers are multiplied by suitable constant factors to make it visible.

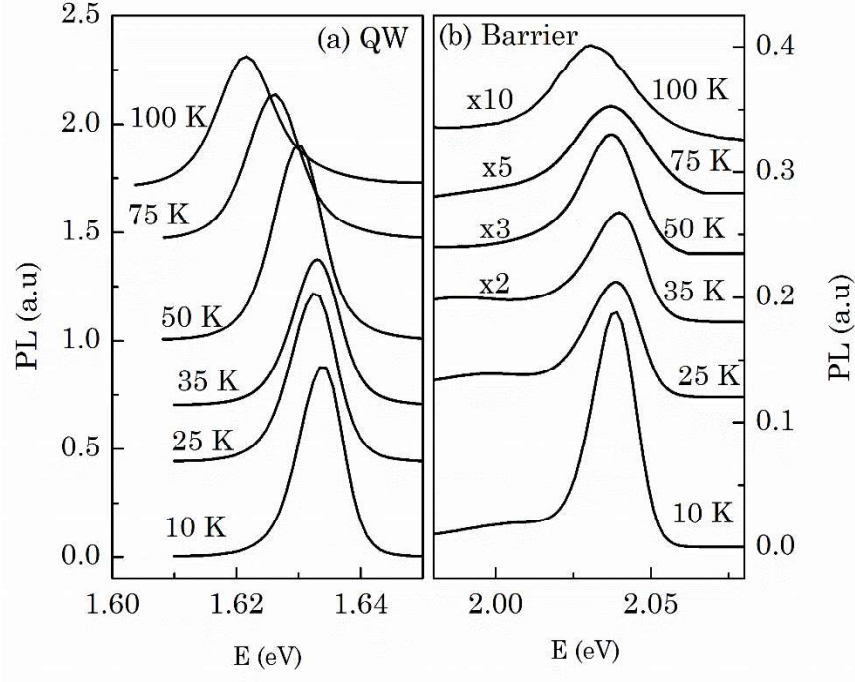


Figure 6.17 Temperature dependence of PL peak corresponding to (a) Quantum well and (b) barrier of a GaAs/AlGaAs quantum well.

By doing the analysis, explained in section 6.3, ρ_l is estimated for both the peaks and are plotted in figure 6.18 (a) as a function of temperature. For the barrier peak, value of ξ is taken 0.5. However, for quantum well, it become temperature dependent and is estimated by applying the method explained in section 6.2. The corresponding values of ρ_e is estimated from the relation $\rho_e = C\rho_l/\xi$. These are plotted in figure 6.18 (b). It can be seen that for both the barrier and quantum wells, ρ_e decrease with rise in temperature. However, it is more rapid in case of quantum well because of added spin relaxation during their transport.

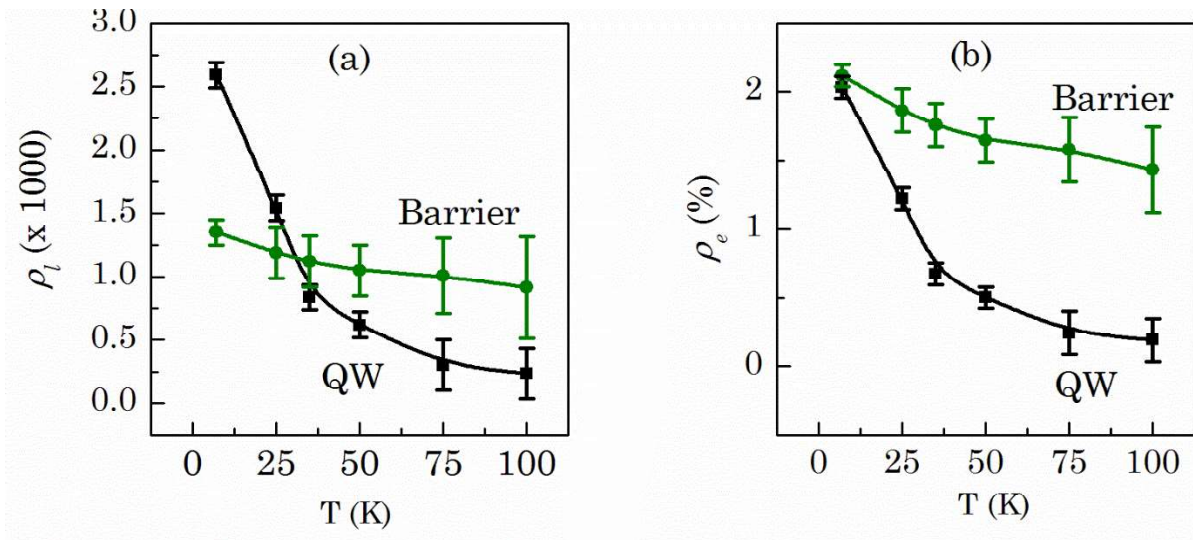


Figure 6.18 (a) Degree of circular polarization of light (ρ_l) and (b) spin polarization of electron (ρ_e) in barrier and quantum well

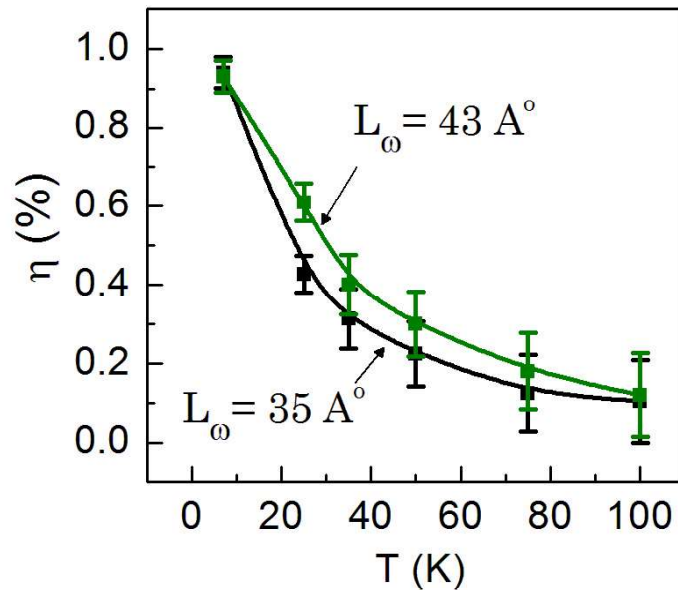


Figure 6.19 Spin transfer efficiency is compared for two different quantum wells

Furthermore, the spin transfer efficiency (η) is estimated by using equation 6.9 and is plotted in figure 6.19. It can be seen that at 10 K, η is almost 100 % indicating minimum loss of spin relaxation. However, it decreases rapidly to within

10 % at 100 K. Similar plot for a 35 Å quantum well is also shown in the same figure.

As pointed out by Puttison et al. [187], η depends on several factors including spin relaxation of electrons within the barrier (AlGaAs) before being injected to quantum well (GaAs). Spin flip scattering across the AlGaAs/GaAs interface and spin relaxation during energy relaxation of the injected hot electrons in GaAs quantum wells are the two important mechanisms. It has been shown that, the D.P spin relaxation time decreases at lower quantum well width which is mainly due to stronger quantum confinement effect [21]. This may be one possible reason behind a small value of η for thin quantum wells. Enhanced values of composition and thickness fluctuations at low QW thickness provide another possible reason.

6.6 ISHE measurement in GaAs/AlGaAs quantum well

From the analysis of the previous section, electron spin polarization (ρ_e) in the quantum well is estimated at several temperature varying from 10 to 100 K. Hence, ISHE measurements can be performed as explained in section 6.1, where the applied current density is correlated to the spin current density by equation (6.1) and is given by $J_s = J_c \rho_e$. For this, GaAs/AlGaAs quantum wells are chosen, which are grown on SI GaAs. Hall bar structure is fabricated as explained in section 3.2.2 and section 5.2. The resistance across the two opposite pair of contacts are measured at

various temperatures. The schematic of the Hall bar structure and corresponding current-voltage measurements at 300 K are shown in figure 6.20 (a) and (b) respectively.

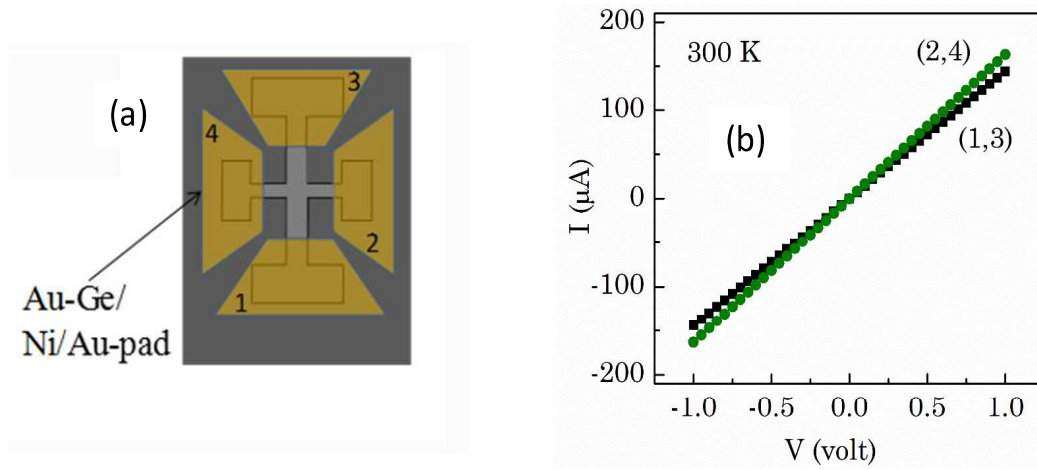


Figure 6.20 Schematic of the fabricated Hall bar structure and measured current voltage behavior at 300 K

For the measurement of ISHE, dc voltage ranging from 0 to ± 5 V is applied across contacts '1' and '3' using Lock in amplifier and I_{ISHE} is measured across contacts '2' and '4'. Laser light of 532 nm ($P_L=3.5$ mW) is incidence on the middle of the two pair of contacts at normal incidence. Care is taken not to illuminate any of the electrical contacts to avoid the artefacts in the measurement. Since the laser light is modulated at 50 kHz, I_{ISHE} is measured at that frequency using Lock in amplifier technique. For this case, equation 1.19 can be re-written as

$$J_{ISHE} = \gamma \left(\vec{J}_S \times \hat{\sigma} \right) \quad (6.10)$$

Since both the conducting paths, i.e. from ‘1’ to ‘3’ and from ‘2’ to ‘4’ have the same cross sectional area, current density can be correlated with measured current. Since $J_s(=J_c\rho_e)$ is known from the applied voltage (V_a) and resistance, and J_{ISHE} is measured experimentally, equation 6.10 enabled us to estimate the spin Hall angle (γ) using the following relation

$$\gamma = \frac{I_{ISHE}}{\left(\frac{V_a}{\Re}\right)\rho_e} \quad (6.11)$$

Here \Re is the resistance across the device, measured using figure 6.20 (b). In figure 6.21, the measured I_{ISHE} is plotted at three different temperatures, as a function of applied bias. The background signal corresponding to misalignment of contacts and Dember voltage are removed by subtracting the current that was measured by orienting the linear polarizer parallel to the PEM axis.

A straight line behavior is observed at all the temperatures. It is predicted that, as in bulk GaAs, sub linear nature should be observed at higher applied bias, because of faster spin relaxation of electrons at higher electric field [75, 133]. However, the maximum field, which is applied here is 50 V/cm. Therefore it is not expected to induce non-linear behavior, which is generally observed at the range of few kV/cm. The measured current is further divided by the response of the measurement circuit, as explained in section 3.5.2. Thereafter, it is put in equation 6.11 to estimate γ , which are plotted in figure 6.22.

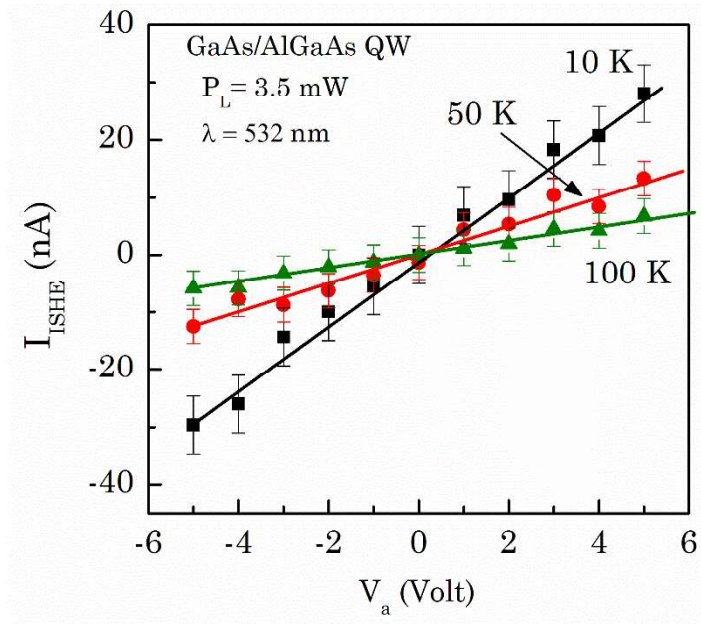


Figure 6.21 Measured I_{ISHE} as a function of applied voltage at three different temperatures.

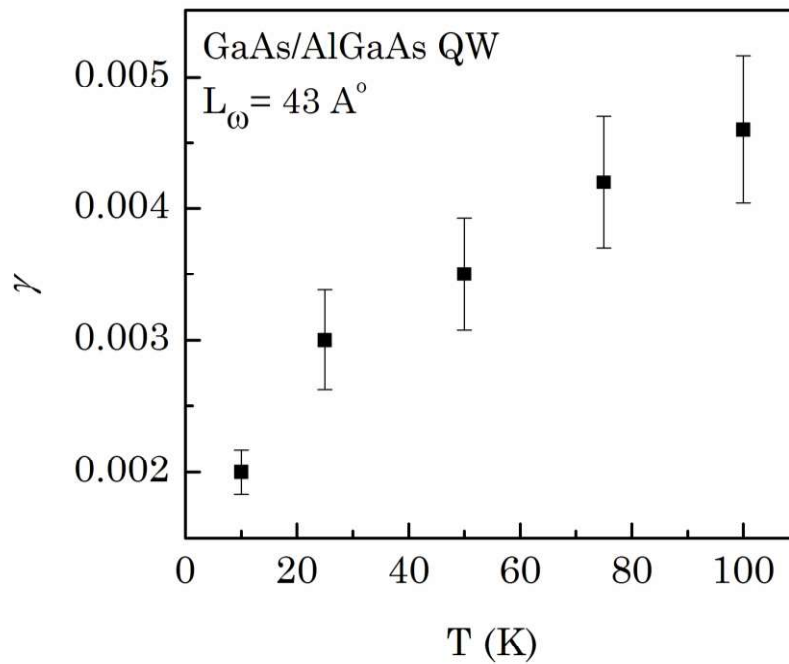


Figure 6.22 Estimated spin Hall angle in GaAs/AlGaAs quantum well as a function of sample temperature

This estimated value of γ , increases from 0.002 at 10 K to 0.0045 at 100 K. Though the numerical values are different than the bulk GaAs case, the temperature dependent are similar for both the cases. This points towards a possible common origin of spin Hall Effect in both cases.

6.7 Outcome of the chapter

This chapter describes the results from the optical orientation technique for the measurement of electron polarization and spin Hall angle in quantum well structures. By *k.p* modeling, a relation is established for estimating the electron spin polarization from the observed degree of circular polarization of the photoluminescence. This method takes into account the coupling between heavy and light holes and therefore requires different input parameters like sample temperature and quantum well thickness. This method is verified by simultaneously measuring the degree of circular polarization of light originated from the recombination of electrons with light and heavy holes in GaAsP/AlGaAs tensile strained quantum wells. Further, the spin transfer efficiency from the barrier to quantum well material in a GaAs/AlGaAs quantum well is also estimated by estimating the electron spin polarization in the barrier and the quantum well materials. It is found to be 98.4% at 10 K, suggesting very good quality hetero-interface of the MOVPE grown layers. However, the efficiency decreases to within 10 % at 100 K because of the increase in carrier scattering due to various spin relaxation mechanism. Beyond 100 K, it is not possible to estimate

the efficiency as photoluminescence from the barrier material disappears. The estimated electron spin polarization is then multiplied to the applied current to correlate it with the effective spin current flowing through the quantum well. This spin current generates a transverse ISHE current, which is measured by Lock in technique and subsequently, the spin Hall angle in GaAs/AlGaAs quantum well is estimated. The spin Hall angle is observed to increase with temperature from 0.002 at 10 K to 0.0045 at 100 K. Further theoretical and experimental work is needed to explain the observed dependence in terms of microscopic details. However, this study establish a method for measuring the spin Hall angle in quantum well by first estimating the electron spin polarization correctly and then correlating it with the measured ISHE induced current.

Chapter 7

Fabrication of a spin- optoelectronic device

7.1 Introduction

It is clear from the recent research work of several groups that an integration of spintronic technology with conventional semiconductors will increase the functionality of the device [12]. With this in mind, efforts are put to develop a functional device that operates under ambient conditions. In chapter 4, the detection of photo-induced Inverse Spin Hall Effect in Au/InP hybrid junction has been already established, where a current of 50 pA was measured at room temperature for 10 mW circularly polarized laser. The magnitude of signal is surely far above the typical noise level in the laboratory. A careful choice of the metal and semiconductor combination have led to this development as described in chapter 4. Since the magnitude of I_{ISHE} varies linearly with the degree of circular polarization of laser beam, it readily indicates towards the use of such a device in the integration of light-polarization information with spintronic technology. It paves the way for the development of a semiconductor detector for detecting the polarization state of the laser beam and the same is discussed in this chapter.

7.2 Methods for the detection of the degree of circular polarization of light

Circularly polarized light has profound importance in various domains of fundamental research and practical applications which includes material characterization using circularly polarized ellipsometry, chiral nanostructure fabrication, manipulation of biological and colloidal matter, quantum teleportation and cancer diagnosis [188-192]. The recent findings are based on numerous innovations in the domain of generation and detection of circularly polarized light. In a conventional photo-polarimeter, the light beam passes through a sequence of analyzing optical elements before the emerging light is measured by a polarization-insensitive linear photo-detector [193, 194]. Although these methods are very robust and extremely reliable but are inherently slow due to the involvement of several opto-mechanical components. Moreover, if one wants to record the time resolved information then a more complex optical configuration is chosen where elliptically polarized light beam is transmitted through rapidly rotating polarizer/analyzer/compensator which are kept in front of a conventional photodiode [195]. For more accurate time resolved measurements, researchers prefer to opt for pump-probe based techniques which are rather cumbersome and the measurements are highly onerous [196]. Irrespective of their critical importance and usefulness, all these conventional methods are rather slow. In order to overcome this limitation, R.M.A. Azzam [197] proposed a novel method based on four independent photodiodes where one can measure all the Stokes parameters of polarized light simultaneously. However, for key applications in advanced optical communication and quantum-

based optical computing, miniaturized integrated devices are desired where ultrafast detection of circularly polarized light is feasible [198-199]. Spin-optoelectronic technology offers a great opportunity for the development of fast and compact devices that can be made by exploiting the interplay between the photon angular momentum and the spin of electrons in a spin-optoelectronic device. In such devices, injection/detection of spin polarized carriers is achieved by depositing a thin layer of magnetic materials on the top of semiconductor [200]. In spite of the remarkable achievements of these structures, a major bottleneck impedes their progress as the devices fail to operate at room temperature. Moreover, the requirement of external magnetic field makes them less attractive for the communication purposes [200]. On the other hand, a few researchers have proposed another interesting technique for the room temperature detection of light helicity where the measurement of polarization state of THz radiations is made possible by implementing the devices based on the circular photo-galvanic effect, linear photo-galvanic effect, and photon drag effects in semiconductors [201-203]. Unfortunately, this technique works in the far-infrared region and is not easy to extend to the visible portion of electromagnetic spectrum since the chosen active components are not transparent to the visible light. Recently, Yang et al. [204] also demonstrated a novel method to detect the circularly polarized light by a chiral organic semiconductor transistor. Although, it is an easy method for the fabrication of such interesting devices, since no magnetic materials/magnetic fields are required, but the handedness of the molecule decides the response of detector towards the helicity of light. It means that two separate detectors with films of

different handedness are needed to record the left and right polarization states of the circularly polarized light. Further, the signal to noise ratio of these devices is rather poor. Moreover, optoelectronic devices based on conventional inorganic semiconductors are generally preferred over their organic counterparts due to the reliability, repeatability and robustness issues.

In these contexts, the spin-photonic devices discussed in chapter 2 and 4 offer a realistic solution. These compact devices are able to detect visible and near infrared light, and can operate at room temperature. Moreover, neither any ferromagnetic material nor a magnetic field is required for the operation of device. Hence, monolithic integration of these devices can be made with existing optoelectronic circuits where high frequency operation is also feasible.

7.3 Factors contributing in the output of a conventional spin-photonic detector

Although, the devices explained in chapter 2, and 4 are able to detect the polarization state of a laser beam, but an important point related to the magnitude of I_{ISHE} causes some concern. As mentioned earlier, I_{ISHE} depends on three factors, i.e. 1) degree of circular polarization, 2) angle of incidence and 3) the intensity of impinging laser beam. Therefore, the magnitude of I_{ISHE} will be decided by the intensity and polarization state of laser beam even for a given incidence angle, as shown in figure 7.1 (a) and (b)

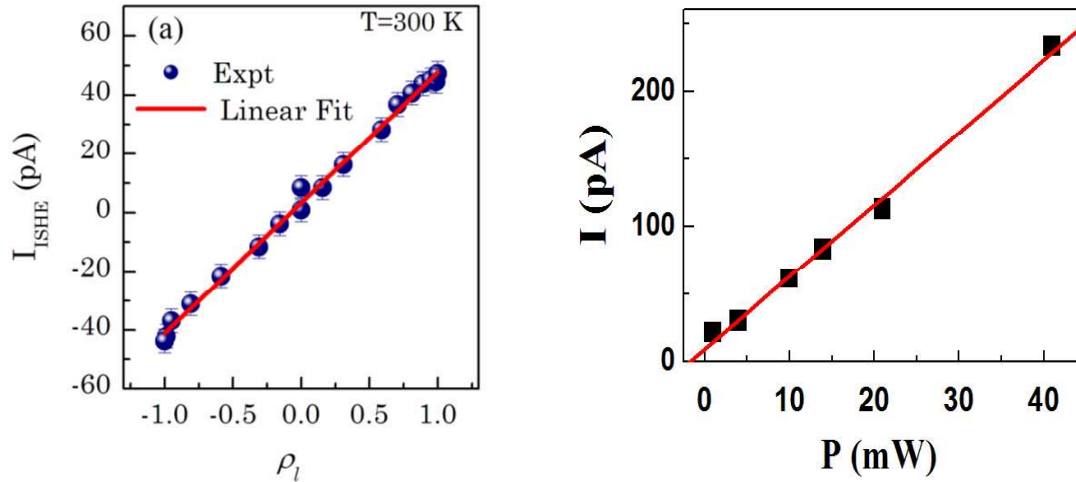


Figure 7.1 The magnitude of I_{ISHE} plotted as a function of (a) degree of circular polarization, and (b) Intensity of a laser beam

Therefore, for an unambiguous determination of the polarization state by ISHE detector a careful calibration against the intensity of laser beam is essential. Moreover, such a calibration must be carried out using an independent photo-detector. This is important since any fluctuation in the incident intensity may provide misleading information about the polarization state if the intensity is not measured simultaneously. This is a common issue concerning almost all polarization detectors that are in operation today.

In fact, Ganichev et al. [201] reported the simultaneous measurement of intensity and helicity of terahertz radiation using separate detectors. However, inclusion of an independent detector for the laser intensity unnecessarily complicates the issue and it is extremely desirable if a single device can simultaneously measure the degree of circular polarization along with the intensity of a laser beam. Such a device shall provide an unambiguous detection of the polarization state of a laser beam independent of its intensity.

7.4 Proposal of a three terminal device as one possible solution

A possible solution to the aforementioned problem arises by realizing that the metallic Au forms Schottky contacts with InP where a built-in electric field is associated with the metal-semiconductor junction. This creates an asymmetry in the motion of photo-generated electrons, although at the time of generation they are distributed symmetrically in the k -space. This asymmetry i.e. the difference in the number of electrons moving in opposite direction ($n_{-k} - n_{+k}$) creates a photo-voltage, which is a measure of the incident intensity. Therefore, it is possible to measure both the light polarization and intensity simultaneously, if an additional measurement is done across the Schottky contact in the same geometry.

7.5 Fabrication of two different detectors on a single chip

To implement the above solution, a device is fabricated with an additional electrode, whose fabrication details are similar to the methods explained in section 4.2. Two 100-nm-thick Au-pads are evaporated at the two edges of Au thin layer, which are labelled as contact '1' and '2' respectively in figure 7.2 (a). These two contacts are used to measure the I_{SHE} that flows between the two Au-pads. Indium Ohmic contact, labelled as contact '3' in figure 7.2 (b) is made at the other edge of InP sample which is used for the simultaneous measurements of the photo-voltaic current (I_{PV}) that flows between the contacts '2' and '3' due to the light illumination.

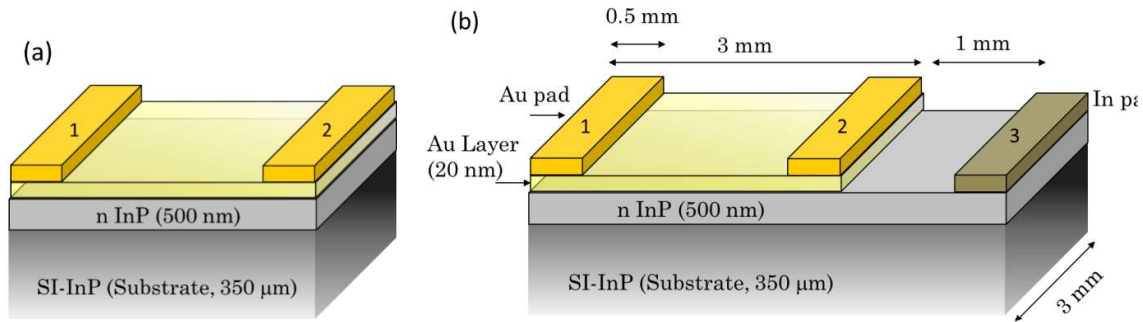


Figure 7.2 (a) Two terminal device to measure only ISHE, (b) Three terminal device for the measurement of I_{ISHE} and I_{PV} simultaneously.

For the proper functioning of the device, it is necessary to ensure that the contacts are working as per the desired experimental configurations. In view of this, a set of experiments are performed and the representative plots are shown in figure 7.3 (a) illustrating the room temperature Current-Voltage (I-V) characteristics of the two sets of contacts. Linear and rectifying nature of the two sets of contacts i.e. '1' & '2' and '2' & '3' ensure the suitability of the device for the measurement of I_{ISHE} and I_{PV} respectively.

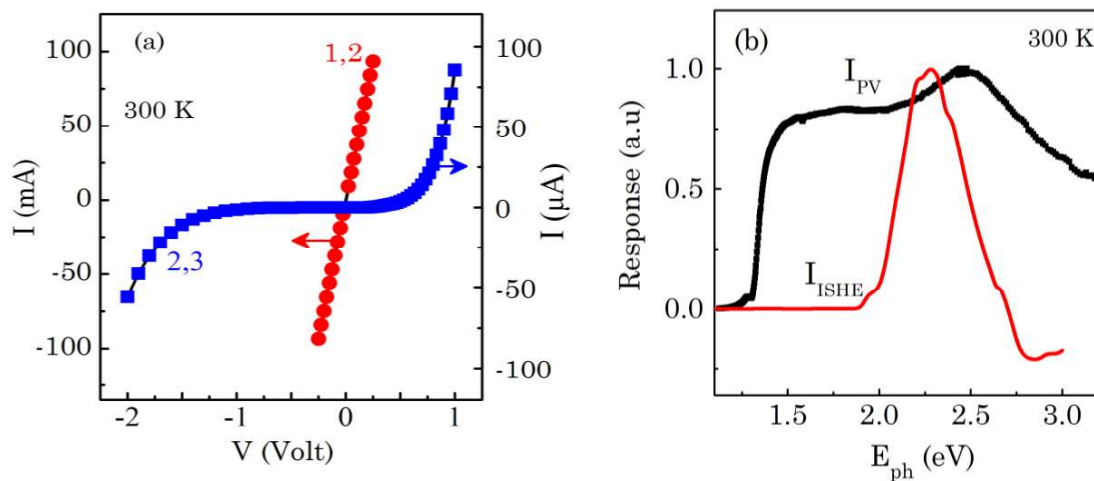


Figure 7.3(a) I-V graph of contacts (1,2) and (2,3) respectively. (b) Measured I_{PV} and numerically estimated I_{ISHE} in Au/InP structure. For I_{ISHE} calculation, the barrier height is taken to be 0.72 eV. The spectra are normalized to their peak values

A barrier height of the magnitude of 0.72 eV is measured from the forward biased I-V characteristics which is reasonable. The capacitance across the contacts ‘2’ & ‘3’ is also measured as 18.1 nF which provides a depletion width of 54 nm and a built-in electric field of approximately 120 kV/cm at the junction. For the measured barrier height, the I_{ISHE} spectrum is numerically calculated following the procedure described in chapter 2, and the same is plotted as red curve in figure 7.3 (b). Further, the spectral dependence of I_{PV} is also measured by using a Lamp-monochromator geometry and is plotted as black curve in figure 7.3 (b). These two curves clearly demonstrate the suitability of fabricated device for the simultaneous measurement of I_{ISHE} and I_{PV} in the range of 2 - 2.6 eV.

7.6 Simultaneous and independent measurement of I_{ISHE} and I_{PV}

During the measurements, laser light with wavelength of $\lambda=532$ nm ($E_{ph}=2.33$ eV) uniformly illuminated the Au layer as schematically shown in figure 7.4. The angle of incidence is kept at 60° . The magnitude of I_{ISHE} is maximum at this angle which is predicted by the numerical simulations, explained in chapter 2 and is also observed in the experiments explained in chapter 3. In this experiment, the incident laser beam undergoes two types of modulations before being absorbed by the sample. One is the polarization modulation, induced by using a Photo-elastic modulator (PEM-100 of Hinds make) operating at $\omega_p=50$ kHz while the other is the intensity modulation, induced by a mechanical chopper operating at much lower frequencies (ω_c) varying from 172 Hz to 3 kHz. The polarization induced current (I_{ISHE}) and the photo-voltaic current (I_{PV}) are separately measured by using two independent lock-in amplifiers synchronized

to PEM (Ref. 1) and mechanical chopper (Ref. 2) frequencies respectively. All the measurements are performed at room temperature.

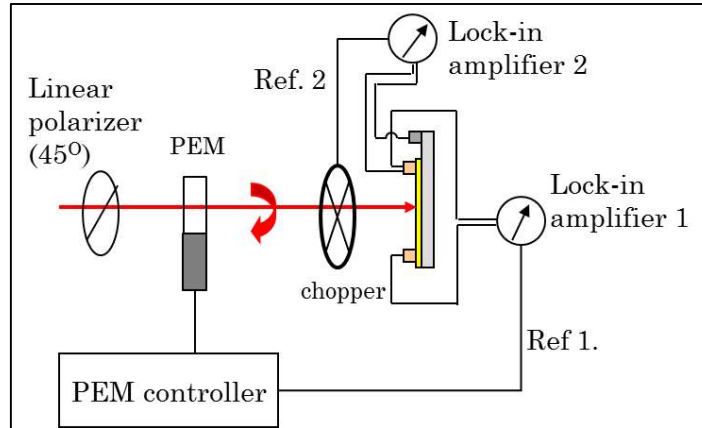


Figure 7.4 Schematic of experimental set up to measure I_{ISHE} and I_{PV} simultaneously.

7.7 Results and discussion

Figure 7.5 (a) shows the dependence of I_{ISHE} on the phase shift/retardation (δ) between the parallel and perpendicular components of the linearly polarized light. It is measured by switching off the mechanical chopper. A sinusoidal dependence of I_{ISHE} on retardation confirms the spin-optoelectronic origin of signal. A cyclic change in the polarization state of light, varying from the linear to circular through the elliptical polarization state and vice versa, is schematically depicted on the top of figure 7.5 (a).

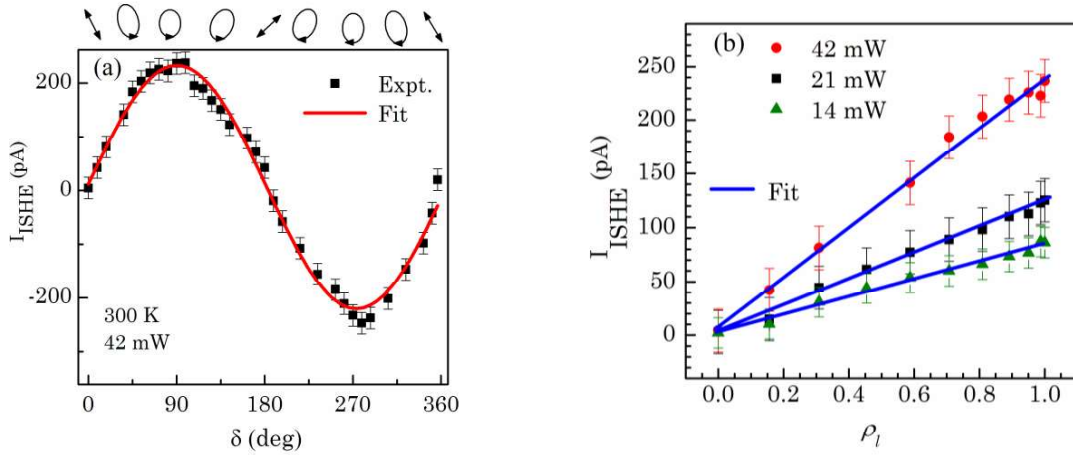


Figure 7.5 (a) I_{ISHE} as a function of δ , (b) I_{ISHE} as a function of the degree of circular polarization (ρ_l) at three laser powers only for the first quarter of sine wave. On top of figure 7.5 (a), polarization ellipses corresponding to various retardations are shown.

By noting the sign and magnitude of I_{ISHE} , one can unambiguously measure the polarization states of light. It can be appreciated in a better way if one plots I_{ISHE} as a function of degree of circular polarization (ρ_l) where ρ_l is calculated from the phase shift induced by the PEM. Such a plot is shown in figure 7.5 (b) at three representative laser powers. Here, ρ_l is varied from zero to one depending on the phase shift that changes from 0 to 90°. It makes only a quarter of the complete sine wave shown in figure 7.5 (a). Note that a similar plot with corresponding sign and slope will repeat for the next three quarters. Hence, hereafter all the graphs are plotted for the first quarter only.

Now, if the chopper shown in figure 7.4 is also switched on, the laser will be doubly modulated. However, the frequency of modulation by mechanical chopper is much lower than that of the PEM module. Hence, no adverse effect on the operation of ISHE detector is expected due to the dual modulation. It can be appreciated from figure 7.6 that the dual modulation does not hamper the

measurement of I_{ISHE} apart from a reduction in the magnitude. The fall of magnitude of I_{ISHE} under dual modulation mode does not depend upon the frequency of mechanical chopper which was varied from 172 Hz to 3 kHz during the measurements.

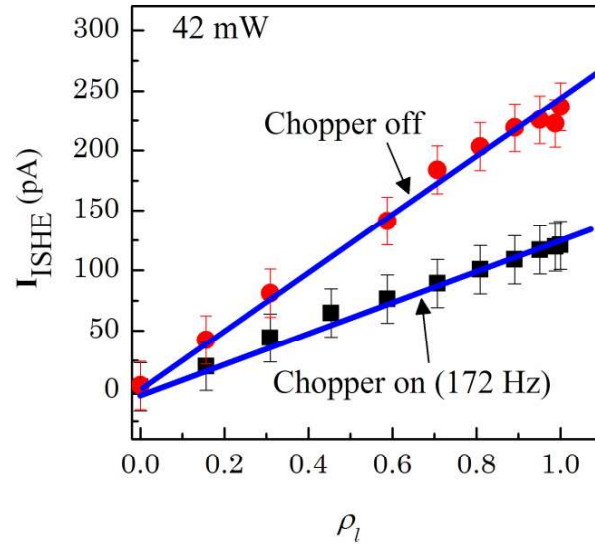


Figure 7.6 ISHE plotted as a function of ρ_l in the presence and absence of mechanical chopper.

The results can be explained more conveniently by the following Stokes vector analysis. The stokes vector of light emerging from the combination of 45° linear polarizer, PEM and mechanical chopper is given by

$$S = \Pi(\omega_c t) \begin{bmatrix} 1 \\ 0 \\ \cos(\Delta(t)) \\ \sin(\Delta(t)) \end{bmatrix} \quad (7.1)$$

The output of the chopper is given by the Π function, which is 1 if $0 \leq \omega_c t \leq \frac{1}{2}$ and 0 if $\frac{1}{2} \leq \omega_c t \leq 1$. Since I_{PV} responds to the first component of the Stokes vector, it is proportional to $\Pi(\omega_c t)$, whose Fourier transform is a sinc function. Hence, it can be conveniently detected by a Lock-in amplifier synchronized to ω_c .

On the other hand I_{ISHE} responds to the fourth component of the Stokes vector, which is proportional to $\Pi(\omega_c t) \sin(\omega_p t)$. The Fourier transform of this function has peaks at higher harmonics of ω_p , in addition to the peak at ω_p . This is the reason why I_{ISHE} is measurable at ω_p even under double modulation. Had it been a sine function instead of Π , the resultant ISHE signal would have been observed at $(\omega_p \pm \omega_c)$ and not at ω_p .

7.8 Investigation of cross talk between the two detectors made of a single chip

It is understood that, simultaneous measurement of the degree of circular polarization and intensity of a laser beam is possible using the two pair of contacts, only if there is cross talk between them. It is checked by performing two simultaneous and independent measurements for I_{ISHE} and I_{PV} at 50 kHz and 172 Hz respectively using the two experimental configurations described earlier in figure 7.4. The results of these two measurements performed simultaneously under the dual modulation mode are depicted in figure 7.7. As is already explained, the signal measured at 50 kHz across the contacts ‘1’ and ‘2’ varies linearly with ρ_p , even under simultaneous measurement conditions as shown in figure 7.7 (a). It is also known from table 1.4, that the conventional semiconductors have at least four orders smaller spin Hall conductivity compared to metals like Au and Pt. Therefore, no polarization dependent signal is expected across the contacts ‘2’ and ‘3’, which is indeed the case as shown in figure 7.7 (a). It confirms the absence of I_{ISHE} between this particular pair of contacts. Similarly, I_{PV} is measured at 172 Hz across the contacts ‘2’ and ‘3’ as

shown in figure 7.7 (b). However, no photocurrent is expected to flow between the contacts ‘1’ and ‘2’ since these are formed on the gold metallic layer, and Au-layer has a very low resistivity ($3.7 \text{ m}\Omega^{-1} \text{ cm}^{-1}$) at room temperature. It is indeed seen in figure 7.7 (b) where no I_{PV} signal is recorded across the contacts ‘1’ and ‘2’.

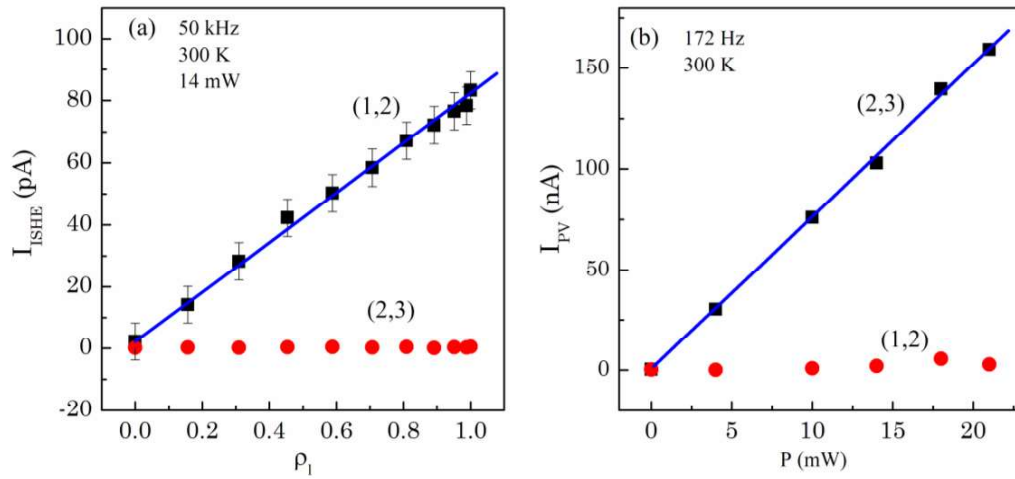


Figure 7.7 Simultaneous measurement of the intensity and polarization state of light, (a) A comparison of I_{ISHE} measured at 50 kHz across the contacts ‘1’&‘2’ and ‘2’&‘3’. and (b) A comparison of I_{PV} measured at 172 Hz chopping frequency across the contacts ‘1’&‘2’ and ‘2’&‘3’ as a function of incident laser power

It ensures that no cross talk occurs between the two pair of contacts where no I_{ISHE}/I_{PV} signal is generated across the respective pair of contacts i.e. [‘2’&‘3’]/ [‘1’&‘2’]. It is shown in figure 7.7(b) where the magnitude of I_{PV} depends linearly on the power of incident laser beam. This linear dependence provides an excellent online calibration tool for the intensity of incident beam. It therefore provides an unambiguous detection of the degree of circular polarization of laser beam irrespective of any possible fluctuations in the intensity. Although, the intensity of laser beam remains stable during our measurements, nevertheless,

any deviation in the detection of the polarization state of laser beam caused by small fluctuations in the intensity can easily be taken care under the proposed configuration.

It is also important to comment on the frequency cut-off of the developed detectors. A fast response of ISHE detector is essential to ensure a high speed of communication and is an important figure of the merit. Note that the ISHE detector developed here works very well at 50 kHz which is limited by the operating frequency of PEM module. Similar to the conventional high speed electronic devices, the frequency response of ISHE detector can easily be tailored by using the available technologies. Frequency response of a photo-detector is primarily decided by its capacitance and the transit time of electrons in the device. The geometrical issues are critical to optimize the capacitance of a semiconductor device to ensure its operation at high frequencies. Moreover, the proposed device works without any bias voltage. Application of a reverse bias across the contacts '2' and '3' might further improve the frequency response of PV detector.

7.9 Outcome of the Chapter

A novel spin-optoelectronic detector for the simultaneous measurement of the degree of circular polarization and intensity of a laser beam is developed. The detectors is based on a unique device configuration where two pair of contacts made on the Au/InP hybrid structure are used to measure the magnitude of I_{ISHE}/I_{PV} signal simultaneously. It is also demonstrated that no cross talk occurs between the two pair of contacts. The developed detector genuinely responds to

the variations in the polarization state of light where the sign and magnitude of ISHE signal systematically vary from linear to circular through the elliptical polarization state and vice versa. Simultaneous measurement of the intensity of laser beam nullifies the intensity dependence of ISHE signal and therefore provides an unambiguous detection of the polarization state of a laser beam. An unambiguous measurement of the ellipticity of emitted, transmitted, reflected, or scattered light can provide useful information about the optical anisotropy of a wide range of media. The proposed spin-optoelectronic detector can be very useful in several advanced photonics and communication applications.

Chapter 8

Summary and future perspectives

8.1 Summary of the current work

During the course of this thesis, transport properties of optically generated spin polarized electrons in various III-V semiconductor bulk and quantum well structures are investigated. It is successfully demonstrated that Inverse Spin Hall Effect (ISHE) can be an effective method to electrically detect these spin polarized electrons in semiconductors.

This work starts with a numerical simulation of ISHE in metal/semiconductor hybrid structures. Since the available literature on this subject is very limited, the realization of such experiments are extremely challenging. Therefore by numerical simulations, prior knowledge of necessary experimental conditions like light wavelength, angle of incidence, optimal combination of materials and their influence on the magnitude of ISHE signal is obtained. Systematic numerical calculations based on the analysis of both energy and spin relaxation phenomena for optically induced hot electrons, tunnelling and thermionic transport effects at the metal/semiconductor interface and

circular dichroism for the light transmitted through the metal layer are carried out.

Based on these theoretical predictions, Au/InP hybrid structure is judiciously chosen. Moderately doped ($n \sim 3.6 \times 10^{17} \text{ cm}^{-3}$) InP epi-layers of high crystalline quality are grown by MOVPE and the sample is fabricated using e-beam evaporation technique. In this structure, a genuine ISHE signal is obtained over a broad temperature range of 10 to 300 K. The spintronic origin of ISHE signal is established based on its dependence on the angle of incidence and degree of circular polarization. Temperature dependence of ISHE signal is explained by considering a model based on the spin relaxation of photo-induced hot electrons.

In the next step, ISHE signal is observed in bulk semiconductors at oblique incidence without the involvement of a metallic layer. This extremely challenging task is accomplished in a MOVPE grown GaAs thin film of high crystalline quality. A clear signature of ISHE phenomenon is seen over a broad temperature range of 10 to 300 K. By analyzing the polarization properties of photoluminescence (PL) signal, the spin relaxation time of electrons in GaAs is measured which is observed to vary from 2.47 ns at 10 K to 0.55 ns at 200 K. By using this spin relaxation time, the spin diffusion equation is then solved to find out the spin current density originating from the spin diffusion at the surface of semiconductor. By coupling the results of ISHE measurements with estimated spin current density, the magnitude of spin Hall conductivity is estimated for bulk GaAs. To explain the variation of spin Hall conductivity from

4.17 $\Omega^{-1}\text{cm}^{-1}$ at 10 K to 12.3 $\Omega^{-1}\text{cm}^{-1}$ at 200 K, inclusion of phonon and dynamic impurity scattering in numerical calculations is found to be essential.

In case of quantum well systems, estimation of electron spin polarization from the degree of circular polarization of PL requires a modelling of the band structure. Based on 4 band k.p calculation, a relation is derived and a method is proposed to estimate the electron spin polarization uniquely from simultaneous analysis of heavy and light hole related transitions. The validity of this method is experimentally verified by carefully conducting experiment in GaAsP/AlGaAs tensile strained quantum well. Spin transfer efficiency from barrier to quantum well layer is estimated by analysing the polarization properties of PL signal emitted by both the barrier and quantum well in a GaAs/AlGaAs system. At 10 K, this efficiency turns out to be around 98 %, which reduces to below 5 % at 100K. Various possible reasons behind this kind of observations are discussed. A clear ISHE signal is measured for GaAs/AlGaAs quantum well sample.

Finally, a proof of concept demonstration of a spin-optoelectronic device, which can detect light intensity and polarization simultaneously in an integrated optoelectronic platform is also shown. The prototype device is fabricated based on Au/InP hybrid structure, where a three terminal device is made by incorporating two independent detectors on the same chip that are used to measure the degree of circular polarization and intensity of a laser beam simultaneously and independently. The working principle of the detector is based on two independent fundamental phenomena occurring in Au/InP hybrid structures, namely, Inverse Spin Hall Effect (ISHE) and the Photo-Voltaic (PV) Effect. The all-electronic compact device is fast, operates at room temperature,

and opens up the possibility of many applications in an integrated optoelectronic platform.

8.2 Future perspectives

Though spin Hall Effect and Inverse Spin Hall Effect are now established phenomena, still a lot of research has to be done in this frontline area. Particularly ISHE phenomena in semiconductors need a lot of attention as the field of semiconductor spintronics is still not as mature as its metal counterpart. A few future directions where the current research opens up new research frontiers are listed below,

1. Spin Hall conductivity in semiconducting material is not yet fully understood. Suitable models have to be built for including several scattering mechanism like phonon and dynamic impurity scattering in the calculation of spin Hall conductivity.
2. Photo-induced ISHE method can be used to estimate spin Hall conductivity of bulk materials, which is expected to depend on the crystallographic direction. It is supported by the fact that the vector sum of Dresselhaus and Rashba spin orbit effect is highly direction dependent. Systematic experimental work needs to be focused in this direction.
3. The effect of quantum confinement (quantum well, quantum wire) on the spin Hall conductivity is not yet fully understood and the same needs to be investigated.
4. Photo-induced ISHE in semiconductors has not yet been conducted in high magnetic field environment. It is expected to be a method of choice to

measure spin relaxation time, when the optical method of Hanle effect fails, either because of the nature of the sample or due to experimental limitations.

5. Further improvement in spin optoelectronic devices, like increase in sensitivity and improvement in frequency response is anticipated in future. This will increase the functionality of the device and will lead to practical applications.
6. Finally, it can be said that Spin-optoelectronic technologies are still in infancy, and a lot of innovative developments in this frontline research area are expected.

Bibliography

1. Supriyo Bandyopadhyay, Marc Cahay, *Introduction to spintronics*, CRC Press, Taylor & Francis Group (2008)
2. N.F. Mott, and H. S. W. Massey, *The Theory of Atomic Collisions*, 3rd ed. Clarendon, Oxford (1965)
3. Teruya Shinjo, *Nanomagnetism and spintronics*, Elsevier, Amsterdam, (2009)
4. R. Jansen, J. Phys. D: Appl. Phys. **36**, R289 (2003)
5. P. Grunberg, R. Schreiber, Y. Pang, M.B. Brodsky and H. Sowers, Phys. Rev. Lett. **57**, 2442 (1986)
6. Peter A. Grünberg, Nobel Lecture: *From spin waves to giant magneto resistance and beyond*, Rev. Mod. Phys. **80**, 1531 (2008)
7. Albert Fert, *Nobel Lecture: Origin, development, and future of spintronics*, Rev. Mod. Phys. **80**, 1517 (2008)
8. D. Awschalom, D. Loss, and N. Samarth, *Semiconductor Spintronics and Quantum Computation*, Springer, New York (2002)
9. A. M. Bratkovsky, Rep. Prog. Phys. **71**, 026502 (2008)
10. Michael Oestreich, Jens Hübner, Daniel Hägele, Markus Bender, Nils Gerhardt, Martin Hofmann, Wolfgang W. Rühle, Heinz Kalt, horsten Hartmann, Peter Klar, Wolfram Heimbrod, Wolfgang Stolz; *Spintronics: Spin Electronics and Optoelectronics in Semiconductors*; Springer Berlin Heidelberg, Berlin (2001)

11. Igor Zutic, Jaroslav Fabian and S. Das Sarma, *Rev. Mod. Phys.* **76**, 323 (2004)
12. D.D. Awschalom and M. E. Flatte, *Nature Physics*, **3**, 153 (2007)
13. S. A. Wolf, D.D. Awschalom, R. A. Buhrman, J. M. Daughton, S. von Molna, M. L. Roukes, A. Y. Chtchelkanova, D. M. Treger, *Science*, **294**, 1488 (2001)
14. J. Sinova and A.H. MacDonald, *Semiconductors and Semimetals* **82**: 45, (2008)
15. Jasprit Singh, *Electronic and Optoelectronic Properties of Semiconductor Structures*, Cambridge University Press, Cambridge, UK (2003)
16. R. Winkler, *Spin–Orbit Coupling Effects in Two-Dimensional Electron and Hole Systems*, Springer, Berlin (2003)
17. G. Vignale, Ten Years of Spin Hall Effect, *J Supercond. Nov. Magn* **23**, 3 (2010)
18. S.L. Chuang, *Physics of Optoelectronics Devices*, John Wiley and Sons. Inc. (1995)
19. A. Manchon, H. C. Koo, J. Nitta, S. M. Frolov & R. A. Duine, *Nature Materials* **14**, 871 (2015)
20. F. Meier and B.P. Zakharchenya, *Optical Orientation*, North Holland Press, Amsterdam (1984)
21. M.I. Dyakonov, *Spin Physics in Semiconductors*, Springer-Verlag, Berlin Heidelberg (2008)
22. R. H. Henderson and E. Towe, *J. Appl. Phys.* **79**, 2029 (1996)

23. Lok C. Lew Yan Voon and Morten Willatzen, *The $k \cdot p$ Method: Electronic Properties of Semiconductors*, Springer-Verlag, Berlin Heidelberg (2009)
24. F. Nastos, J. Rioux, M. Strimas-Mackey, Bernardo S. Mendoza, and J. E. Sipe, *Phys. Rev. B* **76**, 205113 (2007)
25. R. Fiederling, M. Keim, G. Reuscher, W. Ossau, G. Schmidt, A. Waag, and L. W.Molenkamp, *Nature* **402**, 787 (1999)
26. M Holub and P Bhattacharya, *J. Phys. D: Appl. Phys.* **40**, R179(2007)
27. Wenfeng Wang, Klaas Allaart, and Daan Lenstra, *Phys. Rev. B* **74**, 073201 (2006)
28. Stephan R. Ichiriu, Ph.D Thesis, California Institute of Technology Pasadena, California (2005)
29. Pil Hun Song and K. W. Kim, *Phys. Rev. B* **66**, 035207 (2002)
30. M.W. Wu, J.H.Jiang, M.Q.Weng, *Physics Reports*, **493**, 61(2010)
31. Jaroslav Fabian, Alex Matos-Abiague, Christian Ertler, Peter Stano, Igor Zutic, *Acta Physica Slovaca* **57**, 565 (2007)
32. Oertel, J. Hübner, and M. Oestreich, *Appl. Phys. Lett.* **93**, 132112 (2008)
33. Y.Yafet, *Solid State Physics*, vol.14, Academic Press, New York (1963).
34. R.J.Elliott, *Phys.Rev.* **96**, 266 (1954)
35. M.I. Dyakonov, and V. I. Perel, *Sov. Phys. Solid State* **13**,3023 (1971)
36. G.L. Bir, A. G. Aronov, and G. E. Pikus, *Sov. Phys. JETP* **42**, 705 (1976)
37. R. Tycko, J.A. Reimer, *J. Phys. Chem.*, **100**, 13240 (1996)
38. M.I. Dyakonov and V. I. Perel, *JETP Lett.* **13**, 467(1971)

39. M. I. Dyakonov and V. I. Perel, *Phys. Lett. A* **35**, 459 (1971)
40. J. E. Hirsch, *Phys. Rev. Lett.* **83**, 1834 (1999)
41. S. Zhang, *Phys. Rev. Lett.* **85**, 393 (2000)
42. Jairo Sinova, Dimitrie Culcer, Q. Niu, N. A. Sinitsyn, T. Jungwirth, and A. H. MacDonald, *Phys. Rev. Lett.* **92**, 126603 (2004)
43. S. Murakami, N. Nagaosa, and S. C. Zhang, *Science* **80**, 1348 (2003)
44. Markus Ehlert, Cheng Song, Mariusz Ciorga, Thomas Hupfauer, Junichi Shiogai, Martin Utz, Dieter Schuh, Dominique Bougeard and Dieter Weiss, *Phys. Status Solidi B* **251**, 1725 (2014)
45. J. Schliemann, *Int. J. Mod. Phys. B* **20**, 1015 (2006)
46. E. M. Hankiewicz and G. Vignale, *J. Phys.: Condens. Matter* **21**, 253202 (2009)
47. Jairo Sinova, Sergio O. Valenzuela, J. Wunderlich, C. H. Back, T. Jungwirth, *Rev. Mod. Phys.* **87**, 1213 (2015)
48. V.K. Dugaev, M.Inglot, E.Ya.Sherman, J.Barnas, *Journal of Magnetism and Magnetic Materials*, **324**, 3573 (2012)
49. Seng Ghee Tan, Mansoor B. A. Jalil, Cong Son Ho, Zhuobin Siu & Shuichi Murakami, *Scientific Reports* **5**, 18409 (2015)
50. G Schmidt, *J. Phys. D: Appl. Phys.* **38**, R107 (2005)
51. J. K. Furdyna and N. Samarth, *J. Appl. Phys.* **61**, 3526 (1987)
52. H. Ohno, A. Shen, F. Matsukura, A. Oiwa, A. Endo, S. Katsumoto, and Y. Iye, *Appl. Phys. Lett.* **69**, 363 (1996)

53. I. Rashba, Phys. Rev. B **62**, R16267(2000)
54. G. Lampel, Phys. Rev. Lett. **20**, 491 (1968)
55. M.I. D'yakonov & V.I. Perel, Sov. Phys. JETP, **33** 1053 (1971)
56. M.I. D'yakonov & V.I. Perel, Zh. ETF Pis. Red, **13**, 206 (1971)
57. A. Hirohata, S. J. Steinmueller, W. S. Cho, Y. B. Xu, C. M. Guertler, G. Wastlbauer, and J. A. C. Bland, Phys. Rev. B **66**, 035330 (2002)
58. P. K. Johnny Wong, Wen Zhang, Jing Wu, Iain G. Will, Yongbing Xu, Ke Xia, Stuart N. Holmes, Ian Farrer, Harvey E. Beere & Dave A. Ritchie, Scientific Reports **6**, 29845 (2016)
59. J A C Bland, S J Steinmuller, A Hirohata, W S Cho, Y B Xu, T Trypiniotis and S N Holmes, J. Phys. D: Appl. Phys. **36**, 2204(2003)
60. Saroj P. Dash, Sandeep Sharma, Ram S. Patel, Michel P. de Jong & Ron Jansen, Nature **462**, 491 (2009)
61. M. Johnson, R. H. Silsbee, Phys. Rev. Lett. **55**, 1790 (1985)
62. Xiaohua Lou, Christoph Adelmann, Scott A. Crooker, Eric S. Garlid, Jianjie Zhang, K. S. Madhukar Reddy, Soren D. Flexner, Chris J. Palmström and Paul A. Crowel, Nature Phys. **3**, 197 (2007)
63. F. G. Monzon, H. X. Tang, and M. L. Roukes, Phys. Rev. Lett. **84**, 5022 (2010)
64. G. Salis, R. Wang, X. Jiang, R. M. Shelby, and S. S. P. Parkin, Appl. Phys. Lett. **87**, 262503 (2005)
65. Chinkhanlun Guite and V. Venkataraman, Phys. Rev. Lett. **107**, 166603 (2011)

66. Y.K. Kato, R.C. Myers, A.C. Gossard, D.D. Awschalom, *Science* **306**, 1910 (2004)
67. J. Wunderlich, B. Kaestner, J. Sinova and T. Jungwirth, *Phys. Rev. Lett.* **94**, 047204 (2005)
68. V. Sih, R. C. Myers, Y. K. Kato, W. H. Lau, A. C. Gossard and D. D. Awschalom, *Nature Phys.* **1**, 31 (2005)
69. S. Matsuzaka, Y. Ohno, and H. Ohno, *Phys Rev. B* **80**, 241305 (R) (2009)
70. Yuriy V Pershin and Massimiliano Di Ventra, *J. Phys.: Condens. Matter* **20**, 025204 (2008)
71. A. Bakun, *Pis'ma Zh. Eksp. Teor. Fiz* **40**, 464. (1984)
72. K. Ando, M. Morikawa, T. Trypiniotis, Y. Fujikawa, C. H. W. Barnes, and E. Saitoh, *Appl. Phys. Lett.* **96**, 082502 (2010)
73. K. Ando, M. Morikawa, T. Trypiniotis, Y. Fujikawa, C. H. W. Barnes, and E. Saitoh, *J. Appl. Phys.* **107**, 113902 (2010)
74. A.A. Bakun, B.P. Zakharchenya, A.A. Rogachev, M.N. Tkachuk, V.G. Fleisher, *Sov. Phys. JETP Lett.* **40**, 1293 (1984)
75. M. Idrish Miah, *J. Phys. D: Appl. Phys.* **40**, 1659 (2007)
76. M. Ehlert, C. Song, M. Ciorga, M. Utz, D. Schuh, D. Bougeard, and D. Weiss, *Phys. Rev. B* **86**, 205204 (2012)
77. G.Y. Guo, Yugui Yao, and Qian Niu, *Phys. Rev. Lett.* **94**, 226601 (2005)
78. Wang-Kong Tse and S. Das Sarma, *Phys. Rev. Lett.* **96**, 056601 (2006)

79. Hans-Andreas Engel, Bertrand I. Halperin, and Emmanuel I. Rashba, *Phys. Rev. Lett.* **95**, 166605 (2005)
80. F. Bottegoni, A. Ferrari, G. Isella, M. Finazzi, and F. Ciccacci, *Phys. Rev. B* **88**, 121201(R) (2013)
81. Liu, L., T. Moriyama, D. C. Ralph, and R. A. Buhrman, *Phys. Rev. Lett.* **106**, 036601 (2011)
82. Seki, T., I. Sugai, Y. Hasegawa, S. Mitani, and K. Takanashi, *Solid State Commun.* **150**, 496 (2010)
83. Valenzuela, S. O., and M. Tinkham, *Nature* **442**, 176 (2006)
84. X.Wang, C. O. Pauyac, and A. Manchon, *Phys. Rev. B* **89**, 054405 (2014)
85. Simranjeet Singh, Marta Anguera, Enrique del Barco, Ross Springell and Casey W. Miller, *Appl. Phys. Lett.* **107**, 232403 (2015)
86. O. Mosendz, J. E. Pearson, F. Y. Fradin, G. E. W. Bauer, S. D. Bader, and A. Hoffmann, *Phys. Rev. Lett.* **104**, 046601 (2010)
87. K. Kondou, H. Sukegawa, S. Mitani, K. Tsukagoshi, and S. Kasai, *Appl. Phys. Express* **5**, 073002 (2012)
88. M. Morota, Y. Niimi, K. Ohnishi, D. H. Wei, T. Tanaka, H. Kontani, T. Kimura, and Y. Otani, *Phys. Rev. B* **83**, 174405 (2011)
89. L.H. Teng, K. Chen, J.H. Wen, W.Z. Lin and T.S. Lai, *J. Phys. D: Appl. Phys.* **42**, 135111 (2009)
90. S. Krishnamurthy, M. van Schilfgaarde and N. Newman N, *Appl. Phys. Lett.* **83**, 1761 (2003)

91. H. A. Macleod, *Thin Film Optical Filters*, Institute of Physics, London, (2001)
92. E. D. Palik, *Optical Constants of Solids*, Vol 1, Academic Press San Diego, CA (1998)
93. H Kurebayashi, T Trypiniotis, K Lee, C Moutafis, S Easton, A Ionescu, J A C Bland¹ and C H W Barnes, *J. Phys. D: Appl. Phys.* **43**, 305001 (2010)
94. Optical spin injection in semiconductor I Gorczyca, P Pfeffer and W Zawadzki, *Semicond. Sci. Technol.* **6**, 963 (1991)
95. D.A. Anderson and N. Apsley, *Semicond. Sci. Technol.* **1**, 187 (1986)
96. G.E. Stillman and C.M. Wolfe, *Thin Solid Films* **31**, 69 (1976)
97. M. Lundstrom, *Fundamentals of Carrier Transport*, Cambridge University Press, London (2000)
98. J. Kainz, U. Rössler and R. Winkler, *Phys Rev. B* **70**, 195322 (2004)
99. A. Dyson and B.K. Ridley, *Phys. Rev. B* **69**, 125211 (2004)
100. M. W. Wu, C. Z. Ning, *Physica Status Solidi (B)*, **222**, 523 (2000)
101. I. Vurgaftman, J. R. Meyer and L. R. Ram-Mohan, *J. Appl. Phys.* **89**, 5815 (2001)
102. R. Kalibjian and K. Mayeda, *Solid-State Electron.* **14**, 529 (1971)
103. H. Kurebayashi, S. J. Steinmuller, J. B. Laloe, T. Trypiniotis, S. Easton, A. Ionescu, J.R. Yates and J.A.C. Bland, *Appl. Phys. Lett.* **91**, 102114 (2007)
104. C. Y. Chang and S. M. Sze, *Solid-State Electron.* **13**, 727 (1970)
105. S.D. Singh, Ph.D Thesis, Homi Bhabha National Institute, Anushakti Nagar, Mumbai (2012)

106. Albert G. Baca, Carol I.H. Ashby, *Fabrication of GaAs devices*, Institution of Electrical Engineers, London (2005)
107. J.R. Sheats, B. W. Smith, *Microolithography: science and technology*, Marcel Dekker, Inc., New York (1998)
108. Inder P. Batra, *Metallization and Metal-Semiconductor Interfaces*, Plenum Press, New York (1998)
109. J. M. Woodall and J. L. Freeouf, *J. Vac. Sci. Technol.* **19**, 794 (1981)
110. J. C. Kemp, *J. Opt. Soc. Am.* **59**, 950 (1969)
111. J. C. Kemp, *Polarized light and its interaction with modulation devices*, Hinds Instruments, Inc., Hillsboro, OR, (1987)
112. M. Wassermeier, H. Weman, M. S. Miller, P. M. Petroff, and J. L. Merz, *J. App. Phys.* **71**, 2397 (1992)
113. M. Idrish Miah, *Optics Communications* **284** ,1254 (2011)
114. *PEM operating manual*, Hinds Instruments, Inc., Hillsboro, OR, (1987)
115. Baoliang Wang and Jennifer List, *Proc. SPIE* vol. **5888**, 436 (2005)
116. Arjun Joshua and V. Venkataraman, *Rev. Sci. Instrum.*, **80**, 023908 (2009)
117. Y.F. Chao, P.L. Lin, *Optics Communications* **283** , 4582 (2010)
118. H. Ma, Z. Jin, L. Wang, and G. Ma, *J. Appl. Phys.* **109**, 023105 (2011)
119. R.A. Matula, *J. Phys. Chem. Ref. Data* **8**, 1147 (1979)
120. R. H. Cornely and T. A. Ali, *J. App. Phys.* **49**, 4094 (1978)
121. W. Ma, X. Zhang, and K. Takahashi, *J. Phys. D: Appl. Phys.* **43**, 465301(2010)

122. S. M. Sze, *Physics of Semiconductor Devices*, 3rd ed., Wiley-Inter science, New York (2006).
123. Abhishek Chatterjee, Shailesh K. Khamari, V. K. Dixit, S. M. Oak, and T. K. Sharma, *J. App. Phys.* **118**, 175703 (2015)
124. Y. Ji, A. Hoffmann, J. S. Jiang, and S. D. Bader, *Appl. Phys. Lett.* **85**,6218 (2004)
125. G. Y. Guo, *J. Appl. Phys.* **105**, 07C701 (2009)
126. G. Mihajlovic, J. E. Pearson, M. A. Garcia, S. D. Bader, and A. Hoffmann, *Phys. Rev. Lett.* **103**, 166601 (2009)
127. T. Seki, I. Sugai, Y. Hasegawaa, S. Mitani, and K. Takanashi, *Solid State Commun.* **150**, 496 (2010)
128. T. Seki, Y. Hasegawa, S. Mitani, S. Takahashi, H. Imamura, S. Maekawa, J. Nitta, and K. Takanashi, *Nature Mater.* **7**, 125 (2008)
129. H. Kurebayashi, T. Trypiniotis, K. Lee, S. Easton, A. Ionescu, I. Farrer, D. A. Ritchie, J. A. C. Bland, and C. H. W. Barnes, *Appl. Phys. Lett.* **96**,022505 (2010)
130. J. M. Mac Laren, X. G. Zhang, W. H. Butler, and X. Wang, *Phys. Rev. B* **59**, 5470 (1999)
131. S. Saikin, Yu. V. Pershin, V. Privman, *IEEE Proc. Circuits Devices Syst.* **152**, 366 (2005)
132. D. J. Hilton and C. L. Tang, *Phys. Rev. Lett.* **89**, 146601 (2002)

133. N. Okamoto, H. Kurebayashi, T. Trypiniotis, I. Farrer, D. A. Ritchie, E. Saitoh, J. Sinova, J. Masek, T. Jungwirth & C. H. W. Barnes, *Nature Materials* **13**, 932 (2014)
134. Michael E. Flatte and Jeff M. Byers, *Phys. Rev. Lett.* **84**, 4220 (2000)
135. Abhishek Chatterjee, Shailesh K. Khamari, R. Kumar, V. K. Dixit, S. M. Oak, and T. K. Sharma, *Appl. Phys. Lett.* **106**, 023509 (2015)
136. J. Hübner, S. Döhrmann, D. Hägele, and M. Oestreich *Phys. Rev. B* **79**, 193307 (2009)
137. M. Idrish Miah, *Spectroscopy Letters* **42**, 8 (2009)
138. L. Kronik, Y. Shapira, *Surf. Sci. Rep.* **37**, 1 (1999)
139. H. J. Weber and G. B. Arfken, *Essential Mathematical Methods for Physicists*, Academic Press, California (2004)
140. G. Duggan and G. B. Scott, *J. Appl. Phys.* **52**, 407 (1981)
141. D.K. Schroder, *Semiconductor Material and Device Characterization*, 3rd ed., John Willey & Sons, Inc., New Jersey (2006)
142. G. M. Martin, J. P. Farges, G. Jacob, J. P. Hallais and G. Poiblaud, *J. Appl. Phys.* **51**, 2840 (1990)
143. G. B. Lush, M. R. Melloch, M. S. Lundstrom, H. F. MacMillan, and S. Asher, *J. Appl. Phys.* **74**, 4694 (1993)
144. D.E. Aspnes, *Surface Sci.* **132**, 406 (1983)
145. Raseong Kim, Mark Lundstrom, arXiv:0811.0116 (2008)
146. F. Cadiz, D. Paget, and A. C. H. Rowe, *Phys. Rev. Lett.* **111**, 246601 (2013)

147. R.C. Miller, W. T. Tsang, and W. A. Nordland, Jr, Phys. Rev. B **21**, 1569 (1980)
148. R. I. Dzhioev, B. P. Zakharchenya, V. L. Korenev, and M. N. Stepanova, Phys. Solid State **39**, 1765 (1997)
149. Shailesh K. Khamari, S. Porwal, V. K. Dixit and T. K. Sharma, Appl. Phys. Lett. **104**, 042102 (2014)
150. R. Giri, S. Cronenberger, M. Vladimirova, D. Scalbert, K. V. Kavokin and M. M. Glazov, M. Nawrocki, A. Lemaitre and J. Bloch, Phys. Rev. B **85**, 195313 (2012)
151. A.N. Chantis, M. van Schilfgaarde, T. Kotani, Phys. Rev. Lett. **96**, 086405 (2006)
152. J. M. Jancu, R. Scholz, E. A. de Andrada e Silva, and G. C. La Rocca, Phys. Rev. B **72**, 193201 (2005)
153. Jacob J. Krich and Bertrand I. Halperin, Phys. Rev. Lett. **98**, 226802 (2007), supplementary information there in.
154. R. J. Seymour, M. R. Junnarkar, and R. R. Alfano, Phys Rev. B **24**, 3623 (1981)
155. H. Mayer and U. Rossler, Solid State Comm. **87**, 81(1993)
156. A. Bruno-Alfonso, N. Porras-Montenegro, E. Reyes-Gomez, L.E. Oliveirad, Physica E **40**, 1464 (2008)
157. B. Andrei Bernevig and Shou-Cheng Zhang, arXiv:cond-mat/0412550 (2004)

158. Cosimo Gorini, Ulrich Eckern, and Roberto Raimondi, *Phys. Rev. Lett.* **115**, 076602 (2015)
159. S. Kuwata, *Journal of Physics: Conference Series* **150**, 022048 (2009)
160. Lingjun Zhou, Vahram L. Grigoryan, Sadamichi Maekawa, Xuhui Wang, and Jiang Xiao, *Phys. Rev. B* **91**, 045407 (2015)
161. Eugene M. Chudnovsky, *Phys. Rev. Lett.* **99**, 206601 (2007)
162. E. M. Hankiewicz, G. Vignale, and M. E. Flatte, *Phys. Rev. Lett.* **97**, 266601 (2006)
163. Sebastian Tolle, Cosimo Gorini, and Ulrich Eckern, *Phys. Rev. B* **90**, 235117 (2014)
164. N.S. Averkiev, L.E. Golub, *Phys. Rev.* **60**, 15582 (1999)
165. M.I. D'yakonov, V.Yu. Kachorovskii, *Sov. Phys. Semicond.* **20**, 110 (1986)
166. X. Cartoixà, D.Z.-Y. Ting, Y.-C. Chang, *Phys. Rev. B* **71**, 045313 (2005)
167. Satoshi Iba, Hiroshi Fujino, Toshiyasu Fujimoto, Shinji Koh, Hitoshi Kawaguchi, *Physica E* **41**, 870 (2009)
168. A. Kawaharazuka, M. Ramsteiner, J. Herfort, H.-P. Schönherr, H. Kostial, and K. H. Ploog, *Appl. Phys. Lett.* **85**, 3492 (2004)
169. Yongke Sun, Scott E. Thompson and Toshikazu Nishida, *Strain Effect in Semiconductors*, Springer (2010)
170. Jun-Wei Luo, Gabriel Bester, and Alex Zunger, *Phys. Rev. B* **92**, 165301 (2015)

171. S. Pfalz, R. Winkler, T. Nowitzki, D. Reuter, A. D. Wieck, D. Hägele, and M. Oestreich, *Phys. Rev. B* **71**, 165305 (2005)
172. R. Cingolani, W. Stolz, and K. Ploog, *Phys. Rev. B* **40**, 2950 (1989)
173. Ashish Arora and Sandip Ghosh, *J. Phys. D: Appl. Phys.* **47**, 045101 (2014)
174. A. Twardowski, C Hermann, *Phys. Rev. B* **35**, 8144 (1987)
175. Michele Virgilio and Giuseppe Grosso, *Phys. Rev. B* **80**, 205309 (2009)
176. J. Planelles, M. Royo, A. Ballester, M. Pi, *Phys. Rev. B* **80**, 1 (2009)
177. J. Andrzejewski, G. Sek, E. O'Reilly, A. Fiore, J. Misiewicz, *J. Appl. Phys.* **107**, 073509 (2010)
178. H. J. Zhu, M. Ramsteiner, H. Kostial, M. Wassermeier, H.-P. Schönherr, and K. H. Ploog, *Phys. Rev. Lett.* **87**, 016601 (2001)
179. Tibor Fördös, Kamil Postava, Henri Jaffrès and Jaromír Pištora, *J. Optics.* **16**, 065008 (2014)
180. R. Mallory, M. Yasar, G. Itskos, A. Petrou, G. Kioseoglou, A. T. Hanbicki, C. H. Li, O. M. J. van't Erve, B. T. Jonker, M. Shen and S. Saikin, *Phys. Rev. B* **73**, 115308
181. C. E. Pryor and M. E. Flatte, *Phys. Rev. Lett.* **91**, 257901 (2003)
182. B. T. Jonker, A. T. Hanbicki, Y. D. Park, G. Itskos, M. Furis, G. Kioseoglou, A. Petrou, and X. Wei, *Appl. Phys. Lett.* **79**, 3098 (2001)
183. Suparna Pal, S. D. Singh, S. Porwal, T. K. Sharma, S. Khan, J. Jayabalan, Rama Chari and S. M. Oak, *Semicond. Sci. Technol.* **28**, 035016 (2013)

184. P. R. Hammar, B. R. Bennett, M. J. Yang, and Mark Johnson, *Phys. Rev. Lett.* **83**, 203 (1999)
185. B. T. Jonker, Y. D. Park, B. R. Bennett, H. D. Cheong, G. Kioseoglou, and A. Petrou, *Phys. Rev. B* **62**, 8180 (2000)
186. R. M. Stroud, A. T. Hanbicki, Y. D. Park, G. Kioseoglou, A. G. Petukhov and B. T. Jonker, *Phys. Rev. Lett.* **89**, 166602 (2002)
187. Y. Puttison, X. J. Wang, I. A. Buyanova, C. W. Tu, L. Geelhaar, H. Riechert, and W. M. Chen *Appl. Phys. Lett.* **98**, 012112 (2011)
188. C.M. Jan, Y.H. Lee, K. C. Wu, C.K. Lee, *Opt. Express* **19**, 5431 (2011)
189. J. Yeom, B. Yeom, H. Chan, K. W. Smith, S.D. Medina, J.H. Bahng, G. Zhao, W.S. Chang, S.J. Chang, A. Chuvilin, D. Melnikau, A.L. Rogach, P. Zhang, S. Link, P. Král, P. and N.A. Kotov, *Nature mater.* **14**, 66 (2015)
190. K. Dholakia and T. Čižmár, *Nature Photon.* **5**, 335 (2011)
191. F.S. Jacob, H. Krauter, R.K. Olsson, B. Julsgaard, H. Hammerer, I. Cirac, and E.S. Polzik, *E.S. Nature* **443**, 557 (2006)
192. B. Kunnen, C. Macdonald, A. Doronin, S. Jacques, M. Eccles, I. Meglinski, *J. Biophotonics* **8**, 317 (2015)
193. Dennis Goldstein, *Polarized Light*, 2nd edition; Marcel Dekker, Inc. New York (1993)
194. P.N. Clout, M.A. Haque, and D.W. O. Heddle, *J. of Phys. E: Sci. Instrum.* **4**, 893 (1971)
195. J. Lee, J. Koh, and R.W. Collins, *Rev. Sci. Instrum.* **72**, 1742 (2001).

196. V. L. Korenev, I.A. Akimov, S.V. Zaitsev, V.F. Sapega, L. Langer, D.R. Yakovlev, Y.A. Danilov and M. Bayer, *Nature Commun.* **3**, 959 (2012)
197. R. M. A. Azzam, *Opt. Lett.* **10**, 309 (1985)
198. R. Vrijen, E. Yablonovitch, *Physica E* **10**, 569 (2001)
199. E. Yablonovitch, H.W. Jiang, H. Kosaka, H.D. Robinson, D.S. Rao and T. Szkopek, *Proceedings of the IEEE*, **91**, 761 (2003)
200. R. Farshchi, M. Ramsteiner, J. Herfort, A. Tahraoui, and H. T. Grahn, *Appl. Phys. Lett.* **98**, 162508 (2011)
201. S.D. Ganichev, J. Kiermaier, W. Weber, S.N. Danilov, D. Schuh, C. Gerl, W. Wegscheider, W. Prettl, D. Bougeard, and G. Abstreiter, *Appl. Phys. Lett.* **91**, 091101 (2007)
202. S.N. Danilov, B. Wittmann, P. Olbrich, W. Eder, W. Prettl, L.E. Golub, E. V. Beregulin, Z.D. Kvon, N. N. Mikhailov, S.A. Dvoretzky, V.A. Shalygin, N.Q. Vinh, A.F. G. van der Meer, B. Murdin and S.D. Ganichev, *J. Appl. Phys.* **105**, 013106 (2009)
203. C. Drexler, N. Dyakonova, P. Olbrich, J. Karch, M. Schafberger, K. Karpierz, Y. Mityagin, M. B. Lifshits, F. Teppe, O. Klimenko, Y. M. Meziani, W. Knap and S.D. Ganichev, *J. Appl. Phys.* **111**, 124504 (2012).
204. Y. Yang, R. C. da Costa, M. J. Fuchter, and A. J. Campbell, *Nature Photon.* **7**, 634 (2013)

10. Appendices

Appendix A

Spin-Orbit interaction

The effect of relativistic effect in atomic and condensed matter physics, ensures that, an electron moving in the atomic potential $V(\mathbf{r})$ feels an effective magnetic field (B_{eff}) acting on its spin [A1]. This is the origin of spin orbit coupling in semiconductor. The presence of B_{eff} implies that the spin polarization of the carriers undergoes relaxation due to the variation of B_{eff} with momentum. Traditionally, B_{eff} is characterized by the energy splitting it induces (Ω) between the electrons of two different spin. In semiconductors, $V(\mathbf{r})$ includes many other forms of potential other than the atomic core, which are the source of inversion asymmetry. In an ideal, defect free semiconductor nanostructures, three principal sources of inversion asymmetry exist, which are explained as.

(i) Bulk inversion asymmetry (BIA)

This is the inversion asymmetry, related to the crystal structure of bulk constituents of nanostructures, such as the asymmetry intrinsic to the zinc-blende crystal structure.

The effective magnetic field because of BIA is given by

$$\Omega_{BIA}(k) = 2\gamma_D \left[k_x(k_y^2 - k_z^2)\hat{x} + k_y(k_z^2 - k_x^2)\hat{y} + k_z(k_x^2 - k_y^2)\hat{z} \right] \quad (A1)$$

It can be seen that the effective field is perpendicular to the wave vector k and its magnitude depends upon the direction of k . Particularly, it vanishes for k along the (111) and (100) symmetry directions and maximum for (110) direction. The spin orbit interaction originating from this mechanism is popularly called Dresselhaus spin orbit interaction.

(ii) Structural Inversion asymmetry (SIA)

SIA refers to the arrangements of semiconducting materials which are not inversion symmetric, such as asymmetric quantum well, single interface hetero junctions or Schottky barrier.

$$\Omega_{SIA}(k) = 2\beta \left[(k_y E_z - k_z E_y)\hat{x} + (k_z E_x - k_x E_z)\hat{y} + (k_x E_y - k_y E_x)\hat{z} \right] \quad (A2)$$

This effective magnetic field is always perpendicular to the effective electric field, irrespective of the crystallographic directions.

The relative strength of Ω_{BIA} and Ω_{SIA} depends on the structure considered. In a ideal symmetric quantum well system, SIA will vanish. Otherwise, both will contribute to the effective magnetic field.

(iii) Native Interface asymmetry (NIA)

Another case of asymmetry arises even in otherwise symmetric quantum wells, where the barrier and quantum wells have different compositions of both cation and anion [A2]. This does not arise for the usual GaAs/AlGaAs quantum wells, because

both have common anion. One of the example can be GaAs-InP system, where two type of interference bonds are possible at the interface; Ga-P and In-As, neither of which appear in the well or barrier material. The growth direction has profound effect on the magnitude of NIA. As is well known, quantum wells grown along (001) have alternating planes of cations and anions. Thus interface bonds are perfectly oriented. On the other hand, quantum wells grown along (110) directions have planes of mixed anions and cations. Thus it vanishes for (110) quantum wells. Further, interface imperfections drastically reduces the NIA, as it mixes the bonding type significantly.

In a realistic system, all of them are simultaneously present upto various extent along with extrinsic contributions like potential arising from defects and deformations and external electric field. The total effective magnetic field is given as the vector sum of all these contributions.

$$\Omega_{eff} = \Omega_{BIA} + \Omega_{SIA} + \Omega_{NIA} + \Omega_{ext} \quad (A3)$$

References

- A1. M.W. Wu, J.H.Jiang, M.Q.Weng, Physics Reports, **493**, 61(2010)
- A2. Spintronics and quantum computations D. Awschalom, D. Loss, and N. Samarth, *Semiconductor Spintronics and Quantum Computation*, Springer, New York (2002)

Appendix B

Stokes vector and Muller calculus

To analyze the polarization state of light, several calculation methods have been developed including those based on the Jones matrix, coherency matrix, Mueller matrix, and other matrices [B1]. Out of these methods, the Mueller calculus is most generally used to express the polarizing optical elements including linear polarizers, wave plates and compensators [B2]. In this method, light of any arbitrary polarization is described by a (1x4) column matrix called a Stokes vector and the polarizing properties of the optical systems are described by a (4x4) square matrix. The polarizing properties of a sample are also completely characterized by the Mueller matrices.

Any arbitrary light beam, with frequency ω and wave vector k , propagating along z -direction can be represented as two independent orthogonal components, $E_x(z, t)$ and $E_y(z, t)$ that have different amplitudes and phases, given by [B3]

$$\begin{aligned} E_x(z, t) &= E_{0x} \cos(\omega t - kz + \delta_x) \\ E_y(z, t) &= E_{0y} \cos(\omega t - kz + \delta_y) \end{aligned} \tag{B1}$$

The stokes vector such light beam is given by

$$S = \begin{pmatrix} S_0 \\ S_1 \\ S_2 \\ S_3 \end{pmatrix}$$

Where S_0 represents the total intensity of the beam

$$S_0 = E_{0x}^2 + E_{0y}^2$$

S_1 represents the preponderance of linearly horizontally (x) polarized light over linearly vertically (y) polarized light

$$S_1 = E_{0x}^2 + E_{0y}^2$$

S_2 represents the preponderance of linear $+45^\circ$ polarized light over linear -45° polarized light

$$S_2 = 2E_{0x}E_{0y} \cos \delta, \quad \delta = \delta_x - \delta_y$$

S_3 represents the preponderance of right circularly polarized light over left circularly polarized light.

$$S_3 = 2E_{0x}E_{0y} \sin \delta$$

Hence, the following Stokes vectors are implied [B3].

Unpolarized light $\begin{pmatrix} 1 \\ 0 \\ 0 \\ 0 \end{pmatrix}$

Linear (X) polarized light $\begin{pmatrix} 1 \\ 1 \\ 0 \\ 0 \end{pmatrix}$

Linear (Y) polarized light $\begin{pmatrix} 1 \\ -1 \\ 0 \\ 0 \end{pmatrix}$

Left circularly polarized light $\begin{pmatrix} 1 \\ 0 \\ 0 \\ 1 \end{pmatrix}$

The Mueller matrix M for a polarizing optical element is defined as the matrix which transforms an incident Stokes vector S into the exiting (reflected, transmitted, or scattered) Stokes vector S' . i.e.

$$S' = \begin{pmatrix} S'_0 \\ S'_1 \\ S'_2 \\ S'_3 \end{pmatrix} = MS = \begin{pmatrix} m_{01} & m_{02} & m_{03} & m_{04} \\ m_{11} & m_{12} & m_{13} & m_{14} \\ m_{21} & m_{22} & m_{23} & m_{24} \\ m_{31} & m_{32} & m_{33} & m_{34} \end{pmatrix} \begin{pmatrix} S_0 \\ S_1 \\ S_2 \\ S_3 \end{pmatrix}$$

If the light beam is passing through a sequence of polarizing optical elements $n=1,2, \dots, N$, the resultant Mueller matrix is given by the right-to-left product of the individual matrices M_n ,

$$M = M_Q M_{Q-1} \dots M_3 M_2 M_1 = \prod_{n=N}^1 M_n \quad (B2)$$

The Mueller matrix of some of the ideal polarizing elements with transmission axis oriented vertically is given as follows

$$\text{Linear polarizer} \quad \frac{1}{2} \begin{bmatrix} 1 & 1 & 0 & 0 \\ 1 & 1 & 0 & 0 \\ 0 & 0 & 0 & 0 \\ 0 & 0 & 0 & 0 \end{bmatrix}, \quad \text{Wave plate, retardance } \delta \quad \begin{bmatrix} 1 & 0 & 0 & 0 \\ 0 & 1 & 0 & 0 \\ 0 & 0 & \cos \delta & \sin \delta \\ 0 & 0 & -\sin \delta & \cos \delta \end{bmatrix}$$

When a polarizing optical elements with Mueller matrix M is rotated about the light beam by an angle θ keeping the angle of incidence fixed, the resulting Mueller is given by $M(\theta) = R(\theta) M R(-\theta)$.

Here $R(\theta)$ is the rotation matrix given by [3]

$$R(\theta) = \begin{bmatrix} 1 & 0 & 0 & 0 \\ 0 & \cos(2\theta) & -\sin(2\theta) & 0 \\ 0 & \sin(2\theta) & \cos(2\theta) & 0 \\ 0 & 0 & 0 & 1 \end{bmatrix} \quad (B3)$$

References

- B1. R.M.A. Azzam and N.M. Bashara, *Ellipsometry and Polarized Light*, North Holland (1987)
- B2. H. G. Tompkins and E. A. Irene, *Hand book of ellipsometry*, William Andrew, Inc. (2005)
- B3. D.H. Goldstein, *Polarized Light*, CRC Press, Boca Raton (2006)

Appendix C

Electron scattering mechanism in III-V semiconductors

Electrons in semiconductors undergo different type of scattering mechanism, that causes energy and spin relaxation. Depending on the energy of electron (E_e) and temperature of crystal (T), some of the mechanism are dominant over others. In this appendix, the scattering mechanism considered in this work are elaborated. Expression for scattering time is given here. The corresponding energy and spin relaxation times can be estimated by using equation – and – respectively.

(i) Ionized impurity scattering

Ionized impurity scattering corresponds to the scattering of electron by the ionized impurity because of their screened coulomb potential. By considering Hydrogenic coulomb potential of the impurities, the scattering time is given by

$$\frac{1}{\tau_{ii}(E)} = \frac{N_I Z^2 e^4 [\ln(1+y) - y/(1+y)]}{16\sqrt{2}\pi\epsilon^2 \sqrt{m^*} E_e^{3/2}} \quad (C1)$$

$$\text{where } y = \frac{8\epsilon m^* (kT) E_e}{\hbar^2 e^2 n}$$

Here, Z is the ionic charge and N_I is the density of ionized impurity.

(ii) Deformation potential scattering

The acoustic mode lattice vibrations induces position dependent band gap in the materials by deforming the crystal. The potential induced by these deformation is

called deformation potential. Under this scattering mechanism, the scattering time is given by

$$\tau_{dp}(E) = \frac{\pi\hbar^4 \rho s^2}{\sqrt{2} E_1^2 (m^*)^{3/2} (kT)} E_e^{-1/2} \quad (C2)$$

Here ρ is the density of the material, s is the velocity of sound and E_1 is the hydrostatic deformation potential.

(iii) Piezo-electric scattering

In ionized crystal, the atomic displacement caused by acoustic mode lattice vibration induces another potential because of piezo-electric effect. Since the III-V semiconductors are partly ionized, electrons get scattered by piezo-electric scattering process. The scattering time because of this mechanism is given by

$$\tau_{pe}(E_e) = \frac{2\sqrt{2}\pi\hbar^2 \varepsilon}{e^2 P^2 (m^*) kT} E_e^{1/2} \quad (C3)$$

Here ε is the dielectric constant and P is the piezo-electric coupling coefficient.

(iv) Polar optical phonon scattering

Due to the dipole moments formed by optical mode lattice vibrations, electrons get scattered strongly in most of the III-V semiconductors. It is called polar-optical phonon scattering and is the dominant mode of scattering at room temperature. The corresponding relaxation time is given by

$$\frac{1}{\tau_{POP}} = \frac{q^2 \omega_p \left(\frac{k_o}{k_\infty} - 1 \right)}{2\pi k_o \epsilon_o \hbar \sqrt{2E_c/m^*}} \left[n(E_p) \sinh^{-1} \left(\frac{E_c}{E_p} \right)^{1/2} + [n(E_p) + 1] \sinh^{-1} \left(\frac{E_c}{E_p} - 1 \right)^{1/2} \right] \quad (C4)$$

Where $n(E_p) = [\exp(-E_p/kT) - 1]^{-1}$ is the probability that a phonon with energy E_p is present. k_o and k_∞ are the static and high frequency dielectric constant respectively. The first term corresponds to the phonon absorption and the second term corresponds to the phonon emission in the crystal.

(v) Inter-valley scattering

When the kinetic energy of the electron becomes larger than the separation energy of Γ -L and Γ -X valley, inter-valley scattering dominates the scattering rate. The corresponding scattering time is given by

$$\frac{1}{\tau_{iv}} = \frac{\pi D_{iv}^2 V}{2\rho\omega} [n(\omega)g(E_e + \omega - \Delta E_{iv}) + (n(\omega) + 1)g(E_e - \omega - \Delta E_{iv})] \quad (C5)$$

Where, D_{iv} is the inter-valley deformation potential, V is the number of identical valley, ρ is the mass density, $g(E_e)$ is the density of state at E_e , and ΔE_{iv} is the inter-valley separation energy.

References

- C1. D.C. Look, *Electrical characterization of GaAs materials and devices*, John Wiley & Sons, New York, (1989)
- C2. M. Lundstrom, *Fundamentals of Carrier Transport*, Cambridge University Press, London (2000)